

THE UNIVERSITY OF HULL

**SOLIDIFICATION OF METAL ALLOYS IN PULSE
ELECTROMAGNETIC FIELDS**

being a Thesis submitted for the Degree of
Doctor of Philosophy, School of Engineering
in the University of Hull

by

Theerapatt Manuwong,
M.Eng, (Chulalongkorn University, Thailand)

April 2015

Abstract

This research studies the evolution of solidification microstructures in applied external physical fields including in a pulse electric current plus a static magnetic field, and a pulse electromagnetic field. A novel electromagnetic pulse device and a solidification apparatus were designed, built and commissioned in this research. It can generate programmable electromagnetic pulses with tuneable amplitudes, durations and frequencies to suit different alloys and sample dimensions for research at university laboratory and at synchrotron X-ray beamlines.

Systematic studies were made using the novel pulse electromagnetic field device, together with finite element modelling of the multiphysics of the pulse electromagnetic field and microstructural characterisation of the samples made using scanning electron microscopy, X-ray imaging and tomography.

The research demonstrated that the Lorentz force and magnetic flux are the dominant parameters for achieving the grain refinement and enhancing the solute diffusion. At a discharging voltage from 120 V, a complete equiaxed dendritic structure can be achieved for Al-15Cu alloy samples, the strong Lorentz force not only disrupts the growing direction of primary dendrites, it is also enough to disrupts the growing directions of primary intermetallic Al₂Cu phases in Al-35Cu alloy, resulting a refined solidification microstructures. The applied electromagnetic field also has significant effect on refining the eutectic structures and promoting the solute diffusion in the eutectic lamellar structure.

The research has demonstrated that the pulse electromagnetic field is a promising green technology for metal manufacture industry.

Dedication

This thesis is dedicated to my Father, Mother, sister and wife, for their love and support throughout my PhD research.

Acknowledgements

I would like to very gratefully acknowledge the Royal Thai Government for awarding me the PhD scholarship to conduct the research.

I also would like to express my sincere gratitude to my supervisor, Dr Jiawei Mi for his persistent support and encouragement, academic advice and guidance throughout the PhD project, especially when the direction of my research changed in my second year study, and when uncertain issues arose in designing and building the novel electromagnetic field experimental apparatus.

Special thanks go to the academic staff in the School of Engineering University of Hull, including Dr Kevin S Fansey, Dr. Jim Gilbert and Prof Ron Patton and Prof Michael Fagan for their support and encouragement; and the technical staff, particularly Mr Peter L. Kazinczi for helping on designing and building the control system for the electromagnetic field experimental apparatus; Mr Tony Sinclair and Mr Garry Robinson for assistance on microstructural characterisation using scanning electron microscopy, and Mrs Sue Taft for X-ray tomography.

Thanks also go to Prof Patrick Grant of Department of Materials, University of Oxford for allowing me to work with his team together at Beamline B16 of Diamond Light Source to conduct the in situ solidification experiments; and beamline scientist Dr Andrew Bodey of I13 on the excellent support of the tomography experiment at beamline I13.

Last but not least, I would like to thank my classmates, colleagues, and friends for the many stimulating technical discussions with them, and the personal help and friendship received from them, including Mr Wei Zhang, Mr J. C. Khong, Mr Dongyue Tang, Mr T. L. Lee, etc just name a few.

Publications and awarded synchrotron X-ray beamtime

The publications generated from my research and the beamtime awarded for future relevant research are:

1. Manuwong, T., et al. "*Solidification of Al Alloys Under Electromagnetic Pulses and Characterization of the 3-D Microstructures Using Synchrotron X-ray Tomography*", Metallurgical and Materials Transactions A 46, 7, 2908-2915, (2015).

2. Manuwong, T., et al. "*Control of Solidification Microstructure Using Programmable Electro-Magnetic Pulses*", proceeding of 4th International Conference on Advances in Solidification Processes Beaumont Estates, Old Windsor, UK, on 8-11 July 2015.

3. Manuwong, T., et al. "*Shocking the Growing Grains during Solidification by Electro-magnetic Pulses*", proceeding of TMS 2015 144th Annual meeting & Exhibition, Orlando, FL, USA, on 5-19 March 2015.

4. A manuscript titled "3-D microstructure characterization and modelling of Al alloys under Electromagnetic field" is under preparation for Acta Materialia.

5. A proposal titled "In situ tomography study of the evolution of solidification microstructures under magnetic pulses" (proposal ID 20141167) has been awarded 9 shift (3 days) of beamtime by TOMCAT of Swiss Light Source, Paul Scherrer Institute (PSI), Switzerland and the experiment conducted on 10-13 June 2015.

Abbreviation

APS	Advanced photon source
BSRF	Beijing synchrotron radiation facility
CET	Columnar-to-equiaxed transition
DLS	Diamond light source
DS	Directional solidification
DSO	Digital storage oscilloscope
DECP	Direct-contact electric current pulse
EMP	Electromagnetic pulse
EMS	Electromagnetic stirring
EMV	Electromagnetic vibration
EPM	Electromagnetic processing of materials
ESRF	European synchrotron radiation facility
ICD	Induced current density
LINAC	Linear accelerator
MFD	Magnetic flux density
PEC	Pulse electric current
PLW	PicoLog for windows
PMO	Pulse magneto oscillation
PSF	point spread function
RF	Radio frequency

SEM	Scanning electron microscopy
STR	Electron storage ring
SXRR	Synchrotron X-ray radiography
TMF	Travelling magnetic field

List of Symbols

σ_y	Yield strength [MPa]
σ_o	Material constant for the starting strength [MPa]
k_m	Material constant
d	Diameter of grain [μm]
μ	Material permeability [T m/A]
μ_o	Permeability of free space (1.26×10^{-6} [T m/A])
μ_r	Relative permeability of copper
ρ	density of particle [kg/m^3]
μ_a	Linear attenuation coefficient [cm^{-1}]
μ_n	Linear attenuation of each element of the alloy [cm^{-1}]
σ	Material conductivity [cm^{-1}]
w	Weight percentage of each element of the alloy
e	Euler number
F	Lorentz force generated by EMP [N/m^3]
F_L	Lorentz force generated by PEC [mN]
B	magnetic flux density [T]
J_e	Input electric current density for EMP coil [A/m^2]
J	Induced current density inside the melt [A/m^2]
I	Input electric current for the electric circuit [A]
L	Length of EMP coil [mm]

L_a	Active length of the sample for PEC [cm]
G	Temperature gradient [$^{\circ}\text{C}$]
g	Gravity [N/m^2]
N	Number of EMP coil turns [turns]
V	Voltage from the input circuit [V]
V_c	Voltage charged into the capacitor [V]
V_d	Voltage discharged from the capacitor bank [V]
t_c	Charging time [ms]
t_d	Discharge time [ms]
t_{full}	Time to fully charge the capacitor [ms]
t_{pulse}	Time of EMP applied to alloy [ms]
f_d	Discharge frequency [Hz]
I_d	Discharge current [A]
R_1	Resistance of resistor in the charging unit [Ω]
Z	Total impedance of the coil [Ω]
C	Capacitance [μF]
E	Energy stored in the capacitor bank [J]
ρ_l	Density of the liquid metal [kg/m^3]
p	Pressure [N/m^2]
u	Velocity [mm/s]
k_T	Turbulent kinetic energy [mm^2/s^2]
ε	Turbulent energy dissipation [mm^2/s^3]

μ_T	Turbulence viscosity [kg/m·s]
I_t	Identity tensor
∇	Laplace operator
D	Solute diffusion coefficient [m ² /s]
a	Transition distance of atoms [μm]
Γ	Mean transition frequency [Hz]
Pr	Probability of transition in the direction

Note: Symbols in bold are Vector

Contents

Abstract	i
Dedication	ii
Acknowledgements	iii
Publications and awarded beamline	iv
Abbreviation	v
List of Symbols	vii
Contents	x
Chapter 1 : Introduction	1
1.1 Background.....	1
1.2 The structure of the thesis	2
Chapter 2 : Literature reviews	4
2.1 Metallic alloys and the solidification processes	4
2.1.1 Metallic alloys and the mechanical strength	4
2.1.2 The solidification processes and microstructures	5
2.1.3 Directional solidification	10
2.1.4 Microstructure refinement during solidification.....	10
2.1.5 Solidification under external physical fields.....	11
2.1.6 The multiphysics of electromagnetic field	12
2.1.7 Applications of electromagnetic field for grain refinement	17
2.1.8 Summary	22
2.2 A review on X-ray imaging and tomography techniques	24
2.2.1 Synchrotron X-ray	24
2.2.2 X-ray attenuation and absorption contrast.....	26

2.2.3 X-ray phase contrast technique	32
2.2.4 In situ studies of metal solidification	33
2.2.5 X-ray tomography	36
2.2.6 Image processing	37
2.3 Modelling of the multiphysics in pulse magnetic field	42
2.3.1 Modelling of solidification	42
2.3.2 The magnetic flux density	42
2.3.3 The induced current and Lorentz force.....	43
2.3.4 The Lorentz force and fluid flow	44
2.4 Summary.....	45
Chapter 3 : Solidification of Al-15%Cu alloys in a static magnetic field with pulse electric current.....	46
3.1 The experimental apparatus	48
3.1.1 The heaters, sample holder and alloy	48
3.1.2 The magnet and pulse current generator	49
3.2 The experiment setup and experimental parameters	52
3.3 The experimental results	54
3.3.1 Dendrite tip fragmentation	56
3.3.2 Dendrite growth under directional solidification.....	65
3.3.3 The effect of PEC on the solid dendrite arrays	73
3.4 Summary.....	77
Chapter 4 : The electromagnetic pulse device and the solidification apparatus	78
4.1 The principle and circuit design of the EMP device	79
4.2. Simulation and optimisation of the designed circuit	82
4.3 The optimised circuit design	88

4.4 The key components of each functional unit of the EMP device ...	89
4.4.1 The power supply	89
4.4.2 The charging unit	89
4.4.3 The trigger unit.....	90
4.4.4 The pulse generating unit.....	90
4.5 The building and commissioning of the EMP device.....	94
4.5.1 The charging unit	94
4.5.2 The pulse generating unit.....	94
4.5.3 The trigger unit.....	94
4.6 The furnace, casting mould and their integration with the EMP device.....	97
4.7 The commissioning of the EMP device and the measurement of the pulse magnetic flux density	100
4.8 Summary.....	102

**Chapter 5 : Solidification of metal alloys under pulse
electromagnetic fields103**

5.1 The selection of alloys and casting of samples	103
5.1.1 The selection of alloy systems	103
5.1.2 The casting of alloys and samples	106
5.2 Solidification experiments under pulse electromagnetic fields ...	108
5.3 Two dimensional microstructural characterisation of the solidified samples	117
5.3.1 The Sn-18Pb alloy samples	118
5.3.2 The Al-15Cu alloy samples	122
5.3.3 The Al-35Cu alloy samples	131
5.4 Three dimensional microstructural characterisation of the solidified samples, X-ray tomography	137

5.4.1 The Al-15Cu samples	139
5.4.2 The Al-35Cu samples	143
5.4.3 The 3-D eutectic structure of Al-Cu alloys	147
5.5 Summary.....	149
Chapter 6 : Modelling of the multiphysics in pulse electromagnetic fields	150
6.1 The governing equations.....	150
6.2 The computational domains.....	152
6.3 The mesh structure	153
6.4 The boundary and initial conditions	153
6.5 The materials properties	154
6.6 The results of the simulation	158
6.6.1 Magnetic flux density	158
6.6.2 The induced currents.....	166
6.6.3 The Lorentz force	168
6.6.4 The velocity field inside liquid metal.....	172
6.7 Summary.....	176
Chapter 7 : Discussion	177
7.1 The novelty of the EMP device	177
7.1.1 Programmable pulse control.....	177
7.1.2 Systematic and module-based design.....	178
7.1.3 Advanced facility for in situ solidification research	180
7.2 Validation of modeling versus experiment	181
7.3 Dendrite growth in a static magnetic field with PEC	182
7.3.1 Dendrite fragmentation due to natural convection	182
7.3.2 Enhanced melt flow due to PEC.....	182

7.3.3 Effects of PEC on dendrite in semisolid region	183
7.3.4 Effects of PEC on solid dendrite arrays.....	184
7.4 Solidification microstructures in pulse magnetic field	184
7.4.1 Effects of EMP on dendrite growth	184
7.4.2 Effects of EMP on the growth of intermetallic phases.....	187
7.4.3 Effects of EMP on the growth of eutectic phase and solute distribution	189
7.5 The advantage of 3-D microstructure analysis	190
Chapter 8 : Conclusions and future works	192
8.1 Conclusions.....	192
8.2 Future works	193
References	194
List of Figures.....	217
List of Tables	225
Appendices	226

Chapter 1 : Introduction

1.1 Background

Metal alloys are the very important structural and functional materials in human society since civilisation began many thousands of years ago, and continue to be the indispensable materials in man-made products, vehicles and infrastructure in the modern world. The physical, functional and mechanical properties of metal alloys are determined mainly by the chemistry, nano and micro metre scale structures (grain size) and defects (voids and/or inclusions), and their characteristic distributions within the alloys. Generally, the smaller, the grain size, the stronger and tougher, the alloys as defined by the classical Hall-Petch relationship. How to achieve an optimal morphology, size and distribution of the grains and those of the defects to maximise the alloy's mechanical properties are the main driving force for metal alloy research for many years.

Many techniques and industrial practices have been developed to refine the grain size of metal alloys through solidification, solid state deformation plus recrystallisation, etc. The conventional methods of adding external grain refiners to refine the solidification structure of metal alloys have been used in industry for many decades [1]. Those methods have inherent problems. Firstly, different alloys need grain refiners of different chemistry, such as Al-Ti-B for Al-based alloys, Zr for Mg-based alloys, etc [1, 2]. Secondly, different operation practices are needed for different alloys systems, and each of the operation inevitably add extra cost to the manufacturing of the alloys and most likely an adverse impact to the environment. To reduce the environment impact and develop a sustainable and green manufacturing strategy, in the past twenty years or so, many researches have been carried out to develop novel grain refining technologies. The most important developments so far have been the uses of external physical field methods,

such as ultrasound waves and/or electric or magnetic field based methods to control the nucleation and growth of grains during metal solidification because they are essentially generic physical methods irrespective of the chemistry of the alloys involved. For example, direct-contact electric current pulse (DECP) and electromagnetic stirring [3-5] have been showed to be effective techniques for grain refinement. However, many studies have also showed or demonstrated the limitation or drawbacks of some of those techniques. For instance, the DECP method is efficient in processing small volume of melt when the electrical probes used are in direct contact with the melt held in a stationary crucible. But it is difficult to be used in dealing with large volume of melt in a continuous casting operation. The conventional electromagnetic stirring method is a non-contact method, suitable for continuous casting operations. However it is very challenge to apply it uniformly in a large volume of melt, and often a huge amount of energy with dangerously high electric current or voltage [6, 7] are needed. Hence, intensive worldwide researches are continuing to search the generic and energy efficient physical field methods for metal manufacture industry in order to control the gain nucleation and grain growth during solidification regardless of the alloy chemistry. This is the technical and industrial background of the research described in this thesis.

1.2 The structure of the thesis

The thesis consists of 8 chapters as detailed below.

Chapter 1 is a brief introduction of the technical and industrial background concerning the research, and the structure of the thesis.

Chapter 2 reviews the literatures that are directly relevant to the research, and they are grouped into four sections: (1) metallic alloys and solidification processes, (2) the external physical fields, (2) material characterisation using synchrotron X-ray, and (4) computational modelling.

Chapter 3 describes in details the in situ synchrotron X-ray studies of dendrite growth and the fragmentation behaviour under the pulse electric current, including the experimental apparatus and setup, the resulting X-ray images, the processing of the images, and the underlying science revealed by those images.

Chapter 4 describes in details the design, building and commissioning of an electromagnetic pulse (EMP) device and the solidification apparatus, and their integration to form a novel EMP solidification apparatus.

Chapter 5 presents the metal samples and their microstructures manufactured using the EMP device under different solidification conditions. The microstructures of the alloys with and without EMP treatment are characterised in 2-D using optical and scanning electron microscopy, and in 3-D using Synchrotron X-ray tomography.

Chapter 6 describes the computational model developed to simulate the multiphysics of the pulse electromagnetic field, including the pulse magnetic flux density, the induced current, the pulse Lorentz force and melt flow velocity field. The validations of the simulated magnetic flux densities versus the measured ones are also presented.

Chapter 7 discusses in details the novelties of the EMP device developed, the effects of the EMP parameters on the formation of different microstructures, and the dominant control parameters identified via the comparison between experiments and simulations.

Chapter 8 is the conclusion chapter, summarising the major findings and contributions of the research to this important research field. Possible future directions to continue this work are also briefly discussed.

Chapter 2 : Literature reviews

In this chapter, the literatures that are relevant to this research are critically analysed and reviewed. It consists of three parts: (1) the fundamental and applied research concerning the solidification of metal alloys under external physical fields, (2) X-ray imaging and tomography techniques that were used in this research for the characterisation of the macro/microstructures of the alloys made under different solidification conditions, and (3) the finite element based multiphysics modelling methodologies that were used in this research to simulate the multiphysics phenomena in pulse electromagnetic fields.

2.1 Metallic alloys and the solidification processes

2.1.1 Metallic alloys and the mechanical strength

Metallic alloys are the widely used structural materials in human society, and from the mechanical property point of view, a combination of high strength, high ductility, low density are often needed. Depending on the applications, high temperature creep strength or fatigue or fracture toughness may also be required for the materials. The mechanical strength of metal alloys is predominantly governed by the size of the grains as described by the Hall-Petch relationship [8-12]:

$$\sigma_y = \sigma_0 + k_m d^{-\frac{1}{2}} \quad (2.1)$$

Where σ_y is the yield strength, σ_0 is a material constant for the starting strength, k_m is a material constant and d is the diameter of grain.

This equation shows that the yield strength is inversely-proportional to the square root of the grain size. So when the grain size of material is decreased, the material yield strength is increased. Therefore, reducing the grain size, i.e. the microstructure of materials would normally increase the strength of the materials [13], as the example shown in Fig. 2.1. The common processing technology used to refine the grain size of materials is to control the nucleation and grain growth during solidification. For metallic alloys in the as-cast condition, the most dominant factors to determine their mechanical properties are the morphology and grain size of the microstructures plus any casting defects.

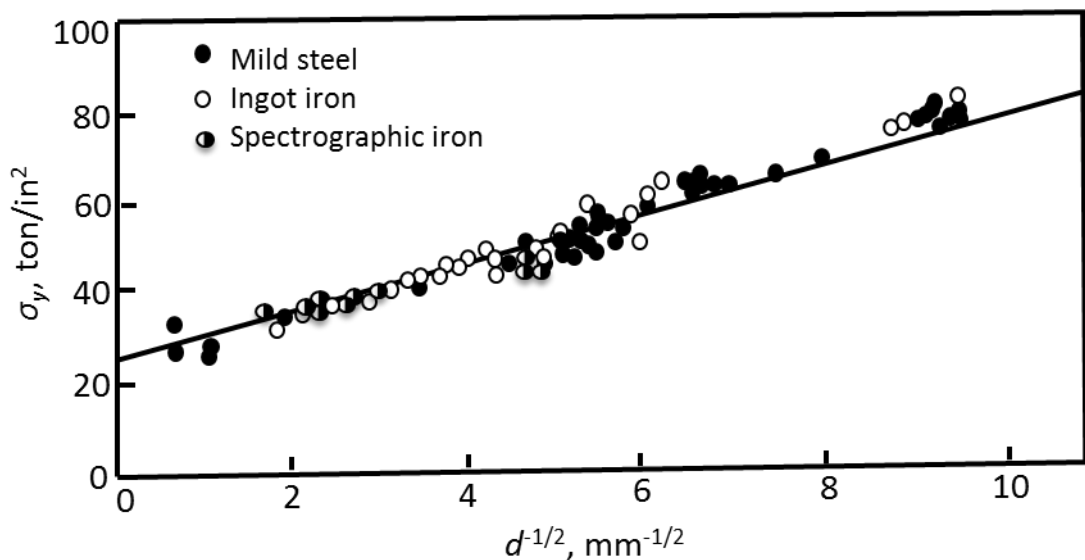


Fig. 2.1. The relationship of grain size and yield stress of steel and iron [13]

2.1.2 The solidification processes and microstructures

When liquid metal is cooled to below the melting point, phase changes from liquid to solid occur, and this process is generally called solidification. There are two main stages of solidification: grain nucleation and crystal growth (solid-liquid interface movement) [14].

Nucleation is the step where the solute molecules dispersed in the solvent start to gather into cluster. Crystal growth is the subsequent growth of the nuclei that succeed in achieving the critical cluster size. When cluster reaches a critical size, it becomes a stable nucleus and continues to grow. The crystals increase in size by progressive addition of atoms and grow until they meet other crystals. In engineering materials, a crystal is usually referred to as a grain. A grain is simply a crystal without smooth faces because its growth is impeded by contact with another grain or a boundary surface. The interface formed between grains is called grain boundary. In metals, the crystals normally form a pattern consisting of a main branch with many side branches. A crystal with this morphology is called a dendrite.

2.1.2.1 Dendrite structure

Generally, solidification leads to two types of grain morphologies: columnar and equiaxed. In most industrial applications the desired morphology of grains is fine equiaxed grains. Moreover, according to the Hall-Petch relationship, fine grain size gives higher yield strength and more isotropic and uniform mechanical properties [15].

When solidification starts from a 'cold' surface, the nuclei of crystals initially are formed from the chill wall of mould. As the heat is extracted by the mould wall to environment, the grains grow against the direction of the heat flow to form columnar dendrite microstructure called 'the directional growth', this is a columnar zone. Finally, the inner equiaxed growth occurred again due to the flow of heat from the dendrites in the liquid zone. They can also originate from broken dendrite side-branches [16]. Fig. 2.2 shows the formation of dendrite microstructures.

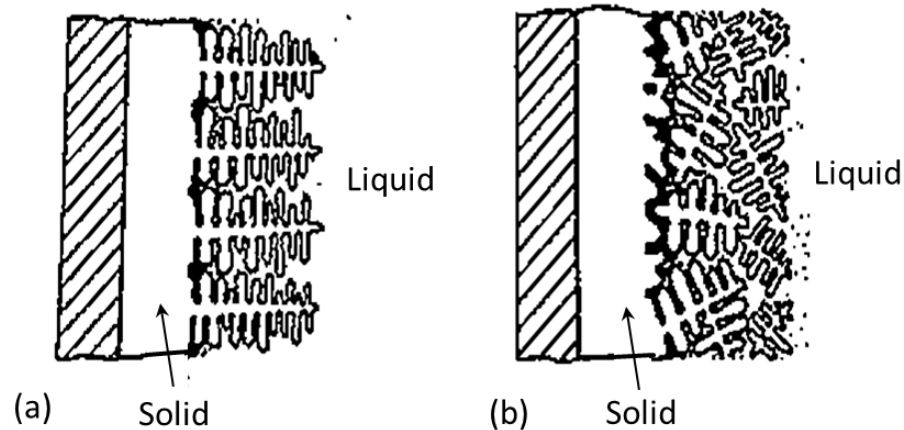


Fig. 2.2. The formation of dendrite microstructures during the solidification, (a) columnar dendrite and (b) equiaxed dendrite [16].

Columnar-to-equiaxed transition (CET) [17-20] occurs during columnar growth when new grains grow ahead of the columnar front in the undercooled liquid. Under certain conditions, these grains can stop the columnar growth and then the solidification microstructure becomes equiaxed. A transition of columnar to equiaxed growth occurs when the nucleation of equiaxed grain formed in the liquid ahead of the columnar zone.

Dendrite microstructure is usually the tree-like pattern which has trunk and branches, often called dendritic arms. Depending on the competitive mechanism between heat and solute transfer, the branch can develop into 2nd, 3rd or higher order arms.

2.1.2.2 Defects in casting

During solidification, the common defects [21] normally occur in casting are described in following section.

Chemistry segregation of solutes often occurs upon freezing of alloys. Segregation refers to non-uniformity of chemical composition [22], is a

consequence of rejection of solutes by the solid into the interdendritic liquid. Segregation also is subdivided into macrosegregation and microsegregation. Microsegregation results from freezing of solute-enriched liquid in the interdendritic spaces. Macrosegregation is non-uniformity of composition in the cast section on a larger scale.

Metal alloy shrinks during solidification because its volume in the solid state is smaller than that in the liquid state. If a solidifying metal cannot be fed by its surrounding liquid due to some blockage to compensate the shrinking during solidification, then shrinkage defects or voids will occur inside the solidified metal, and this is called volumetric shrinkage [23]. Shrinkage is sometime result of bad design of mould such as sprue is too thin and too long so the melt is cooled before flow into the cavity of mould. Moreover, shrinkage porosity can be occurred when the alloys have a wide freezing range.

Porosity is small voids within the solid metal after solidification [24]. Porosity is a common casting defect that results from insufficient feeding. As liquid metal flows through the interdendritic regions, the dendrite arms continue to thicken and minimize interdendritic feeding. During solidification, some interdendritic regions become blocked. The blocked interdendritic liquid shrinks as it solidifies, thus causing interdendritic porosity in the casting.

Hot tears are irregularly internal or external cracks occur immediately after the metal has solidified due to the metal is weak when it is hot [25, 26]. Hot tears form at the grain boundaries or at the interdendritic regions. When it solidifies the residual stresses in the solid metal cause the hot tear. Hot tears often occur on poorly designed mould such as having sudden section changes or having no proper fillets and improper placement of gates and risers or incorrect pouring temperatures.

Bubbles damage occurs from the gas bubbles inside liquid metal. The bubbles can be held by liquid metal during solidification, however, after solidification the solid metal release gas out in the form of bubbles, so porosity and pore form [27]. Porosity and pore regularly occurs on the surface and inside of the solid metal, respectively.

Inclusion is a metal contamination often caused by 'slag' in liquid metal [28]. Some of slag is metal oxides, nitrides, carbides, or sulphides which are trapped in the liquid metal during flowing into the mould. They can come from material that is eroded from furnace or contaminates from the mould. Generally, microstructure and defects formed during solidification are very important factor in determining the properties and quality of casting products [29].

Reasons for these defects are usually not well-prepared melt and mistakes in the casting. The defects give non-uniformly microstructure of material effects to the mechanical properties of materials.

Casting defects have a detrimental effect on mechanical properties not only fatigue life, but also tensile strength and fracture toughness by stress concentration and reduction of effective area. Tensile, fracture toughness and fatigue strength have very good linear relationship with defect volume fraction because maximum defect area fraction or size may be dependent on defect volume fraction [30].

In summary, the mechanical properties of materials are determined by all factors mentioned above. The required microstructure for the enhancement of mechanical properties is fine equiaxed grain and uniformly microstructure thus the grain refinement is necessary. When the cast grain size is reduced (grain changes from columnar to equiaxed) or the structure is globular instead of dendritic the mechanical properties of castings is improved [12, 14, 31, 32].

2.1.3 Directional solidification

Directional solidification (DS) is a special casting process, designed to control the growth of solidification microstructure and to form a desired direction of metal structure. Directional solidification occurs when an appropriate thermal gradient established in the gap between a hot zone and a cold zone during crystal growth. This process can be used to avoid the formation of grain boundaries, particularly in the direction perpendicular to the dendrite growth direction. Directional solidification technology [33] is also an important research methodology for studying fundamental solidification theory [34] because directional solidification can achieve controllable cooling rates with a broad range of solidification structure formed from near-equilibrium to far-from equilibrium conditions [34].

2.1.4 Microstructure refinement during solidification

As mentioned in previous sections, the mechanical properties of cast alloys, such as strength and ductility, are mainly determined by the grain structure and defect formed during solidification processes. To achieve an optimal morphology, size and distribution of the grains and those of the defects (voids and/or inclusions) in order to maximise the alloy's mechanical properties are the main driving force for research concerning metal alloys for many years.

Several methods are known that can realise grain refinement in solidification processes such as adding external grain refiners [35], cooling the alloys by rapidly extracting the heat away during solidification (rapid solidification) [36], stirring or "shaking" the solidifying melt by mechanical and/or electromagnetic vibrations [37], or ultrasonic waves [38].

The basic mechanism to refine solidification microstructure is to increase the nucleation density and control the grain growth. The common mechanisms used to promote the formation of an equiaxed microstructure are: i) grain inoculation – adding external grain refiner particles into the

melt to promote heterogeneous nucleation [39] which has been used in industry for many decades, for instance, using Al-Ti-B in Al alloys[40], Zr for Mg-based alloys [2, 35], Be for Ti-based alloys [41, 42] and Ce for steel [43, 44]. However, different inoculating particles of different chemical compositions, and different operation practices are needed for different alloy systems, and each of the operation inevitably add extra cost to the manufacturing of the alloys and most likely an adverse impact to the environment.

Thus, in the past 20 years or so, many external physical field based techniques have been developed in order to control the solidification microstructures via the mechanisms of promoting nucleation, dispersion and grain multiplication under physical fields or mechanical force but without any chemical additions. The typical examples are pulse electric current [45], ultrasonic waves [46], static or variable magnetic fields [47] and electromagnetic stirring [48], etc. The techniques that are directly relevant to this research are briefly reviewed in the following sections.

2.1.5 Solidification under external physical fields

External physical fields are able to produce force inside the solidifying melt, disturbing the growth of grains or dendrites, or breaking the growing dendrite arms to act as embryonic nuclei for the subsequent new grains to grow upon. This process is often called dendrite fragmentation or grain multiplication process [49]. The force also produces strong convection to disperse the newly formed dendrite fragments throughout the solidifying melt, so that grain growth can take place uniformly inside the whole solidifying melt volume, resulting in a refined grain structures. The basic theory and governing equations concerning the electromagnetic field are briefly reviewed here.

2.1.6 The multiphysics of electromagnetic field

The concept of applying electromagnetic fields to materials processing was initiated by Asai [50] in 1989, and it was termed as Electromagnetic Processing of Materials (EPM). Since then, 7 series of international conferences have been already dedicated to the development in this field, and the 8th conference to be held in France on 12-16 Oct 2015. The multiphysics phenomena and the governing equations for the key variables of an electromagnetic field are briefly described below (the meaning of the symbols used below can be found in the List of Symbols at the beginning of the Thesis, i.e. page vii):

i) The magnetic pressure, P_m is defined as:

$$P_m = \frac{B^2}{2\mu} \quad (2.2)$$

This is the variable to govern the shape of the magnetic field.

ii) The Lorentz force generated by the interaction between an imposing direct electric current and the magnetic field is given by:

$$\mathbf{F} = \mathbf{I} \times \mathbf{B} \quad (2.3)$$

This force is the main driving force to create strong convection in the melt.

iii) The suppression force when applying a direct magnetic field on a moving molten metal is calculated by:

$$\mathbf{F}_s = \sigma(\mathbf{v} \times \mathbf{B}) \times \mathbf{B} \quad (2.4)$$

iv) The levitation force that is against the gravity due to the electromagnetic field is:

$$\mathbf{J} \times \mathbf{B} = \rho g \quad (2.5)$$

v) The force to create a melt splashing when the electromagnetic force is much higher than gravity can be calculated by:

$$F_q = \frac{|I|^2}{\sigma} \quad (2.6)$$

vi) the joule heat created by the magnetic field is governed by:

$$q = \frac{1}{T} \int_0^T \frac{J^2}{\sigma} dt. \quad (2.7)$$

In 1990, Garnier [51] reported that many European companies and research centres had an internationally leading position in developing magnetic field based techniques for materials processing, for example: i) the use of magnetic field for single crystal manufacturing to control the temperature and velocity fluctuation in the liquid metal during crystal pulling process, ii) application of electromagnetic stirring for induction melting of oxides and ceramics with very high melting point and in rheocasting, iii) using the electromagnetic field to impose and control the shape of liquid metal jet, iv) the levitation melting for continuous casting of very reactive and high melting point materials, and v) controlling the stabilization of liquid metal free surface of strip casting.

Moreover, Takahashi [52] summarised that the applications or impositions of electromagnetic field can be classified into 6 types: i) Simultaneous imposition of direct current and stationary magnetic field, ii) Imposition of alternating current, iii) Imposition of alternating magnetic field, iv) Imposition of travelling magnetic field, v) Simultaneous imposition of

alternating current and alternating magnetic field and vi) Imposition of stationary magnetic field.

Relevant to grain refinement, two main basic approaches have been studied and used [53]:

i) Conducting a direct contact current directly into the melt via contacting electric probes and interacting with the magnetic field.

ii) Generating an induced current in the melt, allowing it to interact with the magnetic field as described in Eq. 2.3. The physics and pros and cons of the two methods are briefly discussed below.

2.1.6.1 Direct contact current

The Lorentz force (\mathbf{F}) that is induced by the interaction between an electric current (\mathbf{I}) and the magnetic field (\mathbf{B}) it is passing through [54-57] can be calculated by Eq.2.3.

Fig. 2.3a shows the direction of the Lorentz force induced from the interaction of a current (input via the direct-contact of the electrode with the melt) with magnetic field (induced or stationary magnetic field). It follows the right hand rule. Using this approach, electromagnetic vibration, direct electric current pulse (Fig. 2.3c) and pulse electromagnetic force can be realised.

Fig. 2.3b presents the induced Lorentz force by the use of an alternating current inside an alternating magnetic field. This technique is called electromagnetic vibration.

Fig. 2.3d shows the concept of, in a contact manner, applying pulse electric current into a stationary magnetic field created by a permanent magnet.

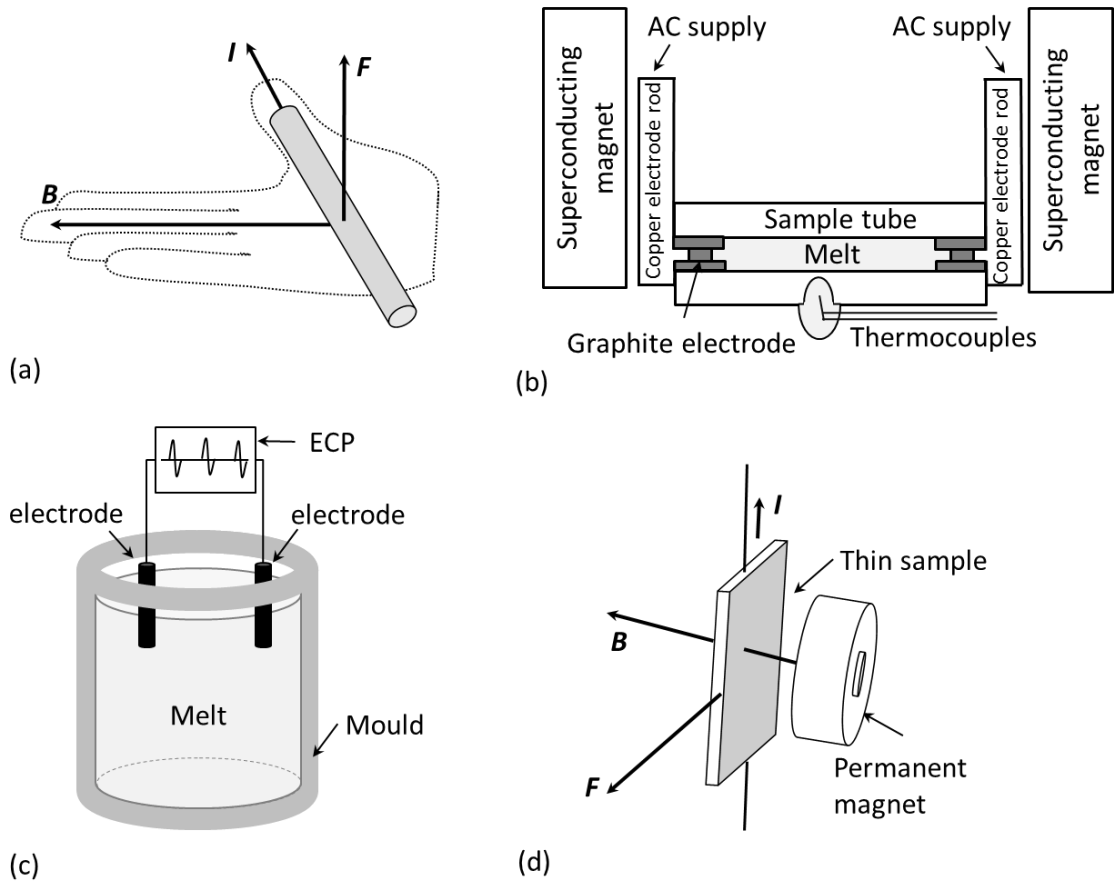


Fig. 2.3. (a) The right hand rule, (b) the Lorentz force generated in an electromagnetic vibration technique, (c) the direct-contact pulse electric current technique and (d) the contact pulse electric current technique.

2.1.6.2 Induced current

When an electric current passes through a coil or solenoid wire, the induced current occurs inside the metal surrounded by the coil. The electromagnetic force produced by the interaction of the induced current and the induced magnetic field is shown in Fig. 2.4a. Lorentz force is generated with its direction pointing towards the centre of the system according to the right-hand rule.

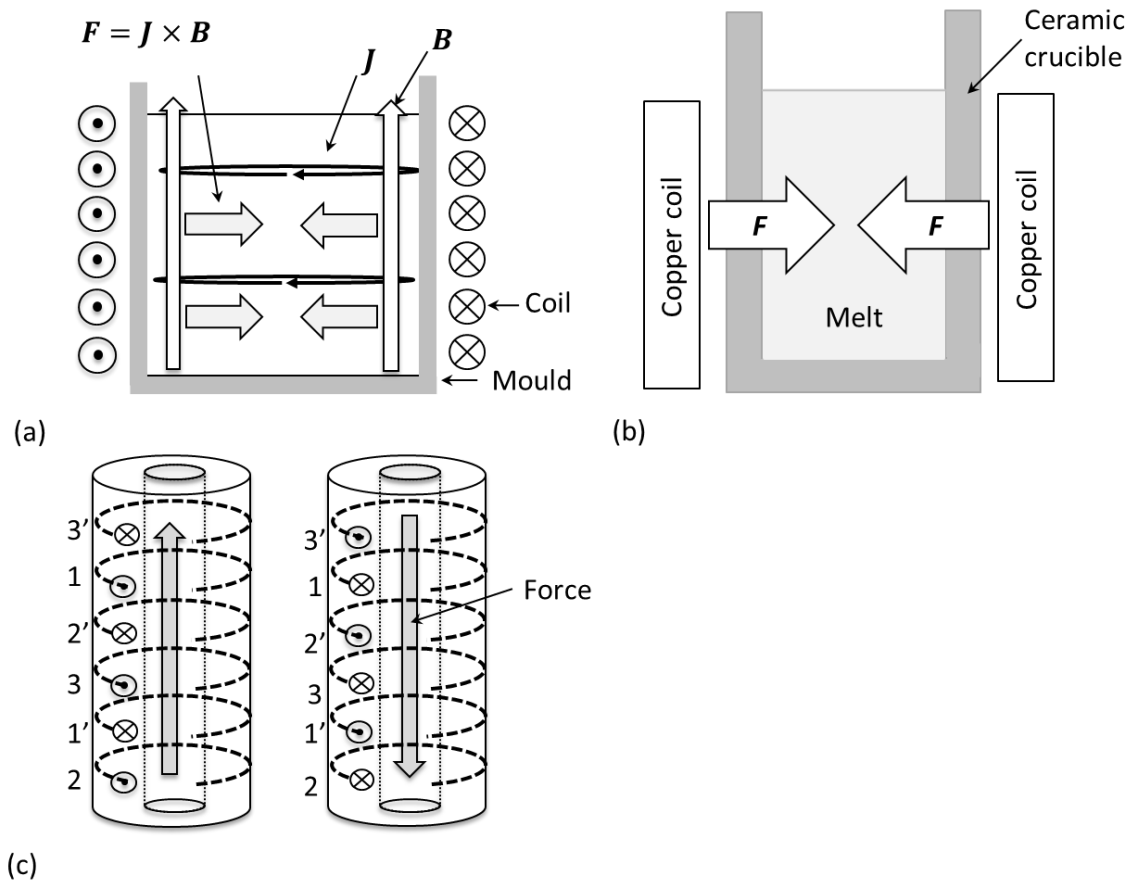


Fig. 2.4. (a) The Lorentz force generated from the interaction between an induced current and the induced magnetic field, (b) the setup of the electromagnetic stirring and pulse magneto oscillation, (c) schematic view of the travelling magnetic field, and the Lorentz force directions.

Fig. 2.4b shows a simplified setup for electromagnetic stirring and pulse magneto oscillation. The two techniques are quite similar in term of the physical setup, despite the function of induced Lorentz force is different due to the difference in how the induced current is generated. The details of the two techniques are described in next section.

Fig. 2.4c shows the principle of travelling magnetic field, this technique is quite unique due to Lorentz force direction is different from other techniques.

2.1.7 Applications of electromagnetic field for grain refinement

The effect of electromagnetic field on grain refinement was first observed in 1970 by Israiloff [58] due to dendrites breaking up by the use of an electromagnetic vibrator. Later, in 1970s, electromagnetic stirring for structure refinement was developed by Chernysh [48] in 1973; and after 1975, the electromagnetic vibration technique was started to be used in the solidification of Al and Al alloys [59]. Later the methods were demonstrated successfully in refining steel by Takeuchi [60] and Sahu [61]. A number of specific methods have been developed for grain refinement so far as described below.

2.1.7.1 Electromagnetic vibration (EMV)

This technique was successfully applied to refine the microstructure of Al alloys since 1975 by Nishimura [59] and it has been studied with gradually increasing interest. The principle of EMV is that the electromagnetic force generate from the simultaneous imposition of a direct magnetic field and an alternating electric field of the current density on a conducting liquid as schematically shown in Fig. 2.3b. The AC current passes through the sample via the copper electrode rods in the present magnetic field of superconducting magnet. The interaction of both two fields causes the electromagnetic force.

The force acts on the particles of the conducting liquid and causes them to vibrate. The vibration occurs when the alternating electric current induces an alternating magnetic field with the same frequency which then interacts with the electric current itself and induces an alternating electromagnetic force composed of a time-independent component and a time-variable component leading to a frequency twice that of the original electric current.

The vibrating electromagnetic force is generated inside the liquid, with a frequency equal to that of the applied electric field and a direction perpendicular to the plane of the two fields [62]. On the other hand, the

liquid is directly vibrated at the same frequency as the alternating current. The vibration causes the liquid flow strongly related to the frequency of the AC current, but the static magnetic field is only affect the alignment of the microstructure to their magnetization direction [63]. Some of researchers used EMV to act as a sonic or ultrasonic vibrator. When high intensity sonic or ultrasonic waves are transmitted through molten metals, the following benefits can be found for the melt including grain refinement, dispersive effects, and degassing, which can reduce porosity. The cavitation effect can prevent the agglomeration of fine particles or tiny phases in the melt from happening [54]. Vives [64] have studied the effect of EMV and found that the microstructure of Al alloys under EMV were refined. The effects of EMV were confirmed by the experiment of Li [63] using variable vibration frequencies, the results exhibited that the higher frequency, the finer of the grain size of alloys.

2.1.7.2 Direct-contact electric current pulse (DECP)

The DECP is also electromagnetic force generator, but the setup is different from electromagnetic vibration. The electrodes of DECP are immersed into the liquid metal as shown in Fig. 2.3c. Generally, DECP consists of the electrodes and current generator to generate the electromagnetic field when the current passing through the electrode into the molten metal. The area surrounds the electrodes are effective regions that the forming nuclei will be influenced.

When DECP is directly applied, the shock wave or the pressure gradient by the high pulse discharged into the liquid metal interrupts the growth of dendrite, fracturing dendrite arms during solidification [6, 45]. The higher the pulse voltage or current applied, the stronger force produced. High pulse voltage can be generated by using a capacitor bank [5, 6]. The electric current discharged from the capacitor bank is a short pulse, and after the discharge current instantaneously reached its peak value, the amplitude declined with time rapidly. The electromagnetic induced by the oscillating discharge current results in the vibration of the melt [65]. Li [45]

found that DECP improves the nucleation rate near the upper surface of the ingot by joule heat, which promotes heterogeneous nucleation. DECP induces force to move the nucleus from the top surface to the bottom, the solidification structure is refined. This method was also used in early 1990 by Nakada [5], and high voltage generated from a capacitor bank was applied into liquid or semi-solid materials. The large pressure gradient generated inside the melt led to the microstructure breaking down.

Some researchers [6, 7, 45] argued that the grain size of material is refined under the effect of direct electric current pulse and high voltage with short-time of electromagnetic force applied at the early and the late stage of solidification. Ma [66] showed that the position of the electrodes also influences the refinement, where the effective positions to immerse the electrodes are at the two ends of the mould, or at top and bottom. Moreover, Xi-bin's [49] simulation confirmed that the effective point of the DECP is at the two ends of electrodes.

2.1.7.3 Pulse electric current (PEC)

The research team of the material group of Oxford University has designed and built a pulse electric current (PEC) [67] device (the equipment and setup are described in the following chapter). This technique is modified from the Misra [68]. The purpose is to study in situ the effect of PEC on the growth and fragmentation of dendrites using synchrotron X-ray.

For the Lorentz force generated in this way, the direction of the force will change relative to the change of the electric current vector. In the case of using AC current, the electric current of a sine wave will lead to a sine wave of force. In addition, the amplitude of the force is dependent on the amplitude of the electric current passing through the sample.

2.1.7.4 Electromagnetic stirring (EMS)

EMS has already been shown successfully in grain refinement since 1973 [48]. Theoretically, EMS uses the electromagnetic force to stir the melt by oscillating the liquid and creating the cavitation and convection phenomena for promoting grain refinements [64, 69]. EMS creates an inhomogeneous Lorentz force in the metal by alternating magnetic field. In the case of an axisymmetric induction coil surrounding a cylindrical specimen, the force is normal to the surface of the alloy in the plane of the coil, but decreases with the depth. Fig. 2.4a demonstrates schematically the principle of EMS.

Ogsawara [70] stated that during crystal growth, the columnar grains formed and grew from the bottom of the mould. However, after the EMS was applied the microstructure changed from long blocky to globular structure. The equiaxed grains occurred at the upper part of mould while the agglomeration induced by electromagnetic force toward inner the melt [71]. The effects of this technique contributes to grain refinement in the manner of the flow stir the mushy zone and partially remelt dendrite arms and produced lower thermal gradient in the liquid and therefore the undercooling region was extended to promote CET transition [72].

Vives also [64] showed that the grain of material experienced more force when the amplitude of the electromagnetic force was increased by varying the current amplitude and magnetic field. Hernandez [73] revealed high AC current resulted in better microstructure refinement and more globular microstructure. Increasing of stirring power obviously improved the performance of grain refinement. Further, Yoshikawa [71] found that heavily alloyed materials are more sensitive to the electromagnetic force than lower composition materials.

The properties of alloys have been improved after the EMS treatment [74], and Lei [75] revealed that EMS changed the grain size of Mg-Li-Al-Zn alloys from long block to global shape with an improvement in tensile strength. Zheng also [76] studied the change of grain size, fractal dimension and

shape fraction under the EMS and found that the increase of stirring power could obviously affect the grain size, fractal dimension and shape factor of the primary phases.

2.1.7.5 Travelling magnetic field (TMF)

TMF is a direct technique to introduce an electromagnetic force (body force) to the sample in the direction related to gravity. The force is created by means of applying out-of-phase currents to a number of coils. Three phases current applied as shown in Fig. 2.4c, the three phases (1-1'), (2-2'), (3-3') are fed by three alternating current shifted in time. The Lorentz force is induced inside of a conducting melt [77] in the cylinder container and the force direction acts in the axial directions, against gravity or parallel to gravity. This force induces the liquid flows during crystal formation, the flows disturb the growth of grain and stir the nuclei distributes in the direction of flow.

The force direction depends on the travelling field created from current path. So that, the force can either enhance or reduce the buoyancy effect of gravity to flow the melt [78]. Metan *et.al* [79] studied the influence of the travelling fields on Al-Si alloys. They reported that the forced convection within the solidifying melt causes grain refinement but with alteration microstructure forming. Zaidat [80] considered the directional solidification of Al-Ni alloys under the influence of a travelling magnetic field and observed a disturbance of the equiaxed microstructure. The effect of the TMF enhances the nucleation and the growth of equiaxed grains.

2.1.7.6 Pulse magneto oscillation (PMO)

Recently, a novel, non-contact technique has been developed and named as pulse magneto oscillation (PMO). It was first studied by Gong [81] using the setup in Fig. 2.4b, PMO stores electric power using a high capacitance capacitor, then discharges the pulse current into a coil which induces a pulse Lorentz force. The Lorentz force causes the vibration of the liquid

metal due to the coil contact the outer surface of sample container. The inner melt will be shocked by the pulse oscillating wave so that the structure can be refinement. Grain refinement is achieved mainly due to the nucleus increase in the solidifying melt then the growing grains block other columnar grains, leading to equiaxed grains. Gong also showed that the grains of pure aluminium were refined when PMO applied and mentioned that the nucleus falls off the mould wall and drifts in the melt, the nucleus increase in the solidifying melt by the Lorentz force of PMO.

Several researchers [82, 83] studied the effect of PMO on pure Al, one studied the effect of PMO in different solidification stages, the structure is best refined during the nucleation stage and the first half period of crystal growth [81]. During nucleation stage, the nuclei experienced the Lorentz force then fall off from the mould wall and grow during its fall off. The grain grew into an equiaxed morphology and impinged the primary dendrite that grew from the bottom of the mould.

The most important issue is to generate sufficient pulse Lorentz force. They found that the magnitude of Lorentz force depends on three parameters: the linear current density, oscillation frequency and discharge frequency [82]. Moreover, lower pulse frequency and high pulse current are more effective for refinement [84].

2.1.8 Summary

For all electromagnetic field techniques reviewed so far, the main advantages are:

i) They are green manufacturing technologies because there are no residual detrimental materials left inside the alloys after solidification, and sufficient electromagnetic expulsive force can be generated to act on the solidifying melt [50]. It offers a clean processes in environmental perspective, since there is no contact between the melt and the power source due to the intrinsic properties of electromagnetic fields [85, 86].

ii) They are generic methods. The effect of electromagnetic force is only dependent on the difference in electric conductivity and those between the different elements or phases in the melt but independent of chemical compositions or state (solid, liquid).

However, the electromagnetic field techniques also have disadvantages depending on the setup and its characteristics:

i) For the direct-contact techniques, the parts or probes of those apparatus have to merge or attach to the melt to transmit the currents into the melt. The immersed part of device is contacting the molten sample which causes contamination of the melt and damage of the device.

ii) The direct-contact techniques are effective for refinement of small volume of melt, but have limitation in applying the current into a large volume of melt.

iii) For non-contact techniques, there is a need of high electric current or voltage (a huge consumption of energy) to generate huge amount of force into the melt in order to break up the grain structure during solidification, Therefore it is also difficult for large volume of melt.

Based on the above reviews and analyses, an energy efficient electromagnetic pulse (EMP) device was designed and developed in this research with the aim of combining the above mentioned advantages together. The principle, design and the manufacturing of this device is very detail described in Chapter 4.

2.2 A review on X-ray imaging and tomography techniques

The microstructures of the alloy samples made in this research were characterised using scanning electron microscopy and X-ray imaging and tomography techniques. This chapter gives a detailed review on the X-ray imaging and tomography techniques and instrument used.

2.2.1 Synchrotron X-ray

Synchrotron is an electron accelerator facility in which electrons are produced by an electron gun, and then accelerated up to high speed through travelling in a linear accelerator (LINAC), a booster synchrotron and a large storage ring. It is designed to produce very intense beams of X-rays, infrared and ultraviolet light which generally called synchrotron light.

The Linear accelerator is used to accelerate the electrons to an extreme relativistic energy of a hundred million electron volts (100 MeV) using radio frequency (RF) cavities. The booster synchrotron contains a series of bending magnets which used to curve the electrons around the bends, and a radio-frequency (RF) voltage source is used to accelerate the electrons from their straight direction. Here they reach energy of GeV range before they are transferred into the storage ring. The electron storage ring (STR) uses electromagnets (bending magnets) to curve the electron beam between adjacent straight sections and store the electrons while they lose energy in the form of light. As the electrons follow this curved path they generate synchrotron light. This light can then be channelled out of the storage ring and into the experimental stations, so called beamlines. All beamlines are located at tangents to the storage ring to guide narrow beams of light to experimental stations where the light is focused for use in experiments [87].

Synchrotron light has a huge range of applications including chemistry, cultural heritage, earth science, engineering, environmental science, life science and materials science. Currently, around the world many of the 3rd

generation synchrotrons are built to serve users, for example the Diamond light source (DLS), the Advanced Photon Source (APS), and the European Synchrotron Radiation Facility (ESRF).

Diamond Light Source is the national synchrotron facility of United Kingdom. It has 31 beamlines with the range of energy used are from 1.2 eV to 150 keV. The synchrotron source support many research fields [67, 88].

The APS at Argonne National Laboratory is a national synchrotron-radiation light source research facility located in Chicago of United states of America. 40 beamlines are offered in this synchrotron with the energies used ranging from 3-100 keV [89, 90].

More than 15 synchrotron facilities are in Europe[91], however, ESRF is located in Grenoble of France which operates the most powerful synchrotron radiation source in Europe, 6 GeV of electron energy and it has more than 40 beamlines. It supports very diverse research areas, including physics, chemistry and materials for example. In situ and real-time 3-D experiments often carry out at ESRF[92].

However, Asia also has around 15 synchrotron facilities. For example, Beijing Synchrotron Radiation Facility (BSRF) is located in Beijing, China. There are 14 beamlines and 14 experimental stations at BSRF which can also support the diversity of research works.

The key advantages of using Synchrotron X-ray for metal research are (1) when using high energy, it can penetrate thick materials for imaging internal structure non-destructively; (2) the very high brilliance of the X-ray (very high photon flux) make it possible to do time-resolved research in situ to visualise the dynamic events of materials at micron or even submicron length scale, and in a time scale down to microsecond. Many new phenomena have been discovered in the solidification process by the use of synchrotron X-rays to study those behaviour in situ and in real-time, and

compared them with modelling [93, 94]. The principle and the techniques used are reviewed here.

2.2.2 X-ray attenuation and absorption contrast

When X-rays pass through materials, its energy is absorbed or scattered. These absorption and scattering are called attenuation. Some photons travel completely through the material without interacting with any of the material's particles. The number of photons transmitted through a material depends on the thickness (distance travelled), density and atomic number of the material, and the energy of the individual X-ray photons. The photon flux passing through materials can be calculated [95] by:

$$I = I_0 e^{-\mu_a x} \quad (2.8)$$

Where μ_a is linear attenuation coefficient and x is the distance travelled. μ_a describes the fraction of an X-ray beam that is absorbed or scattered per unit thickness of the absorber. This value basically accounts for the number of atoms in a cubic centimetre volume of material and the probability of a photon which is scattered or absorbed from the particles of materials.

μ_a is dependent upon the density of a material, and when travelling through a dense material, the opportunity of the photons to be absorbed and scattered is higher. At the same X-ray energy, different materials have different linear attenuation coefficients, and those for the typical metal elements are showed in Fig. 2.5.

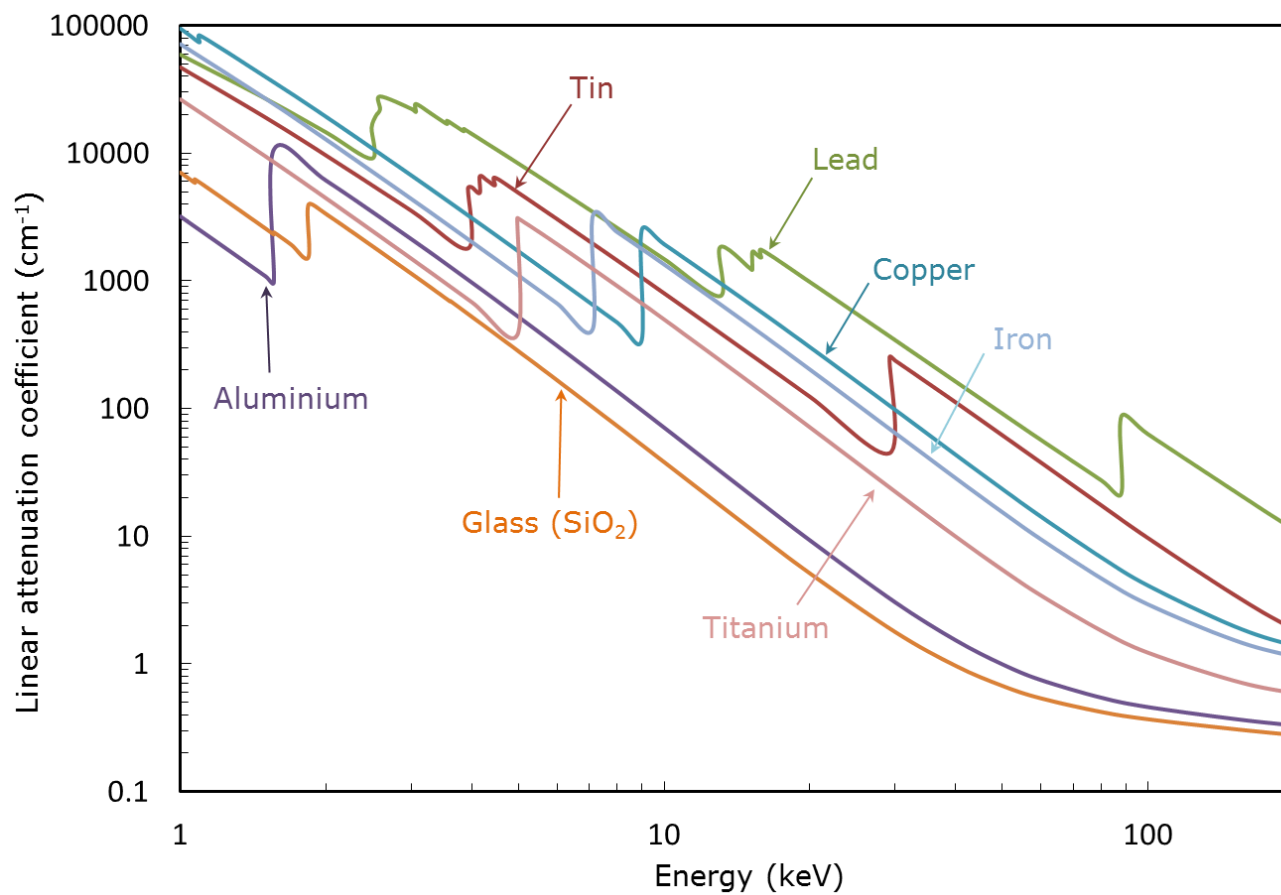


Fig. 2.5. The X-ray linear attenuation coefficients of typical metal elements in the X-rays energy range of 1-200 keV

Another useful term is the so called mass attenuation coefficient, which measures the intensity of X-rays travelling through per unit mass material, and is defined as $\left(\frac{\mu_a}{\rho}\right)$ with the unit of cm^2/gram .

To convert a mass attenuation coefficient $\left(\frac{\mu_a}{\rho}\right)$ to a linear attenuation coefficient (cm^{-1}), simply multiplying it by the density (ρ) of the material.

$$\mu_a = \left(\frac{\mu_a}{\rho}\right) * \rho \quad (2.9)$$

Moreover, the graphs of the mass attenuation coefficients of the elements from $Z = 1$ to 92 are available on the National Institute for Standards and Technology website [96]. For an alloy containing multiple elements, the linear or mass attenuation coefficients can be calculated using a mix rule below

$$\mu_{\text{mix}} = (w_1 \times \mu_1) + (w_2 \times \mu_2) + \dots + (w_n \times \mu_n) \quad (2.10)$$

Where W is the weight percentage of each constituent element of the alloy and μ_n is attenuation of each element.

Using linear attenuation coefficients, the attenuation or often called absorption contrast of the different constituent elements and/or phases in a metal alloy can be calculated for the purpose of choosing the suitable alloy composition and selecting the appropriate X-ray energy range to achieve the best absorption contrast for imaging studies [97]. This is particularly important for achieving the best imaging conditions to study the evolutions of the different phases during solidification, because the composition of the phases change continuously with the change of temperature during solidification.

Taking Al-Cu binary alloy as an example, Al and Cu have sufficient attenuation difference as showed in the linear attenuation coefficients in Fig. 2.6 and 2.7. Hence, Al-Cu alloys with different Cu percentage (3, 6, 10, 20 and 30wt%Cu) were extensively studied as the model systems for fundamental solidification research [98-103] using X-ray with the energy ranging from 4 to 20 KeV [98]. The acquired images in [98] showed that the contrast from the samples with 3 and 6wt% Cu was slightly low, and 10 to 20wt%Cu gave the sufficient contrast for imaging. Al-15wt%Cu was therefore chosen as the experimental alloys in most research, because it also has a typical hypoeutectic structure during equilibrium solidification and the α -Al phase usually has a very typical dendritic morphology [103].

The other important factor in X-ray absorption is the sample thickness [104, 105]. The thickness of the sample (X) can be calculated by:

$$X = \frac{-1}{\mu_{\text{mix}}} \ln \frac{I}{I_0} \quad (2.11)$$

Where X , I_0 , I and $\frac{I}{I_0}$ are the thickness of sample, the initial X-ray intensity, the transmitted X-ray intensity through the sample, and attenuation length, respectively. To have sufficient X-ray transmission through a sample for imaging, normally, the ratio of $\frac{I}{I_0}$ needs to be

$$\frac{I}{I_0} = \frac{1}{e} \quad (2.12)$$

Where e is the Euler number, meaning that the X-ray has a probability of $\frac{1}{e}$ not been absorbed, or to say that the attenuation length is the distance where about 63% of the X-rays have been absorbed by the sample.

Fig. 2.6 shows the sample thickness of Al-15%Cu and Al-35%Cu alloys and Al₂Cu phase. It clearly shows that more Cu in the alloy, the lower the X-ray transmission. From Fig. 2.6a, it shows that the X-ray can penetrate through both alloys and the attenuation length are limited to 1000 μm and 600 μm for Al-15%Cu and Al-35%Cu, respectively.

In addition to absorption contrast due to attenuation, synchrotron X-ray image can have phase contrast as well [106].

Fig. 2.6b and 2.7 show the attenuation length of Al-15wt%Cu for the X-ray energy range in 3-30 keV. It clearly shows that the minimum and maximum thickness of the sample needs to be between 7 and 1000 μm . The high contrast is at the absorption edge of linear attenuation coefficient which is at 8.898 keV, where the absorption length of Al is about 109 μm as shown in Fig. 2.7.

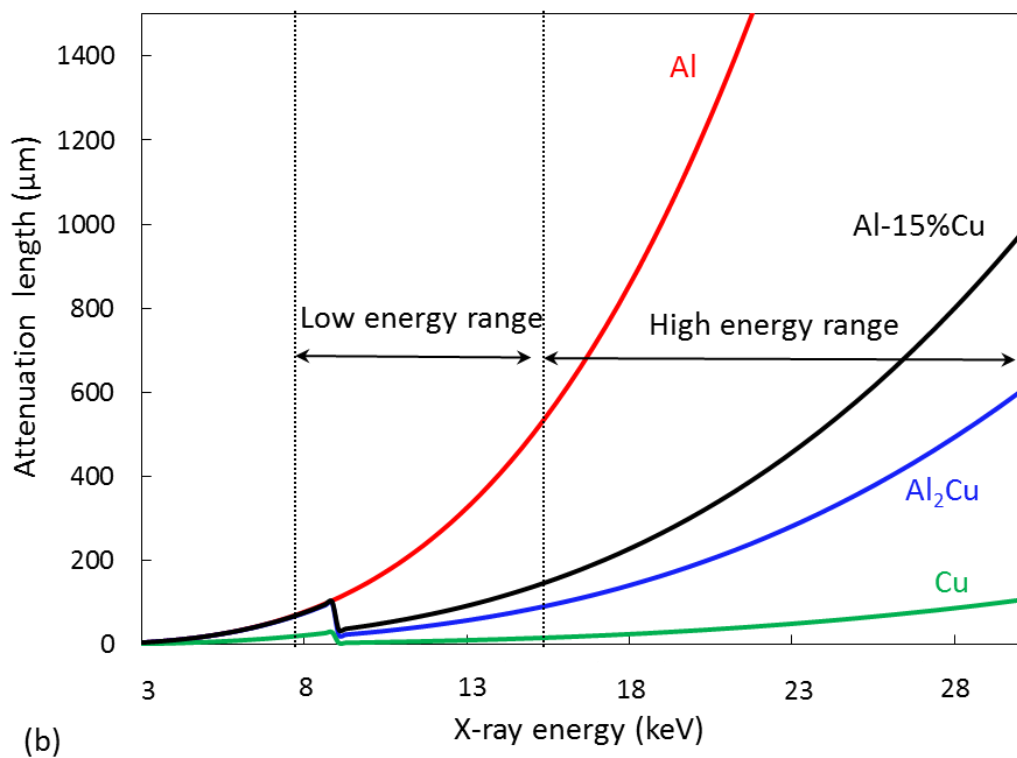
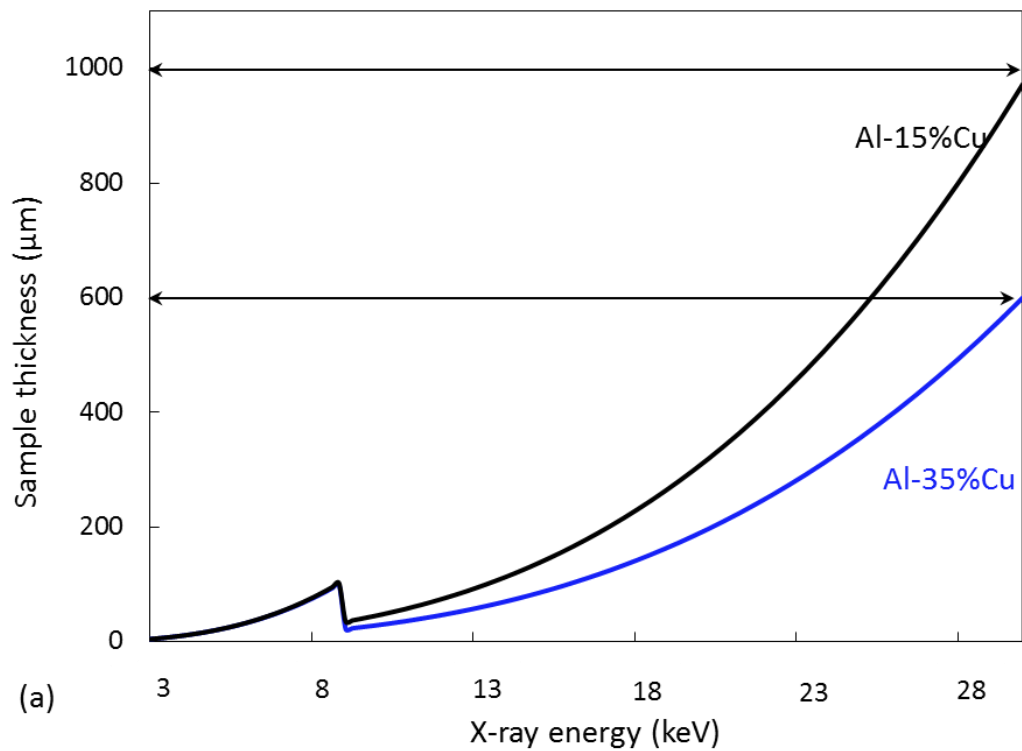


Fig. 2.6. The sample thickness and attenuation length of (a) Al-15%Cu and Al-35%Cu and (b) Al_2Cu phase and Al, Cu phase

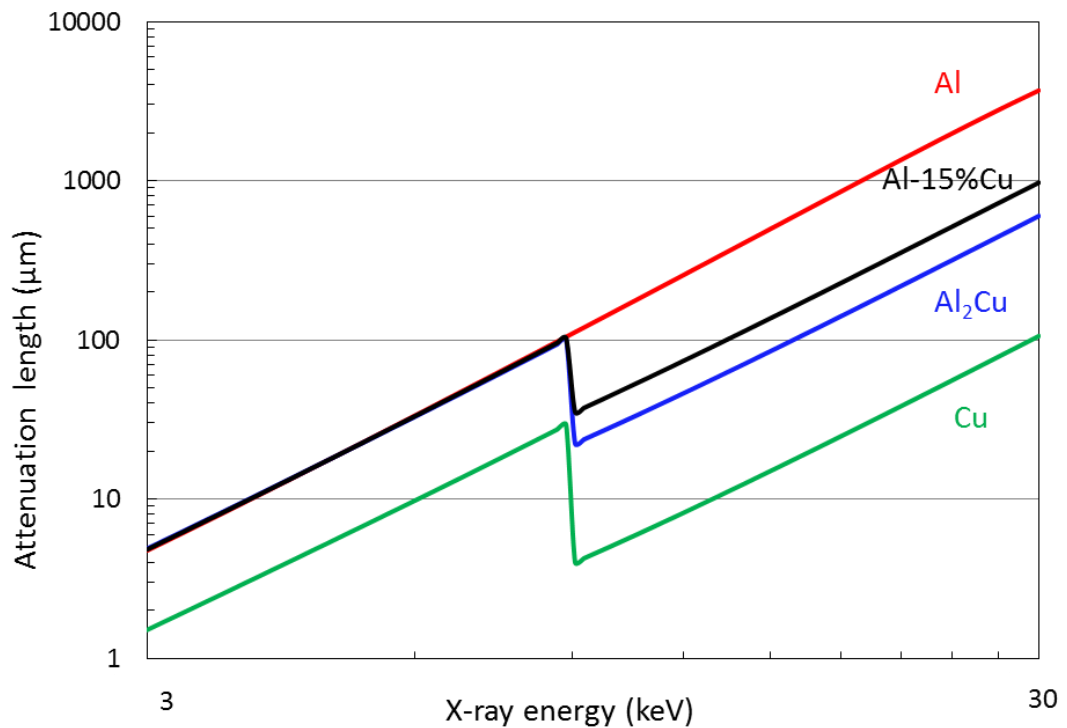


Fig. 2.7. The attenuation length of Al-15wt%Cu, Al, Cu and Al₂Cu phase for the energy range 3-30 keV.

2.2.3 X-ray phase contrast technique

This contrast is produced when a coherent X-ray beam refracts from the internal structures of different indices of refraction inside the sample. A difference in the refractive index between each constituent phase and its surroundings causes a phase shift.

Phase contrast technique can be used to enhance the contrast of hard X-ray absorbing image especially for the low density constituent phases within sample. The gradient in the transmitted beam arising from refractive index variations in the sample leads to contrast in image[107].

2.2.4 In situ studies of metal solidification

Since 1990s, the 3rd generation synchrotron X-ray facilities have major advance in improving X-ray detectors and increasing in beam brilliance (photon flux) and coherence in order to produce very sharp and clear images. A wide range of dedicated materials and engineering specific beamlines have been also developed in many synchrotron facilities and made them available for material scientists and engineers. These developments make synchrotron X-ray a very powerful scientific tool to study in real-time the mechanism and behaviour of material during the solidification processes, especially on visualising dendrite growth and fragmentation behaviour.

Fig. 2.8a shows the typical experimental setup that was used in almost all similar researches. Samples were located between an X-ray source and a detector system (scintillator to CCD camera). The X-ray that pass through the sample is captured by the detector. The detector contained a scintillation crystal which transforms the X-ray signals detected into visible light. The image formed on scintillator was then projected onto the chip of a CCD camera via an optical microscope and then stored as digital information [93]. The image is formed by the difference of grey scale dependent on the intensity of transmitted X-rays. The areas inside the sample that have low X-ray absorption render higher grey value on the pixels of the image as showed by the image of Al-Cu alloy in Fig. 2.8a. The relevant in situ solidification researches are briefly reviewed here.

In 1996, the intense and coherent monochromatic X-rays was first used by Mathiesen [108] for in situ studies of interfacial and phase-specific spatiotemporal structures which appear during nonequilibrium growth in binary alloys. The cellular and dendritic solidification of Sn-Pb alloys were revealed during solidification process. However, in later experiments (2002) Al-Cu alloys were used instead of Sn-Pb alloys as it has lower absorption. The Columnar and equiaxed of Al dendrites and Al-Cu eutectic growth were investigated as well as the formation of defects such as hot tears and gas pores of Al-Cu alloys during the directional solidification.

Since Mathiesen's pioneer work, extensive studies have been carried out to observe the mechanism and phenomena of microstructure evolution of alloys during solidification in situ [72, 109-113] and in real-time [49, 93, 101, 114]. Several important phenomena such as dendritic and eutectic growth of Al-Cu alloys [100, 112], Columnar to Equiaxed Transition (CET) in refined Al alloys [109, 110], fragmentation of dendritic crystals during columnar growth of Al-Cu [115] have been studied. In particular, microradiography was used extensively to study the solidification of alloys such as Sn-Pb [108], Ti-Al-Ta [116], Ga-In [117] in real-time. For example, Mathiesen [99] studied the fragmentation of Al-20wt%Cu and revealed the mechanism of fragmentation due to the remelting of the dendrite arm showed by the image sequences acquired. Nguyen Thi [118] used X-ray imaging to study the interface of metallic alloys and improved the quality of X-ray imaging by the phase contrast technique by varying the distance between sample and detector.

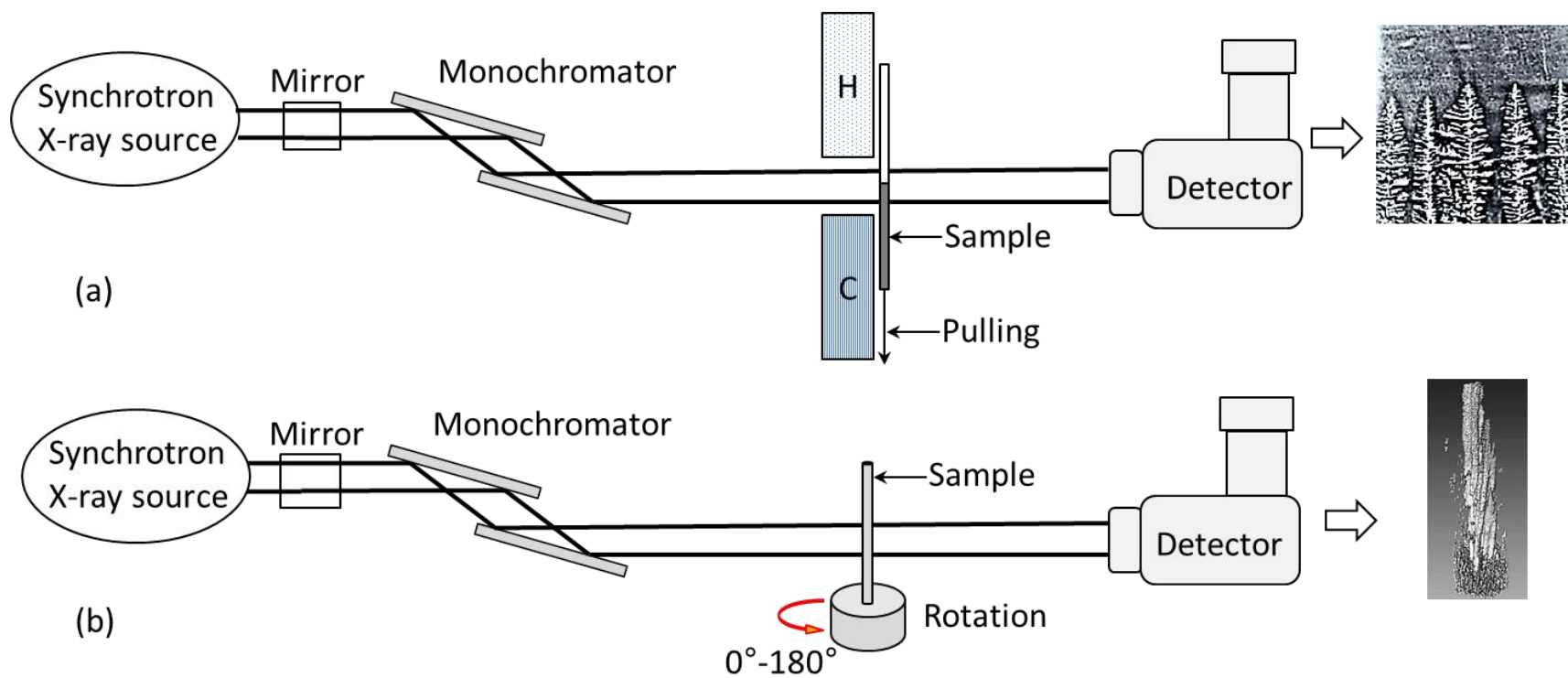


Fig. 2.8. The principle and setup of X-ray (a) imaging and (b) tomography experiments

2.2.5 X-ray tomography

Synchrotron X-ray tomography is based on the detection of the absorption or phase shift contrast of the X-ray beam transmitted through a sample. Transmission images are measured from many different angular positions from the sample to form a set of projections that can be reconstructed into a stack of 2-D layers or slices, and then 3-D structure is reconstructed from the stack of 2-D images [119].

Fig. 2.8b shows the basic setup for X-ray tomography measurement, consisting of an X-ray source, a detector and a rotation system. The transmitted X-ray intensity through the sample is recorded by a high-speed camera, while the sample is continuously rotating from 0° to 180°. The acquired images, or radiographs are often called "projections". In addition, dark-field images (image taken without X-rays) and flat field images (image with X-rays but without the sample) are also recorded for the purpose of image processing. The procedure of the tomography process is illustrated Fig. 2.9.

The practical procedure of converting the 2-D image to 3-D image is as follow. The radiographic projections are taken for many angular positions, creating signograms which later are converted to the image slices (cross-section images perpendicular to the projections). The signograms are converted by filtered backprojection algorithm [120]. Image slices are then reconstructed by stacking all together to produce the 3-D image as the schematically illustration in Fig. 2.9. Visualization and data analysis are made using software, i.e. Avizo, the 3-D microstructure of interest can be segmented via threshold selection. The threshold is carefully chosen from the difference of grey scale pixel value between different phases.

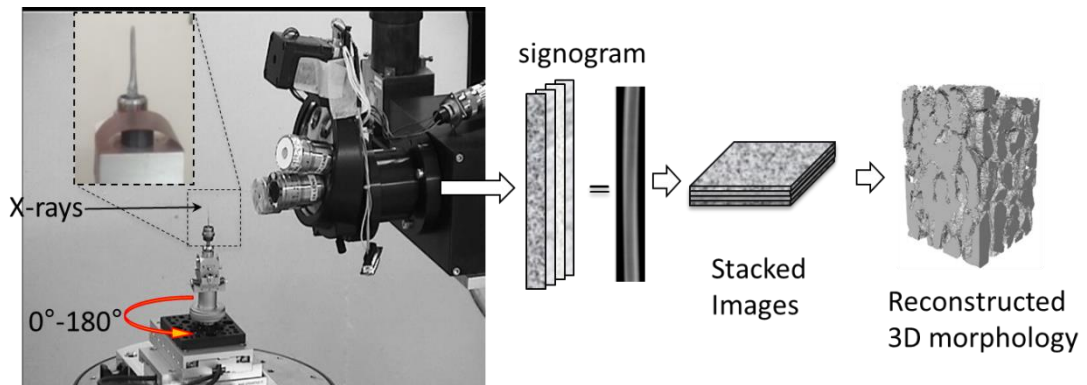


Fig. 2.9. The procedure of 3-D reconstruction

2.2.6 Image processing

This section is described the image processing using for enhance the quality of the image or video from the synchrotron X-ray techniques. Some of the images acquired from synchrotron X-ray might contain defects, noise or speckles which are normally occur during image acquisition.

In general, a digital image can be formalised as a mathematical model comprise of a function of the scene (the object function) and capture process (point spread function, PSF). Additionally, the image will contain additive noise[121] as shown

$$\text{Image} = (\text{PSF} \times \text{object function}) + \text{noise} \quad (2.13)$$

Where PSF is the way information on the object function is spread as a result of recording data, i.e camera. The object function is the object is being imaged (its surface) and noise is the consequence of all unwanted external disturbances occur during data recording.

The most common image enhancement techniques used for image processing are removal of noise, sharpening image edge, softening, gamma correction and contrast-brightness adjustment. However more advanced techniques are needed to process the X-ray images, and the procedure

concerning this research is showed in Fig. 2.10. There are six steps, namely (1) convert video to image sequence, (2) subtract flat field, (3) Fourier transform, (4) inverse Fourier transform, (5) improve quality and (6) convert the processed image sequence back to video.

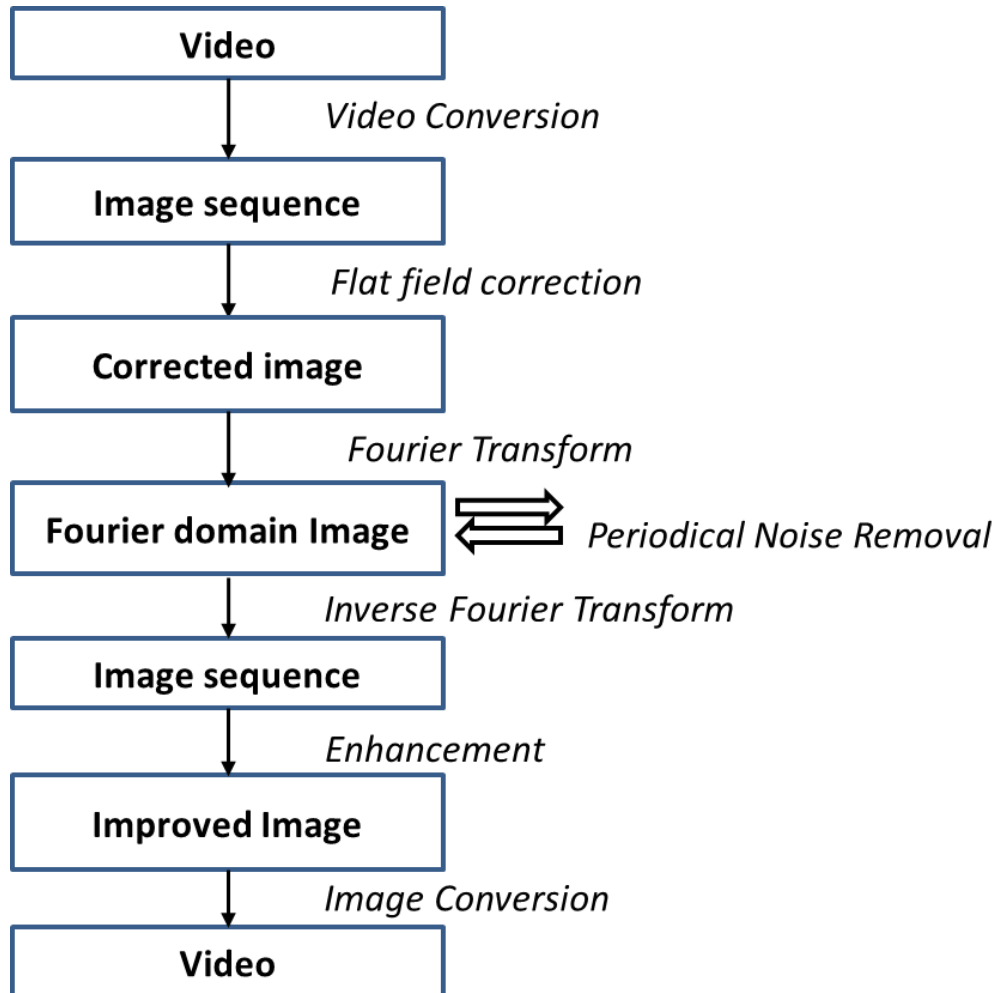


Fig. 2.10. Overview of image processing procedure

2.2.6.1 Video conversion and image conversion

The X-ray images are normally in a video file, converting them into images can facilitate processing. For example at Beamline B16, the acquired video is in CINE file format and uncompressed due to the use of Vision Research's Phantom high-speed cameras. The Cine viewer software is needed to operate on the video. CINE file store pixel data, acquisition parameters,

range time, image time, and analog signals. To process this file, the file has to convert to other available readable format for image processing. CINE format image sequence can be converted to AVI file format, then it can be operated by common image software. The video (AVI format) is read and converted to image sequence in order to process the image frame by frame.

2.2.6.2 Flat field correction

Most of image sequences contain noises and artefacts due to X-ray optics. Therefore, images have to be corrected by using the flat field correction method [122] to get rid of the noises and artefacts from the raw image by the operation below.

$$\text{Corrected image} = (\text{Raw image} - \text{Dark field}) / (\text{Raw image} - \text{Flat field}) \times \text{mean of (Flat field} - \text{Dark field)} \quad (2.14)$$

In the solidification process, the raw image is the image of the sample taken during solidification, while the flat field image is taken at the same region but during a fully melted liquid state. In this way, the flat field image is the background image before solidification start. The mean of flat field image is the mean of pixel value of the flat field image.

2.2.6.3 Fourier transform and inverse Fourier transform

For periodical noise reduction, Fourier transform is used to decompose an image into its sine and cosine components. The output of the transformation represents the image in the Fourier or frequency domain, while the input image is the spatial domain. In the Fourier domain image, each point represents a particular frequency contained in the spatial domain image.

For the raw image $f(x,y)$ with image size $M \times N$, the 2-D Discrete Fourier Transform is given by [123]:

$$F(u, v) = \frac{1}{MN} \sum_{x=0}^{M-1} \sum_{y=0}^{N-1} f(x, y) e^{-i2\pi(\frac{xu}{M} + \frac{yv}{N})} \quad (2.15)$$

where $f(x,y)$ is the image in the spatial domain and the exponential term is the basis function corresponding to each point $F(u,v)$ in the Fourier space. The equation can be interpreted as: the value of each point $F(u,v)$ is obtained by multiplying the spatial image with the corresponding base function and summing the result.

Note that $\frac{1}{MN}$ is the normalization term in the forward transformation. This normalization is also applied to the inverse transform instead of the forward transform, but it should not be used for both.

After the image is converted to the Fourier domain image, the periodical noise positions have to be identified. The periodic noise signal always appears as a paired high intensity pattern along the vertical axis in the Fourier domain. Once the noise position is defined, the band rejected filter or band stop filter [123] is then used to replace the noise pixel as showed in Fig. 2.11b and 2.11c.

The Fourier domain image is then converted back to spatial image using inverse Fourier transform, the periodical noise is therefore reduced. The inverse Fourier transform operation is given by:

$$f(x, y) = \sum_{u=0}^{M-1} \sum_{v=0}^{N-1} F(u, v) e^{i2\pi(\frac{xu}{M} + \frac{yv}{N})} \quad (2.16)$$

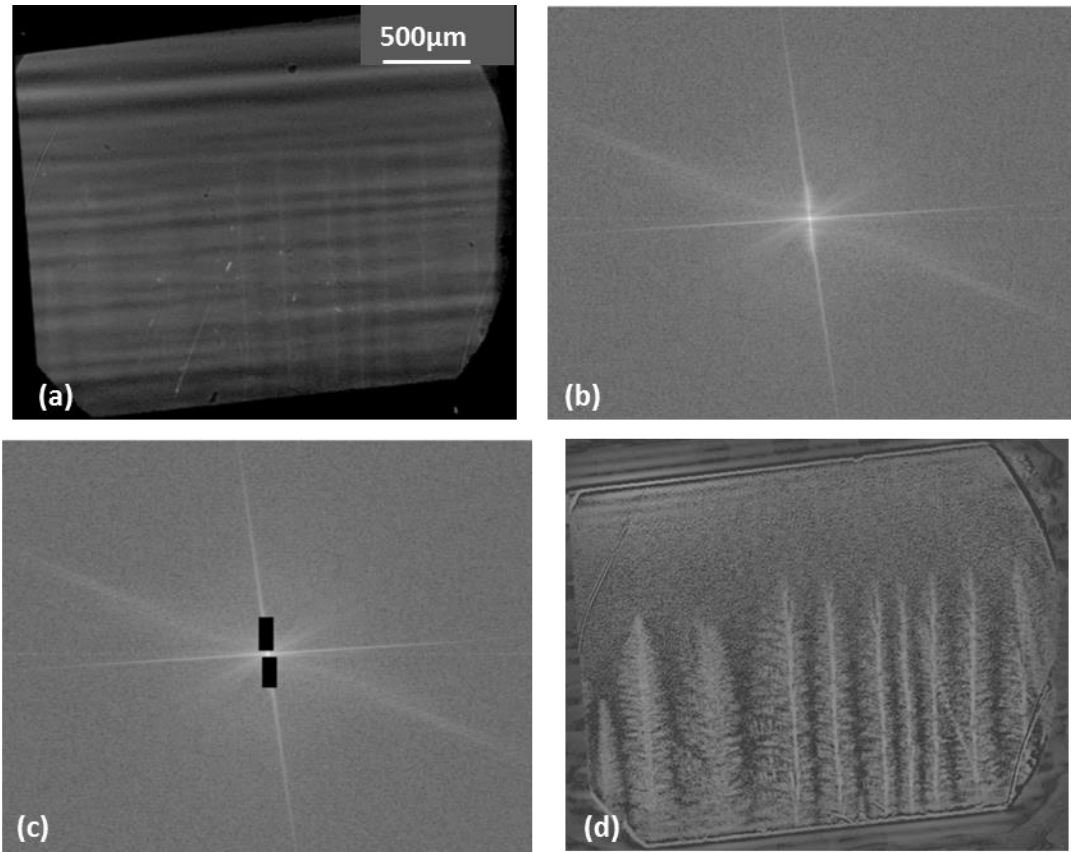


Fig. 2.11. The comparison of images between (a) original, (b) Fourier domain image, (c) Fourier transform with band rejected filter on the periodical noise and (d) processed images.

2.2.6.4 Enhancement

In addition, the image is further improved with enhancement techniques which adding the constant value, C to the image so called the contrast and brightness adjustment:

$$\text{Adjusted image} = \text{raw image} + C \quad (2.17)$$

Finally, after image processing, the periodical noise is reduced and the artefacts are removed. The processed image is obviously reveals the information of dendritic structure of alloy as shown in Fig. 2.11d.

2.3 Modelling of the multiphysics in pulse magnetic field

2.3.1 Modelling of solidification

Solidification simulation or modelling was started in the simulation of steel ingots [124]. Since then, computer simulation of solidification has been widely used in many alloys and casting processes [125, 126], for example continuous casting [127], stationary casting [128], directional solidification [129], phase field simulation [130] and grain growth [131, 132]. In addition, many computational models concerning electromagnetic field has been developed [133, 134] to calculate the magnetic flux [135], electromagnetic force, etc [136]. Many studies have simulated the electromagnetic force, especially the Lorentz force and enhanced fluid flow in the conventional electromagnetic field, much less studies have been devoted to the pulse electromagnetic field, especially for quantitative characterize the multiphysics [137]. This section reviews the relevant methods to be used in the simulation chapter of this thesis.

2.3.2 The magnetic flux density

Magnetic flux density is the most important variable needed to be simulated and quantified. It has been studied and simulated using the finite element method [138, 139]. For example, Zhang [140] showed the effect of magnetic flux on the grain growth, and the magnitude of magnetic field is dependent on the input current. Similarly, Deng [141] used the FEA model to simulate magnetic flux and magnetic force on the workpiece and found that the magnetic flux is proportional to the discharge voltage. The experiment based on that simulation generated successful results. Wang [142] simulated the magnetic flux from the coil and also found that the magnetic flux density direction is approximately parallel to the centreline of the coil and peak value is dependent on the discharge current into the coil.

Theoretically, the magnetic flux density of the electromagnetic field generated from a helical-shaped coil can be calculated using the equations below [143].

$$0 = \nabla \cdot \mathbf{B} \quad (2.18)$$

$$\mathbf{B} = \mu_0 \mu_r \frac{N}{L} \mathbf{I} \quad (2.19)$$

where \mathbf{B} is the magnitude of the magnetic field (the magnetic flux density measured by Tesla (T), μ_0 is the permeability of free space (1.26×10^{-6} T m/A), μ_r is the relative permeability of copper, \mathbf{I} is the magnitude of the current passing through the coil, L is the length of coil and N is number of coil turns.

2.3.3 The induced current and Lorentz force

When the current pass through the coil, the magnetic flux and induced current are created in the conductive material inside the coil. The induced current can be calculated [141] by

$$J = N \frac{dB}{dt} \quad (2.20)$$

Where \mathbf{B} is the induced magnetic flux density inside melt, N is the number of turns in the secondary winding,

The electromagnetic force is generated as the result of interaction of magnetic flux and induced current and can be calculated by

$$\mathbf{F} = \mathbf{J} \times \mathbf{B} \quad (2.21)$$

2.3.4 The Lorentz force and fluid flow

The Lorentz force is a volume force that acts on the alloy melt to create an enhanced fluid flow [37]. Navier–Stokes equation [144] was normally used to simulate the fluid flow:

$$\rho \left(\frac{\partial \mathbf{u}}{\partial t} + \mathbf{u} \cdot \nabla \mathbf{u} \right) = \nabla(-p + \nabla \mathbf{u}) + \mathbf{F} \quad (2.22)$$

Natarajan [145] showed that the electromagnetic force can generate a strong rotational flow driven by the circulation of the force at the billet corners.

Vizman [146] developed a model to study the effect of rotating magnetic field on producing a stabilized convection in a cylindrical melt volume. The model showed the convection flow of the liquid metal in the boundary volume is the results of the Lorentz force distributed in the liquid metal. Mihelcic et al [147] and Hall et al [148] simulated the laminar melt flow in the magnetic Czochralski processes. Weiqiang [149] used a 2-D model to compute the steady-state flow of an Al melt in centrifugal casting with electromagnetic stirring.

Spitzer [150] presented a turbulent flow model for continuous casting with the stirring of a rotating magnetic field. 3-D numerical model was also built by Chung [151] to simulate the recirculatory flow at the top of the casting due to both a buoyancy force and electromagnetic stirring.

Ma [152] demonstrated that there are two directions of force generated in the melt during pulse magnetic field. The axial force causes the convection of the melt while radial force produces the vibration of melt.

The k- ϵ turbulence model [153] was used by Baokuan [154] to study the molten metal flow pattern due to argon gas and electromagnetic force. The experimental measurement and numerical modelling agreed well. The k- ϵ

model offers the simplest level of closure since it has no dependence on the geometry of flow-regime input and is stable and suitable for turbulence models for some applications and uses as the default setup for handling turbulence flows in Comsol Multiphysics [155].

Recently, Liang [156] studied the effect of pulse electromagnetic force on Al alloys, where the convection of fluid flow is the main factor to flow the nuclei from the top surface to the bottom of ingot. The simulation also showed that the relationship between (height/diameter, H/D) ratio of ingot and the effect of magnetic field, the smaller H/D ratio resulted in larger current density, electromagnetic force and convection on the top surface of the melt, leading to nucleation and subsequent grain formation.

2.4 Summary

This literature review consists of three parts.

The first part reviews the key literatures and methods that are directly relevant to the research presented in this thesis, especially concerning metal solidification and external physical fields with a focus on the electromagnetic field methods.

In the second part, the techniques used for microstructure characterization are reviewed and presented with a special emphasis on the use of synchrotron X-ray 2-D imaging or 3-D tomography methods.

Finally, simulation and modelling of solidification under the electromagnetic field were briefly reviewed with the purpose to explain the key variables and the governing equations to be used in this research, not on the full assessment of the modelling development in this field, because there are too many literatures on this aspect, and a comprehensive review of all the development is beyond of the research.

Chapter 3 : Solidification of Al-15%Cu alloys in a static magnetic field with pulse electric current

This chapter describes the synchrotron X-ray in situ studies of Al-15%Cu alloys solidified in a static magnetic field with the application of pulse electric current (PEC). The experiments were carried out jointly with the researchers from the Processing of Advanced Materials Group in the Department of Materials, Oxford University. The in situ study is one of the key research tasks defined in the EPSRC project – EPSRC Centre for Innovative Manufacturing in Liquid Metal Engineering (EP/H026177/1, £5.1 Million, 01/05/2010 – 31/10/2015) involving Brunel, Oxford and Birmingham Universities. Dr Jiawei Mi, my supervisor, made vital contributions in writing and proposing the in situ solidification research agenda in the proposal when he worked at Oxford University in 2009. Together with colleagues from Oxford, he co-authored three successful proposals (EE6767-1, MT7440-1 and MT7818-1) and won 15 days of synchrotron X-ray beam time from the Diamond Light Source (DLS) in year 2011 – 2012 as detailed in Table 3.1. Since I joined Dr Mi's group in February 2012, I worked together with the Oxford researchers and participated two experiments (MT7440-1 and MT7818-1) at beamline B16 of DLS in 2012.

This chapter describes some of the key functions of the experimental apparatus used in the experiments, and the results obtained from the two experiments. These have direct relevance to the novel electromagnetic pulse device described in Chapter 4, the modelling in Chapter 6 and the discussion in Chapter 7.

Table 3.1. The synchrotron X-ray experiments that produced the results presented in this Chapter

Proposal code	Proposal title	Beamline and Experiment date
EE6767-1	Synchrotron X-ray imaging of dendrite fragmentation during solidification	I12 of DLS 27/07 - 01/08/11
MT7440-1	X-ray imaging of dendrite fragmentation during solidification of Al alloys induced by an external field	B16 of DLS 29/02 - 05/03/12
MT7818-1	X-ray imaging dendrite fragmentation induced by an electromagnetic field	B16 of DLS 11/07 - 16/07/12
EE8542-1	In situ study of optimal processing conditions to deliver embryonic nuclei for grain self-refinement in clean metals under ultrasound cavitation	I12 of DLS 20/06 - 25/06/13

3.1 The experimental apparatus

As briefly described in [67], the solidification apparatus was designed and made at Oxford in 2010 – 2011 by mimicking the similar Bridgman type furnace used by Mathiesen, *et al* [98] with the addition of a ring-shaped permanent magnet plus a pulse electric current generator, and the corresponding control system. Dr Mi made a valuable contribution on the initial design, building and commissioning of the apparatus. In order to describe and present more clearly the experiments conducted and the data and images obtained from the experiments, each unit and its key function of the apparatus are again explained briefly in this chapter.

3.1.1 The heaters, sample holder and alloy

The heaters were made by firstly winding electric resistance heating wires into coil and then embedding the coil into the machined slots of a Duratec 750 plate (a machinable ceramic plate). The heating and temperatures (up to 1000 °C) are controlled independently and recorded using National Instrument modules and the Lab View software. Two copper plates are used to cover the heating coils and transfer the heat onto the thin foil sample inside the sample holder (an envelope-type holder with an internal gap of $\sim 250 \mu\text{m}$) made by thin quartz sheet. It was made by welding together three sides of two rectangular thin quartz sheets of 100 μm thick. The quartz holder was held by a mechanical clamp and pressed tightly against the two copper heating plates. The gap between the two heating plates can be adjusted in order for the different X-ray beam sizes, view fields and temperature gradients (G) of the sample to be tuned during the experiments. This whole assembly can be also arranged horizontally. This flexibility allows different thermal controls to be realised, for example, directional solidification either in parallel or anti-parallel with gravity (g) direction or in horizontal direction, near isothermal solidification condition, etc.

The temperatures of the samples were measured using two K-type thermocouples (250 μm diameter wire) embedded inside the two heaters, and the thermal gradient is calculated based on the temperature difference and the distance between the two thermocouples. The achievable thermal gradient is in range of 30-55 K / mm.

Al-15%Cu alloy was chosen because it gives enough X-ray absorption contrast for imaging at the X-ray energy range of 3-30 keV as described in detail in Chapter 2. Plates of the dimension of 7 mm \times 20 mm \times 300 μm were machined off from the as-cast Al-15%Cu alloy ingots and then ground and polished to \sim 200 μm thick before encapsulated and sealed into the quartz sample holder. Two chromel wires of 125 μm diameter were inserted into the quartz holder (Fig. 3.1e) for introducing pulse current after the Al-15%Cu is melted.

3.1.2 The magnet and pulse current generator

A ring-shaped permanent magnet (5.2 mm I.D., 15 mm O.D. and 7.0 mm countersink) and a signal generator from AIM-TTI Instruments (model TG5011, Function generator, 50MHz) were used to generate the pulsed magnetic field and the Lorentz force inside the samples [157]. The magnet was placed \sim 3 mm away from the sample to create a static magnetic field around the sample with the flux in y-direction. The pulse generator produces electric currents with the designed wave forms and frequencies that pass through the sample in z-direction via the two chromel wires. The interaction between the current and the magnetic field generate the Lorentz force inside the sample in x-direction as explained in Chapter 2 (Fig. 2.3d). The permanent magnet is made of ferrite ring magnet (COMUS group), and is magnetized axially with a magnetic surface of 0.1 T. The effective range of the magnetic field is within \sim 5 mm from the surface of the magnet. The 5.2 mm inner ring is for X-ray beam to pass through.

The signal generator (Fig. 3.1b) is a multifunctional wave form generator that can generate alternative currents in sine wave form with a frequency from 0.5 mHz to 50 MHz, or square-shaped current pulses have a rise time below 8 ns. The currents output from the generator are introduced into the sample through the two chromel wires inserted at the two ends of sample. The voltage of the current is limited to 15 V, and the frequency used in the experiments were 0.5, 1, 10, 1000 and 100000 Hz. The magnitude of the force acting on the sample is calculated by [158]:

$$\mathbf{F}_L = \mathbf{BI} \sin(\theta) L_a \quad (3.1)$$

Where $\theta = 90^\circ$ is the angle between the electric and magnetic field, $L_a = 1$ cm is the active length of the sample, I is the electric current and \mathbf{F}_L is the force. All experiments used a sine-wave form with a peak-to-peak amplitude of 30 V, inserted into a 50 Ω circuit corresponding to a current of $I = \pm 300$ mA. The magnetic field \mathbf{B} at 3 mm from the magnet surface was 0.1 T, therefore the force $\mathbf{F}_L = \pm 0.3$ mN.

Fig. 3.1c shows a schematic of the solidification apparatus, comprising of (1) two heaters (an upper and a lower heater) and a temperature control system, (2) a sample holder and a mechanical clamp to hold the sample in place and perform the up-and-down movement, and (3) a ring-shaped permanent magnet and a pulse current generator (model TG5011, Function generator, 50MHz) for producing pulse electric currents.

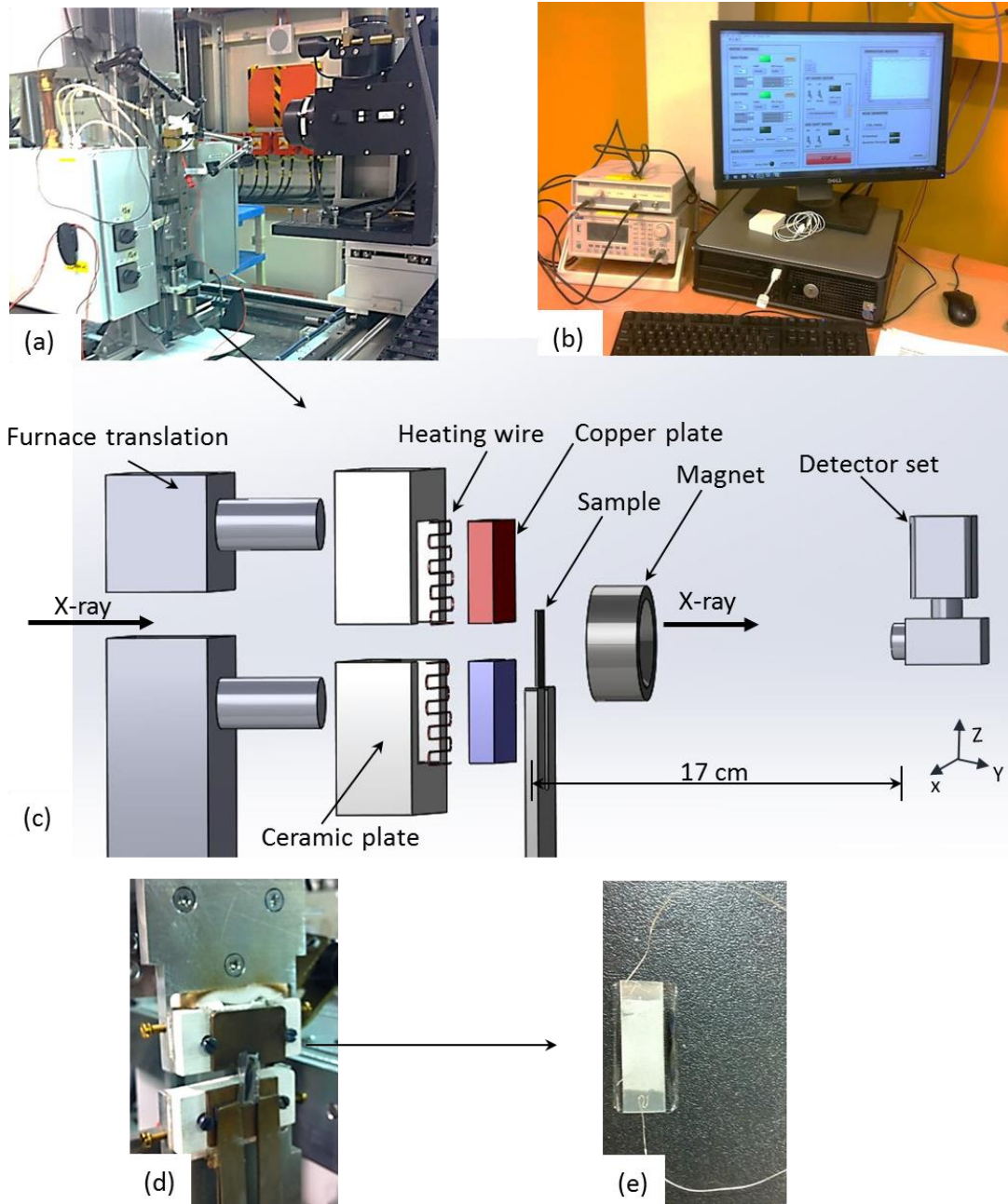


Fig. 3.1. (a) A photo, showing the solidification apparatus mounted on the sample stage of beamline B16 of DLS, (b) a photo, showing the pulse signal generator, the temperature control and data login system, (c) a schematic, showing the solidification apparatus and experimental setup, (d) the mounting of the quartz holder held by the mechanical clamp and pressed against the copper heating plates, and (e) the Al-15%Cu thin foil sample encapsulated inside the quartz sample holder with two chromel wires connected for introducing pulse current after the alloy is melted

3.2 The experiment setup and experimental parameters

Fig. 3.1a shows the solidification apparatus, samples and the permanent magnet assembly mounted on the sample stage of beamline B16 experiment hutch, while the pulse generator and temperature control and data logging system were in the control room. The controls of the temperatures of the heaters and the samples, the movement of the samples, the generation and application of pulse current into the samples, and the synchronisation of the X-ray imaging and trigger of the image recording were all achieved using the National Instrument LabView software integrated with the FieldPoint modular distributed I/O system. The data monitoring, recording and operation control are operated via the custom-designed user interface as showed in Fig. 3.1b.

A monochromatic X-ray of 18 keV with the beam size of 3×3 mm was used in the experiment. Fig. 3.2 shows that the squared-shaped beam is illuminating the ceramic Duratec plates and the sample set between the small gap of the two heaters (the glowing gap). By turning on and off the light of the experimental hutch, the square-shaped X-ray beam and the small gap between the two heaters (the temperature of the heater was ~ 730 °C) can be clearly seen, especially the square-shaped fluorescent image of the beam because of the interaction between the X-ray and the Duratec ceramic materials.

The sample-to-detector distance was set at 17 cm [98, 159]. The X-ray radiated through the sample and hit onto the detector set which consists of a $150 \mu\text{m}$ thick single crystal cadmium tungstate (CdWO_4) scintillator and Optique Peter Lens module. The image sequences were captured by using a high speed camera – Phantom 7.3 CMOS camera. The field of view was 800×600 pixels, giving a spatial resolution of $5.5 \mu\text{m}/\text{pixel}$ using the objective lens $\times 4$ magnifications. The image acquisition rate used was 30 frames per second.

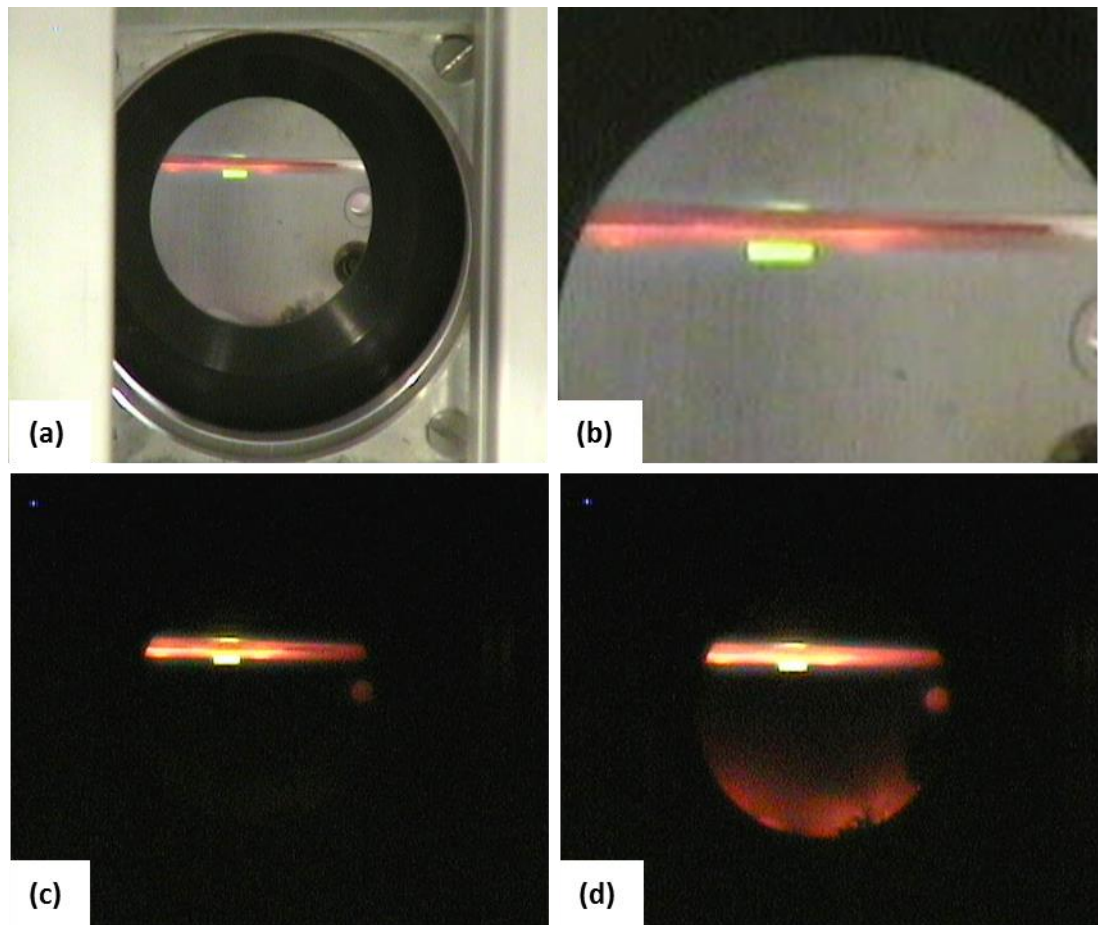


Fig. 3.2. The fluorescent image of the square-shaped X-ray beam illuminating the Duratec ceramic plates and the sample under heating, the image were taken (a and b) with control room light turning on and (c and d) the light turning off

3.3 The experimental results

A total of 102 experiments with different solidification and current pulse conditions were carried out and they were categorized into two main groups as detailed in Table 3.2. In each experiment, typical image sequences of the solidifying microstructures were taken and recorded. Fig. 3.3a shows a typical raw image extracted from the original image sequence (before applying any sensible image processing method) acquired in the experiments of anti-parallel (with gravity) directional solidification. A parallel array of dendrites can just be seen with relatively weak contrast. Unfortunately, there are many lines of periodical noises (pointed by the arrows) due to the camera and a lot of artefacts (in circles) because of the defects in the scintillator, causing blurring of the images and sometime loss of the important features of interest. Therefore, a careful processing of the raw images is essential to remove or minimise the noises or defects so as to reveal real features of interest. Using the image processing methods described in chapter 2, especially, the Fourier transform and inverse Fourier transform techniques, much of the noises and artefacts can be removed or minimised. Fig. 3.3b shows that after applying those image processing techniques, and adjusting the brightness and contrast, the parallel array of dendrites are clearly revealed (comparing the dendrite pointed by the white arrow before and after processing).

Table 3.2. *The in situ experiments conducted and the parameters used.*

Pulse parameter		Solidification direction versus gravity		Number of experiment
Frequency	Wave form	In-parallel	Anti-parallel	
0.5 Hz	sine	-	3	3
1 Hz	pulse	-	6	6
1 Hz	sine	8	32	40
10 Hz	sine	-	4	4
1 kHz	sine	1	3	4
1 MHz	sine	1	3	4
No	No	10	31	41
Sum		20	82	102

By analysing all video sequences obtained from the 102 experiments, five video sequences from the anti-parallel (with gravity) directional solidification experiments were selected and presented in this Chapter because they have direct relevance to the results described in Chapter 4, 5 and 6. The experimental parameters used for the five cases are listed in Table 3.3.

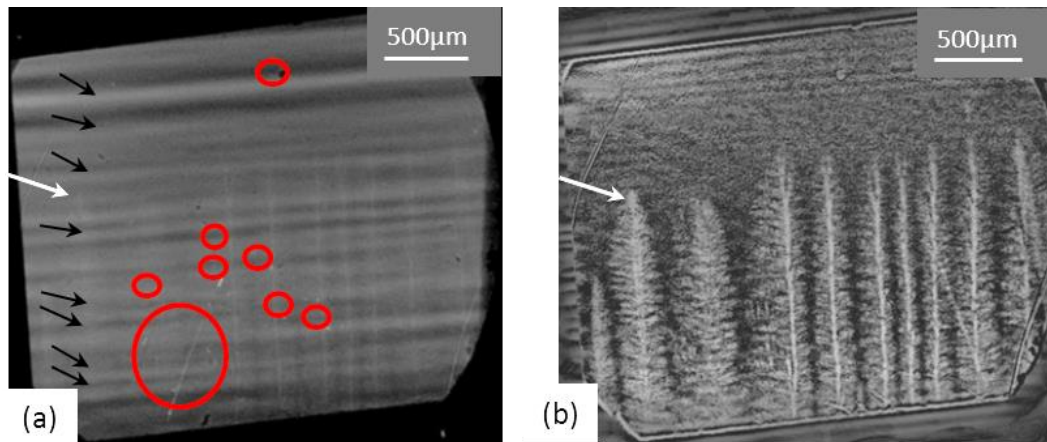


Fig. 3.3. (a) A typical raw X-ray image that contains an array of faint dendrites, and many lines of periodical noises (pointed by black arrows) and defects (in circles); and (b) the same image processed using Fourier transform and inverse Fourier transform techniques, and the array of dendrites are clearly revealed.

3.3.1 Dendrite tip fragmentation

From image sequence acquired during in situ experiment, the fragmentations and movements of dendrite tips are observed and divided into the fragmentation without and with the PEC applied. Firstly, the dendrite tip fragmented from its original arm without PEC applied and after fragmented, it naturally flows up to the liquid zone. While second dendrite fragmented and moved according to the frequency of the PEC applied.

3.3.1.1 Dendrite fragmentation without PEC

Fig. 3.4 shows the measured temperatures by the two thermocouples attached to the upper (T1) and lower copper (T2) heating plates. Firstly, the sample was heated above the liquidus temperature (612 °C) by using both heaters and stabilised for a short while. Then the lower heater temperature started to cool down below the liquidus to nucleate new grains at the bottom edge of the view field. The temperatures of both heaters were carefully controlled to form a relatively constant temperature gradient of ~ 53 K/mm for this case to force the grains grew upwards in the view field.

Table 3.3. The parameters used for the five anti-parallel (with gravity) directional solidification experiments

Experiment		V1	V2	V3	V4	V5
Pulse parameter	Wave form	No	sine	sine	sine	sine
	Frequency, Hz	No	1	1	1	10
	Lorenz force, mN	No	0.3	0.3	0.3	0.3
Thermal parameters	Thermal gradient, K/mm	53	53	47	31	42

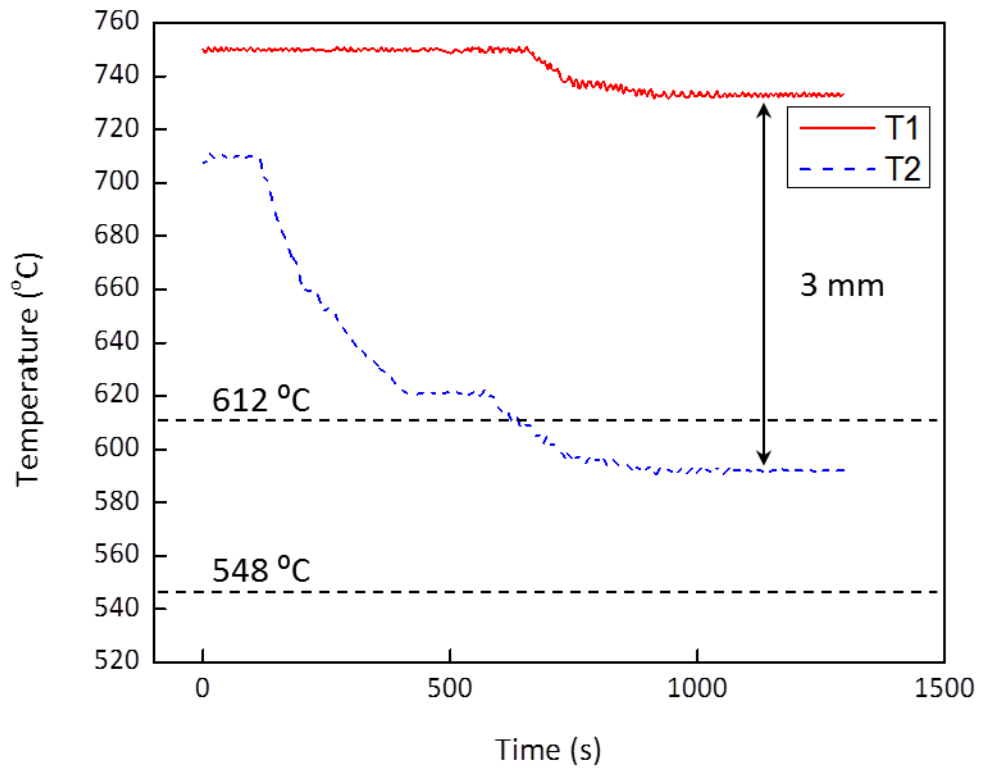


Fig. 3.4. The temperature profiles measured by the two thermocouples, T1 and T2 in the experiment V1

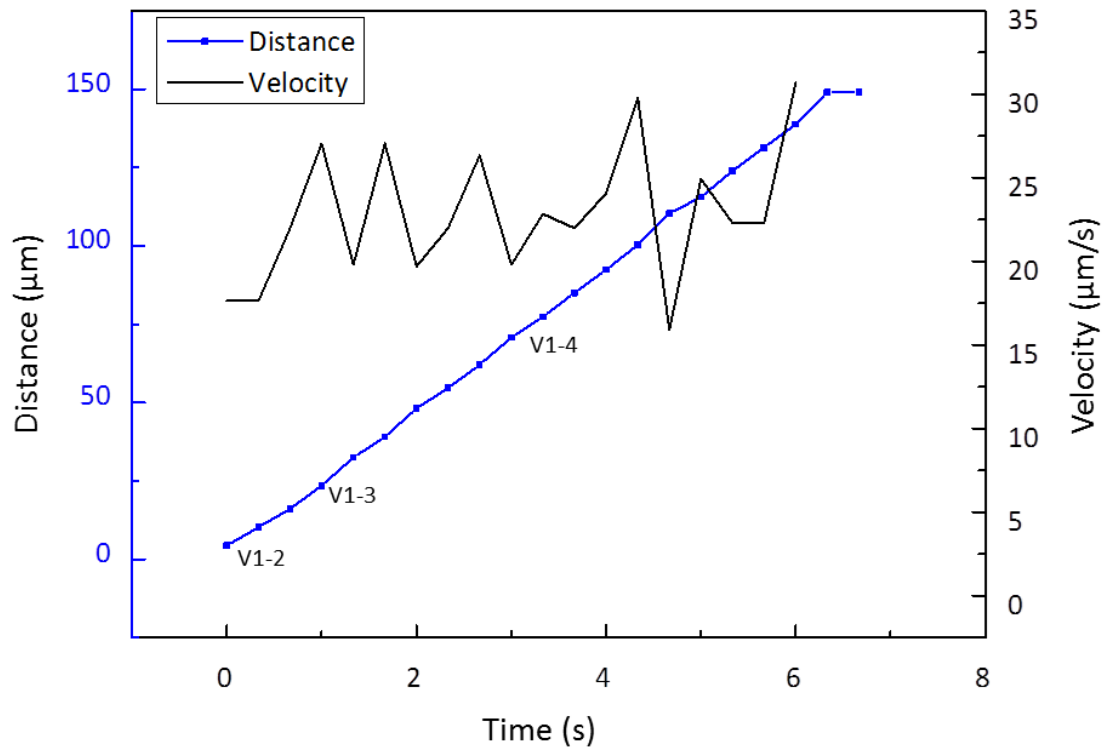


Fig. 3.5. The distance of dendrite detach from its arm and detached dendrite velocity

Fig. 3.6 shows 8 images selected from the video sequences of experiment V1. At 0 s (V1-2), a secondary dendrite branch was seen to start to detach from its primary dendrite, floating upwards into the liquid melt against gravity as seen from V1-3 to V1-6. The distance of the dendrite tip flew up into the liquid melt was tracked and plotted in Fig. 3.5. The white dot showed in V1-2 was the tracking starting point for the detached dendrite. When the detached dendrite approached the position shown in V1-7, it was remelted and dissolved back into the liquid melt as confirmed in V1-8. The dendrites travelled upwards a distance of $\sim 150 \mu\text{m}$ in 7 s driven by the buoyant force because the solid dendrite is an Al rich material, lighter than the Al-Cu melt. The remelting at V1-7 is because of the higher melt temperature near T1.

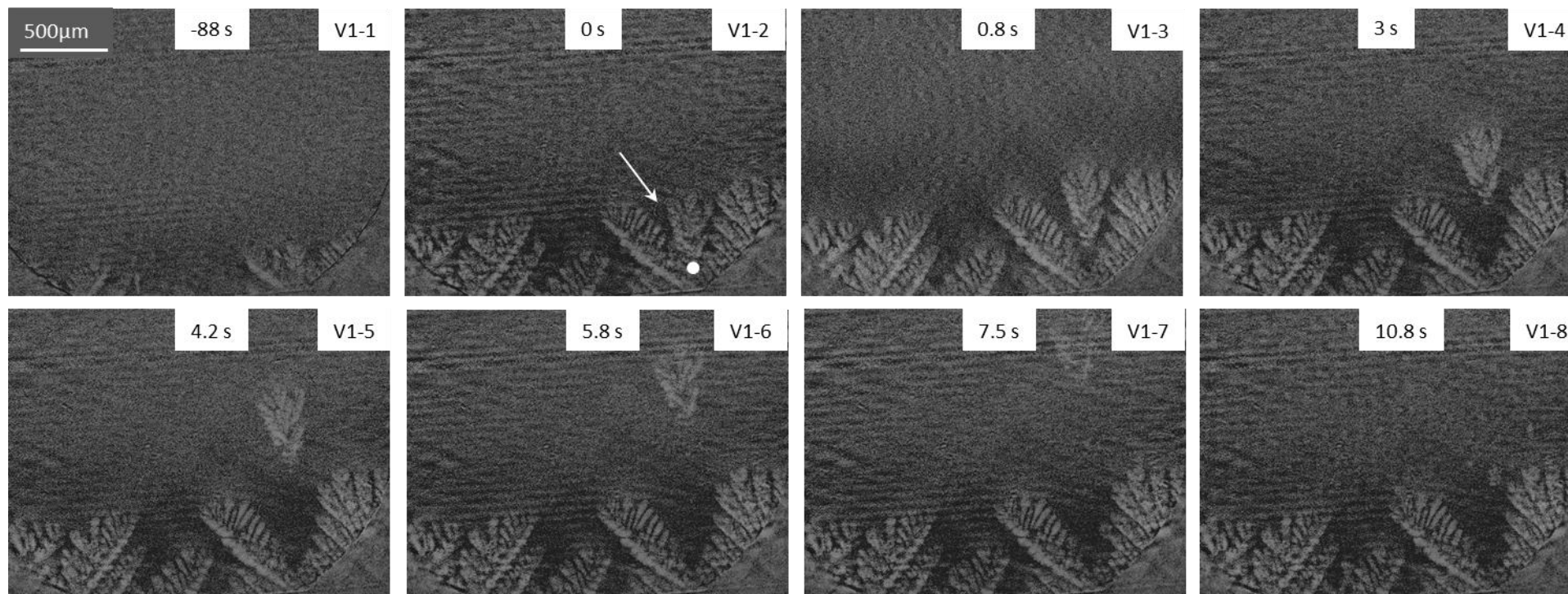


Fig. 3.6. The fragmentation of a dendrite without PEC (from experiment V1)

3.3.1.2 Dendrite fragmentation with PEC

Fig. 3.7 shows the measured temperature profiles of T1 and T2 for the experiment V2. Again, after sample was melted, and the temperatures of both heaters were stabilised for a little while, the lower heater temperature was decreased to below the liquidus until dendrite grains were showed to grow in the view field. The temperature gradient was again controlled at ~ 53 K/mm. After finishing the imaging, the lower heater temperature was increased to remelt the grown dendrites and then the experiments can continue without changing samples.

Fig. 3.9 shows 16 images (V2-1 \sim V2-16) extracted from the videos of experiment V2 with the PEC applied continuously from 0 s (V2-1) to 7.6 s (V2-16). The accurate temperature controls forced grains to nucleate at the bottom edge of the view field, while the majority of the alloy in the view field was still in liquid state. A small dendrite grain was found at 0 s (pointed by a white arrow in V2-1), and grew bigger and bigger from V2-2 to V2-7. At the same time, the dendrite oscillated under the action of the applied PEC. The cyclic movement path of the dendrite tip was tracked and plotted in Fig. 3.8, and the oscillation has an amplitude of ~ 300 μm with a frequency of 1 Hz, resonating the PEC frequency. At V2-8, the dendrite was found to detach from the base and floated upwards following the cyclic path as showed in Fig. 3.8. Clearly, coupling with the static magnetic field given by the ring-shaped permanent magnet, the applied PEC generates sufficient Lorentz force to move the liquid melt and the solid dendrites floating inside in a cyclic manner.

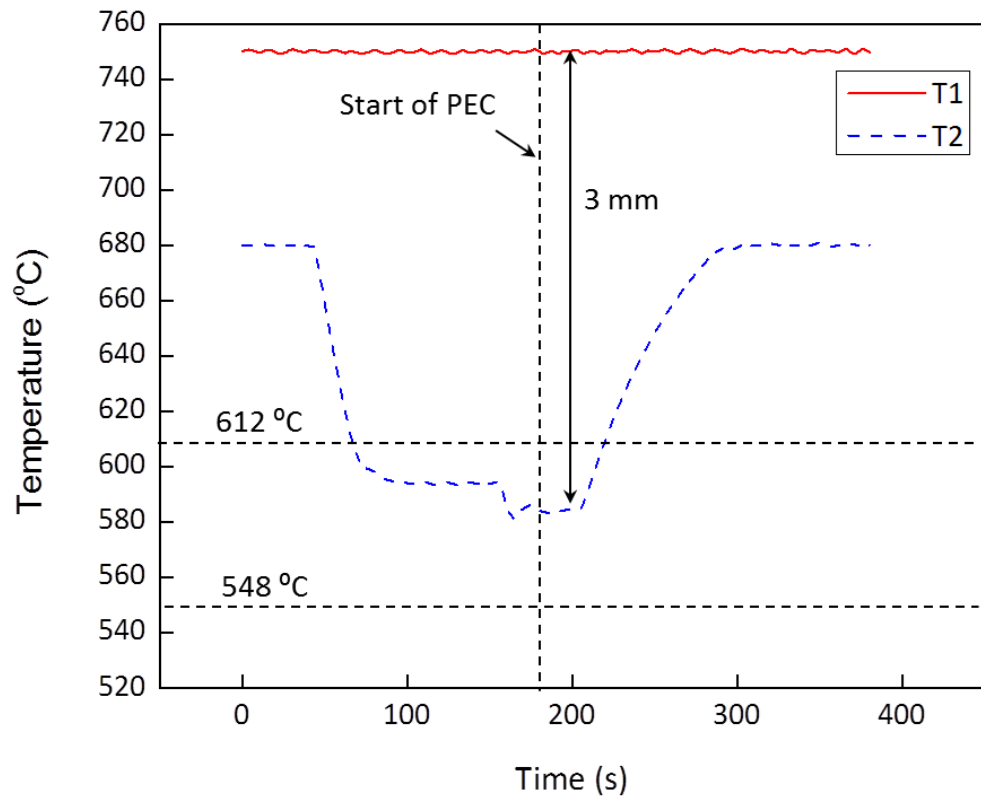


Fig. 3.7. The temperature profiles measured by the two thermocouples attached to the upper ($T1$) and lower ($T2$) heaters in experiment V2

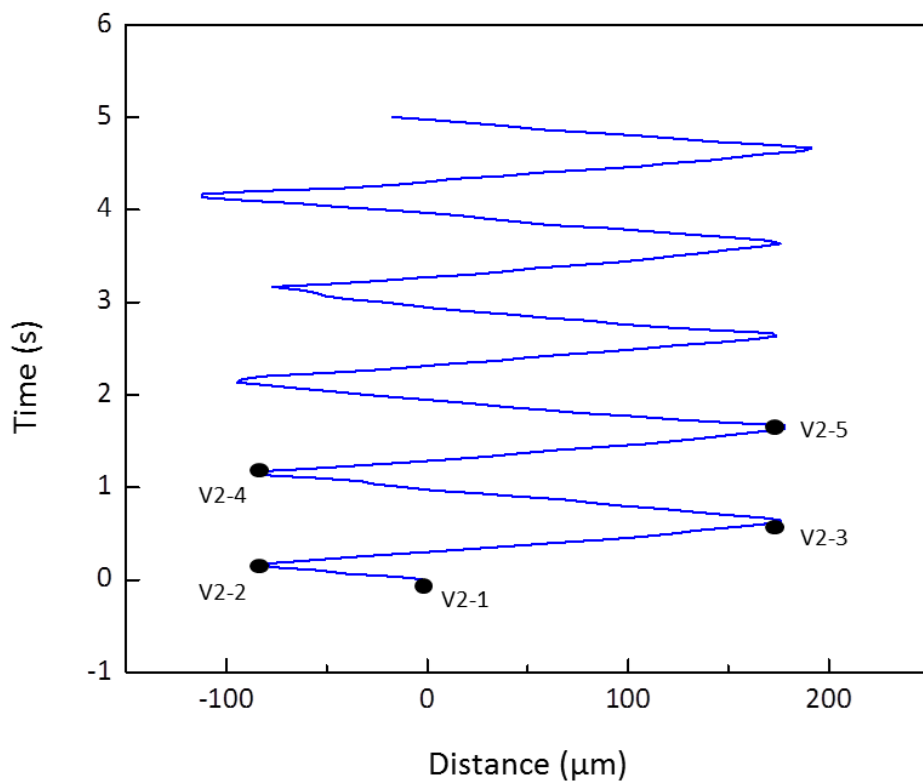


Fig. 3.8. The cyclic movement path of the dendrite after detached from its primary dendrite under the PEC, measured from the images in Fig.3.9

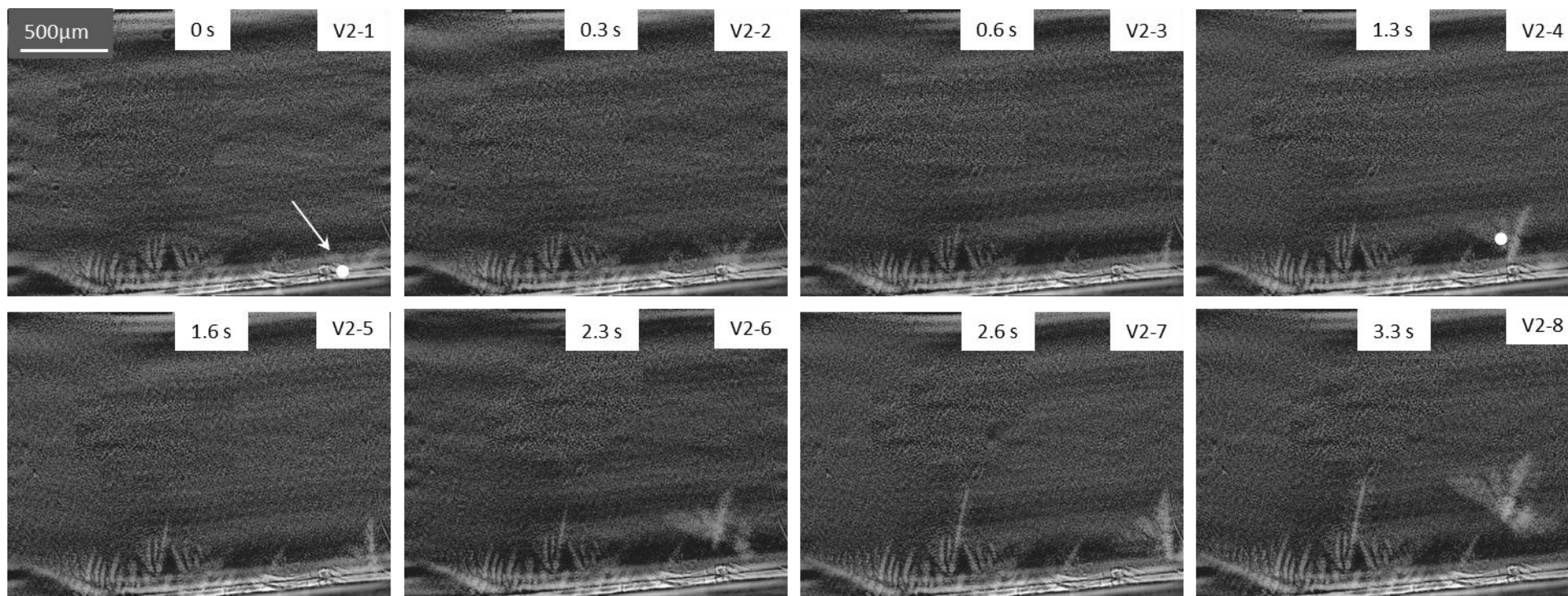


Fig. 3.9. The cyclic movement of the detached dendrite tip under the applied PEC. Images are extracted from the video of experiment V2

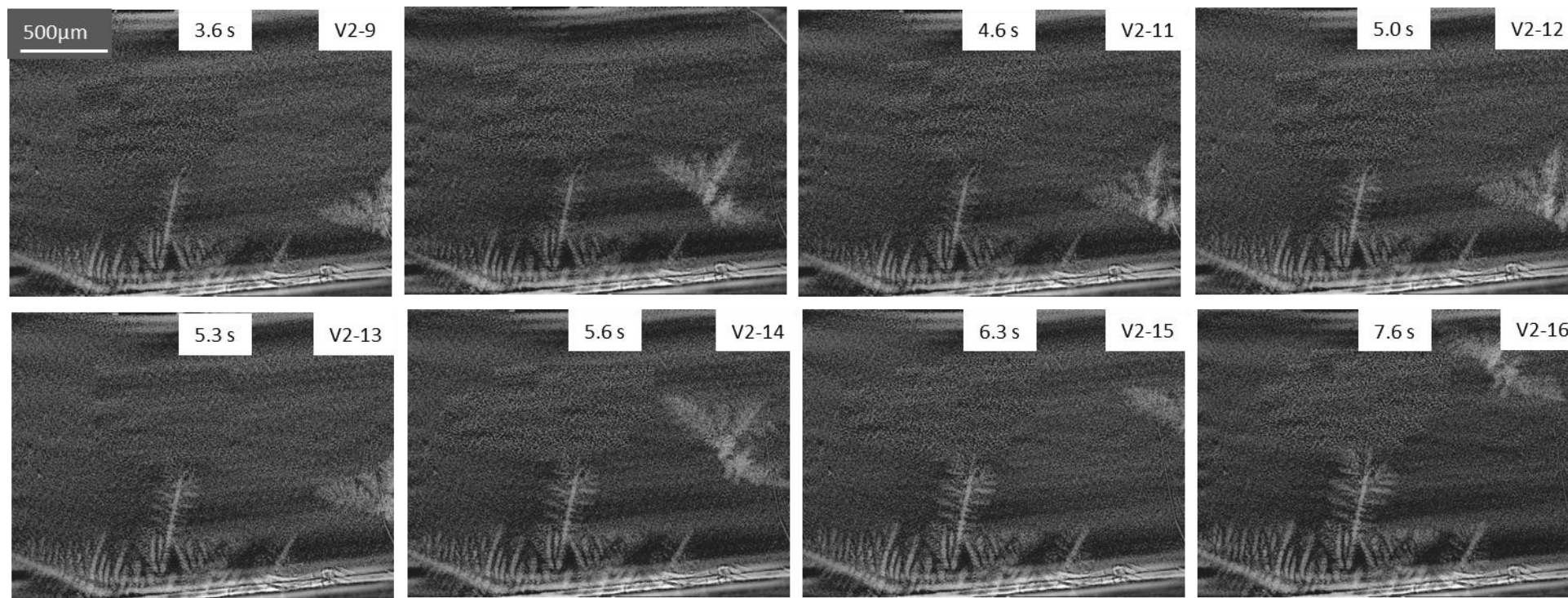


Fig. 3.9.(continue) The cyclic movement of the detached dendrite tip under the applied PEC. Images are extracted from the video of experiment V2

3.3.2 Dendrite growth under directional solidification

Fig. 3.10 shows the measured temperature profiles of T1 and T2 for the experiment V3. The combinations of temperature controls (a temperature gradient of 47 K/mm) allowed near-parallel dendrites to grow into the view field.

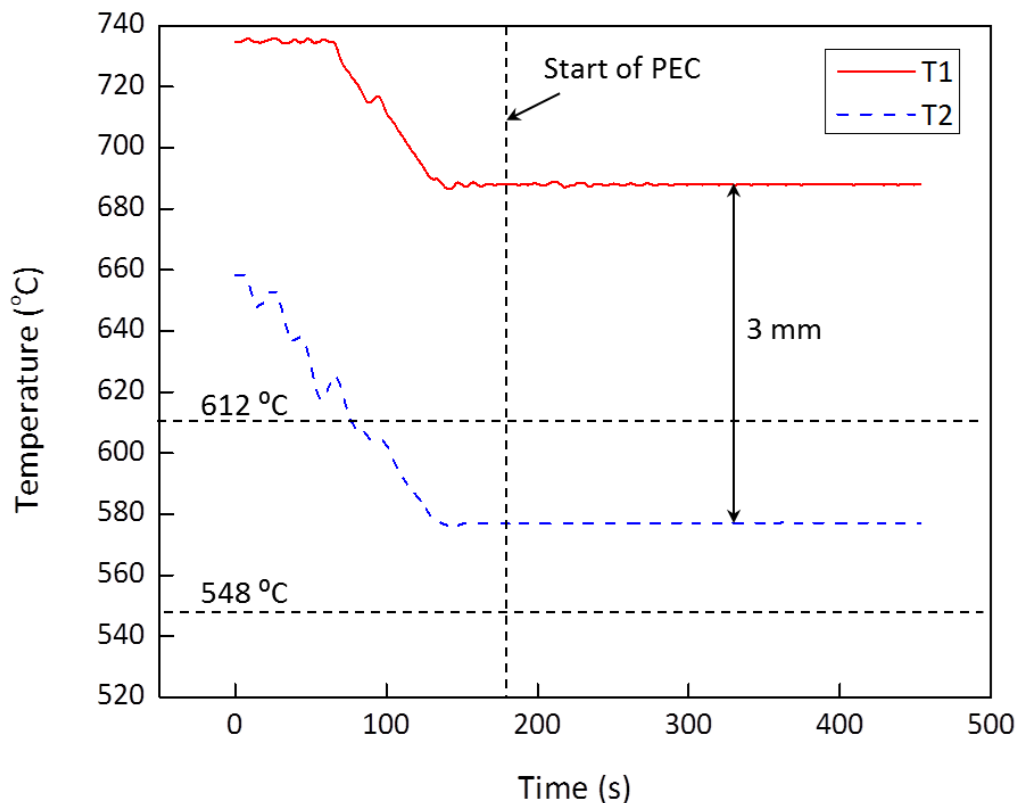


Fig. 3.10. The temperature profiles measured by the two thermocouples attached to the upper (T1) and lower (T2) heaters in experiment V3

Fig. 3.11 shows images (V3-1 ~ V3-8) selected from the video of experiment V3, starting at the moment when the dendrites grew into the view field from 0 to 27 seconds.

Gradually, a total of 10 dendrites grew into the view field with primary and secondary arm well developed under the imposed temperature gradient. The dendrite tip growth rates of four dendrites (marked D1, D2, D3 and D4 in V3-5) were measured by tracking the advance of the tips. The growth rate measurements were made by firstly placing a tracking marker on the

tip of the tracked dendrite, and then counting the advance of the tracking marker and the associated time from the subsequent video frames. The tracking procedure started when the dendrites firstly appeared at the bottom in the view field and finished when the dendrite growth reached a steady-state. The measured grown lengths of D1- D4 were plotted using Origin software against the time and showed in Fig. 3.12, and finally the growth rate of the dendrite can be calculated by:

$$V = \frac{L_2 - L_1}{t_2 - t_1} \quad (3.2)$$

Where L_1 and L_2 are lengths of the dendrites measured at the image frames at t_1 and t_2 respectively.

Fig. 3.11 (V3-1~V3-8) and Fig. 3.12 show that the dendrites grew faster when they first appeared in the view field, then gradually slowed down, and finally almost stopped growing after occupied about 2/3 of the view field due to the imposed constant temperature gradient. The lengths of dendrites D3 and D4 are approximately 1900-2000 μm , while the lengths of dendrite of D1 and D2 are around 1700 μm .

Fig. 3.12 shows the growth rate of four dendrites. Two lines present the growth rate of dendrites without detachment while other two dendrites grew and detached from main branch. First two lines show that the growth rate decreases from 200 $\mu\text{m/s}$ to a constant growth rate of $\sim 10 \mu\text{m/s}$ and nearly stop. On the other hand, other two lines show that the growth rate drop suddenly because dendrites detached from the branch. However, the dendrites grew again with the similar growth rate after the tips were broken off.

During the growth of dendrite under the controlled temperature gradient, the liquid-solid interface was formed at the tip of the dendrites. Fig. 3.11(V3-9~V3-16) shows that the dendrites growth was stopped when occupied 2/3 of the view field, and then PEC was applied at 27 s after V3-8. The dendrite tip (pointed by the white arrow) started to fracture and detach from its main trunk. The broken off dendrite flew up in a cyclic movement according to the frequency of PEC. At 46s, dendrite D2 started to detach from its main trunk and flew up into the liquid zone similarly to dendrite D1. Fig. 3.11 (V3-17~V3-24) shows further 8 images to track the two detached dendrites (D1 and D2). They flew up into the liquid zone and remelted.

Fig. 3.13 shows the growth of dendrite D1 from 0 s to 37.01 s, but it broke off at 38.01 s as the PEC applied followed by a similar growth rate as before. Fig. 3.14 shows the similar phenomena for dendrite, D2.

Fig. 3.15 shows the cyclic movement path of the broken off dendrite tip from dendrite D1. It oscillated with an amplitude of 15 μm and a frequency of 1Hz, again according to the frequency of the PEC applied.

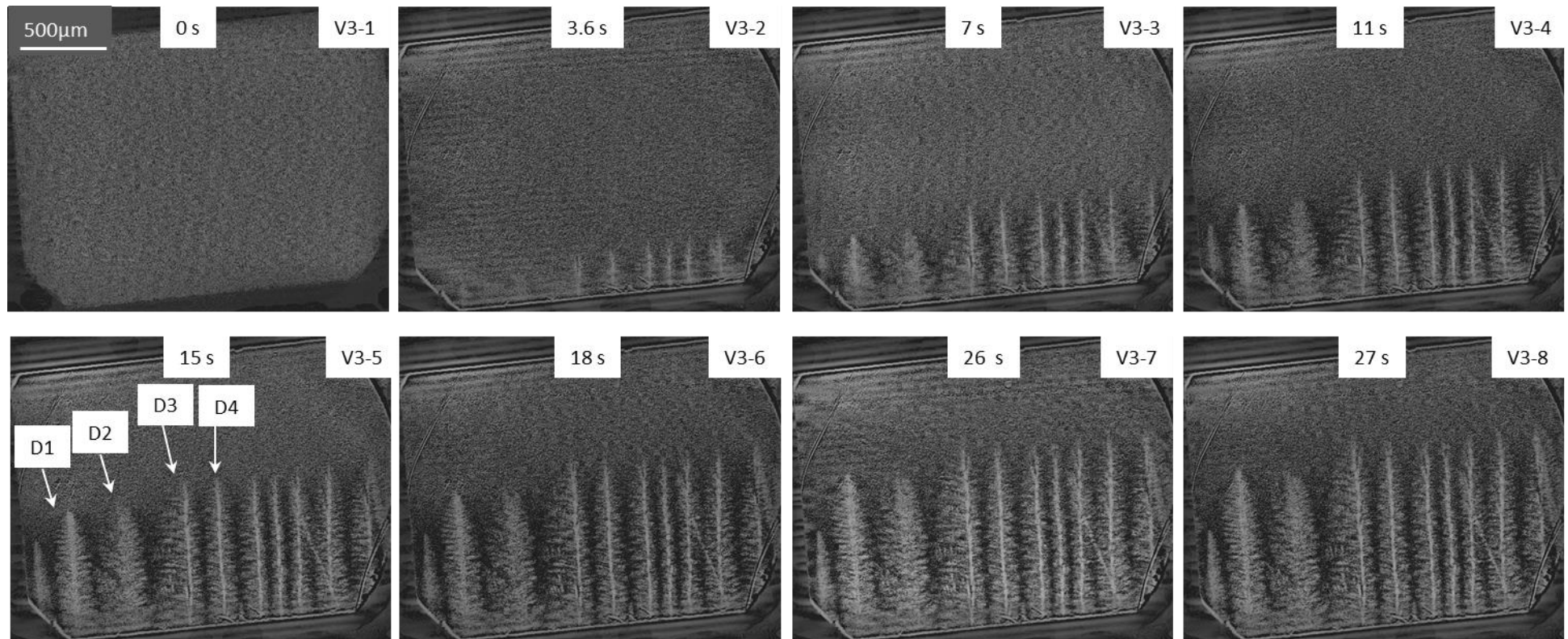


Fig. 3.11. Eight images selected from the video of experiment V3, showing the growth of 10 dendrites against gravity before applying PEC. The growths of four dendrites, D1, D2, D3 and D4 are tracked

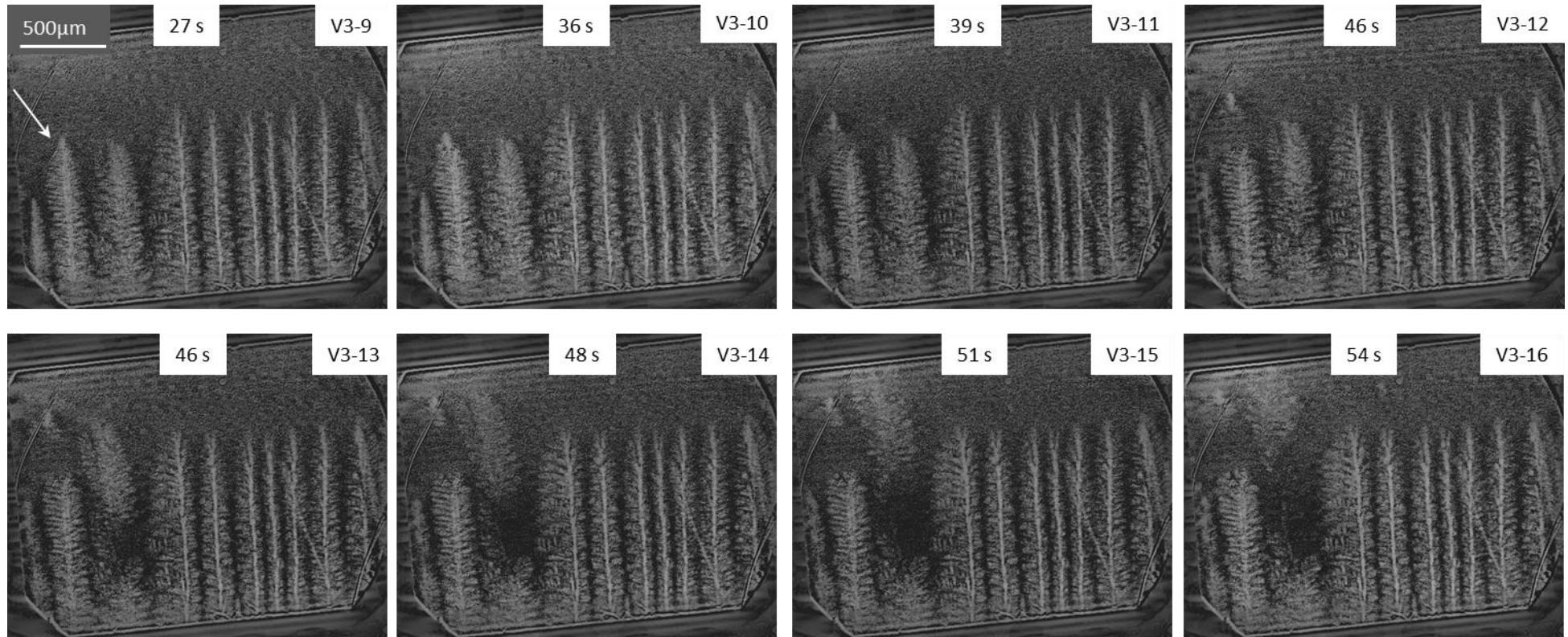


Fig. 3.11. (continue) Further 8 images, showing the detachment of dendrites under the applied PEC, the growths of four dendrites D1-D4 are tracked

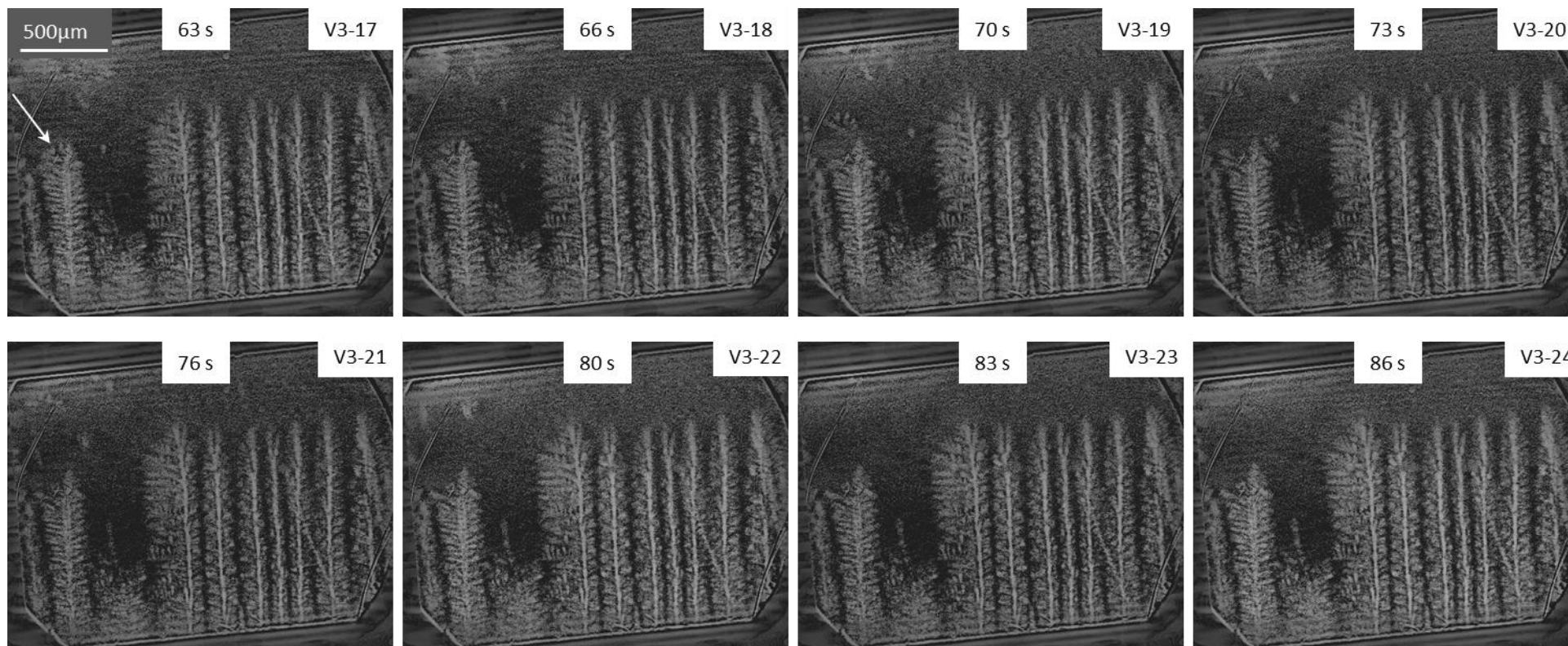


Fig. 3.11. (continue). Further 8 images, showing the continuous growth of the dendrites under the applied PEC

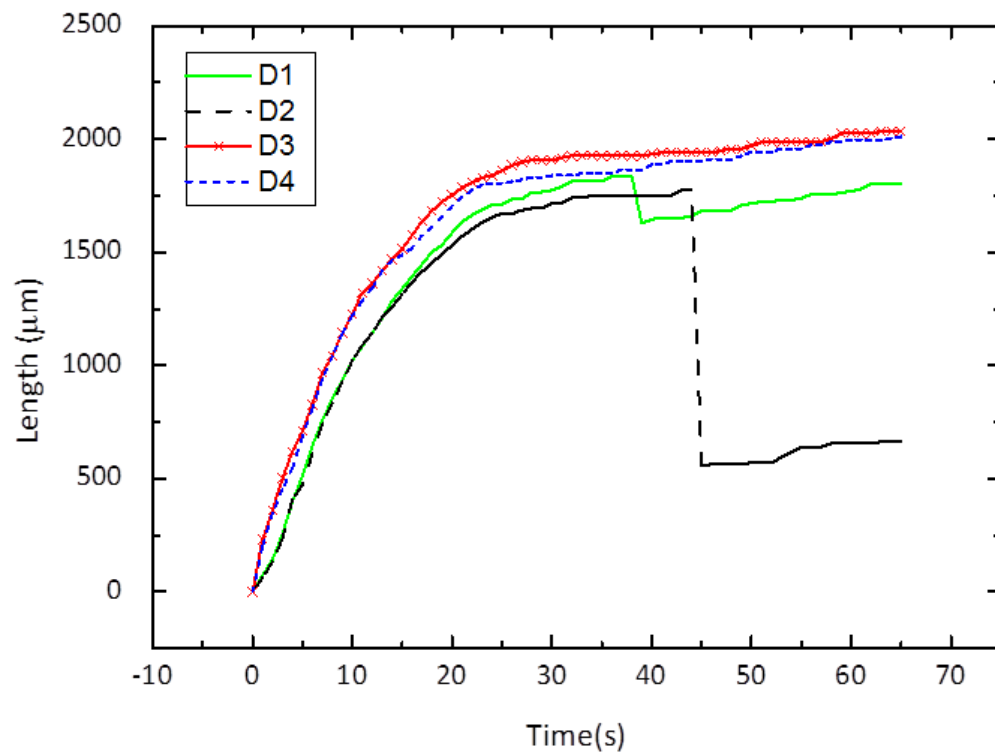


Fig. 3.12. The grown lengths of dendrites D1-D4 as a function of time

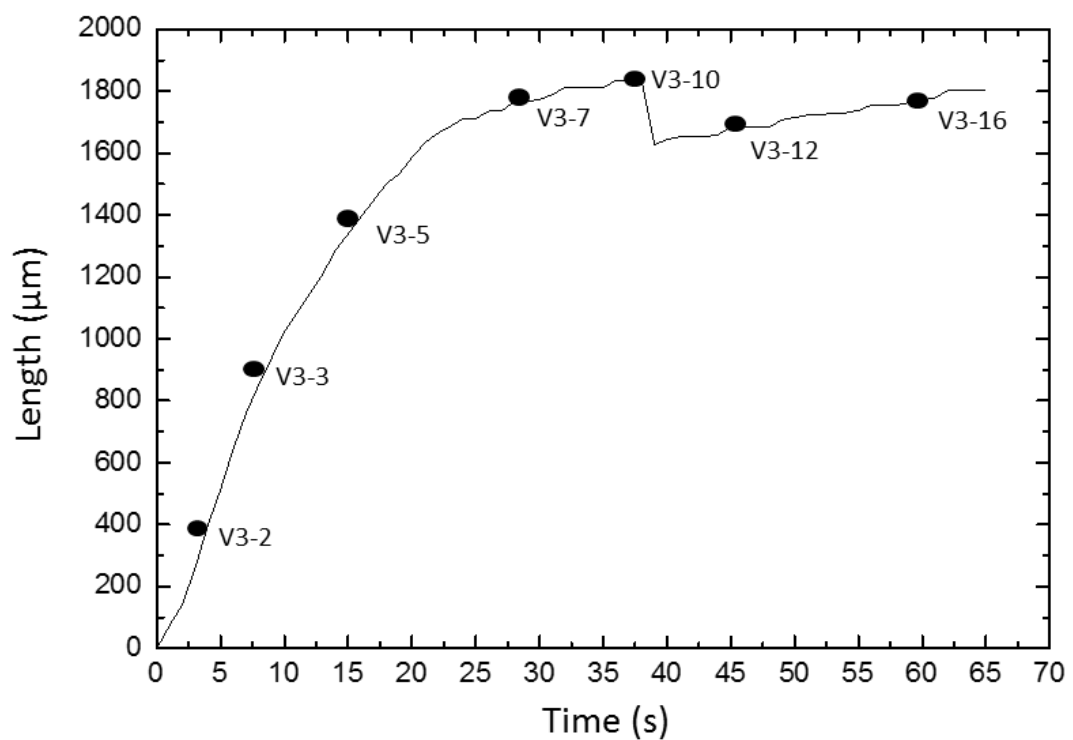


Fig. 3.13. The growth of dendrite D1 and the moment of the dendrite tip breaks off.

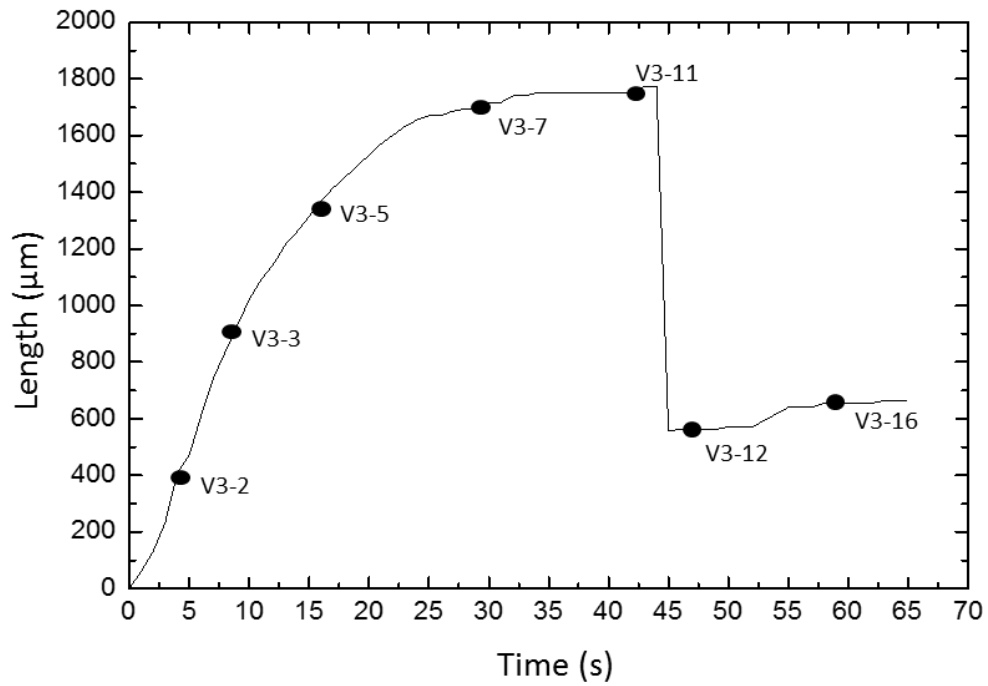


Fig. 3.14. The growth of dendrite D2 and the moment of the dendrite tip breaks off

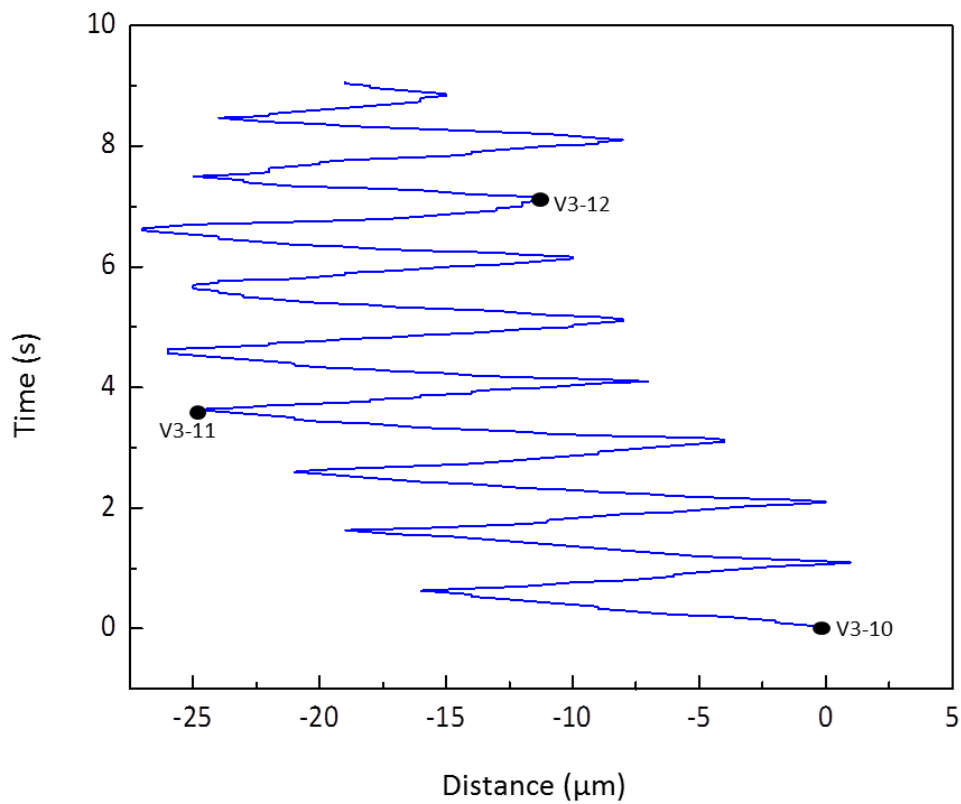


Fig. 3.15. The cyclic movement path of the broken off dendrite tip from D1 with a frequency of 1Hz

3.3.3 The effect of PEC on the solid dendrite arrays

The influence of applied PEC on the complete solid dendrite arrays are presented in this section.

Fig. 3.16 shows the measured temperature profiles of T1 and T2 for the experiment V4. The combinations of temperature controls (a temperature gradient of 31 K/mm) allowed near-parallel dendrites to grow into and occupy almost the whole view field. The remelting the sample caused two peaks appear on the graph as seen in Fig. 3.16.

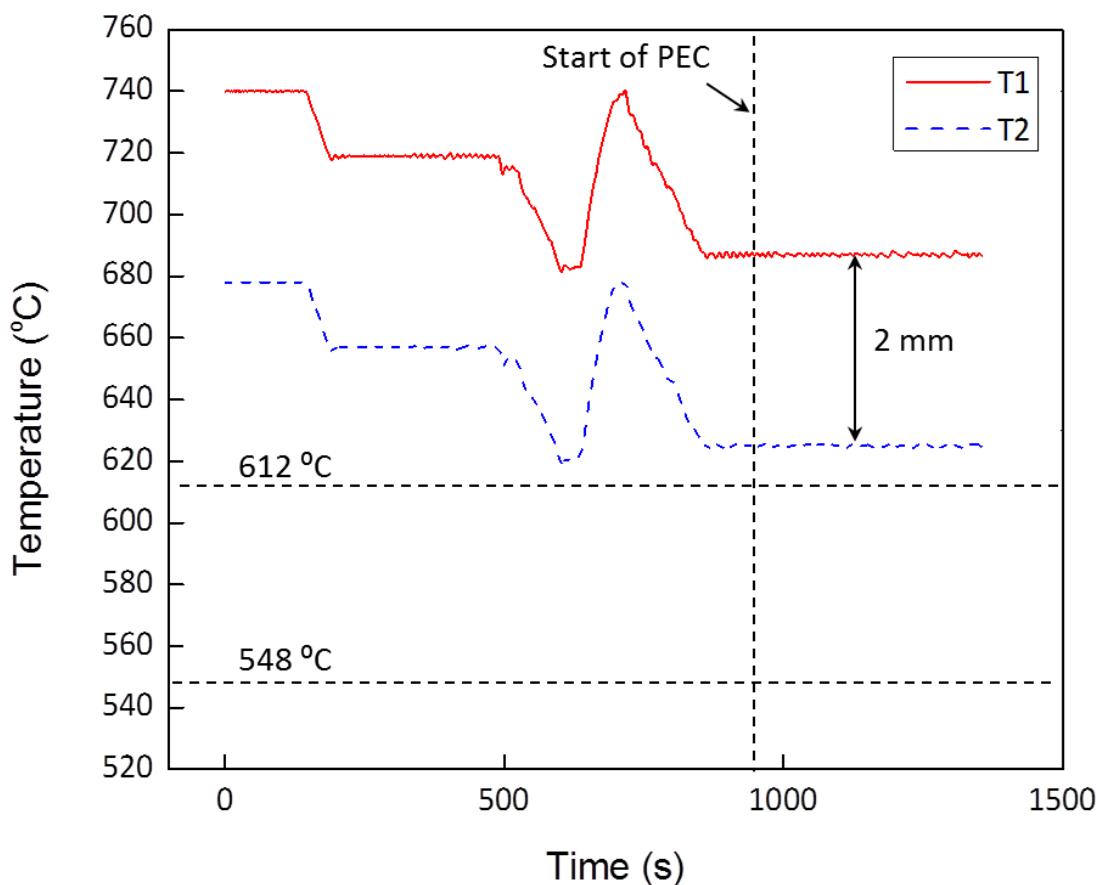


Fig. 3.16. The temperature profiles measured by the two thermocouples attached to the upper (T1) and lower (T2) heaters in experiment V4

Fig. 3.17a shows 4 images containing an array of near-parallel dendrites. Dendrite (pointed by an arrow) was found to vibrate when PEC applied. The movement of the vibration was tracked with the white dot as the tracking point, the grey bar show the displacement (D) of the dendrite moved by the

force from its original arm. The tracked movement is plotted in Fig. 3.17b. Clearly, the vibration follows the PEC frequency.

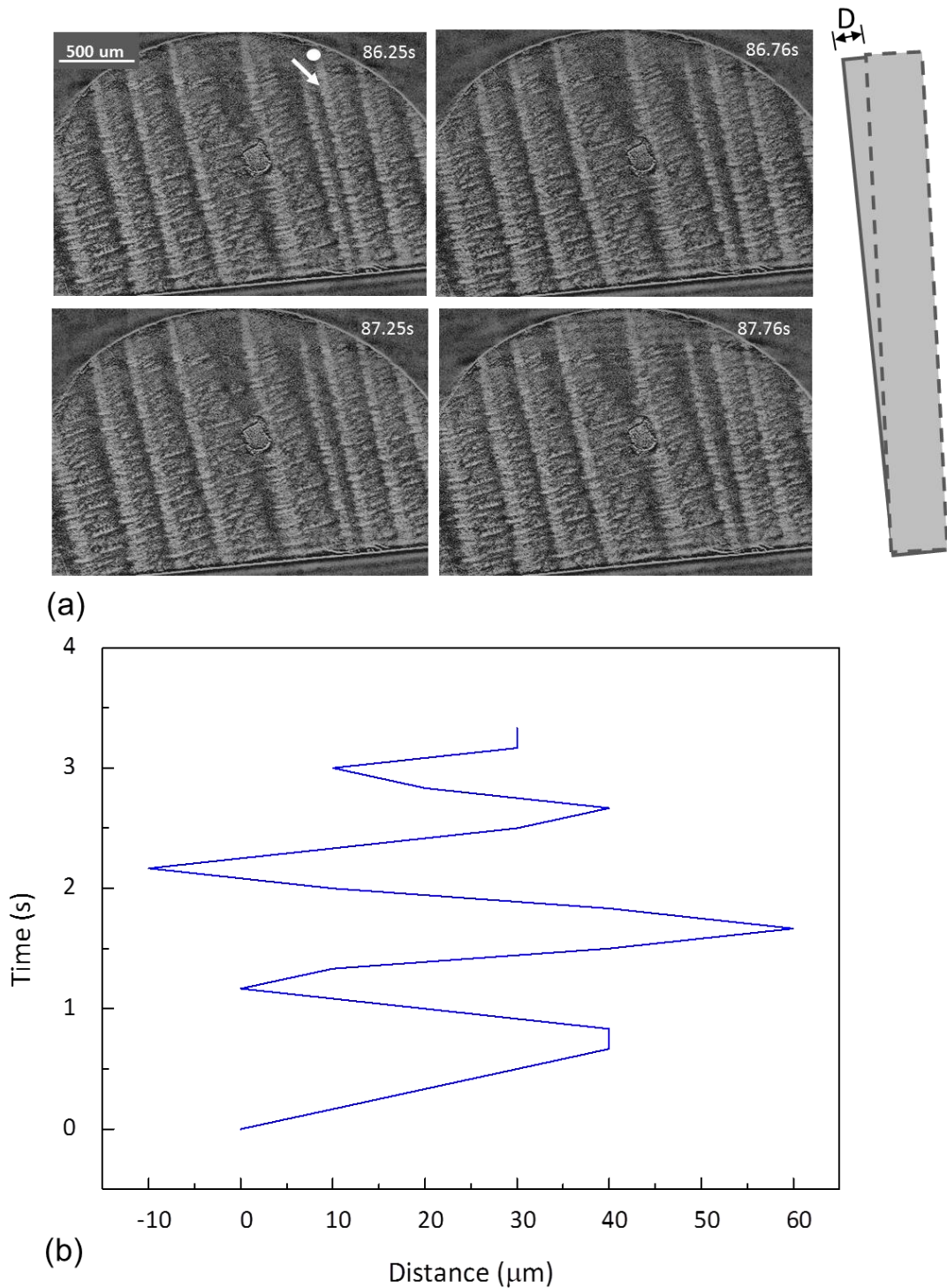


Fig. 3.17. (a) Four images from the video of experiment V4, showing an array of solid dendrites oscillate harmonically under the 1 Hz PEC applied. (b) the oscillated path of the wobbled dendrites

Fig. 3.18 shows the temperature control of experiment V5 to form an array of similar parallel dendrites as shown in Fig. 3.19a. In this case, the PEC of 10 Hz was applied. Dendrite from the right hand side (pointed by an arrow and dash line) was tracked with the white dot as the tracking point on the dendrite. This tracking point is located at the tip of the dendrite which gives the maximum movement.

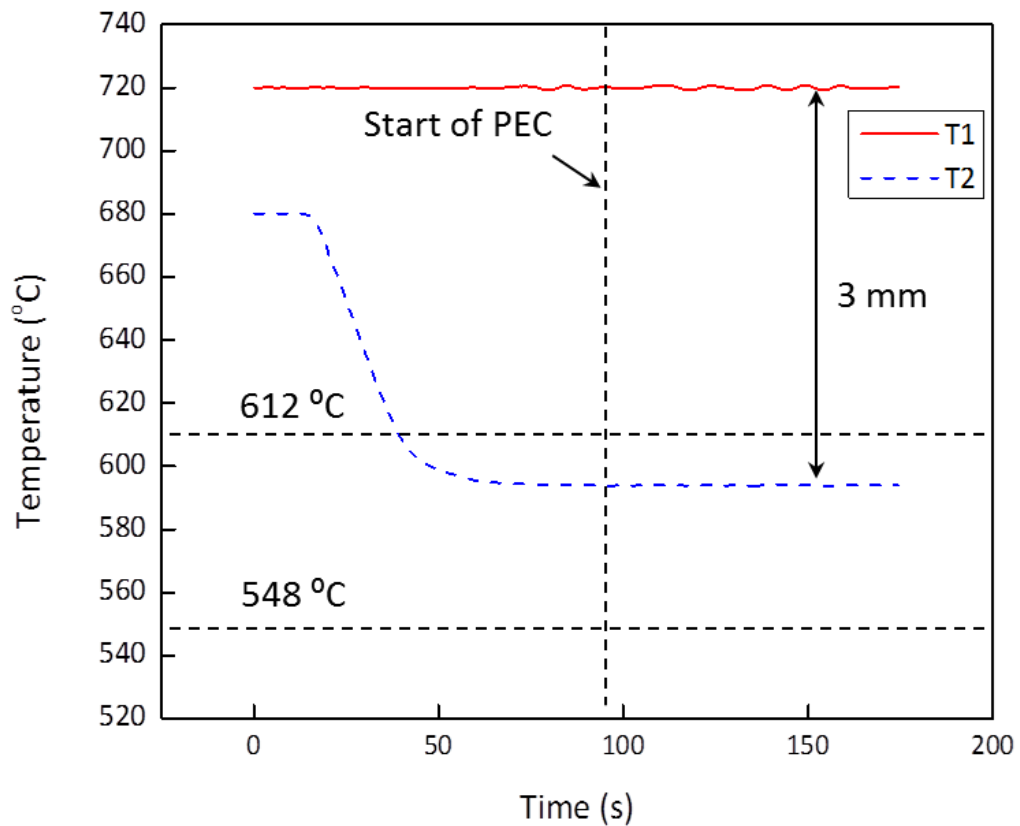
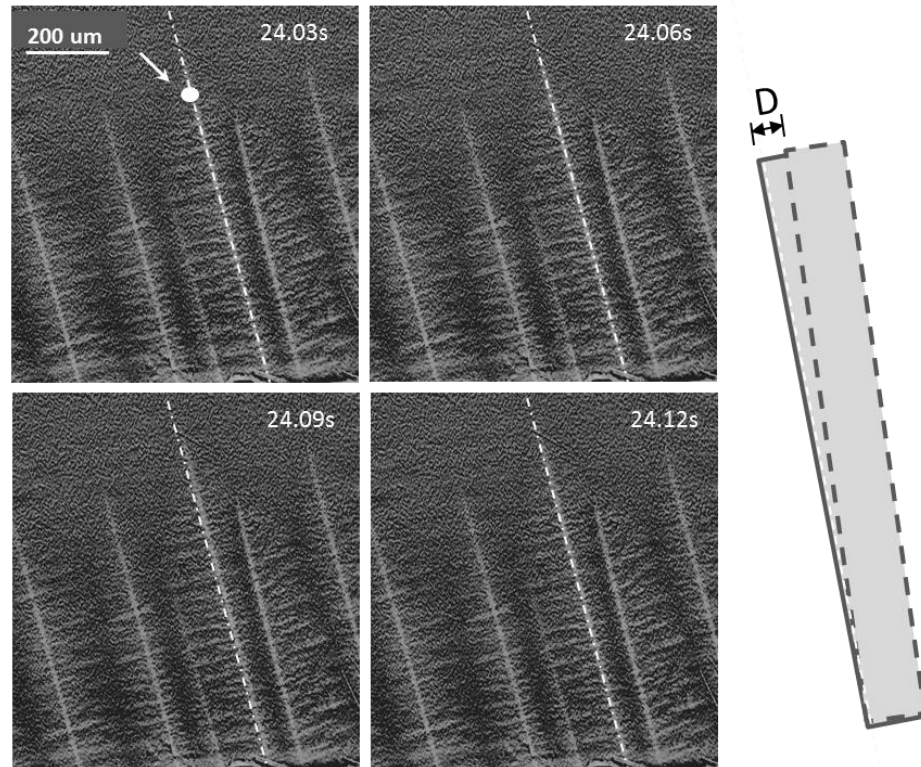
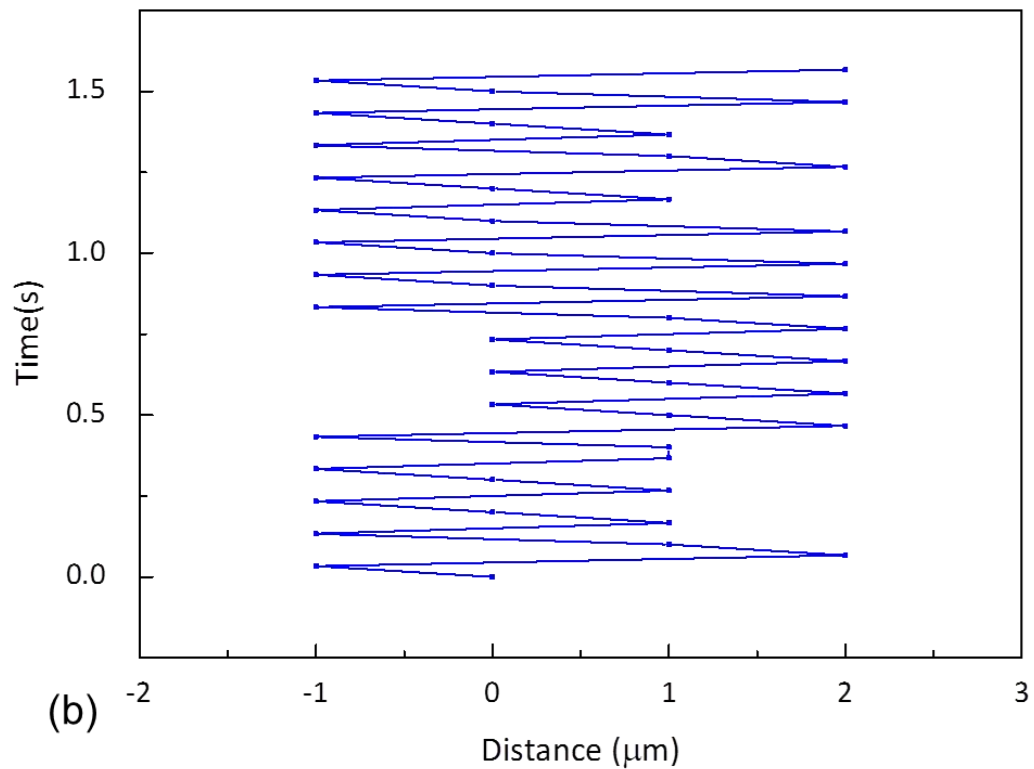


Fig. 3.18. The temperature profiles measured by the two thermocouples attached to the upper (T1) and lower (T2) heaters in experiment V5

Fig. 3.19b shows the oscillated path of the tracking point. The oscillation is presented in term of displacement from the original arm and tracked in every 10 frames or 0.33 second. The displacement amplitude of dendrite under 1Hz frequency is 25 μm (Fig. 3.17b) while the displacement amplitude from 10 Hz is 1.5 μm (Fig. 3.19b). Moreover, comparison of both figures shows that dendrite with low frequency displace from its original more than that of the higher frequency.



(a)



(b)

Fig. 3.19. (a) Four images from the video of experiment V5, showing an array of solid dendrites oscillate harmonically under the 10 Hz PEC applied. (b) the oscillated path of the wobbled dendrites

3.4 Summary

This chapter describes the in situ experiments using synchrotron X-ray technique to observe the behaviour of the dendritic microstructure during solidification under applied PEC.

Many series of image sequences were acquired for the Al-15%Cu solidified without and with PEC. Five typical image sequences were presented. All experiment results indicate that the PEC coupled with the static magnetic field can generate sufficient Lorentz force to move the liquid melt, semisolid dendrites and the solid dendrites during the solidification process.

Based on the experiments and the experience gained from these experiment, a novel pulse electromagnetic device which can generate much strong Lorentz force was designed and built (detailed in chapter 4) to study the effect of the electromagnetic force on bulk alloy samples.

Chapter 4 : The electromagnetic pulse device and the solidification apparatus

This chapter describes in details the design, building and commissioning of a novel, programmable electromagnetic pulse (EMP) device and a small scale solidification apparatus for studying metal solidifications in pulse electromagnetic fields. Fig. 4.1 shows the key functional units of the EMP device and its integration with the solidification apparatus. The novelty of this EMP device is the trigger unit, and it was designed to generate magnetic and current pulses with programmable amplitude, duration and frequency into the metal alloys during solidification in order to study their effects on the solidification microstructure.

The design principle of the electric circuit and the key elements of each functional unit of the EMP device are described first, followed by its commissioning and integration with the solidification apparatus.

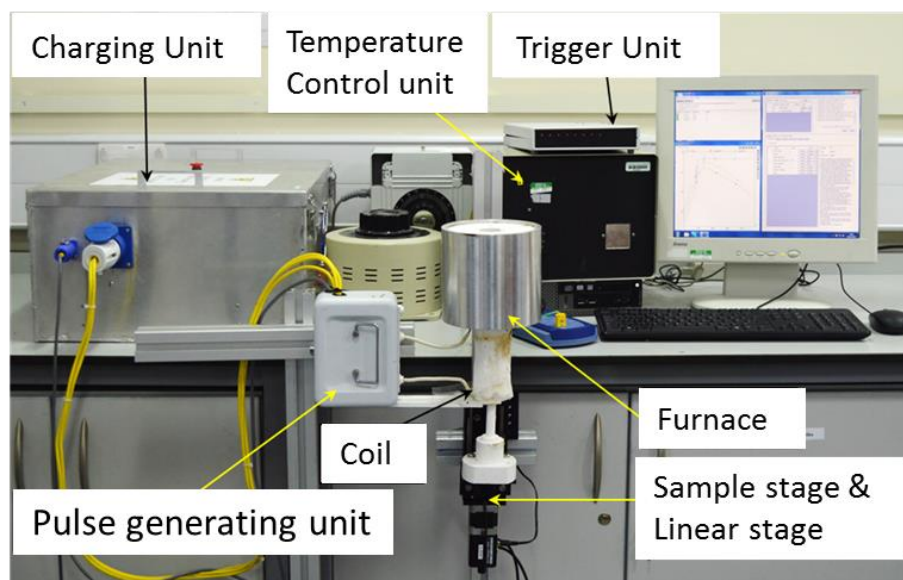


Fig. 4.1. A photo, showing each functional unit of the programmable EMP device, the small-scale solidification apparatus and the temperature control system.

4.1 The principle and circuit design of the EMP device

Pulse electric devices are very common in electric industry, for example, pulse magnetic field and pulse electric discharging devices or equipment in assembling, spot welding, cutting and circuit breaker [160]. Since 1990s, research on applying direct-electric current pulse [6], pulse magnetic fields [161, 162] and pulse magneto oscillation [81] into metal solidification processes have been carried out and continued to today.

The basic principle to produce an electric current or magnetic pulse is to use a specially-designed electric circuit to charge an energy storage device such as a capacitor using a low current electricity over a relatively long period of time, and then release the charged energy inside the capacitor in a very short period of time into a working unit to generate a high current pulse [163]. Basic principles of EMP is based on PMO, the setup and technique of how to generate and apply the pulse to a sample is similar to the PMO, and both use an induction coil to apply the external field to the sample without contact. Fig. 4.2 shows the schematic setup of the EMP.

The induction coil (copper wire) is a solenoid surrounding the sample as seen in Fig. 4.2. Low current is charged into the capacitor bank and then high current is discharged into the induction coil, generating an induced current (J) inside melt and induced magnetic flux (\mathbf{B}). The interaction between J and \mathbf{B} generates the Lorentz force inside sample. The amplitude of the force is dependent on the input voltage and charging time of the current into the capacitor bank.

The fabrication and detail of EMP device and experiment will be described in the following sections.

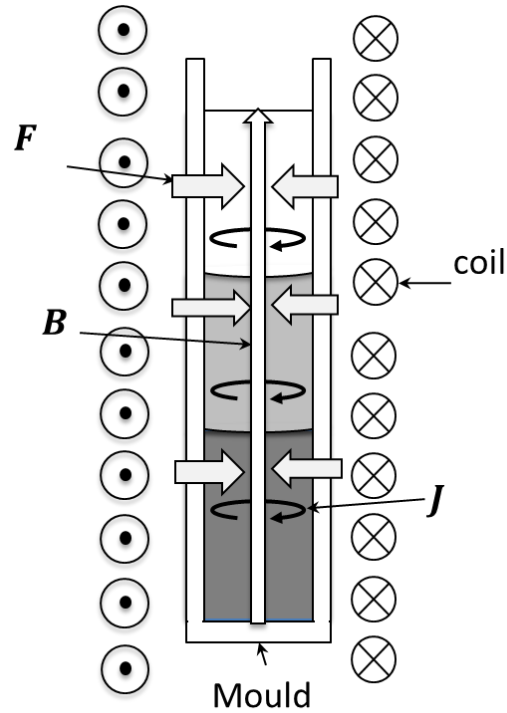


Fig. 4.2. The schematic setup of EMP and induced force

Fig. 4.3 shows the conceptual design of the electric circuit for the EMP device based on this principle.

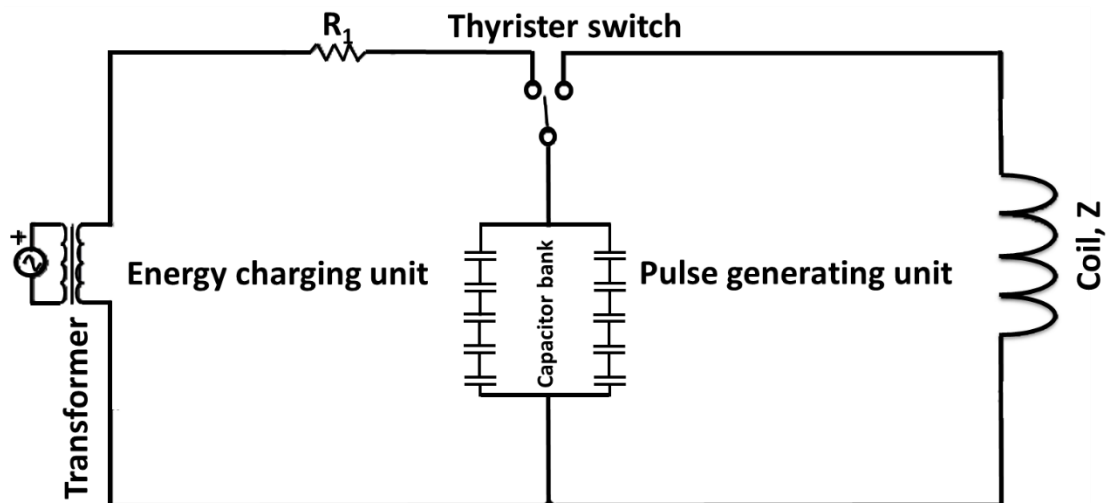


Fig. 4.3. The conceptual design of the electric circuit for the EMP device

The electric circuit comprises of two basic functional units: (1) a charging unit and (2) a pulse generating unit.

In the charging unit, an AC current delivered from a transformer is used to charge a capacity bank. The voltage and energy stored inside the capacitor and the time needed to charge the capacitor can be calculated by [164, 165]:

$$V_c = V \left(1 - e^{\left(\frac{-t_c}{R_1 C} \right)} \right) \quad (4.1)$$

$$E = 0.5 C V_c^2 \quad (4.2)$$

$$t_c = -R_1 C \ln \left(1 - \frac{V_c}{V} \right) \quad (4.3)$$

$$t_{full} = 5 \times R_1 C \quad (4.4)$$

Where V is the voltage output from the transformer, V_c is the voltage charged into the capacitor, t_c is charging time, R_1 is the resistor in the charging unit, C is the capacitance, E is the energy stored in the capacitor bank, and t_{full} is time needed to fully charge the capacitor [166].

After the capacitor bank is fully charged, the stored energy is released, via a high voltage switch controlled by the trigger unit, in very short period of time into an induction coil (the pulse generation unit) to create a short-time, high current pulse. The voltage discharged and the discharging time can be calculated by

$$V_d = V_c e^{\left(\frac{-t_d}{ZC}\right)} \quad (4.5)$$

$$t_d = -Z C \ln \left(\frac{V_d}{V_c}\right) \quad (4.6)$$

$$I_d = \frac{V_d}{Z} \quad (4.7)$$

Where V_d is the voltage discharged from the capacitor bank, Z is the total impedance of the coil, t_d is the discharge time and I_d is the discharge current.

4.2. Simulation and optimisation of the designed circuit

NI Multisim V 13.0 (National Instrument software) was employed to simulate the designed circuit in order to optimise the components used for the EMP device for producing the desired voltage pulse and frequency during discharging. The simulated circuit design is shown in Fig. 4.4, and the main parameters and components tested in the simulation here are the input voltage (V), resistor (R1), the capacitance of the capacitor (C), the Thyristor switch and the coil.

Firstly, a 120 V DC current was used as the input current for the charging unit (Fig. 4.4). Two oscilloscopes (2 and 1) are connected in parallel with the capacitor bank and the coil, respectively, to monitor and record the charging and discharging behaviours of the two units.

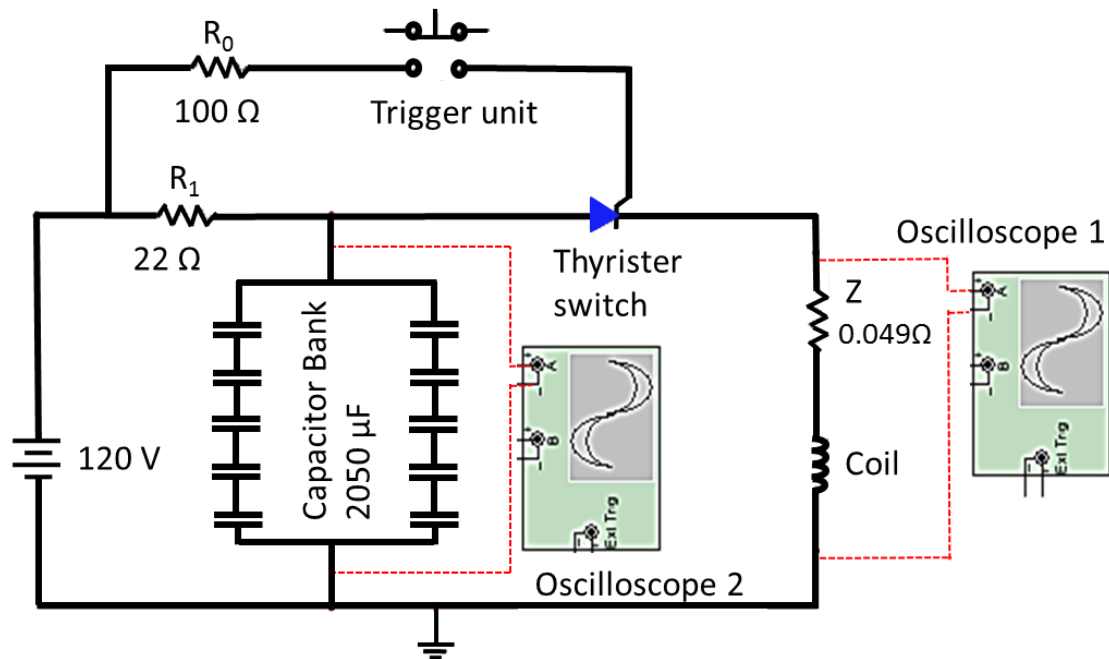


Fig. 4.4. The electric circuit used in the simulation

For the charging unit, the most important parameter for the designed circuit is the time needed to fully charge the capacitor, and it defines the charging and discharging frequencies for the EMP device. The time for charging a capacitor is governed by Eq. 4.3, and the time for fully charging can be calculated by Eq. 4.4 [166].

Table 4.1 lists the standard resistors and capacitors that are available from the electric components supplier (RS online company, <http://uk.rs-online.com/>). Using a fixed charging voltage of 120 V in the simulation, four different R_1 , each with three different C were tested. The fully charging time (t_{full} in Table 4.1) is in the range of 9.02 - 963.5 ms. Apparently, a shorter charging time will lead to a higher frequency for the EMP device to produce the desired pulse. For example, in 1 second, using a charging time of 9.02 ms, EMP device can produce 111 pulses, i.e. 111 Hz pulse; but if using a charge time of 963.5 ms, only 1 pulse can be delivered in 1 second, i.e. 1 Hz pulse. Fig. 4.5a shows the simulated voltage charging profiles and the fully charging time, t_{full} , can be broadly categorised in four ranges as noted in Table 4.1: (1) $t_{\text{full}} < 90$ ms, (2) $90 < t_{\text{full}} < 180$ ms, (3) $180 < t_{\text{full}} <$

400 ms, and (4) $t_{full} > 400$ ms. In order to produce a pulse in the frequency range of 1 – 10 Hz, the charging time of < 100 ms is needed. Based on this requirement, Fig. 4.5b shows the charging profiles of four R1 and C combinations that broadly meet this requirement. The discharging profiles of the four combinations were also simulated and showed in Fig. 4.5c. The case of $R1=10 \Omega$, $C=2050 \mu F$ gives the shortest charging time, but has a slightly longer discharge time. The case of $R1=47 \Omega$, $C=820 \mu F$ gives the second shortest charging time, but results in a big under-damped profile. The case of $R1 = 22 \Omega$, $C = 2050 \mu F$ and that $R1 = 10 \Omega$, $C = 4100 \mu F$ have very similar charging and discharging profile. But a higher R1 can better protect the reverse discharge current flow from charging unit.

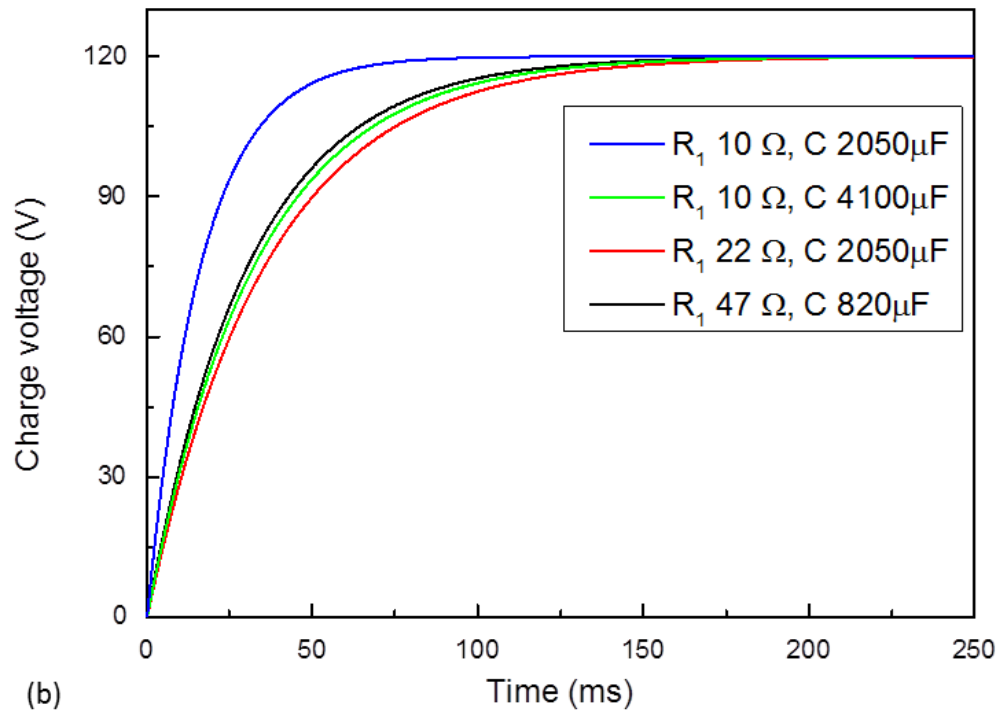
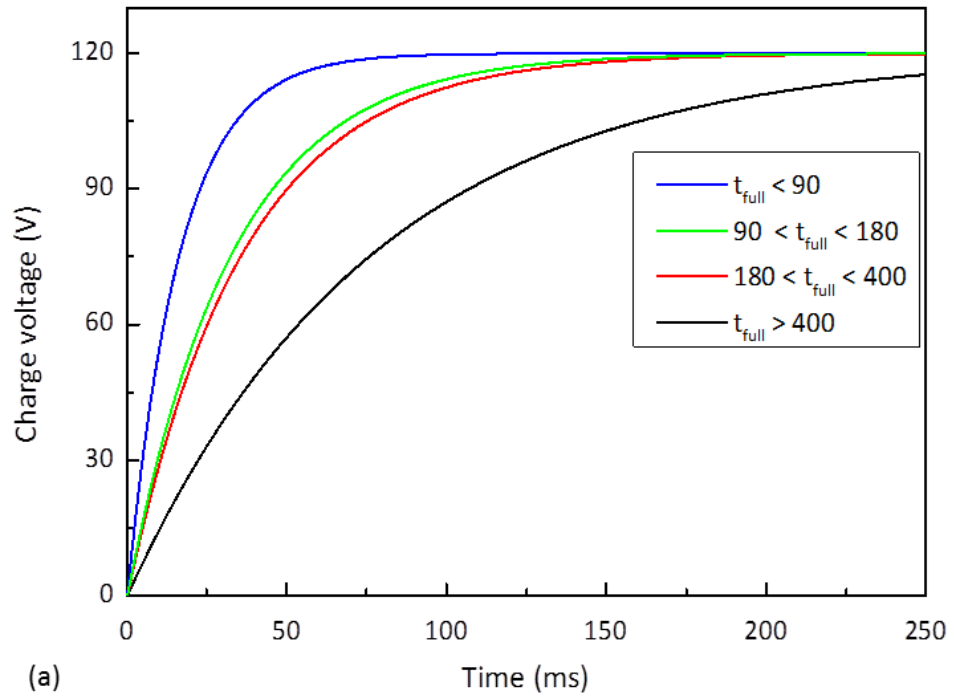
To further study the characteristics of the discharged pulse when using different impedance for the coil, three impedance values were tested ($Z=1$, 0.1 , and 0.01Ω). Fig. 4.5d shows the discharge profiles with $R1 = 22 \Omega$, $C = 2050 \mu F$ and three different Z. Clearly higher Z leads to a longer discharging profile, while a lower Z gives a larger under-damped profile.

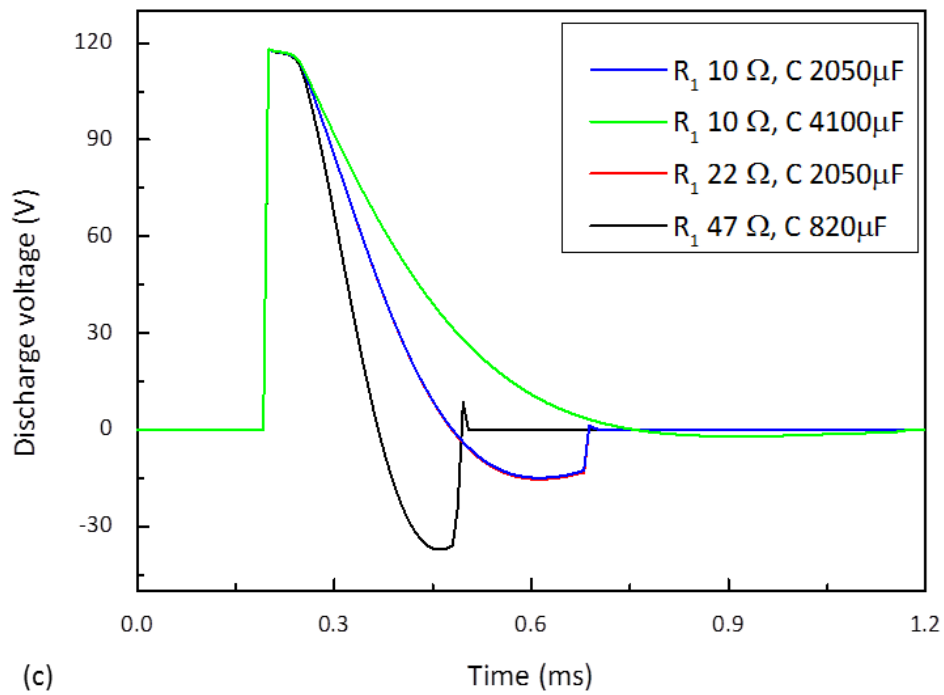
Based on the above simulation and discussion, $C=2050 \mu F$, and $R1=22 \Omega$ were chosen for the circuit, which can provide relative quick charging and discharging with the pulse frequency range of $1 \sim 10$ Hz with relatively small under-damped profile.

Table 4.1. The time needed to fully charge the EMP device when using R1 and C of different values

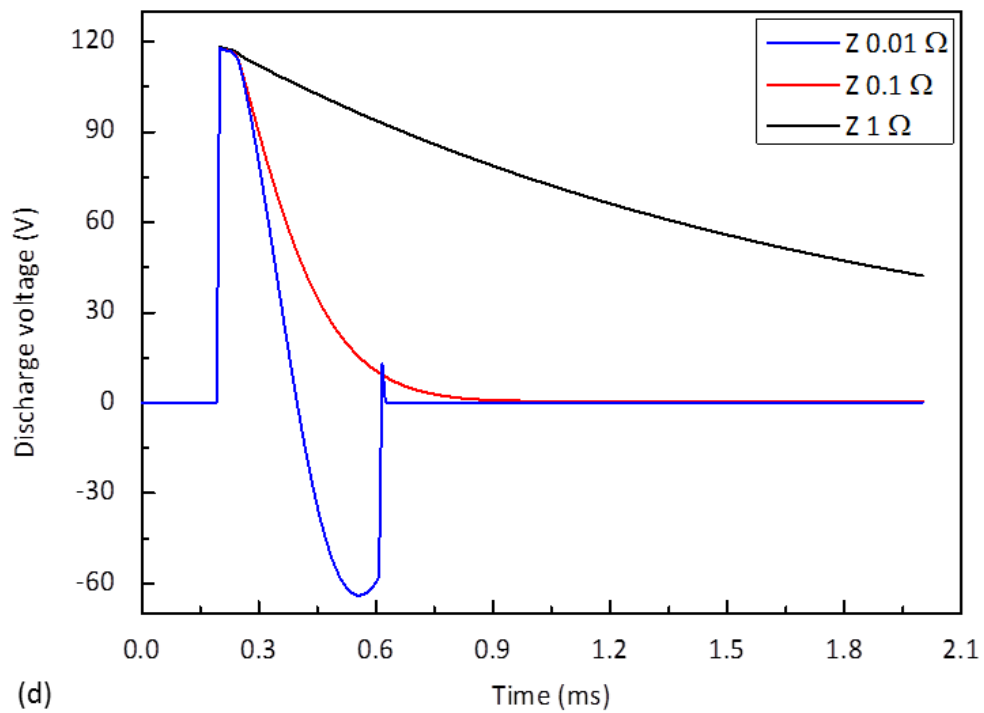
R1 (Ω)	47			22			10			2.2		
C (μF)	4100	2050	820	4100	2050	820	4100	2050	820	4100	2050	820
t_{full} (ms)	963.54 ⁴	481.75 ⁴	192.7 ³	451 ⁴	225.5 ³	90.2 ²	205 ³	102.5 ²	41 ¹	45.1 ¹	22.55 ¹	9.02 ¹

Note: 1: t_{full} < 90 ms;2: 90 < t_{full} < 180 ms;3: 180 < t_{full} < 400 ms;4: t_{full} > 400 ms





(c)



(d)

Fig. 4.5. (a) The voltage charging profiles for the charging unit when using different combination of R_1 and C , (b) the voltage charging profiles in range of $180 < t_{full} < 400$ ms, (c) discharge profiles from $180 < t_{full} < 400$ ms and (d) the profiles of discharge voltage resulting of the change of Z .

4.3 The optimised circuit design

Fig. 4.6 shows 3 cycles of the charge and discharge profiles simulated using $C=2050 \mu\text{F}$, and $R_1= 22\Omega$. The charge and discharge time for the EMP device is used from around 100 and 0.5 ms, respectively. By considering the practical issues such as managing thermal load and electric shock to an acceptable level for safety operations in laboratory, the actual design of the circuit is showed in Fig. 4.7. The key novelty is the trigger unit, it has an ability to allow the pulsed current discharged to the coil with adjustable frequency.

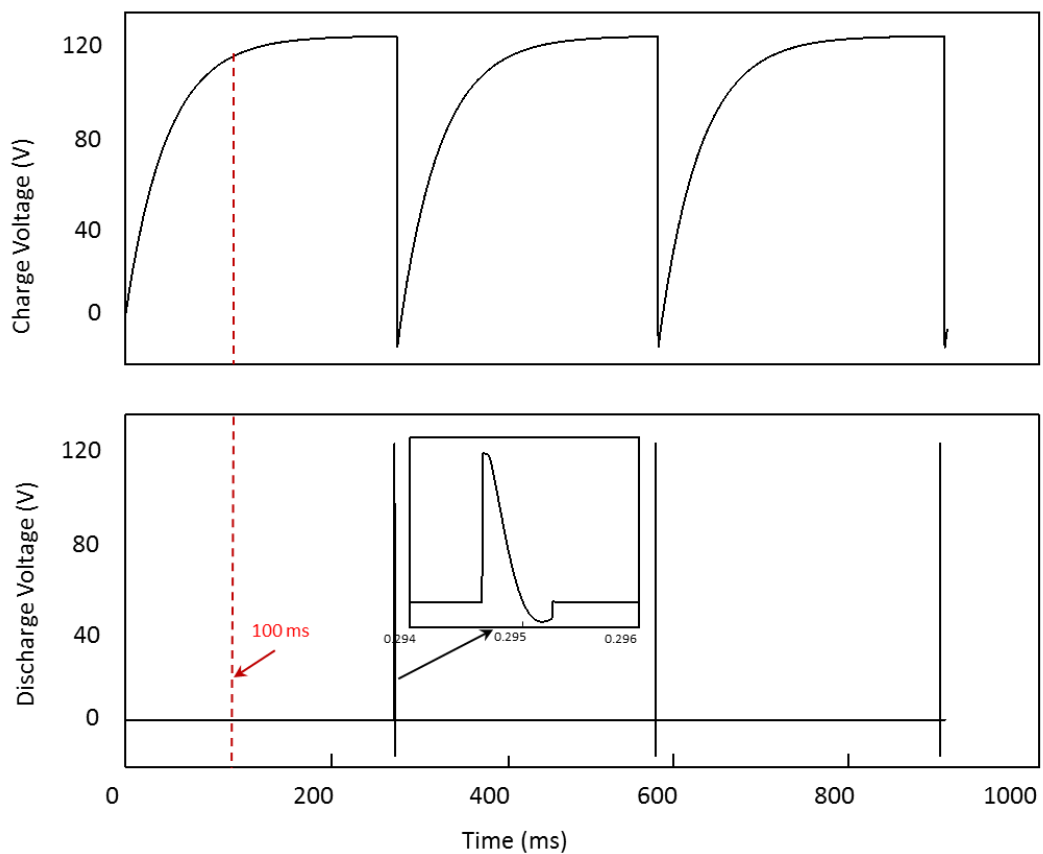


Fig. 4.6. The charging and discharging profiles in three cycles for the optimized circuit design.

4.4 The key components of each functional unit of the EMP device

Each of the functional units of the EMP device and the key elements or components are showed in Table 4.2 and described in details here.

4.4.1 The power supply

A variac transformer that can vary the voltage in the range of 0-270 V is used to provide different voltage inputs. A rectifier is added to convert the AC current from the transformer to DC current to charge the capacitor.

4.4.2 The charging unit

Two resistors are added in the charging unit. The first is a 22 Ω resistor and is used to limit the current inside the system because most of the electric components used in the laboratory are standard ones that requires working current below 13 A. The second is a 220 Ω resistor and is used to prevent the discharged current from "flowing" back to the charging unit because it is significantly higher than the resistance of the coil.

A capacitor bank is used to store the charged energy. It is an energy storage device with adjustable capacity depending on the numbers of the capacitors used. As shown in Table 4.2, the capacitor bank has a capacitance of 2050 μF 800 V [167], built up from 10 capacitors (a parallel connection of two 5 serially connected capacitors) with each individual capacitance of 820 μF 400 V. The serial connection builds up the higher voltage capacity while the parallel connection increases the capacitance.



4.4.3 The trigger unit



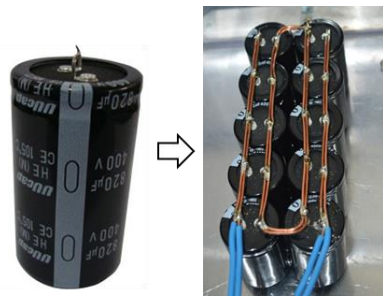


Thyrister switch, a high voltage switch, is used to allow the discharged current flow into the coil. In fact, this switch is a part of the trigger unit and normally opens to isolate the charging unit and the coil. When a trigger signal is received from the trigger unit, the Thyrister switch is closed and current is discharged into the coil.

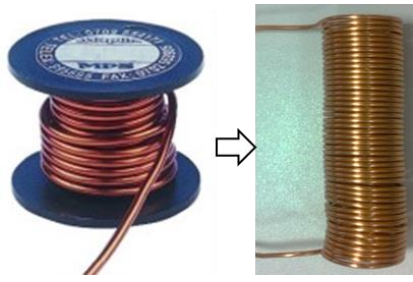
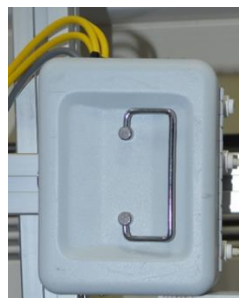
4.4.4 The pulse generating unit

The induction coil for generating the magnetic pulse was made using 5 m long 2 mm diameter enamelled copper wire (14 SWG).

Table 4.2. The main components used in each unit of the EMP device

Unit	Component	Component photo and model
The power supplier	Variac transformer	
		Carroll & Meynell 4.8 kVA, 1 Output, 240 V ac, 20000 mA
The charging unit	Bridge rectifier	
		Semikron SKB 30/16 A1

	Resistors	
		Amico High Power Ceramic Tube Resistor 150 W 220 Ω
		
		Arcol HS100 Series Aluminium Housed Axial wire-wound Panel Mount Resistor, 22 Ω \pm 5%100 W
	Capacitor bank	
		Cornell Dubilier's capacitor, SLPX821M400H9P3, 820 μ F 400 V And Capacitor bank (2050 μ F 800 V)
The trigger unit	Thyrister switch	
	IC 555 Timer	

		LM555CN/NOPB, Timer, 4.5 → 16 V, 8-Pin MDIP-8
The pulse generating unit	Induction coil	
		Enamelled Copper Wire 2mm 14swg
	Connection box	
		Aluminium Box with key lock

The other minor components of EMP device are listed in the Table A.1 in Appendix 1.

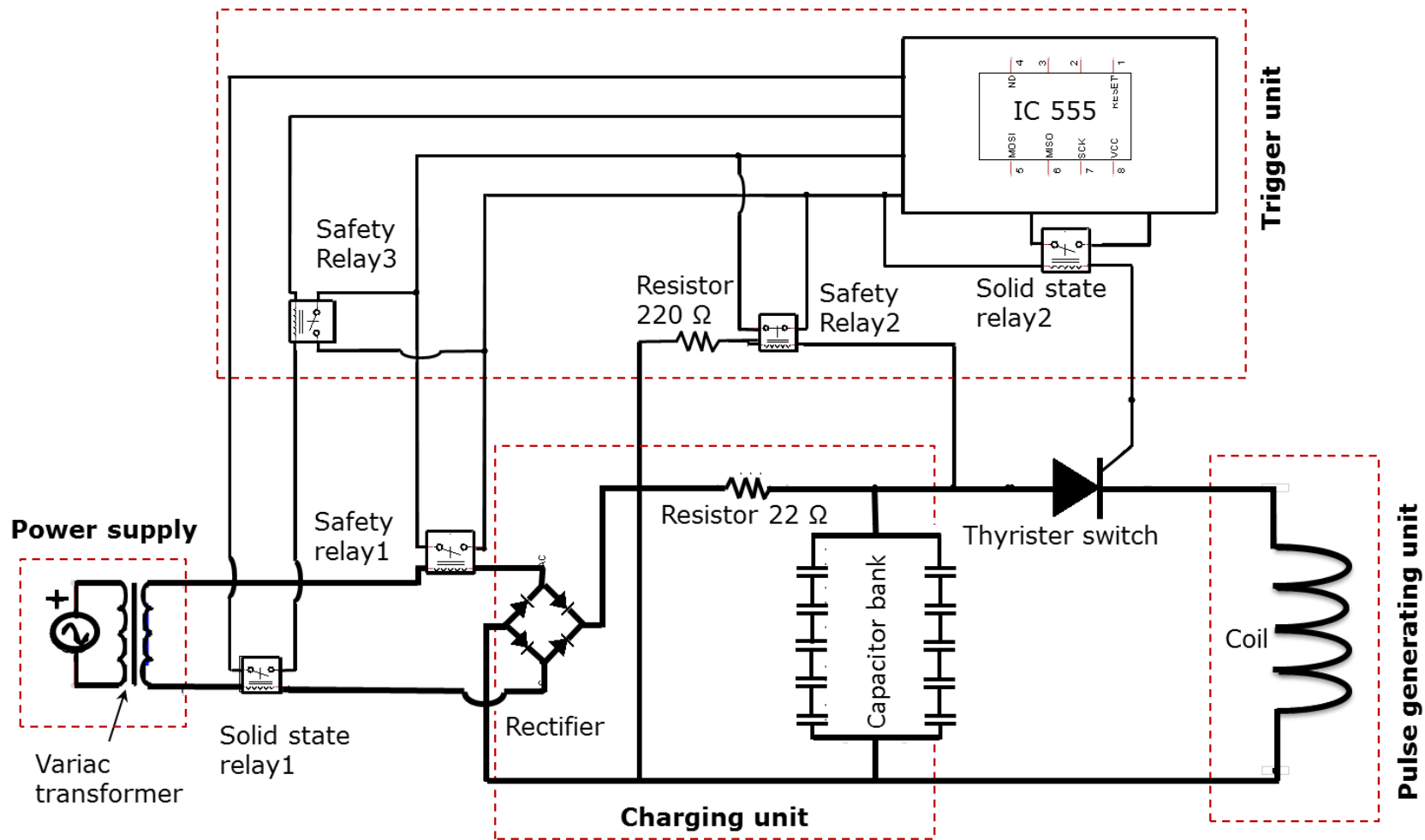


Fig. 4.7. The actual circuit design of the EMP device

4.5 The building and commissioning of the EMP device

4.5.1 The charging unit

The power to the charging unit is provided by the transformer which was connected to the mains (standard electric current, 240 V) of the laboratory. Fig. 4.8 are two photos that show (1) a box (610 mm × 460 mm × 260 mm made by 2 mm thick Aluminium sheet) to accommodate the charging unit and (2) the components and wiring of the charging unit. Table 4.2 shows the key electric components inside the Aluminium box, including a capacitor bank, resistors, rectifier, Thyristor switch, solid state relays and safety relays, and an emergency stop button set on the top of the aluminium box cover.

4.5.2 The pulse generating unit

Fig. 4.9 shows that the pulse generating unit has a connection box and a coil linked to the box via a socket. An enamelled copper wire of 2 mm in diameter was used to wind into a coil of solenoid shape with an inner diameter (I.D) of 40 mm and a length of 120 mm. Then mouldable mastic (Fiberfrax grade 120) was used to cast and wrap around the copper coil to hold the copper coil in space firmly after the mastic was dried up. The excellent heat insulation properties of the mastic also help to protect the coil from being overheated by the liquid metal alloys during operation. The connection box and the coil were mounted onto a stand made by extruded Aluminium alloy beam, and the position can be adjusted to suit that of the furnace for solidification operation.

4.5.3 The trigger unit

Between the capacitor bank and the connection box and the coil are the trigger unit and the Thyristor switch. Inside the trigger unit, an IC555 Timer/controller was used to control the duration of charging and the frequency of discharging operations. The IC555 and the relevant electric

components were contained inside a polyethylene box with a monitor display set on the top. The command buttons was on the front panel that can perform actions such as switch on or off, changes of discharging frequencies and manual or automatic pulse controls (single or repeated pulses). The duration of discharging time can be programmed from 1 μ s to 1 s. Fig. 4.10 shows the box containing the trigger unit.

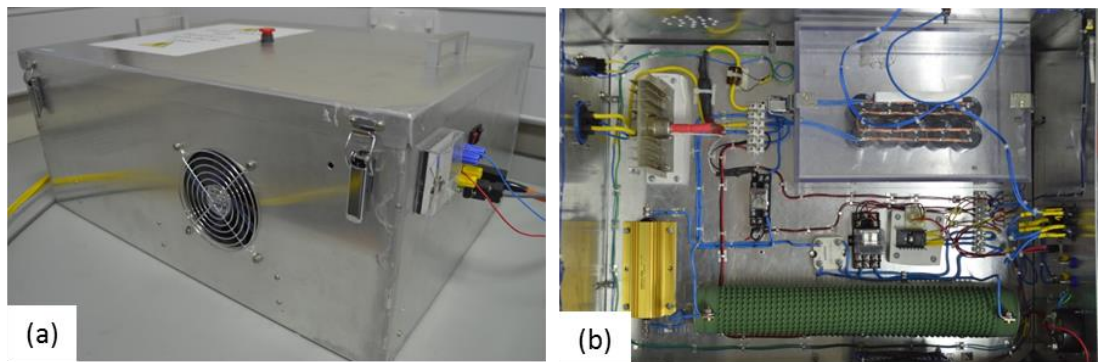


Fig. 4.8. Two photos showing (a) the Aluminium container box for EMP charging unit, (b) the electric and electronic components inside the charging unit.

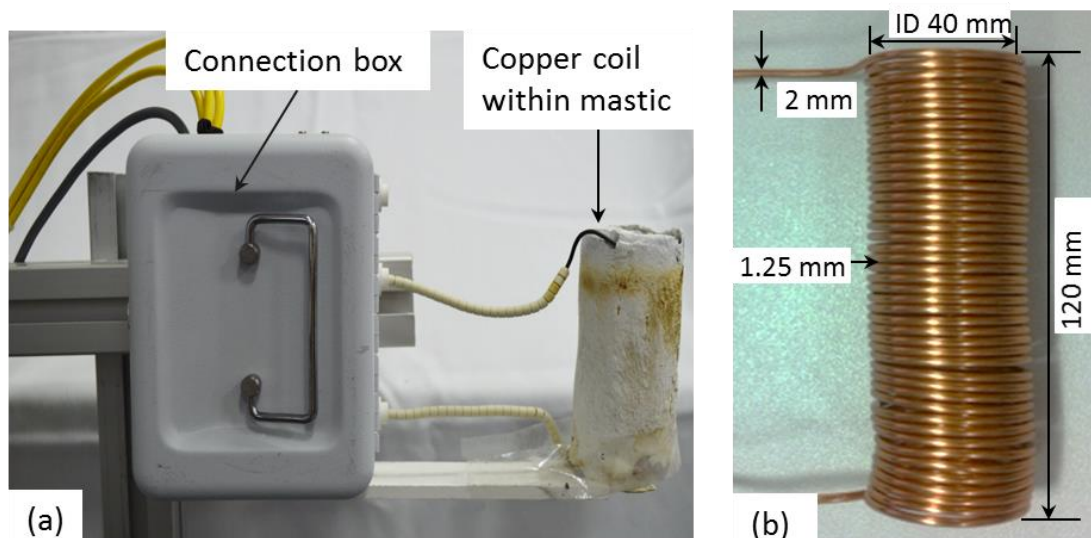


Fig. 4.9. (a) The pulse generating unit with a connection box connected to the copper coil wrapped by Fiberfrax mastic, (b) the helical copper coil inside the Fiberfrax mastic.

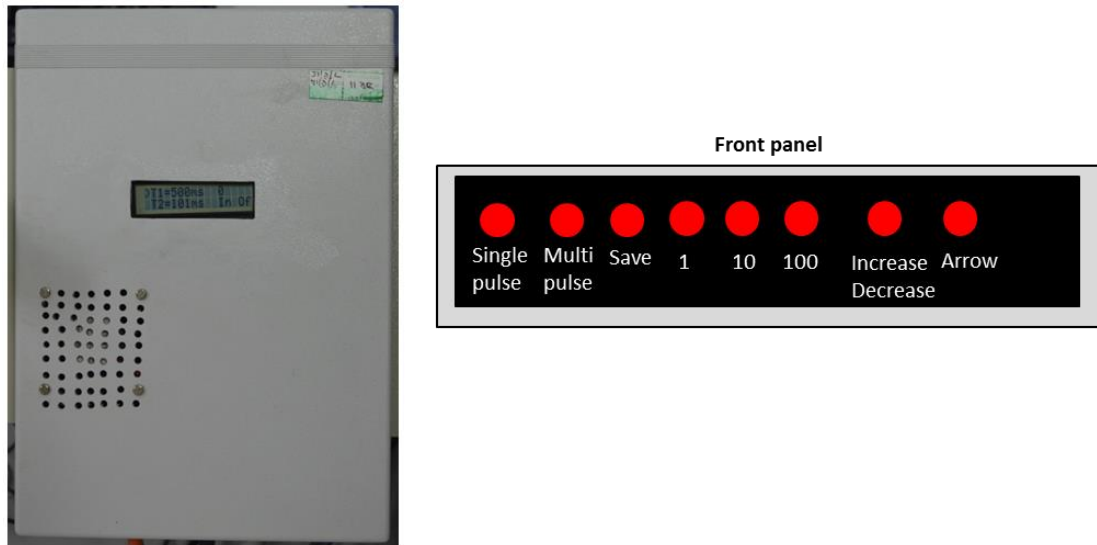


Fig. 4.10. The box containing the trigger unit

The duration and frequency of discharging are realised by two solid state relays controlled by the trigger unit, i.e. the solid state relay 1 and 2 showed in Fig. 4.7, respectively. Solid state relay 1 is controlled by the time setting from IC555 to either start or stop the currents charged from the transformer. Solid state relay 2 is used to control the Thyristor switch to release the current discharge into the coil.

In addition, a few relays were put in place to function as safety relays for the designed circuit. As showed in Fig. 4.7, safety relay 1 and 2 are designed to enable the charging of current into the capacitor bank when received the triggered signal. Safety relay 3 is used to protect the current passing through the coil without the trigger signal.

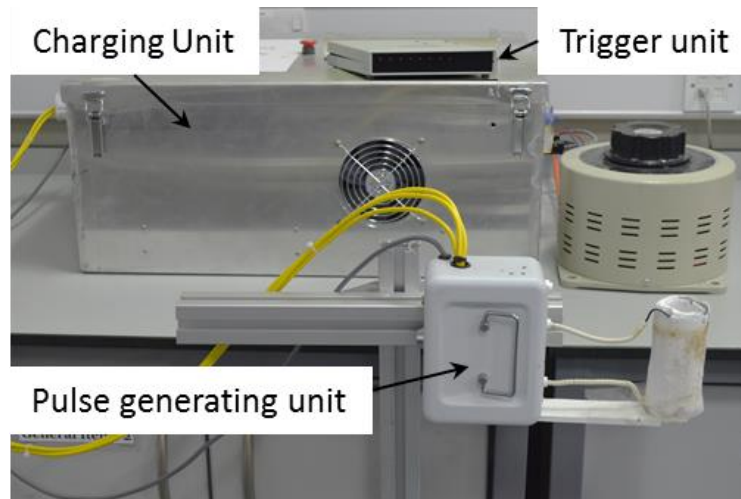


Fig. 4.11. A photo showing the assembled EMP device with all units

4.6 The furnace, casting mould and their integration with the EMP device

A small cylindrical-shaped electric resistance furnace (Fig. 4.12) was designed and made for melting metal alloys. It was made of a heating coil, a Fiberfrax heat insulator (mouldable mastic, Fiberfrax grade 120), ceramic wool and an aluminium cylindrical casing. The overall dimension is 40 mm (I.D) \times 80 mm (O.D) \times 150 mm (height).

Firstly, high electric resistance Nickel-Chromium wires (Ni-20wt%Cr) of \varnothing 0.7 \times 1500 mm long was used to wind into a small \varnothing 10 mm helical coil (small section in Fig. 4.12) then formed a helical heating coil of \varnothing 40 mm and 150 mm long. The designed heating power is 1.4 kW at 120 V. The 120 V electric current is delivered by transforming the standard 240 V using the Variac transformer.

Secondly, the wound coil was held in position using mouldable insulation ceramic mastic (Fiberfrax). The mastic was firstly applied into the gap between the helical coil, forming a tube-shaped furnace (Fig. 4.12). The coil was positioned in the inner surface of the tube and at least one third of each turn of the coil was exposed to air at the inner surface of the tube. The

ceramic paste was then dried for 24 hrs in air and heated to 1000 °C to build the strength.

Finally, the tube was put inside an Al tube casing with some ceramic insulation wool inserted between the Fiberfrax tube and the Al casing to further enhance the insulation (Fig. 4.12). The furnace was then mounted on a purposely designed frame made by extruded Al beams. A close-loop temperature control system, including a solid state relay (SSR, 120/240 Vac, zero voltage switched, rated 1 A continuous, 10 A surge @ 25°C) and a digital PID signal controller (Omega model No. CN8200), and a 8-channel Pico data logger (TC-08), were used to control the temperature measured by using K-type thermocouples (0.5 mm in diameter and 300 mm long). Heating trials showed that the furnace can reach ~1200 °C without difficulty.

Glass tubes made of either borosilicate or quartz were used as the containers to hold the metal alloys that were melted inside the furnace. The bottom end of the glass tubes were set and sealed onto ceramic adaptors that were made by machineable ceramic (Duratec 750). The assembly was then mounted onto a linear stage (T-LSR075A)[168]. The linear stage has a maximum travel distance of 75 mm with a travel step resolution of 0.49 µm/s. operated via the accompanying control software, Zaber Console v1.2.16.2122 [169]. The stage can provide the withdrawal of the glass tubes out of the furnace in a very precise manner, so as to achieve the designed thermal gradients for any specific solidification experiments, such as directional solidification, or mimic other casting operation, such as DC casting [170].

The assembly of furnace with the glass tube and the linear stage is showed in Fig.4.13.

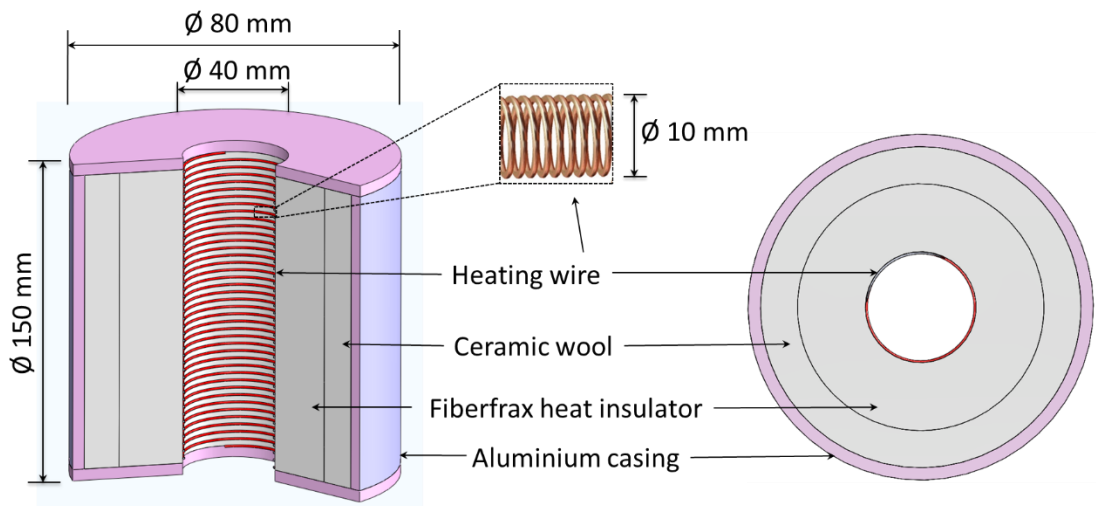


Fig. 4.12. A CAD drawing, showing the dimension and the materials used for making the electric resistance furnace.

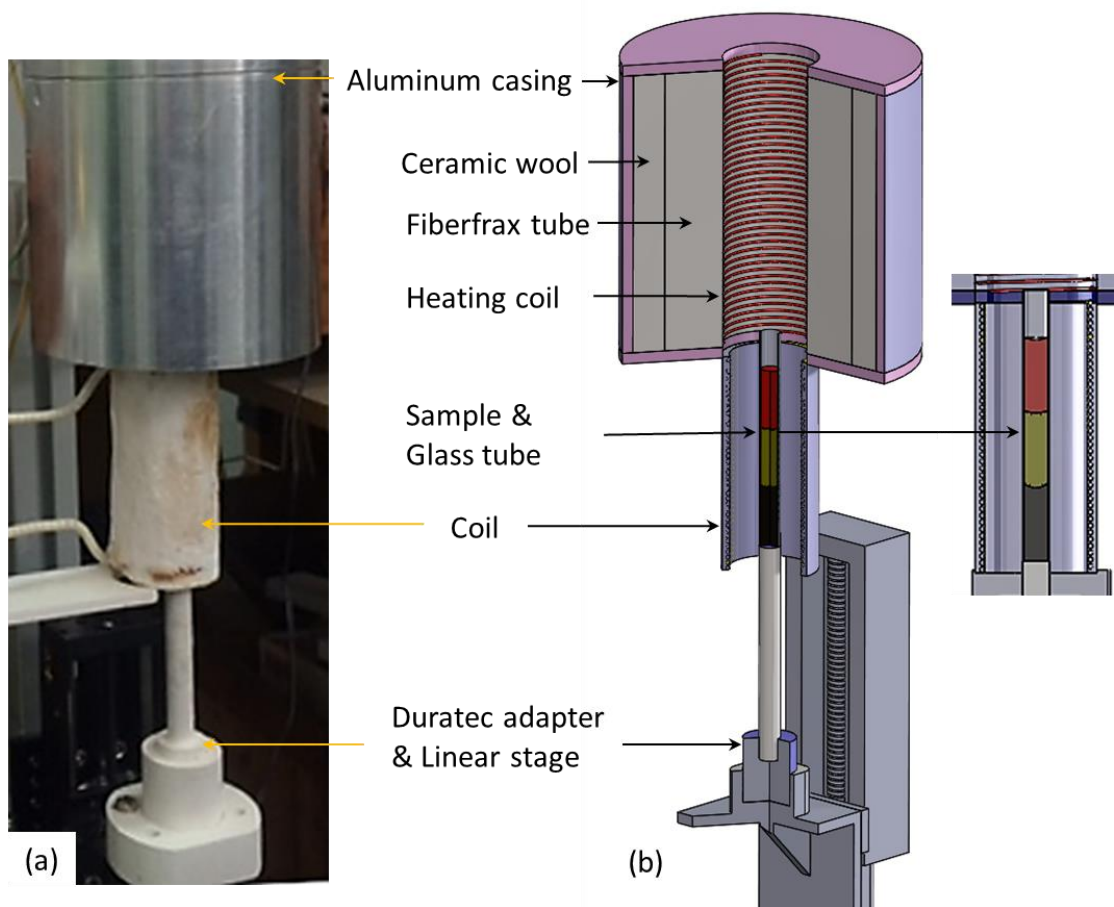


Fig. 4.13. A photo and a 3-D CAD drawing, showing the assembly of the furnace, the glass tube mould and linear stage

4.7 The commissioning of the EMP device and the measurement of the pulse magnetic flux density

A series of commissioning experiments were carried out to test the designed functions of the EMP device with the main focus on the measurement of the generated electromagnetic flux in the designed coil.

The coil can be viewed as solenoid, and the magnetic field or magnetic flux density is formed around the coil in the direction as indicated schematically. The magnetic flux density [171] can be calculated by equation 2.19 previously mentioned:

Generally, the magnetic flux density is uniform in the central region of a long coil, and a Hall probe (the axial type probe) [172-174] was often used to measure the magnetic flux density as detailed in Fig. 4.14.

We used, however, a Gauss meter (model GM08 from Hirst Gauss Meter) [175] for the measurement. It provides a measurement of $\pm 0.5\%$ accuracy of the measured range, and can be linked to a digital oscilloscope for real time monitoring and data login. Fig. 4.14 shows the setup of the measurement using a Hall probe and Gauss meter, and the real-time data monitoring and recording using a digital oscilloscope and the relevant digital storage oscilloscope software. The measured real-time magnetic flux density data be transferred into the computer directly for further analyses (Fig. 4.15).

Fig. 4.15 shows the measured magnetic flux densities at different discharge voltages, 40V, 80V, 120V 160V and 200V. The magnetic flux density peak value increases linearly with the increase of the voltages (Fig. 4.16).

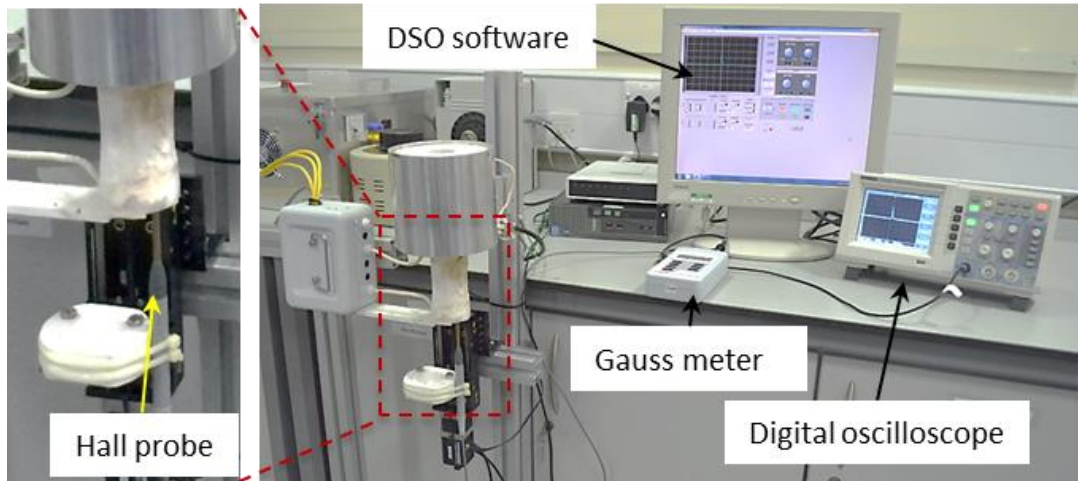


Fig. 4.14. Photos, showing a Hall probe positioned in the middle of the coil, a Gauss meter connected to an oscilloscope for data display and the interlink between the oscilloscope and Digital Storage Oscilloscope (DSO) software.

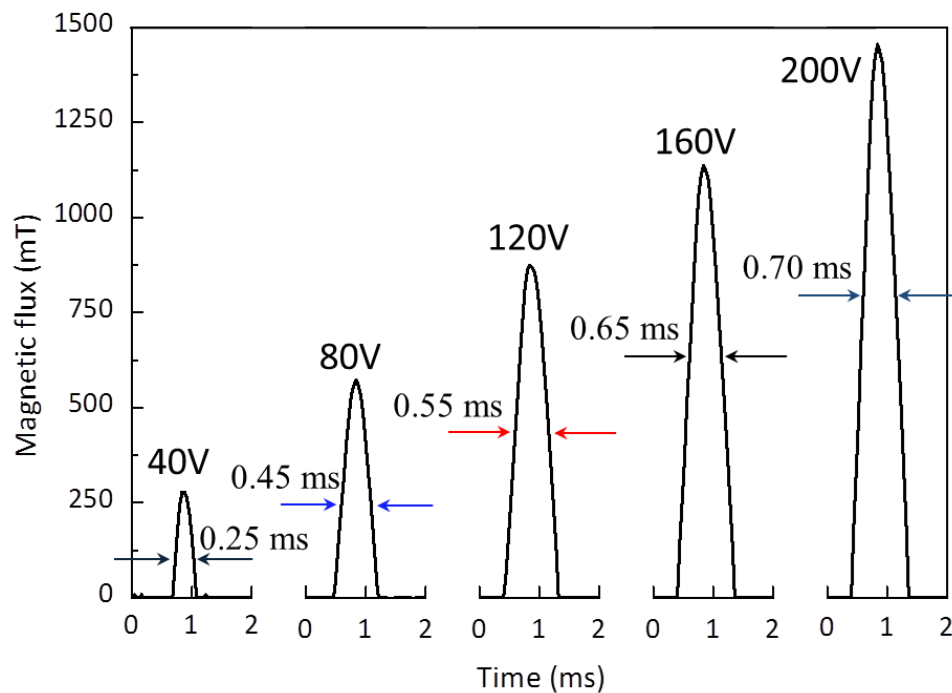


Fig. 4.15. The measured magnetic flux density with different charging voltages.

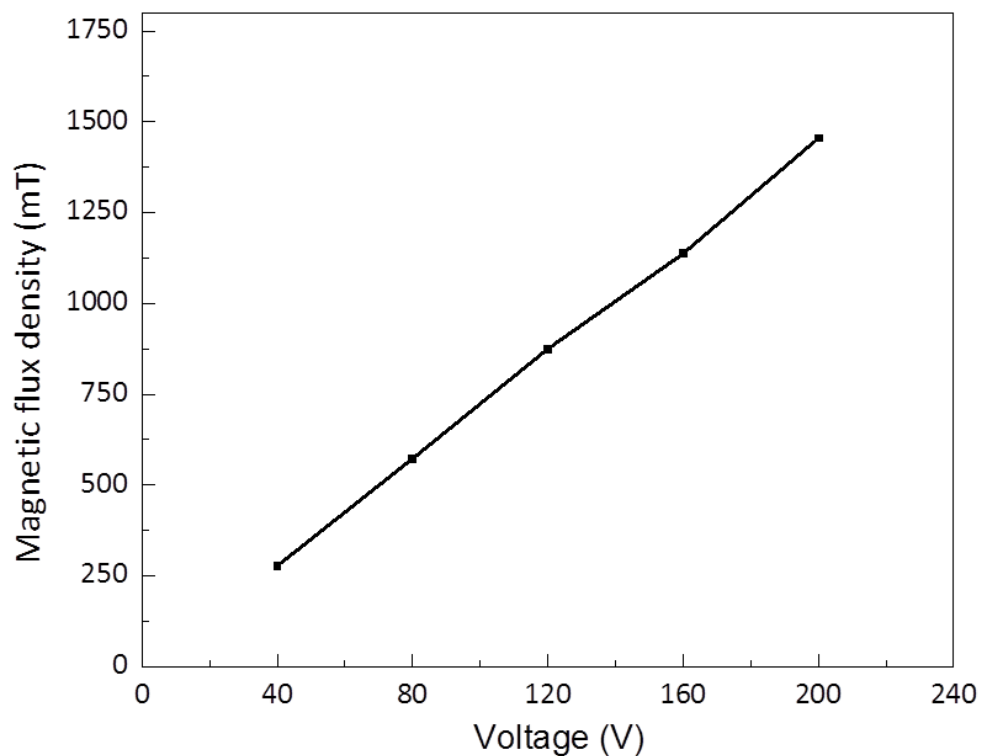


Fig. 4.16. The measured magnetic flux density peak value as a function of the discharging voltage.

4.8 Summary

A programmable EMP device was designed and built for this research. The designed circuit was simulated and optimised using National Instrument NI Mutisim software. The designed functions were fully realised after commissioning. The pulse magnetic flux densities produced by the EMP device at different discharging voltages were measured using a Hall probe linked to a Gauss meter and a digital oscilloscope. The peak values of the measured magnetic flux densities were found to increase linearly with the increase of the discharging voltages with a slope of (7.1 mT/V).

Chapter 5 : Solidification of metal alloys under pulse electromagnetic fields

This chapter describes the microstructural evolutions of a Sn-18%Pb, an Al-15%Cu and an Al-35%Cu alloy during the solidification under pulse electromagnetic fields of different magnetic fluxes and well-controlled thermal conditions. The experiments were performed in the Advanced Materials Laboratory at School of Engineering, University of Hull using the EMP device described in Chapter 4. The resulting solidification microstructures of those alloys were analysed using optical microscopy, scanning electron microscopy and 3-D X-ray tomography.

5.1 The selection of alloys and casting of samples

5.1.1 The selection of alloy systems

The alloys for the experiments were chosen based on the following criteria:

1. Having higher electric conductivity and therefore higher inductive current and sufficient Lorentz force can be generated inside the material via the pulse magnetic field.
2. Having typical dendritic and/or eutectic phases, facilitating the studies of the changes of the dendritic or eutectic phases when subject to different EMP parameters.
3. Comprising of constituent elements and /or phases with sufficient X-ray absorption contrast, facilitating the characterization of the changes of those phases using X-ray imaging and tomography techniques.
4. Having relative low melting temperature, facilitating the casting operations.

Based on the above criteria, a Sn-18wt%Pb alloy (using a short term, Sn-18Pb, hereafter) was firstly selected because of its high electric conductivity for generating high inductive current inside the material [69]. Furthermore, its low melting temperature, low oxidation, excellent wettability, and perfect primary dendritic grains followed by an eutectic type reaction during solidification (Fig. 5.1) make it an ideal model alloy for fundamental solidification studies [176, 177]. It is also important soldering material systems for joining electronic and electric circuits in electric and microelectronics industry.

However, Sn or Pb based alloys are very strong X-ray absorption materials as indicated in Fig. 2.5 of Chapter 2. In order to study the evolution of solidification microstructures in situ using X-ray [92, 109], Al-Cu based binary alloys were selected. The X-ray attenuation lengths of Al and Cu showed in Fig. 2.5-2.7 of chapter 2 indicate that, in the X-ray energy range of 3-30 keV, especially at the absorption edge of Cu around 8.898 keV, the X-ray absorption contrast between Al and Cu are sufficient to produce clear images for the Cu-rich phases using X-ray radiography and tomography techniques [98, 106], ideal for studying the fundamentals of solidification phenomena, for instance, the columnar-to-equiaxed transition (CET) [100], the effects of melts convection and the application of electromagnetic field on the evolution of solidification microstructures [178].

Al and Cu are also the most commonly used metal conductors for transmitting electricity, and the widely used metallic elements in Al-based alloys. In this research, binary alloys, Al-15wt%Cu and Al-35wt%Cu (Al-15Cu and Al-35Cu are used hereafter in the thesis) were chosen because of the primary α -Al dendritic grain structure in Al-15Cu, and the primary θ (Al_2Cu) intermetallic phase in Al-35Cu and the well-understood lamellar eutectic ($\alpha + \theta$) phases in both alloys (Fig. 5.2). The research is then focusing on studying the effects of the different EMP parameters on the change of the primary dendritic grains, the θ (Al_2Cu) phase, and that of the eutectic lamellar structure.

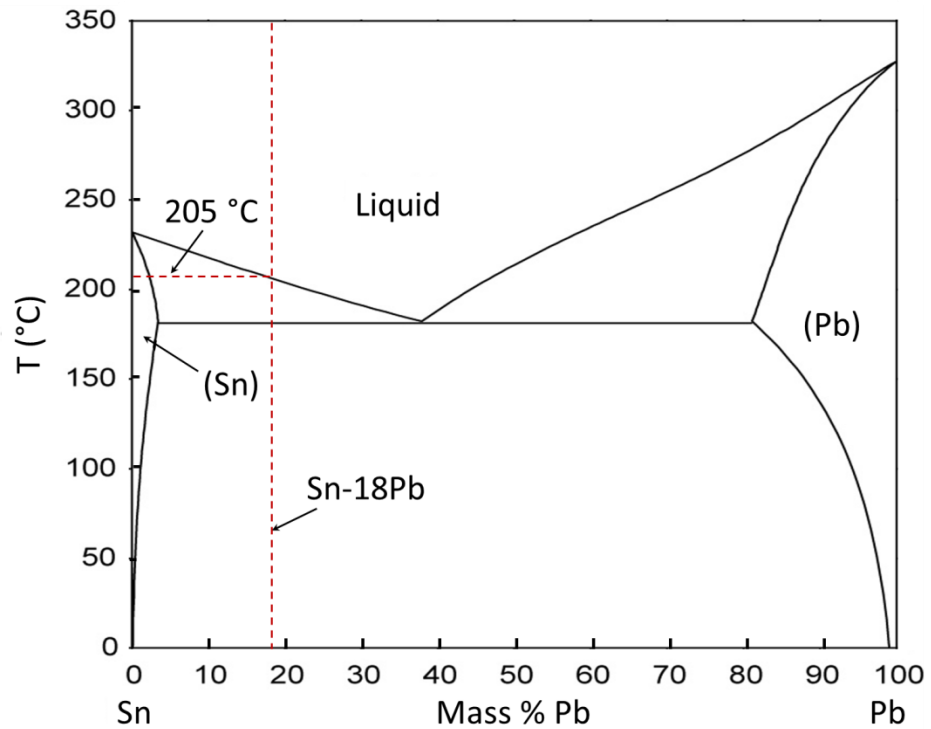


Fig. 5.1. The Sn-Pb phase diagram, and the Sn-18Pb alloy selected for the experiment [179]

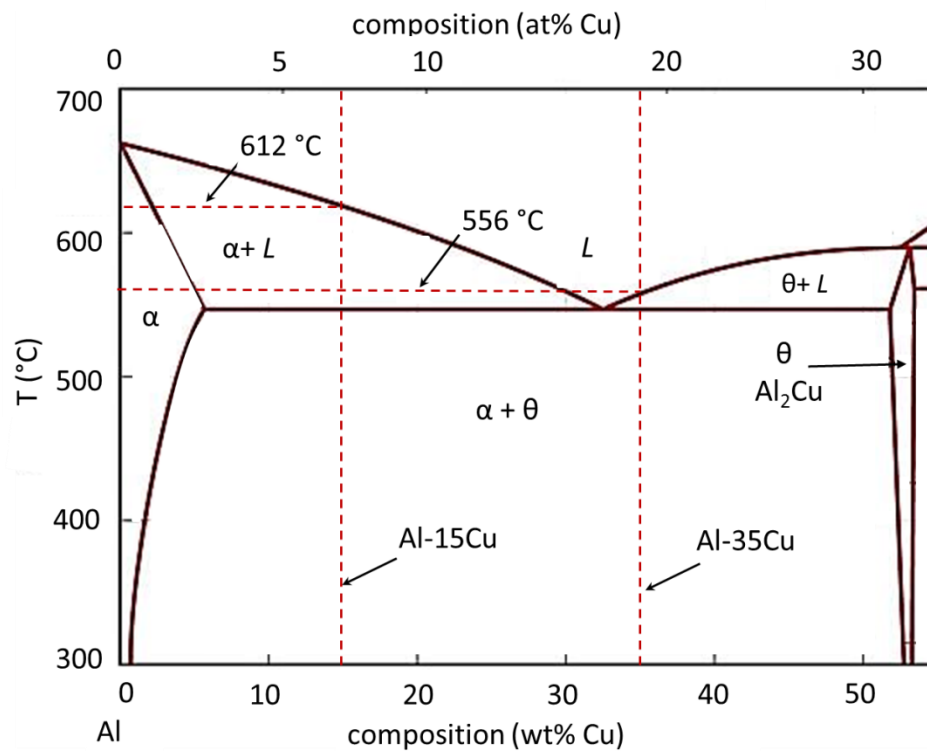


Fig. 5.2. The Al-Cu binary phase diagram [180], and the Al-15Cu and the Al-35Cu alloys used in the experiments.

5.1.2 The casting of alloys and samples

The alloys were made by melting together the pure elemental metals with the correct weight ratios inside a quartz beaker in a furnace. For the Sn-18Pb alloy, pure Sn (99.75 %) and pure Pb (99.97%) were used, while for the Al-Cu alloys, pure Al (99.97%) and pure Cu (99.97%) were used. All alloys were cast into \varnothing 9 mm bars using a custom-made counter-gravity casting apparatus (Fig. 5.3). Borosilicate glass tubes and quartz tubes (both in the dimension of 130 mm long and 9 mm inner diameters) were used as the moulds to cast the Sn-18Pb bars and Al-Cu bars, respectively.

The counter-gravity casting is a method of filling the mould with molten alloy against gravity [181]. Fig. 5.3 shows a schematic (Fig. 5.3a) and a photo (Fig. 5.3b) for the counter-gravity casting apparatus used in this research. It consists of a vacuum pump, a desiccator (acting as a vacuum reservoir), a long glass tube and a system of needle valve and pressure gauge for controlling the level of negative pressure applied.

The glass tubes were used as the casting mould, and one end of tubes was connected to a silicon tube while another end is immersed into the liquid metal held inside the quartz beaker. The silicon tube was linked to the long glass tube which is designed for protecting the vacuum system from the high temperature alloy melt in case of uncontrolled filling melt flowing into the system. The long glass tube also was connected to the desiccator with a negative pressure generated by the vacuum pump and controlled by the control valve and pressure gauge. The control valve is a needle valve that can regulate the air flow rate, allowing the negative pressure to draw the alloy melt uphill and fill into the glass mould in a quiescent manner.

The counter-gravity casting operations avoid the surface turbulence of the liquid metal during the filling process and therefore any entrainment of air bubbles or oxide films during the casting of the alloy bars were minimised. The cast bars are then used in the subsequent pulse magnetic field solidification experiments.

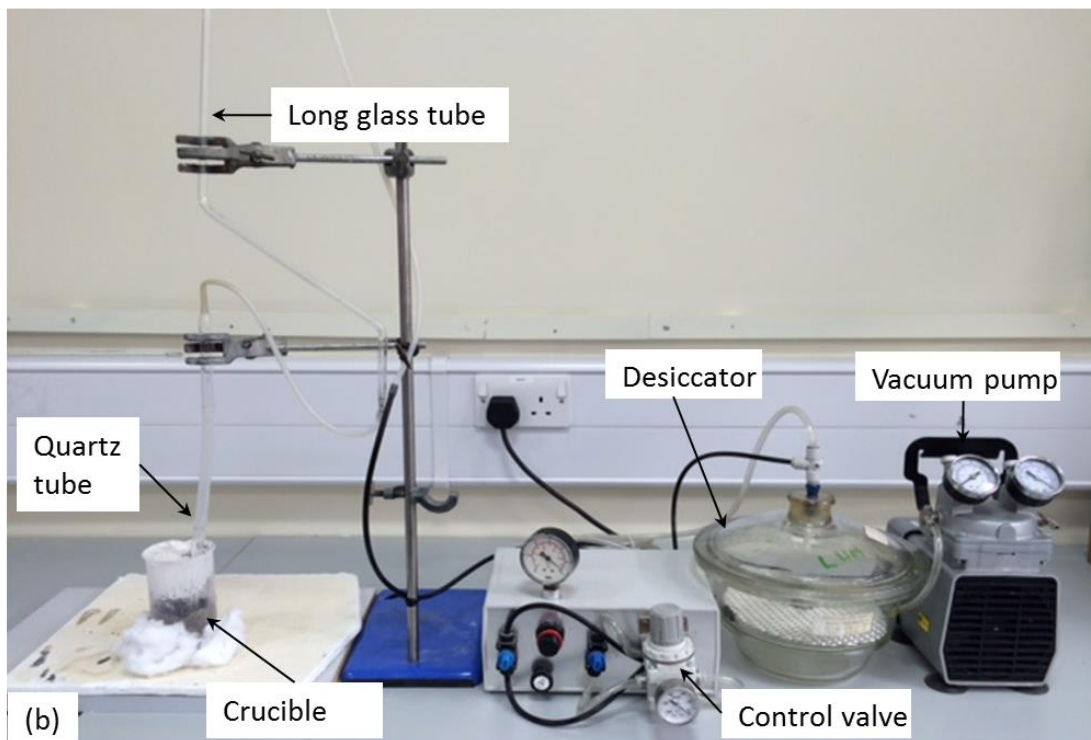
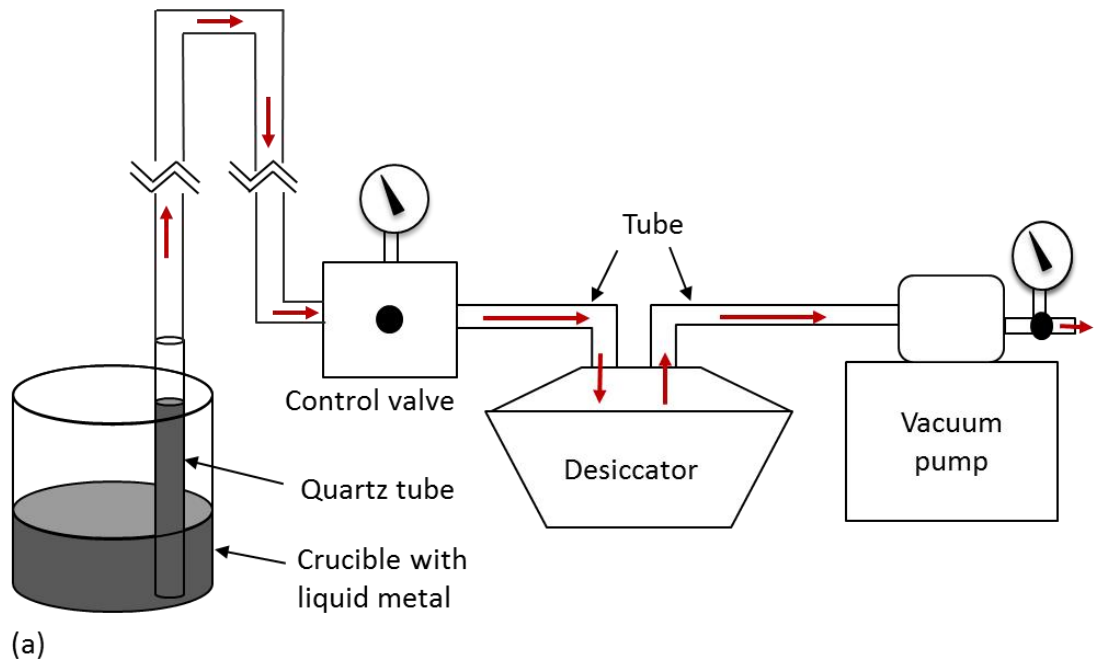


Fig. 5.3. (a) A schematic, and (b) a photo, showing the counter-gravity casting apparatus used in the research.

5.2 Solidification experiments under pulse electromagnetic fields

Fig. 5.4 shows the detailed arrangement of the experimental setup, including the furnace heating coil, the glass tube containing alloy melt, the Duratec rod supporting the glass tube, the locations of three K-type thermocouples (P1 for the furnace, P2, and P3 for the melt), and the copper coil for generating the pulse magnetic field (named EMP coil hereafter) and the centre of the EMP coil pointed by P4. Table 5.1 lists all the samples made and the corresponding experimental parameters used for those samples.

For each experiment, firstly, a cast bar (100 mm) was inserted inside a new glass tube (Borosilicate tubes for Sn-18Pb and quartz tubes for Al-15Cu and Al-35Cu, and all tubes have the same dimension of 9 mm inner diameter and 130 mm long) and then sealed at the bottom end using the supporting Duratec rod and mastic. Secondly, this assembly was mounted on the linear stage, and moved up into the furnace (Fig. 5.4a). Finally, the alloy was melted inside the furnace and held at the targeted temperature for 20~30 minutes to homogenise the melt temperature before being withdrawn downwards with a pre-set travel speed into the EMP coil. The measured temperatures at P1, P2 and P3 during the experiment were recorded using a TC-08 data logger and PicoLog for Windows (PLW) software.

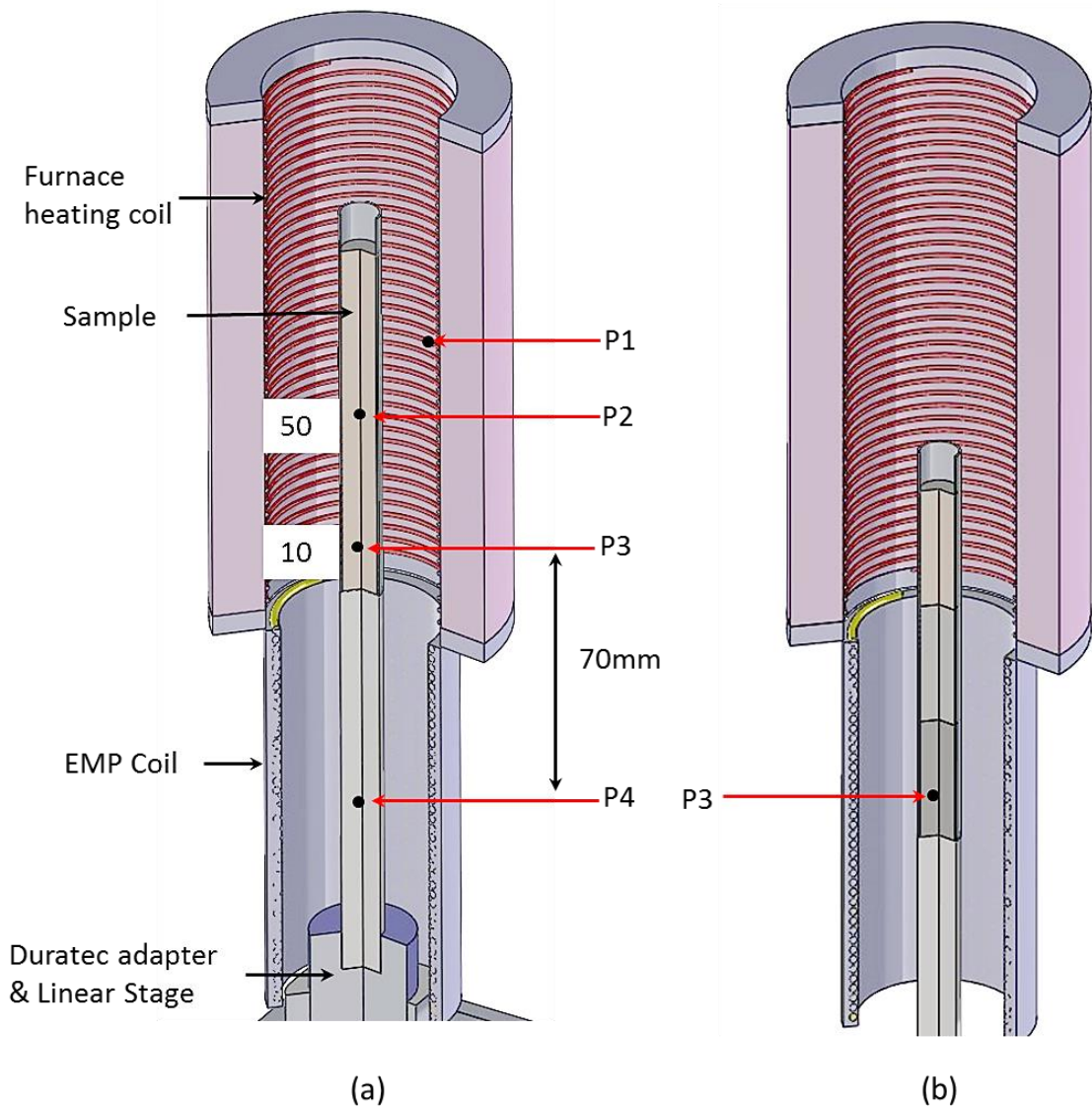


Fig. 5.4. Two CAD drawings, showing (a) the furnace heating coil, the glass tube containing alloy melt mounted on a Duratec ceramic rod and stage, and the EMP coil. Three K-type thermocouples were used to measure and record the temperature of the furnace at P1 and that of the melt at P2 and P3, i.e. 50 mm and 10 mm above bottom end of the glass tube, respectively. P4 is the central location of the EMP coil; (b) the arrangement of after the glass tube was moved down into the EMP coil, i.e. P3 reached P4.

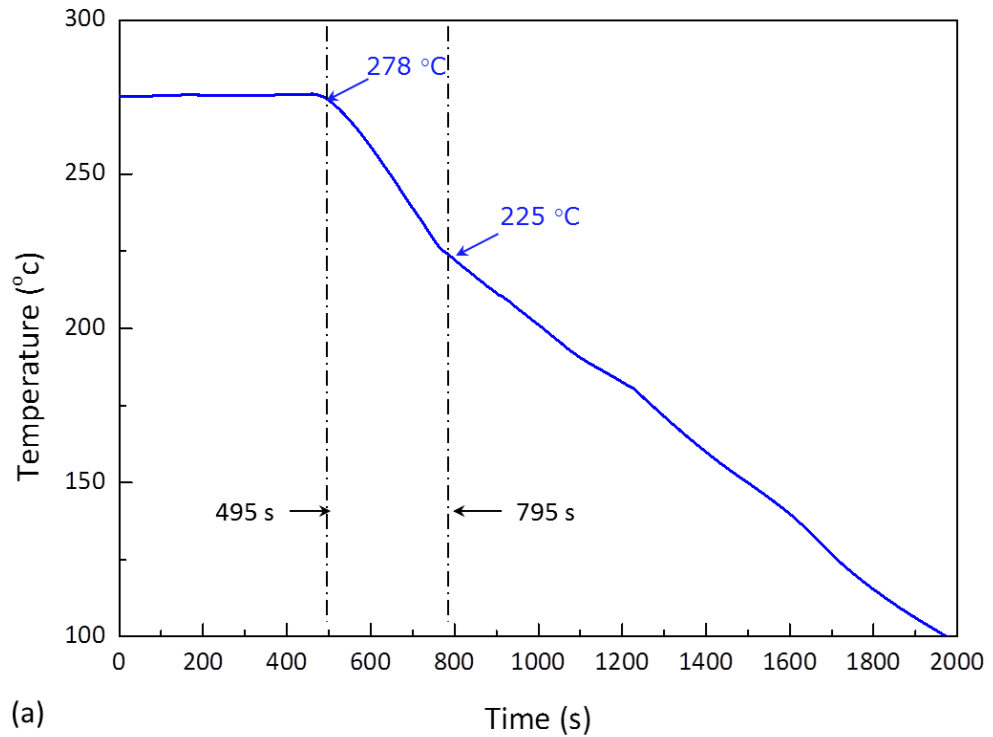
Trial experiments were made to control the temperature of the furnace at P1, and that of the melt at P2 and P3, together with the withdrawal speed of the linear stage in such a way that, after a half of the glass tube length was moved into the EMP coil, i.e. when P3 reached P4 (Fig. 5.4b), the melt started to solidify from P3, forming a progressive semisolid region above P3 inside the glass tube. In this way, the electromagnetic pulses applied can act directly onto the semisolid melt and the liquid melt above P3.

Taking the first sample, Sn-18Pb0V in Table 5.1, for example, the stabilised furnace temperatures measured at P1 was ~ 380 °C, and that of the melt inside the tube were ~ 342 °C at P2 and ~ 278 °C at P3 respectively before withdrawal (Table 5.1 and Fig. 5.6a). The withdrawal speed need to ensure that the starting temperature of ~ 278 °C at P3 is cooled to the liquidus temperature of the alloy, i.e, 205 °C when P3 reached P4, the centre of the EMP coil. As the tube continued to move down, solid phase started to grow at the region above P3 inside the tube (Fig. 5.4b). The cooling rate for Sn-18Pb0V is ~ 0.176 °C/s (calculated from Fig. 5.5a, $[(278-225 \text{ °C})/(795-495 \text{ s})] = 0.176$ °C/s), and the distance between P3 and P4 is 70 mm (Fig. 5.5 a), Therefore the withdrawal speed is $[70 / (278 - 205)] \times 0.176 = 168$ $\mu\text{m/s}$.

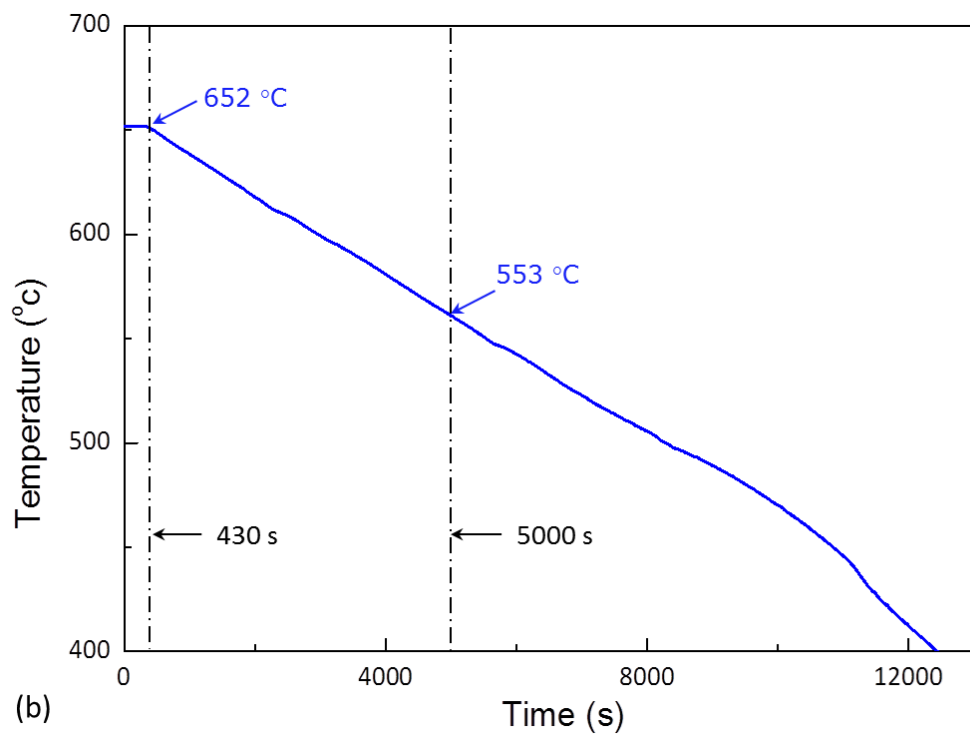
Similarly, for Al-15Cu, the withdrawal starting temperature was 652 °C (Table 5.1 and Fig. 5.6b), the liquidus is 612 °C, and the cooling rate was ~ 0.021 °C/s (calculated from Fig. 5.5b, $[(652-553 \text{ °C})/(5000-430 \text{ s})] = 0.021$ °C/s), the withdrawal speed was $[70 / (652 - 612)] \times 0.021 = 37$ $\mu\text{m/s}$. For Al-35Cu, the withdrawal starting temperature was 600 °C (Table 5.1 and Fig. 5.5c), the liquidus is 556 °C (Fig. 5.6c), and the cooling rate is ~ 0.014 °C/s (calculated from Fig. 5.5c, $[(600-540 \text{ °C})/(5000-800 \text{ s})] = 0.014$ °C/s), so the withdraw speed was $[70 / (600 - 556)] \times 0.014 = 22$ $\mu\text{m/s}$.

The application EMP was actually started immediately when the sample withdrawal started, and continued until the melt completely solidified. The

applied discharge voltage, frequency and duration for each sample are also summarised in Table 5.1.



(a)



(b)

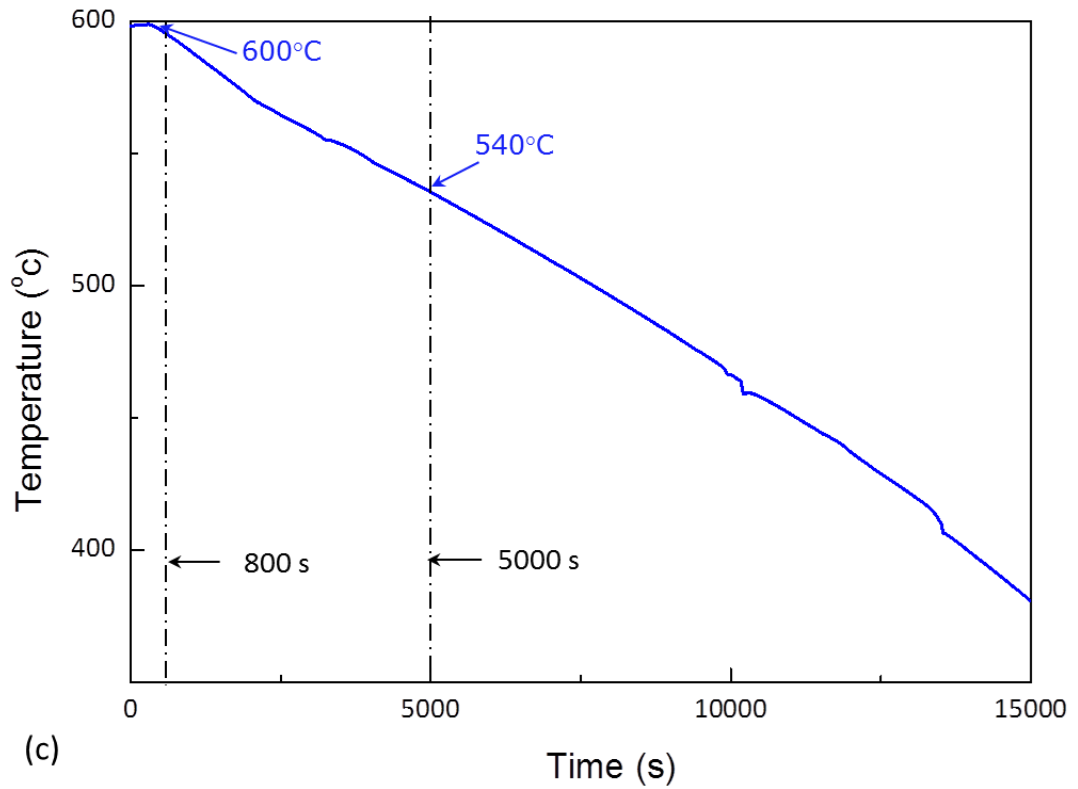


Fig. 5.5. The temperatures of the samples for calculating the cooling rates for (a) Sn-18Pb, (b) Al-15Cu and (c) Al-35Cu

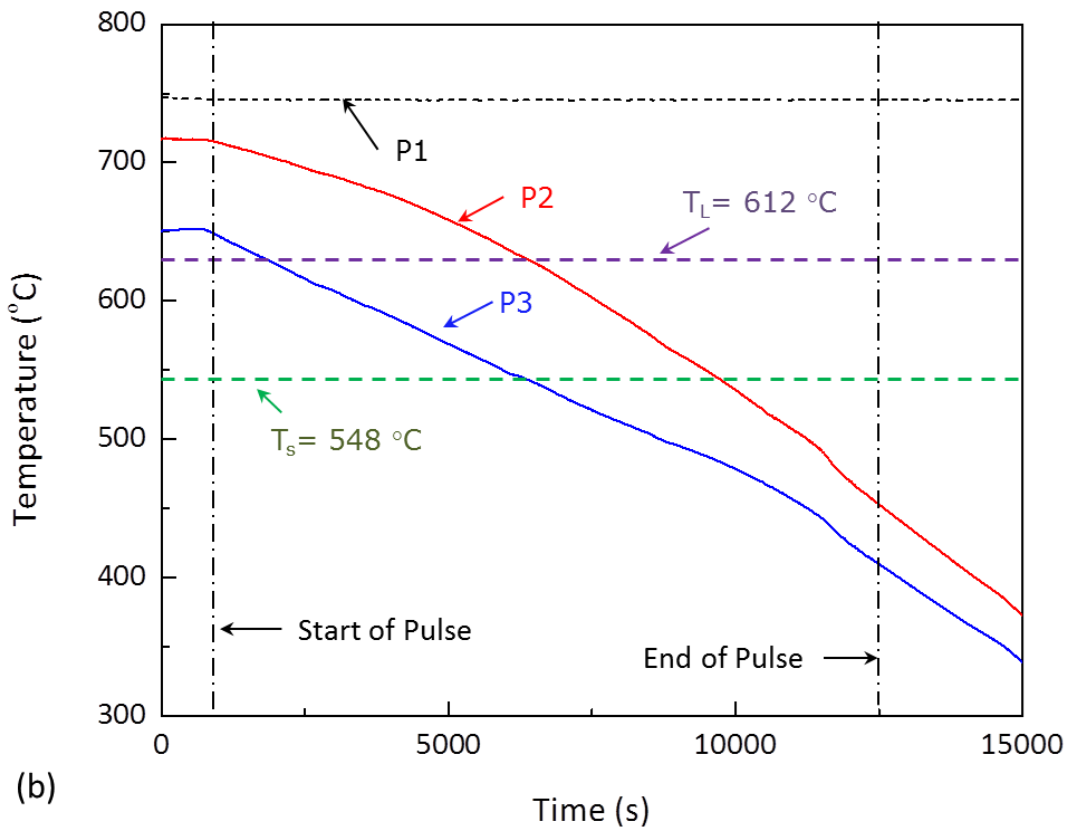
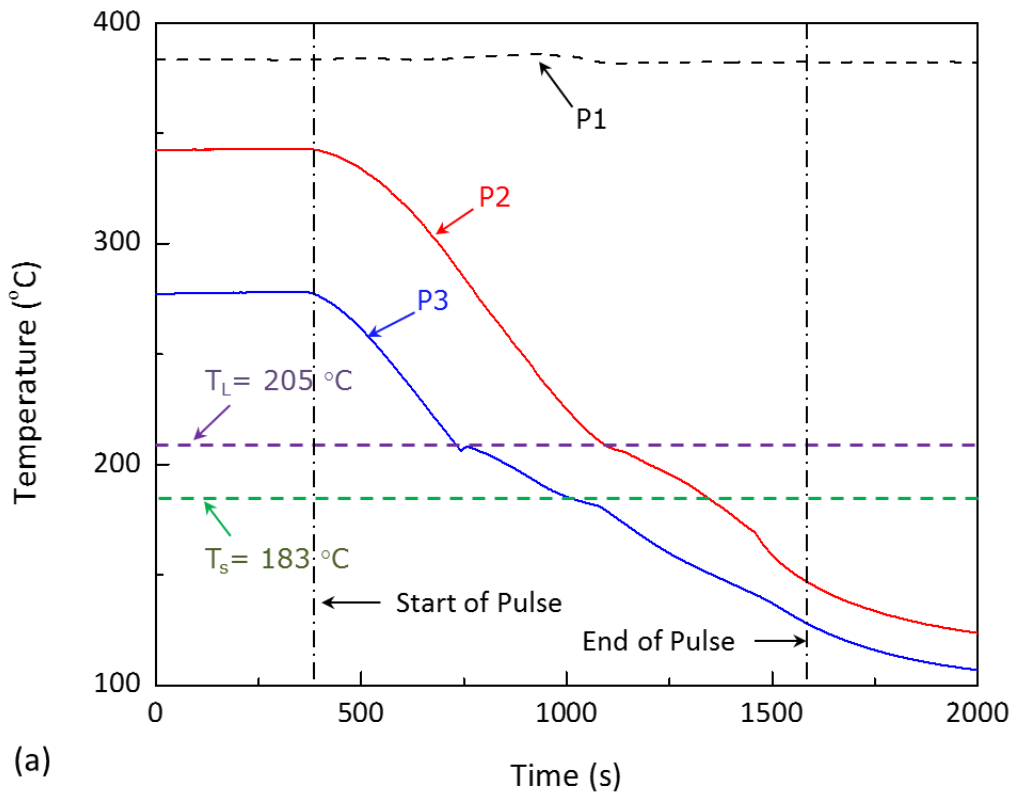
Table 5.1. A summary of the alloys, samples and the parameters used for the solidification experiments without and with electromagnetic fields

No.	Sample	Alloy	Furnace temperature at P1 (°C)	Sample solidification parameter			EMP parameter		
				Temperature at P3 (°C)	Cooling rate (°C/s)	Withdrawal speed (µm/s)	V_d	f_d (Hz)	t_{pulse} (s)
1*	Sn-18Pb0V	Sn-18Pb	380	278	0.176	168	0	0	0
2	Sn-18Pb40V						40	1	1220
3	Sn-18Pb80V						80	1	1410

4	Sn-18Pb120V						120	1	1350
5	Sn-18Pb40V10	Sn-18Pb	380	278	0.176	168	40	10	1230
6	Sn-18Pb80V10						80	10	1480
7	Sn-18Pb120V10						120	10	1400
8**	Al-15Cu0V						0	0	0
9	Al-15Cu40V	Al-15Cu	750	652	0.021	37	40	1	11400
10	Al-15Cu80V						80	1	12000
11	Al-15Cu120V						120	1	11920

12	Al-15Cu120VH						120	1	5690
13***	Al-35Cu0V	Al-35Cu	670	600	0.014	22	0	0	0
14	Al-35Cu120V						120	1	10800

The example of the measured temperature profiles of sample 1*, 8**and 13***are showed in Fig. 5.6a, 5.6b and 5.6c, respectively



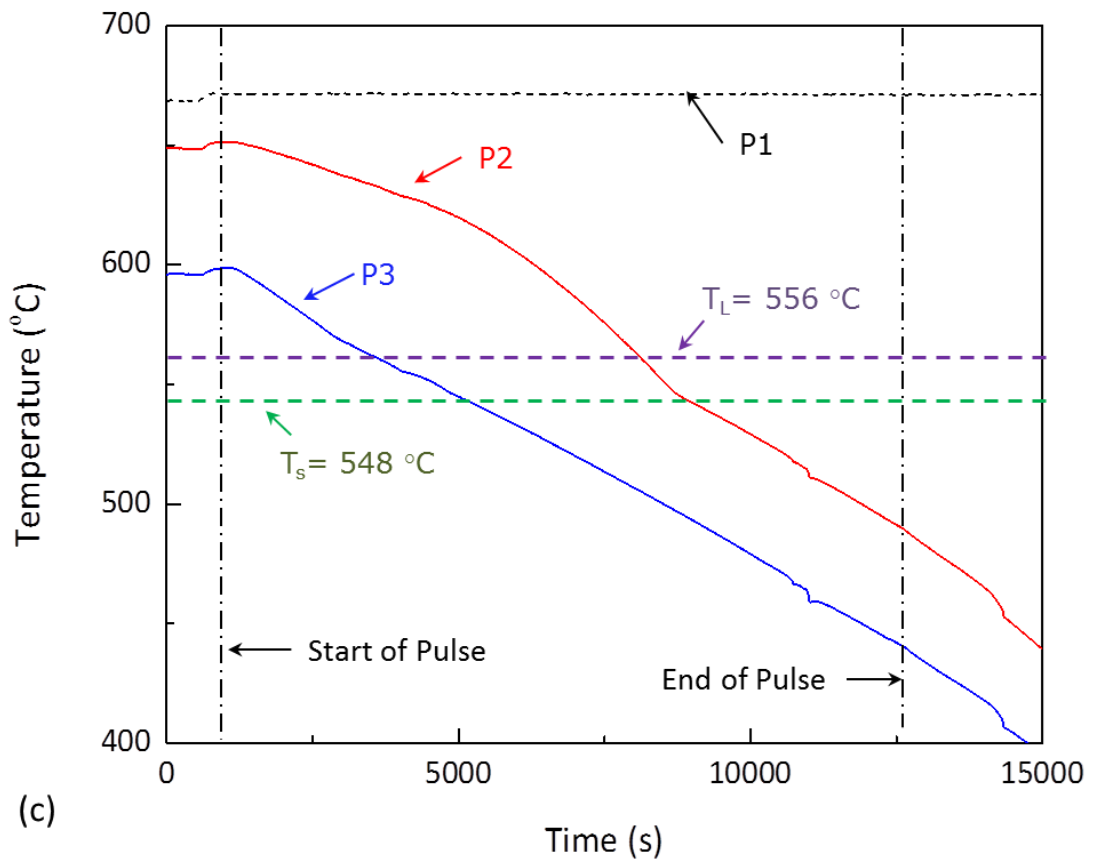


Fig. 5.6. The measured temperature profiles at P1, P2, and P3 for (a) Sn-18Pb no.1, (b) Al-15Cu no.8 and (c) Al-35Cu no. 13 during the solidification experiments.

5.3 Two dimensional microstructural characterisation of the solidified samples

After solidified, all as-cast samples were taken out of the glass tubes and sectioned from the middle longitudinally into two halves, followed by grinding using SiC papers of 600, 1200, 2500 grid size, and polishing with diamond suspension of 6 and 1 μm (with Kemet NLH and NFC polishing pads), and colloidal silica of 0.25 μm (with Kemet CHEM cloth polishing pad). Grinding and polishing were carried out using a semi-automatic grinding machine (Buehler Motopol 12) operated at 150 rpm. Each grinding and polishing step took 20~30 minutes.

The two dimensional (2-D) microstructures of the as-cast samples listed in Table 5.1 were firstly characterised using conventional optical microscopy and scanning electron microscopy (SEM). For each sample, the information concerning the sizes of the primary dendritic grains and the primary intermetallic phases, their growth direction and morphology, and the changes of solute diffusion characteristics because the applications of the pulse magnetic fields was obtained and presented in this section.

5.3.1 The Sn-18Pb alloy samples

Fig. 5.7 shows the typical microstructures of the Sn-18Pb alloy samples formed during the solidification under the pulse electromagnetic fields with the discharging voltages and frequencies listed in Table 5.1. Clearly, Fig. 5.7a shows that, without EMP, the grains grow vertically upwards against the direction of heat flow (the heat was mainly conducted away from the top to the bottom of the sample), forming long dendritic columnar structure with the average length of the primary dendrite arms measured at 2500 μm and the average secondary dendrite arms measured at 250 μm .

Fig. 5.7b, c, and d show that, when an EMP of 1 Hz applied during the solidification, the directions of the primary dendrites had moved from a near-perfect vertical alignment to the inclined angles of 20°, 25° and 12° for the cases of 40 V, 80 V and 120 V, respectively. From the three cases investigated, there is no enough statistical data to draw any conclusion with confidence that there is any quantitative correlation between the growth direction of the primary dendrites and the voltage applied for this 1 Hz pulse. However, what is certain is that the applied pulses did disrupt the growth of the dendrites, because Fig. 5.7b-d clearly show that the very long and near-parallel primary dendrites in Fig. 5.7a were replaced with a series of dendrite clusters along their growth direction. As the increase of voltage, the average size of the dendrite cluster decreased from 63 μm (40 V) to 59 μm (80 V) and to 58 μm (120 V).

Fig. 5.7e-g show that, when the 10 Hz pulses were used, the measured dendrite cluster average sizes are 58 μm (40 V), 57 μm (80 V) and 52 μm (120 V). The dendrite clusters seemed to become smaller compared to the same voltage cases of 1 Hz. Furthermore, more global morphology and randomly oriented grains were seen for the 80 V and 120 V cases.

In Fig. 5.7h, the example of microstructure measurement are shown, primary dendrite trunk (PT), primary-to-primary dendrite arm spacing (PPAS), secondary primary dendrite arm (SPA) and angle of the dendrites. Further, the microstructure measurement of Sn-Pb alloys is listed in Table 5.2

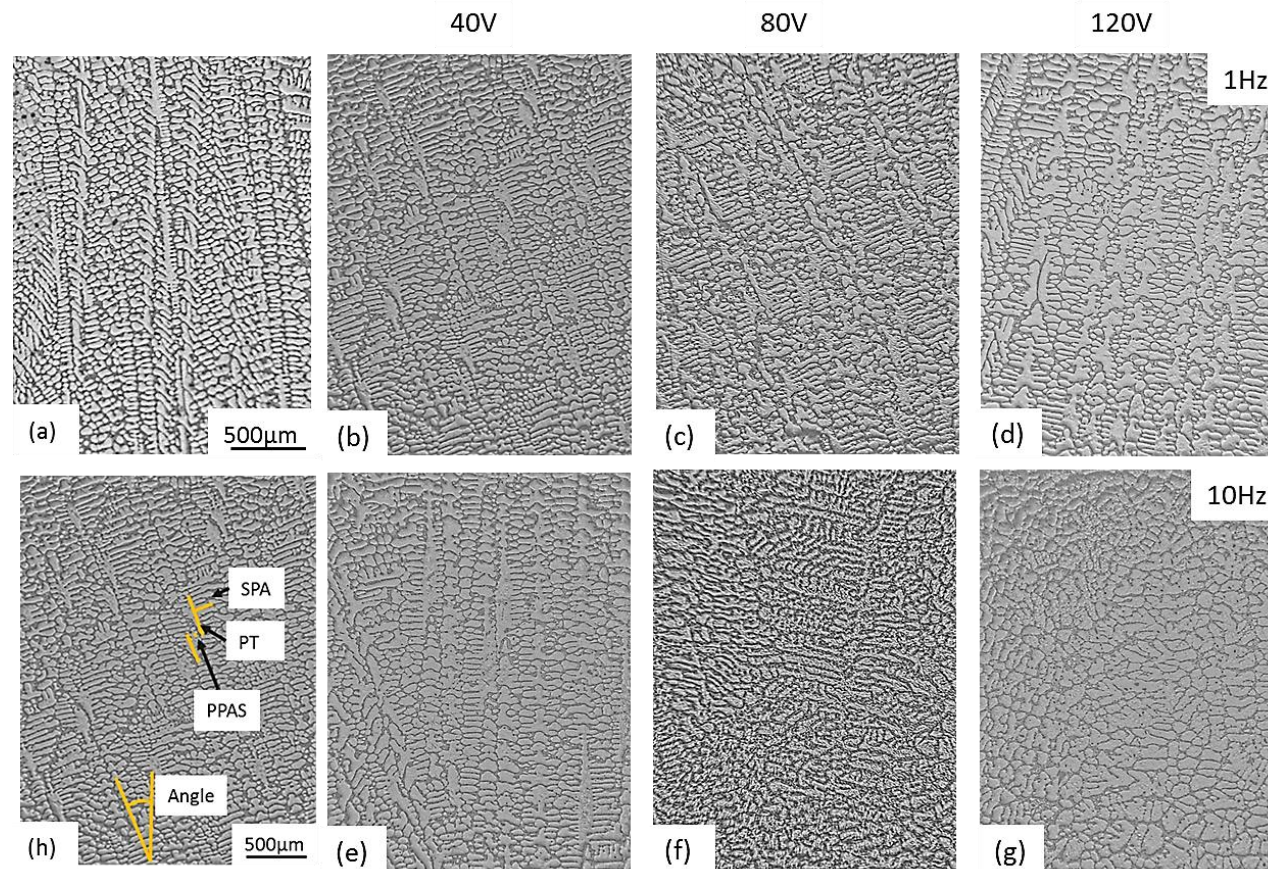


Fig. 5.7. The solidification microstructures of the Sn-18Pb alloy samples (Nos. 1-7 in Table 5.1) cast (a) without EMP; with 1 Hz EMP of (b) 40 V, (c) 80 V, and (d) 120 V; and 10 Hz EMP of (e) 40 V, (f) 80 V, (g) 120 V and (h) the example of microstructure measurement.

Table 5.2. A summary of the microstructure measurement from Sn-Pb samples without and with electromagnetic fields

Sample	Primary dendrite trunk length, μm	Primary dendrite arm spacing, μm	Secondary dendrite arm /its spacing, μm	Dendrite angle
Sn-18Pb0V	2500	500	250/20	2-5°
Sn-18Pb40V	1000	400	200/30	20°
Sn-18Pb80V	340	200	100/40	25°
Sn-18Pb120V	220	206	98/31	12°
Sn-18Pb40V10	700	160	120/20	3-19°
Sn-18Pb80V10	500	90	130/25	72°
Sn-18Pb120V10	280	30	60/35	Random

5.3.2 The Al-15Cu alloy samples

A Zeiss EVO60 environmental scanning electron microscopy (operated at 20 kV, with a work distance of 6.5 mm) was used to comprehensively characterise microstructures of the Al-Cu alloys. To accommodate the samples into the SEM chamber, each Al-Cu as-cast bar listed in Table 5.1 was firstly longitudinally sectioned into two halves, and then one half was chosen and cut into three short segments of ~ 2.5 cm long each, followed by grinding and polishing using the same procedure and materials described at the beginning of this 5.3 section. Further, the microstructure measurement of Al-Cu alloys is listed in Table 5.3.

5.3.2.1 The primary Al dendritic grains

Fig. 5.8 shows the macro and microstructure of Al-15Cu0V (without EMP). The grains grow upwards against the direction of withdrawal, forming very long primary dendritic structure with mature secondary arms from Fig. 5.8-1 and 5.8-6, the primary dendrite trunk width and dendrite arm spacing were measured, as seen the dendrite trunk is ~ 20 μm width while the primary dendrite arm spacing is ~ 120 μm . From the macro level image, the average length of primary dendrite trunks was measured and the average is ~ 15000 μm long.

Fig. 5.9, 5.10, and 5.11 show the macro and microstructures of the samples (Al-15Cu40V, Al-15Cu80V and Al-15Cu120V) treated using 1 Hz EMP with the discharge voltage of 40 V, 80 V and 120 V respectively.

Comparing the macrostructures showed in Fig. 5.8 and 5.9, it can be seen that the primary dendritic grains in Fig. 5.9 grew in the similar upwards direction, forming many long primary dendrites with mature secondary dendrite arms. However, statistically (show a few zoom-in images) the average length of the primary dendrite trunk were reduced to ~ 12000 μm long (macro level image) and ~ 10 μm width (Fig. 5.9-2 and 5.9-3) and the

primary dendrite arm spacing was also reduced to $\sim 80 \mu\text{m}$ (Fig. 5.9-3 and 5.9-6) while the average secondary arm is measured at $60 \mu\text{m}$.

Fig. 5.10 shows that, as the discharge voltage increased to 80 V , the growing directions of the primary dendrites started to move away from the near-vertical-against-gravity direction, and more primary dendrites seemed to grow from the glass tube wall into the centre area (Fig. 5.10-3 and 5.10-4). The length of the primary dendrites became shorter and shorter (an average length of $900 \mu\text{m}$ and $10 \mu\text{m}$ width with a primary dendrite arm spacing $\sim 100 \mu\text{m}$ as shown in Fig. 5.10), while the secondary dendrite arms started to grow bigger and bigger $\sim 120 \mu\text{m}$ as Fig. 5.10-2 and 5.10-5.

Fig. 5.11 shows, at a discharge voltage of 120 V , the growing of the primary dendrites became random, leading to the formation of many equiaxed dendrite grains in the whole polished section. The average length of the primary dendrite trunk is $\sim 100 \mu\text{m}$ with primary dendrite arm spacing of $40 \mu\text{m}$ while the average secondary arm is measured at $\sim 20 \mu\text{m}$.

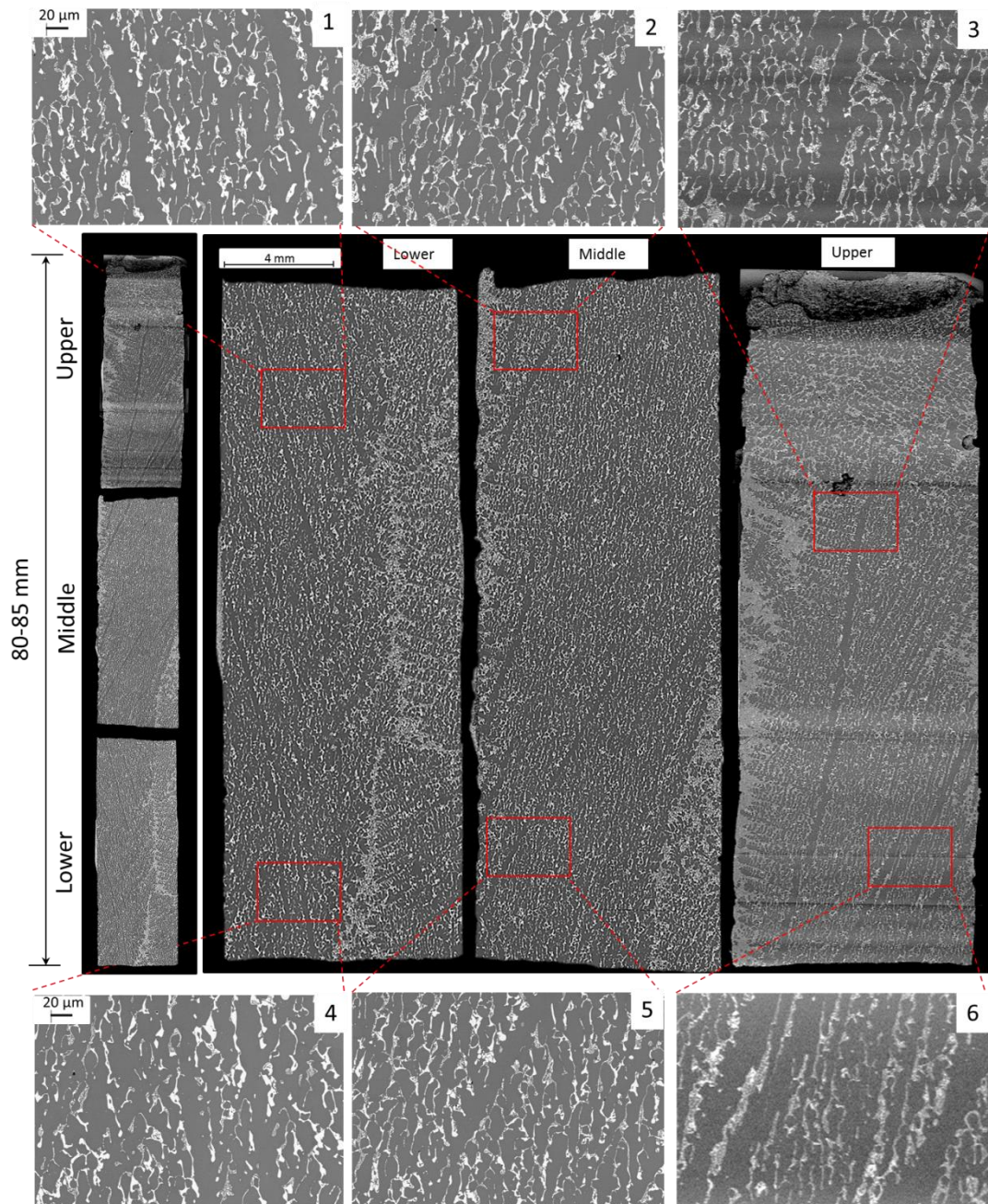


Fig. 5.8. The macro and microstructure of sample Al-15Cu0V (without EMP).

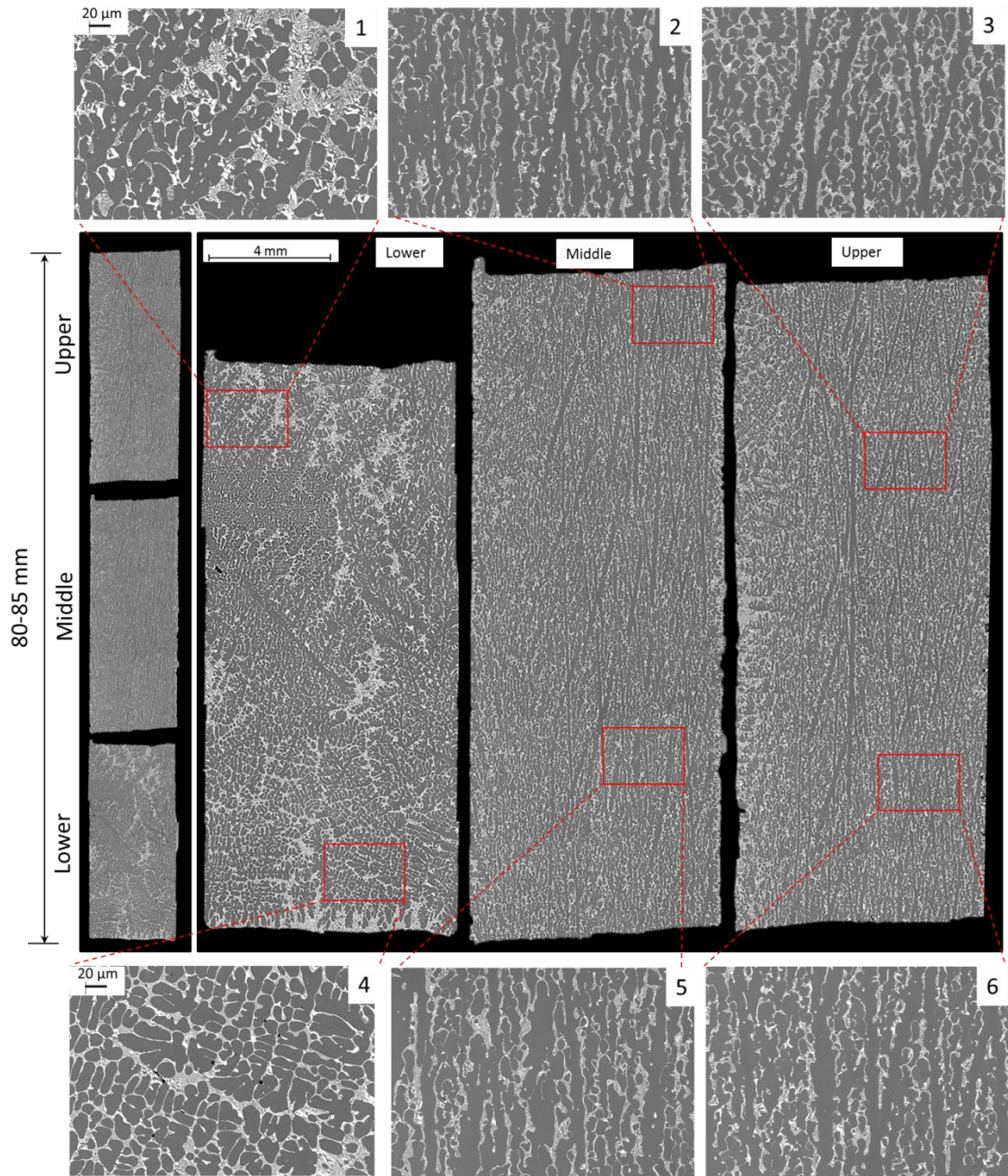


Fig. 5.9. The macro and microstructure of sample Al-15Cu40V (1 Hz, 40V EMP)

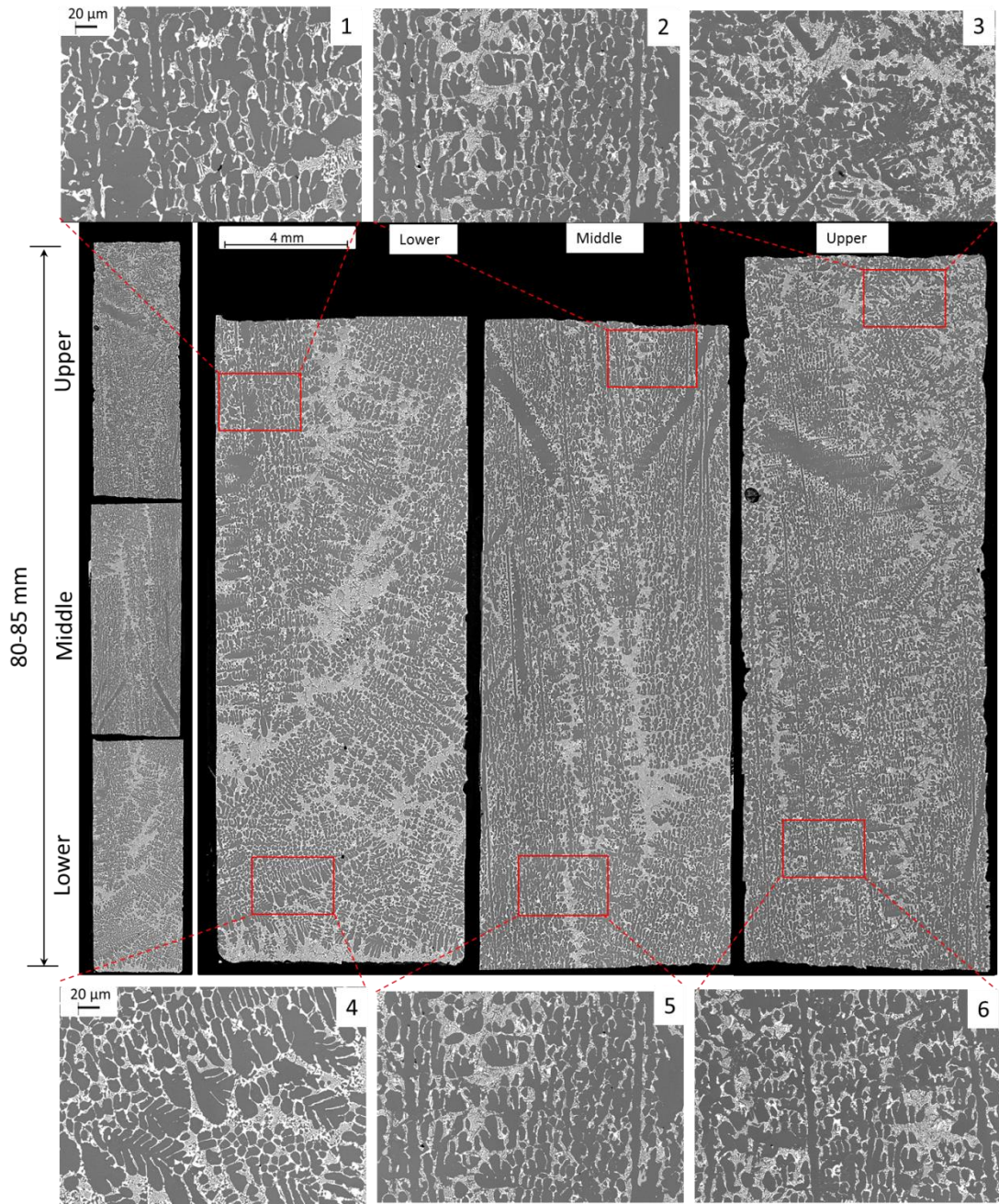


Fig. 5.10. The macro and microstructure of sample Al-15Cu80V (1Hz, 80 V EMP)

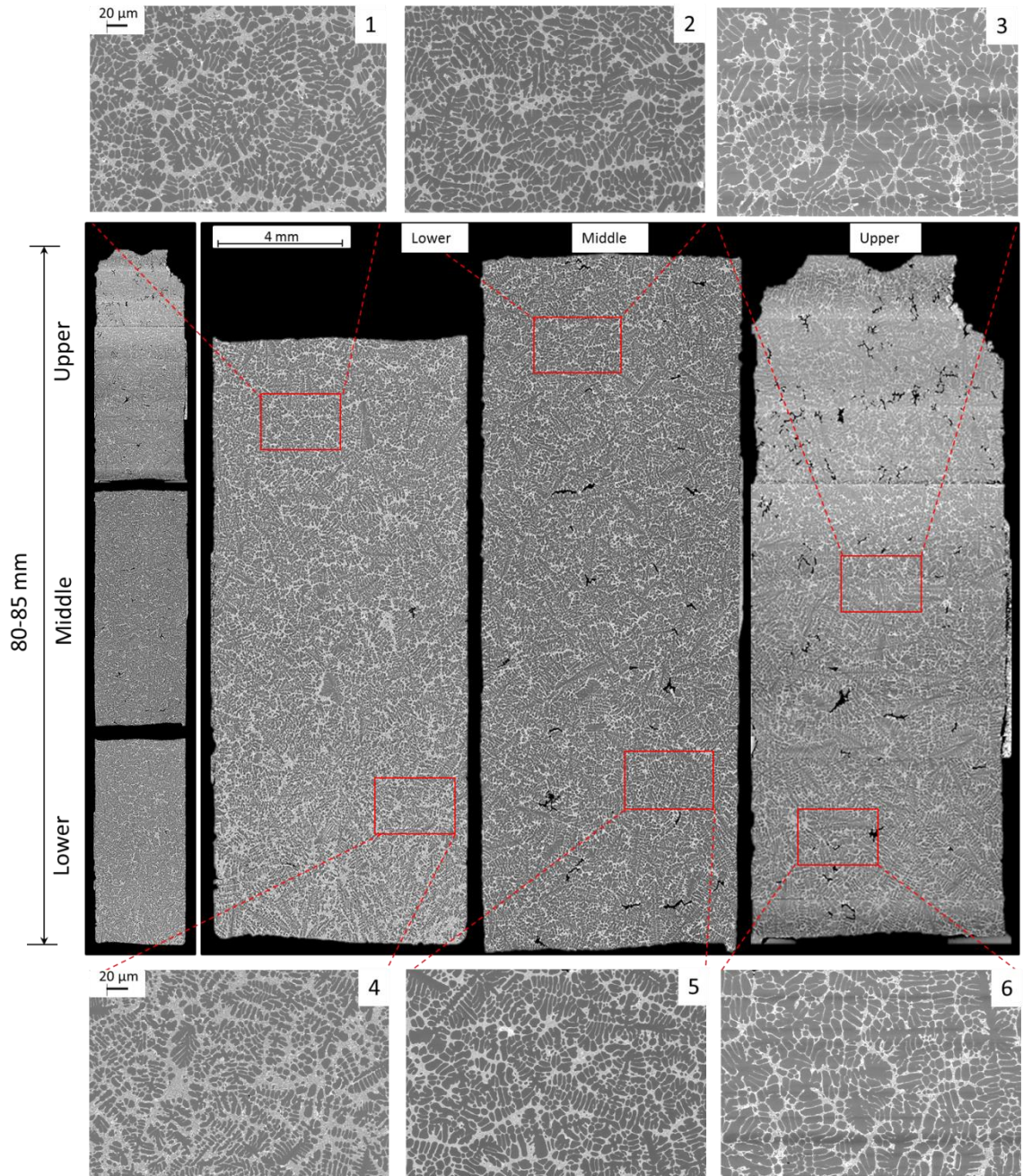


Fig. 5.11. The macro and microstructure of sample Al-15Cu120V (1Hz, 120 V EMP)

5.3.2.2 The eutectic phase

Detailed SEM analyses also found that the electromagnetic pulses applied can strongly influence solute diffusion during solidification, and therefore affect the formation of the eutectic microstructure. The comparison of the eutectic microstructures of the Al-15Cu samples formed without and with EMP is presented in this section.

Fig. 5.12 is a series of backscattered electron images, showing the typical eutectic colonies of the Al-15Cu alloy samples (Nos. 8-11 in Table 5.1) solidified without and with EMP. In general, it can be seen that, as the discharging voltage increased from 0 to 120 V, the size of the eutectic colonies became smaller from ~ 300 to $100 \mu\text{m}$. Within the colonies, the size of the θ (Al_2Cu) phase became smaller from ~ 60 to $20 \mu\text{m}$. Fig. 5.12 shows that, at a higher magnification of $1690\times$ there existed a clear solute diffusion zone at the boundaries of the θ phase (marked by the red squares on each of the left-hand side images) inside the eutectic colonies and these diffusion zone can be more clearly seen in the corresponding enlarged, zoom-in images on the right for each case solidified with EMP. However no such diffusion zones were found inside the eutectic colonies of the Al-15Cu0V sample, i.e. without EMP as seen in Fig. 5.12a.

To further quantify the solute diffusion zones, even higher magnification ($4130\times$) backscattered electron images were taken to highlight the θ phases of interest, and Energy-Dispersive X-ray Spectroscopy (EDX) line scans were performed on the θ phases as clearly showed in Fig. 5.13.

Fig. 5.13 shows the backscattered electron images of $4130\times$ with EDX line scan (the left column) and the distribution of element resulting of EDX line scan (right column). The distribution graph shows that the red line is a relative composition of Al while the purple one is Cu composition inside the θ phases. The Al decreases gradually in the boundary of θ phases while the Cu increases and it decreases of 20-25% compare with area outside θ phases (with pointed arrow), statistical data from the line scans indicated

that the diffusion zones are 3-5 μm wide. It is interesting that with the discharging voltage of 0 to 120 V, the alloys have solute diffusion zone in the similar phenomena and the size of the diffusion zone relatively the same.

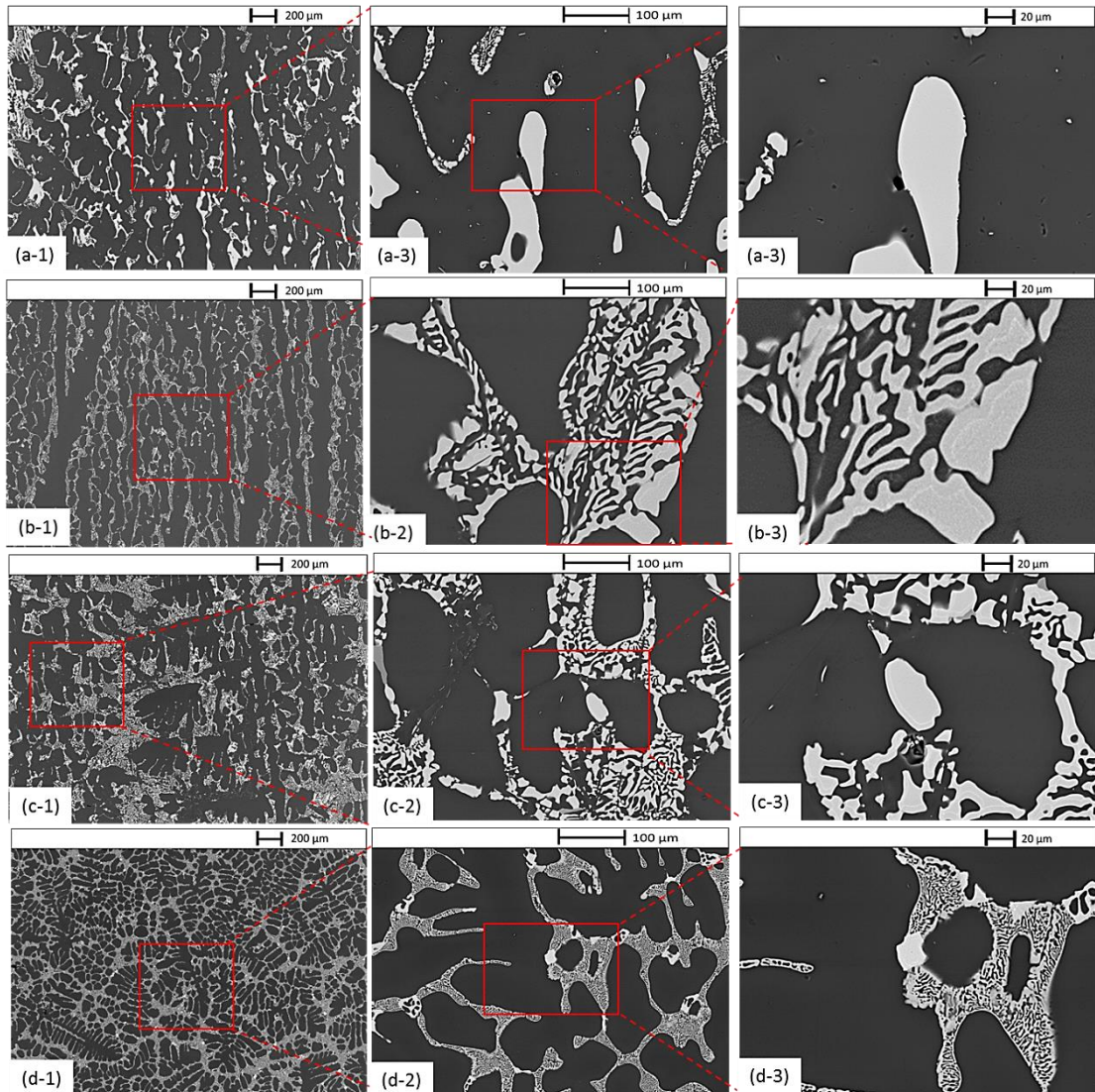


Fig. 5.12. A series of SEM backscattered electron images, showing the eutectic colonies and the θ phases within the colonies of the Al-15Cu samples (Nos. 8-11 in Table 5.1) cast (a) without EMP; and with 1 Hz EMP of (b) 40 V, (c) 80 V, and (d) 120 V. The solute diffusion zones are clearly seen in (b) to (d), but not in (a).

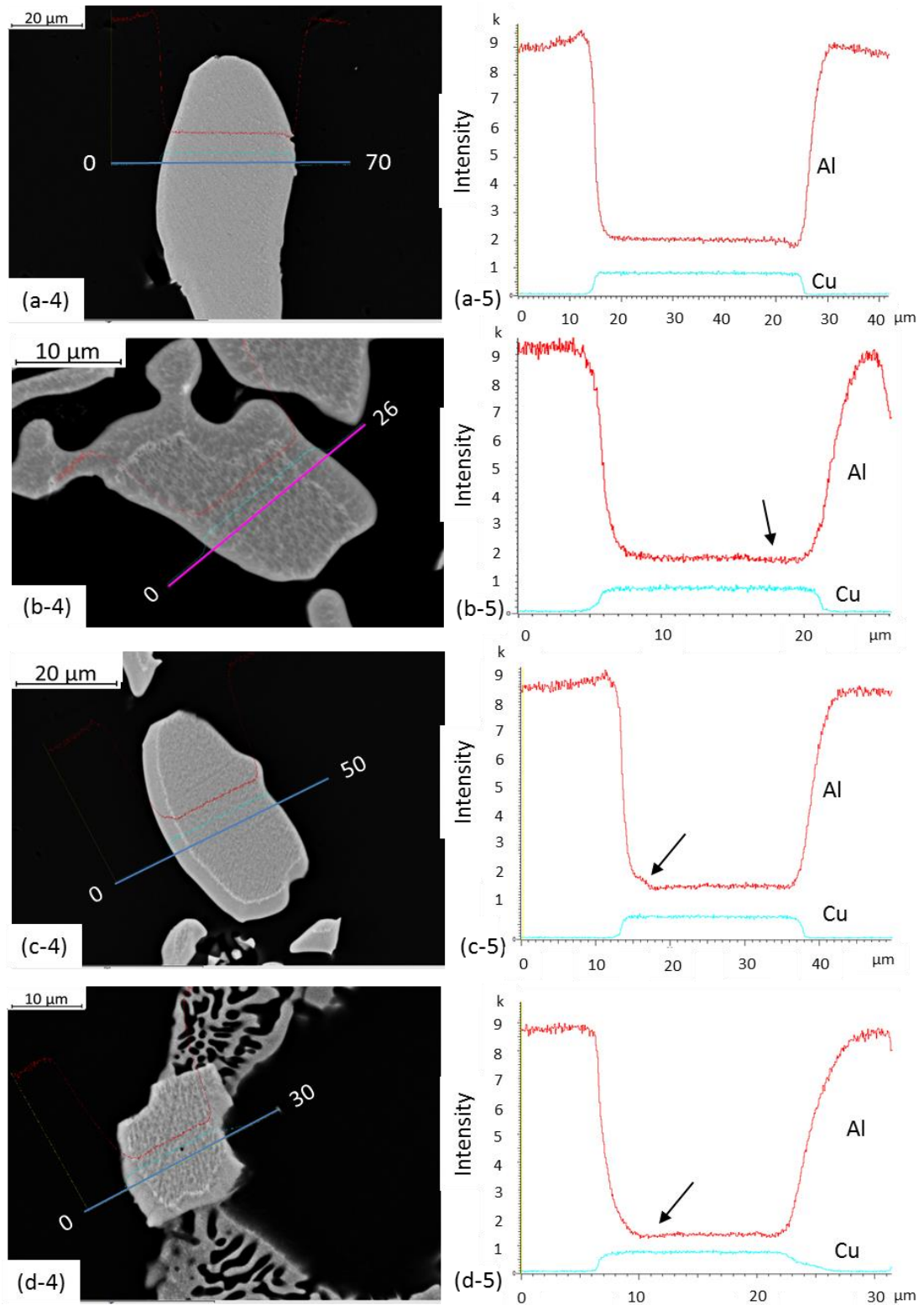


Fig. 5.13. A series of backscattered electron images with EDX lines scans, illustrating the solute diffusion zones along the boundaries of the θ phases inside the eutectic colonies for the Al-15Cu samples (Nos. 8-11 in Table 5.1) cast by (a) without EMP, with 1 Hz EMP of (b) 40 V, (c) 80 V and (d) 120 V respectively.

5.3.3 The Al-35Cu alloy samples

5.3.3.1 The primary θ (Al_2Cu) phases

Fig. 5.14 shows the macro and microstructure of sample Al-35Cu0V (without EMP). Clearly, at the lower part of the as-cast bar, long-thin and near-parallel primary θ phases are seen to occupy a large portion of the polished area. The averaged length and width of the θ phases are ~ 3000 μm length and 100 μm width. The area fraction of the θ phases is calculated as 51%. All evidence indicated that, apart from a small region on the right-hand side bottom corner (highlighted in Fig. 5.14-4), majority of the primary θ phases grew against the gravity to form near-parallel distribution. Fig. 5.14 also shows that, much less bigger θ phases were found in the middle part, and almost none was found in the upper parts of the polished area, indicating that much of the Cu element sunk to the lower part during the solidification experiment.

The areas of interest at the lower, middle and upper parts of the polished bar are showed in the high magnification zoom-in images, it can be seen that the eutectic phase forms in the vertical and near-parallel pattern.

Fig. 5.15 shows the macro and microstructure of sample Al-35Cu120V (1 Hz, 120 VEMP). Similarly, much more θ phases (67%) were found in the lower part, much less 11% in the middle part, and almost none in the upper part. However, for > 80 percentages of the θ phases in the lower part, their morphology changed completely. Many small island-like clusters of θ phases (an average size of 140 μm long and 260 μm wide) were formed, each cluster aligned together in a straight line to form a long string of clusters, and the long strings were then arranged in a near-parallel manner. This morphology is completely different to the long-thin, near-parallel individual θ phase showed in the lower part of Fig. 5.14.

The areas of interest at the middle and upper parts of the polished bar are also showed in the high magnification zoom-in images, it can be seen that apart from the change of θ phase, the eutectic phase form also changed to the random pattern.

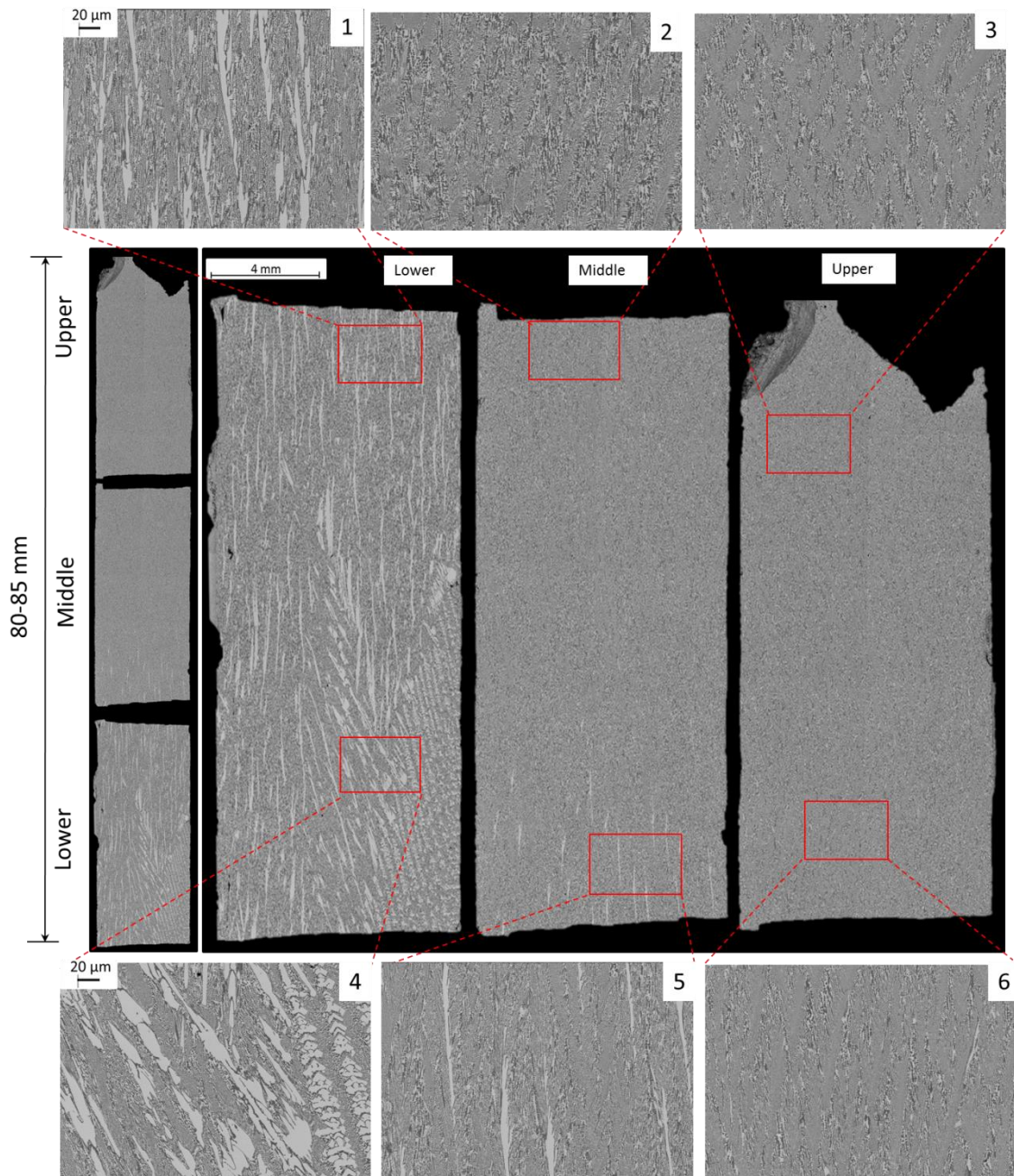


Fig. 5.14. The macro and microstructure of sample, Al-35Cu0V (No. 13 in Table 5.1) cast without EMP.

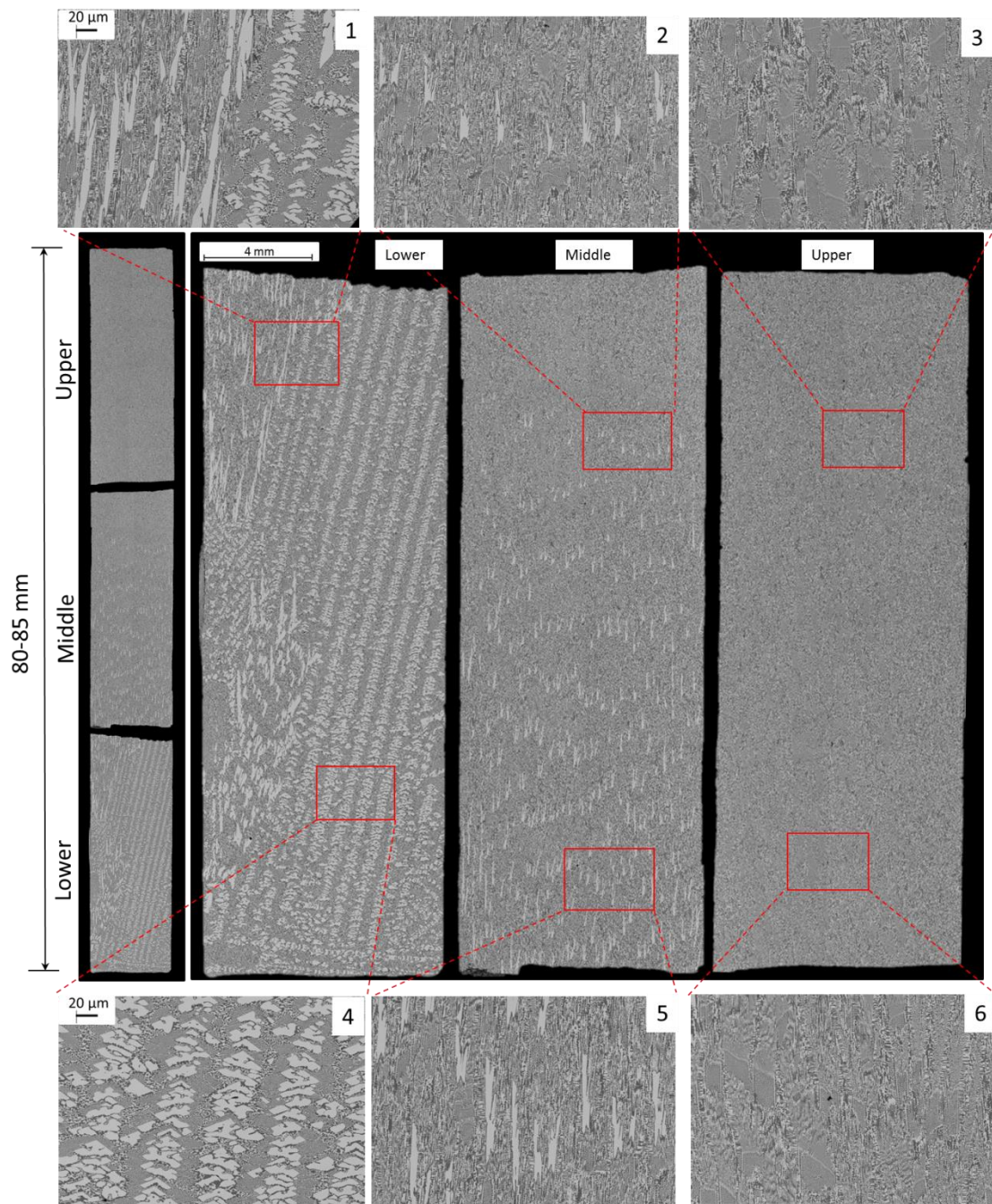


Fig. 5.15. The macro and microstructure of sample, Al-35Cu120V (No. 14 in Table 5.1) cast with 1 Hz, 120 V EMP.

5.3.3.2 The eutectic phase

Fig.5.16 shows the typical eutectic microstructures of sample Al-35Cu0V (without EMP) and Al-35Cu120V (1 Hz, 120 V EMP). Although the general morphology is a bit different, at higher magnification, again, clear solute diffusion zone (with lower Al element) were found to appear along the θ phases of the EMP treated sample, Al-35Cu120V (Fig. 5.16b-2). EDX line scan indicated that the diffusion zone is $\sim 5 \mu\text{m}$ wide.

The atomic contrast from the backscattered images clearly show the diffusion zones contain more heavy element, in these cases, more Cu, and the EDX line scans gave the relative change of the Al and Cu. Based on line scan the relative decrease of the Al in the diffusion zone is calculated at 25 %.

Once again, no such diffusion zone was found for the sample Al-35Cu0V that was cast without EMP.

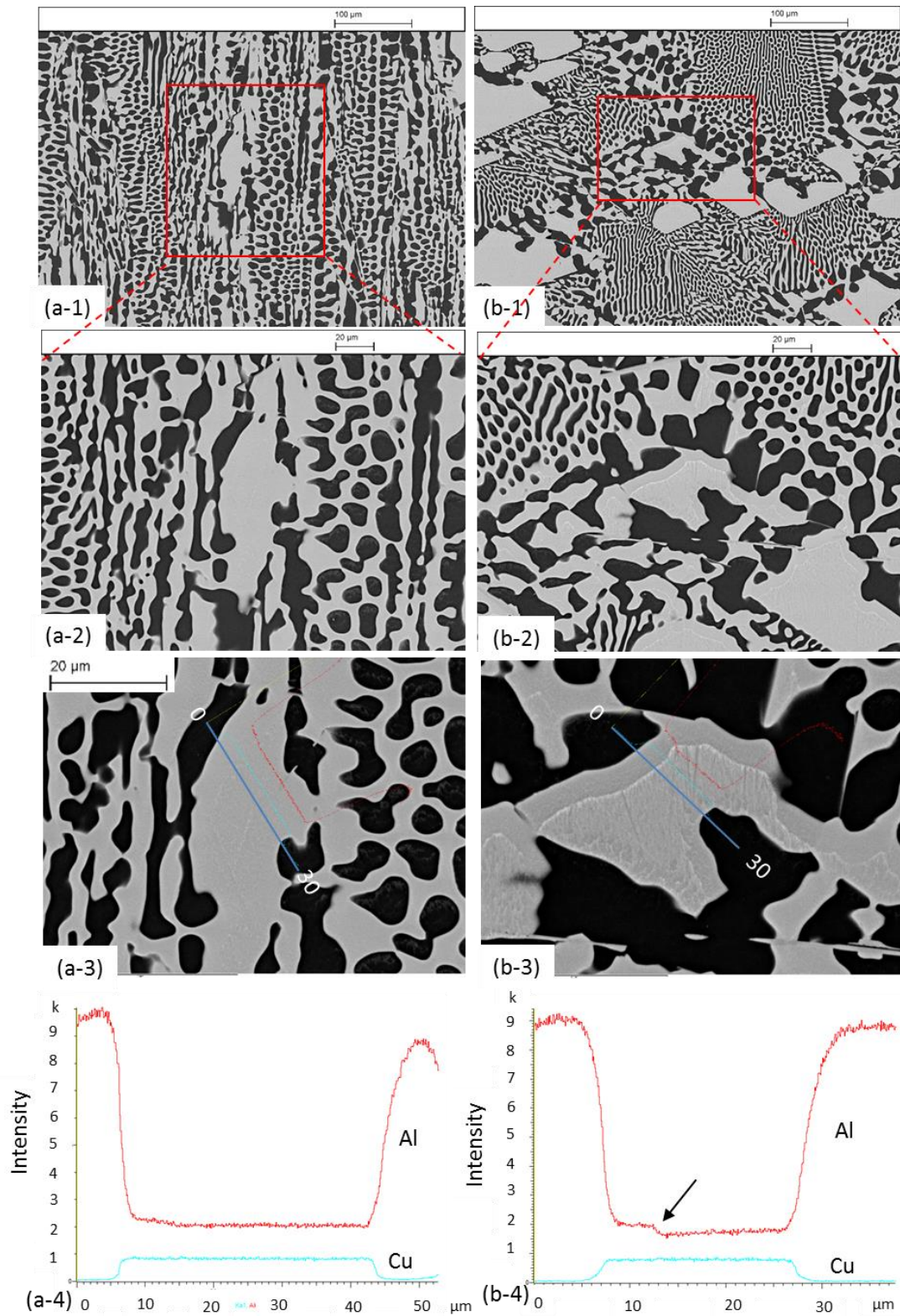


Fig. 5.16. Backscattered electron images with EDX lines scans, illustrating the solute diffusion zones along the boundaries of the θ phases inside the eutectic colonies for the Al-35Cu samples (a) without and (b) with 120 V 1 Hz EMP (Nos. 13 and 14 in Table 5.1)

Table 5.3. A summary of the microstructure measurement from Al-Cu samples without and with electromagnetic fields from 2-D microstructure images

Sample	Primary dendrite trunk length, μm	Primary dendrite trunk width, μm	Primary dendrite arm spacing, μm	Dendrite angle
Al-15Cu0V	15000	20	120	35 °
Al-15Cu40V	12000	10	80	22°
Al-15Cu80V	900	10	120	45°
Al-15Cu120V	500	5	40	Random
Sample	θ phases length, μm	θ phases width, μm	θ phases spacing, μm	Dendrite angle
Al-35Cu0V	3000	100	40	0°
Al-35Cu120V	140	260	20	15°

5.4 Three dimensional microstructural characterisation of the solidified samples, X-ray tomography

The 2-D SEM images presented in Fig. 5.8 to Fig. 5.15 clearly illustrated the changes in the primary Al dendrites, the primary θ (Al_2Cu) phases and the eutectic colonies due to the presence of EMP. However, the 3rd dimensional data is missing, therefore the true 3-D morphologies of the phases cannot be revealed by 2-D images. Obtaining the 3rd dimensional data is essential for achieving a full morphological characterisation of the microstructures of the materials subject to different processing conditions.

Laboratory based X-ray Computing Tomography (X-ray CT) and synchrotron X-ray tomography techniques were used in this research to characterise the 3-D microstructures of the Al-15Cu and Al-35Cu alloy samples, but not the Sn-18Pb samples due to the very high absorption of X-ray.

Fig. 5.17 shows how the area of interest of a sample was selected for doing the tomography scans. Firstly, from the SEM images, a typical area containing the features to be studied in 3-D is selected and then the area was very carefully cut off from the bulk sample, and was ground and polished into needle-shaped sample for subsequent X-ray tomography scans. Based on the attenuation length calculations at 30 keV of energy, the Al-15Cu samples were ground into ~ 3 mm long needle-shaped samples with a tip diameter of < 1.0 mm, while for the Al-35Cu sample, the tip diameter of < 0.6 mm is needed to have a sufficient X-ray transmission at 30 keV.

The laboratory based X-ray CT work was carried out in the Medical engineering laboratory using the X-ray μ CT scanner (HMX 160; X-Tek System), the needle sample was clamped and mounted on the stage with 50 mm from the detector. The sample was rotated from 0 to 180° and the X-ray images were taken for each rotation step. The transmission target used is tungsten (W) and the current output was 20 μA .

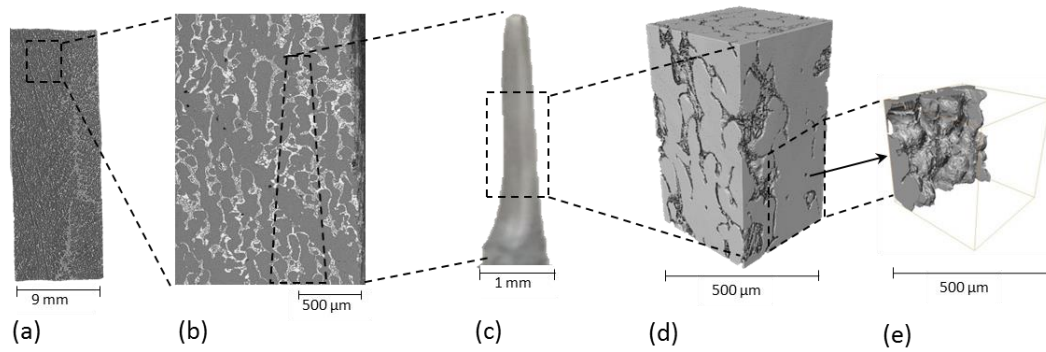


Fig. 5.17. (a) and (b) are SEM images, showing a microstructural feature of interest marked by the dotted lines; (c) the marked area in (b) was selected and carefully made into a needle-shaped sample for tomography scans. (d) The reconstructed 3-D microstructure for the area marked in (c) after reconstruction; and (e) the selected segmentation from (d) to show a primary Al dendrite.

The synchrotron X-ray tomography experiments were carried out mainly at the beamline I13 of Diamond Light Source on 9-15 October 2014 (proposal no. MT9974) , and partially at the beamline for TOMographic Microscopy and Coherent rAdiology experimentTs (TOMCAT) of Swiss Light Source, Paul Scherrer Institute (PSI), Switzerland on 31 October and 1 November 2014 (proposal ID 20140233).

The experimental setup for tomography scans at I13 of DLS was similar to that described in Fig. 2.9 of chapter 2. The sample was placed on the magnetic holder on the sample stage between the X-ray source and detectors. The sample-detector distance was set at 20 mm in order to have low level of in-line phase contrast. The CdWO₄ scintillator-coupled pco.edge 5.5 detector (PCO AG, Germany) was used, and it is a very low noise detector with 2560 × 2160 pixels (a pixel = 6.5 μm × 6.5 μm). The detector has maximum frame rate 100 Hz at all resolution which is suitable for dynamic process. The 8× objective lens in the detector assembly was used to give an effective spatial resolution of 0.81 μm/pixel, and a field of view of 2.1 × 1.8 mm.

In each tomography scan, the sample rotated from 0 to 180°, and 4001 X-ray image projections were taken (17.5 ms exposure time for each projection), including 40 dark field images (without X-ray) and 40 flat field images (with X-ray but without the sample).

Data reconstruction and segmentation were carried out using software DAWN v1.7 [182, 183] and AVIZO v8.0 (FEI, USA), respectively. For each scan, the obtained projection data or signogram (signogram is a sine wave graph image) were firstly transformed into to 2-D cross section images by using the inverse Radon transform method – the so called filtered back projection algorithm with ring artefact suppression function and the parameters used were: ParameterR=0.005, NumSeries=1. Secondly, volume rendering was performed by stacking all of the 2-D cross section images in order to form 3-D image and show the interior features of interest. The 3-D microstructure of interest, for example, a primary dendrite, can then be selected using segmentation by setting the suitable threshold for the features to be selected. The threshold was carefully chosen by analysing the difference in the grey values of the pixels between the primary dendrite and the matrix. The pixels containing the Al primary dendrites have lower grey values \sim 66% (lower X-ray absorption) than those of the matrix containing more Cu element. In this way, the 3-D microstructures of the samples cast without and with EMP were obtained and presented in the following sections.

5.4.1 The Al-15Cu samples

Fig. 5.18 shows the 3-D primary Al dendrites of the Al-15Cu samples cast without EMP and with EMP of 120 V discharge voltages, this tomography images were obtained from the experiment using the lab based X-ray CT scan. The reconstructed 3-D images clearly reveal the full microstructural characteristics of the Al dendrites, such as the growth direction, the size of the primary dendrite trunks, the primary arm spacing, the secondary arm spacing (in Table 5.4), etc which are much rich information compared to those revealed by the 2-D SEM images. The dendrites were disturbed and shorten, the primary Al dendrite, the primary dendrite trunks were shorten

from $\sim 2000 \mu\text{m}$ (without EMP) to $\sim 330 \mu\text{m}$ (with EMP). The direction of the dendrites changed nearly perpendicular to the one without EMP.

Fig. 5.18 also shows the 3-D microstructure of the whole length of the needle sample. The microstructure of Al-15Cu without EMP reveals how the primary dendrites grew.

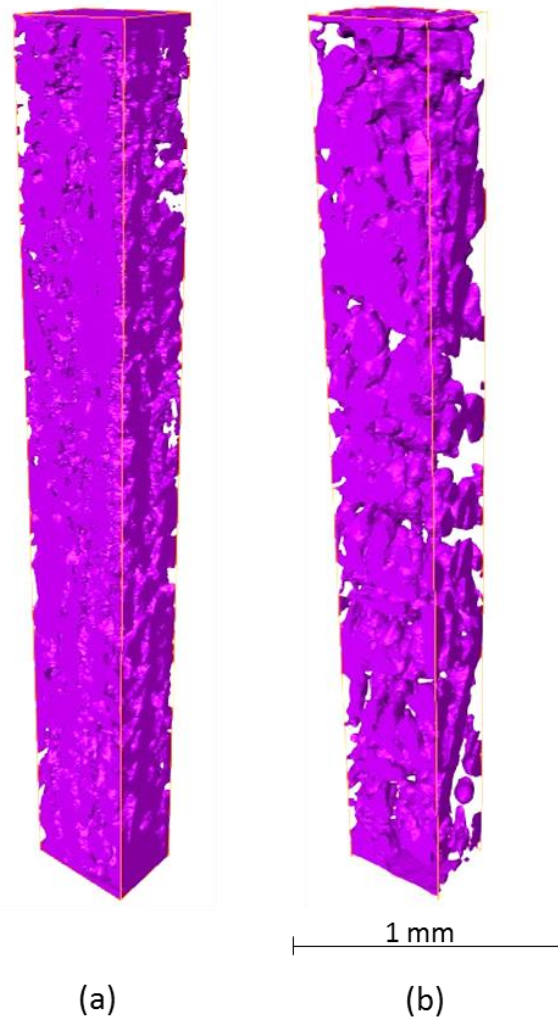


Fig. 5.18. The 3-D primary Al dendrites of Al-15Cu samples (by segmenting out the rest of the matrix) cast (a) without EMP; and (b) with EMP of discharge voltage 120 V 1 Hz. The X-ray images taken from lab based X-ray CT scan.

Fig. 5.19 shows what more rich information can be obtained or extracted from the 3-D tomography dataset comparing to the 2-D SEM images for the similar microstructural features, i.e. the Al primary dendrites in Al-15Cu samples cast without and with EMP (1 Hz, 120 V). The left-hand column shows the typical SEM images. The middle ones are the reconstructed 3-D images chosen from the typical area marked by the rectangle on the SEM images. While the last column shows the segmented primary Al dendrites from the 3-D reconstructed images in the middle column.

Without EMP (Fig.5.19a-1, a-2), the long primary Al dendrites have the average dimension of approximately $\sim 700 \mu\text{m}$ long and $200 \mu\text{m}$ wide, and the volume fraction is approximately 84.6% in this selected volume. In 3-D reconstructed image (Fig. 5.19b-3), the secondary dendrite diameter was measured at $\sim 60 \mu\text{m}$ and they are connected to each other, contrast with the 2-D images shown that they are not connected.

For the case of 1Hz, 120 V EMP, the long dendritic grains were clearly disrupted (Fig.5.19b-1, b-2) and the extracted dendrite show that the growth direction became random (Fig.5.19b-2), and the primary dendrites size decrease to $\sim 300 \mu\text{m}$ and it formed the snow flake shape with 4 branches (Fig. 5.19b-3) within the 2-D images this information was missing.

In order to ensure the effect of EMP to the sample, the experiment is designed to apply the pulse to half of the sample during directional solidification process, so called 'half-sample treatment'. The EMP is applied during sample is withdrawal out of the furnace and continuously apply for half sample. Then the pulse stops since the middle of the sample moving into the EMP coil. The microstructure of Al-15Cu120VH (sample no. 12 in the Table 5.1) of this condition treatment is shown in Fig. 5.20.

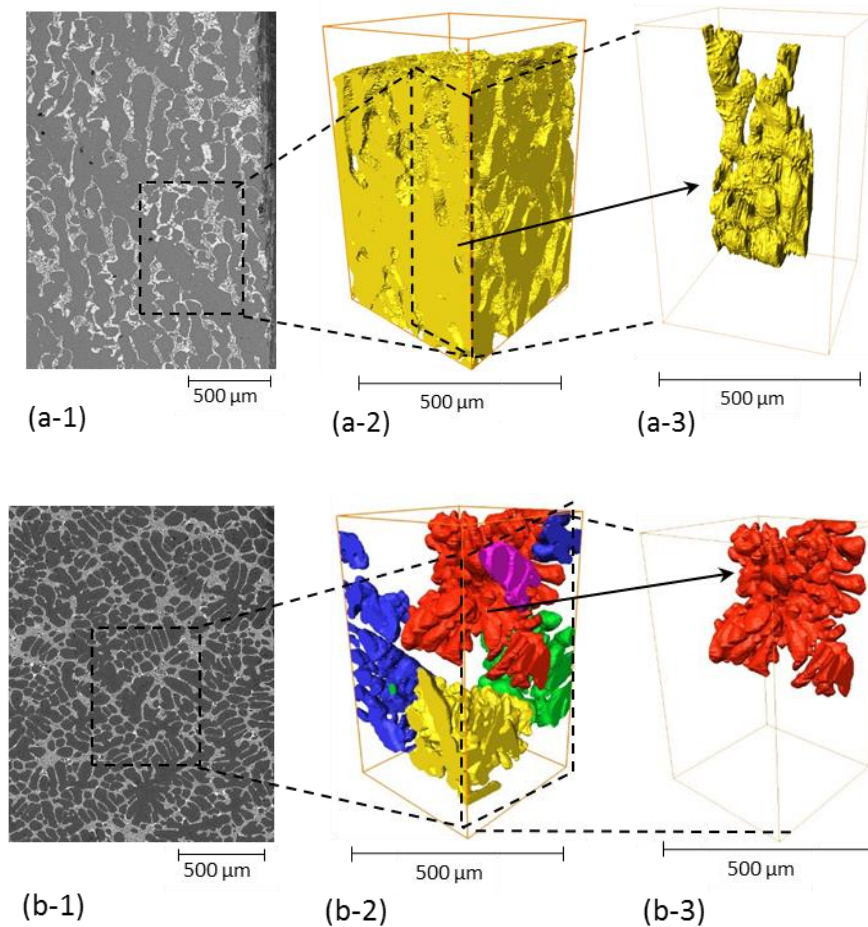


Fig. 5.19. Comparison of the 2-D and 3-D dataset for the primary Al dendrites from the samples (a) Al-15Cu0V and (b) Al-15Cu120V. The tomography obtained from I13, DLS.

Fig. 5.20 shows the 2-D microstructure and 3-D tomography of Al-15Cu120VH alloy with half-sample treatment. The results correlate with the experiment that the lower part was treated with the EMP but the dendrites on the top part are freely to grow without treatment. In Fig. 5.20a, the dendrites are short in the area of the lower part while the dendrites form columnar microstructure from the middle of sample to the upper part. The red-dot line used to indicate the area where the change of microstructure is presented. The microstructure of the upper half of sample grew directional solidification with long morphology. However, the direction of the dendrites is around 45° away from the withdrawal direction might be the reason of un-uniform heat transfer inside alloy bar. The direction of the dendrite

cannot be controlled to be parallel to withdrawal direction as the heat transfer issue involved.

Fig. 5.20b presents the 3-D reconstructed image, showing the difference morphology shape of dendritic microstructure. The upper part presents the columnar structure with the primary dendrite trunk 80 μm diameter while the lower part contains the equiaxed morphology.

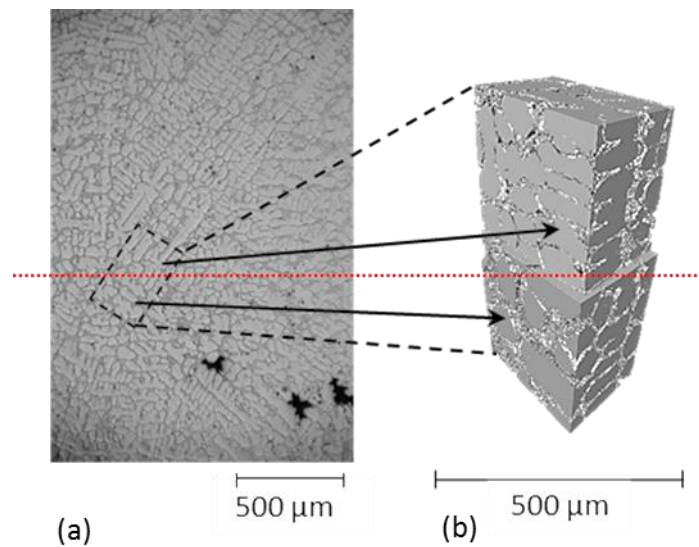


Fig. 5.20. The 2-D and 3-D microstructure of: Al-15Cu120VH with EMP treatment on half-sample. The tomography obtained from TOMCAT, PSI.

5.4.2 The Al-35Cu samples

Fig. 5.21 shows the 3-D primary θ (Al_2Cu) phases of Al-35Cu samples without and with EMP (1 Hz, 120 V). The full microstructural characteristics of the θ phases, such as the growth direction, the size of the θ phases are shown in Table 5.4.

In 3-D images, it clearly seen that the main θ phase has separated braches formed $\sim 20\text{-}30^\circ$ from the main branch which cannot be seen from the 2-D images. While the one with EMP, the θ phases formed in two direction, 30° and 90° with the withdrawal direction. These two directions also cannot be identified from the 2-D images.



Fig. 5.21. The 3-D primary θ phases of Al-35Cu samples (by segmenting out the rest of the matrix) cast (a) without EMP; and (b) with EMP of 1Hz, 120 V. The X-ray images taken from lab based X-ray CT scan.

Fig. 5.22, the 3-D images and 2-D SEM images are compared, the growth directions and the orientations of the primary phases were clearly revealed with any misunderstanding.

Especially, for the case of treated by EMP, most of the primary Al_2Cu phases were showed to be shortened, and many changed the growth direction from vertically against the gravity to horizontal direction (Fig.5.22b-2, b-3), with many others having the growing direction no longer aligned vertically and in a parallel manner.

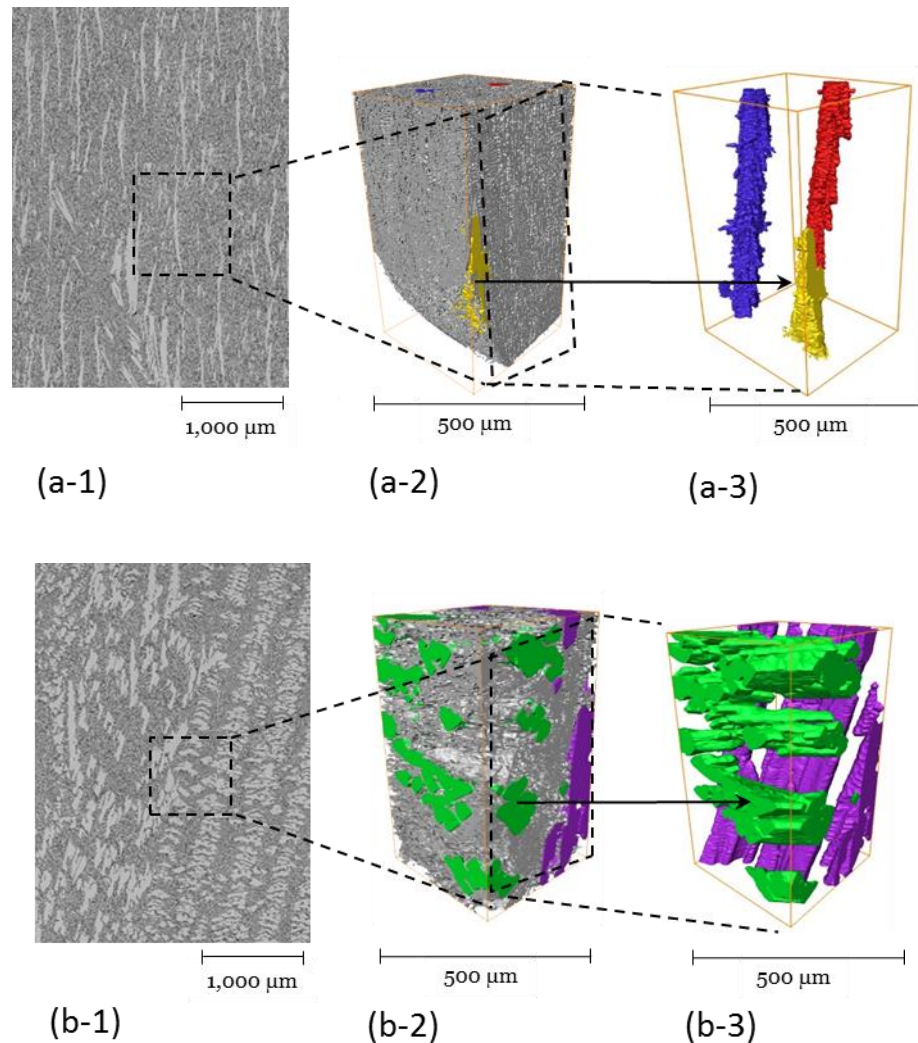


Fig. 5.22. Comparison of the 2-D and 3-D dataset for the θ phases of Al-35Cu (a) without and (b) with 120V 1Hz of EMP treatment. The tomography obtained from I13, DLS.

The morphology of Al-35Cu alloy without EMP treatment, the θ phases are long and thinner compare with θ phases of with EMP.

With EMP treatment the primary dendrites of Al-35Cu change the morphology, size and number. The size of phases are shorter so that the amount of dendrites is increased then phases fraction increased. Nonetheless, for both alloys cast without and with EMP, the eutectic phases remained the similar morphology.

Table 5.4. A summary of the microstructure measurement from Al-Cu samples without and with electromagnetic fields from 3-D microstructure images

Sample	Primary dendrite trunk length, μm	Primary dendrite arm width, μm	Primary dendrite arm spacing, μm	Dendrite angle
Al-15Cu0V	2000	250	120	35 °
Al-15Cu120V	300	40	40	Random
Sample	θ phases length, μm	θ phases width, μm	θ phases spacing, μm	Dendrite angle
Al-35Cu0V	3000	60	300	0-2°
Al-35Cu120V	1500	120-150	60	30° and 90°

5.4.3 The 3-D eutectic structure of Al-Cu alloys

In Fig. 5.23, the 3-D images and 2-D SEM images are compared, the 3-D eutectic structures were clearly revealed and the complex 3-D morphology of eutectic colony and their interconnection and orientation are presented. To show the eutectic structures, the primary dendrites were removed from the 3-D morphology. Fig. 5.23a-3 and 5.23b-3 show the eutectic structure after primary dendrites were removed.

Particularly, in the EMP treated case, the eutectic structure was showed to be disturbed and refined, resulting smaller lamellar spacings (Fig.5.23b-2, b-3).

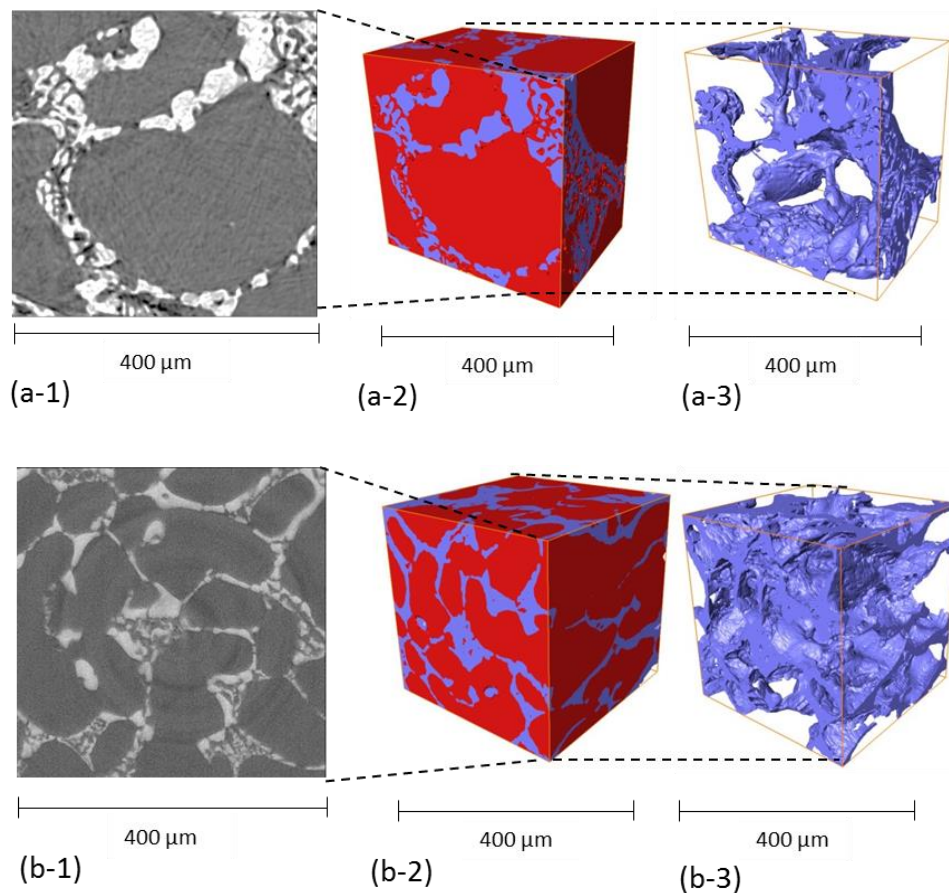


Fig. 5.23. A series of images of the eutectic structures of Al-15Cu (a) without, (b) with 120V 1Hz of EMP treatment. The tomography data were obtained from I13, DLS.

Fig. 5.24 shows the 2-D SEM and 3-D tomography images of the eutectic structures of the Al-35Cu alloy without and with EMP treatment. The eutectic structures were shown to grow in parallel and vertically against gravity. To show the eutectic structures, the primary dendrites were removed from the 3-D morphology. Fig. 5.24a-3 and 5.24b-3 show the eutectic structure after primary dendrites were removed.

In contrast, for the alloy treated by EMP, the eutectic morphologies were disturbed and changed the direction from vertically against the gravity to horizontal direction, forming a more random pattern (Fig.5.24b-2, b-3).

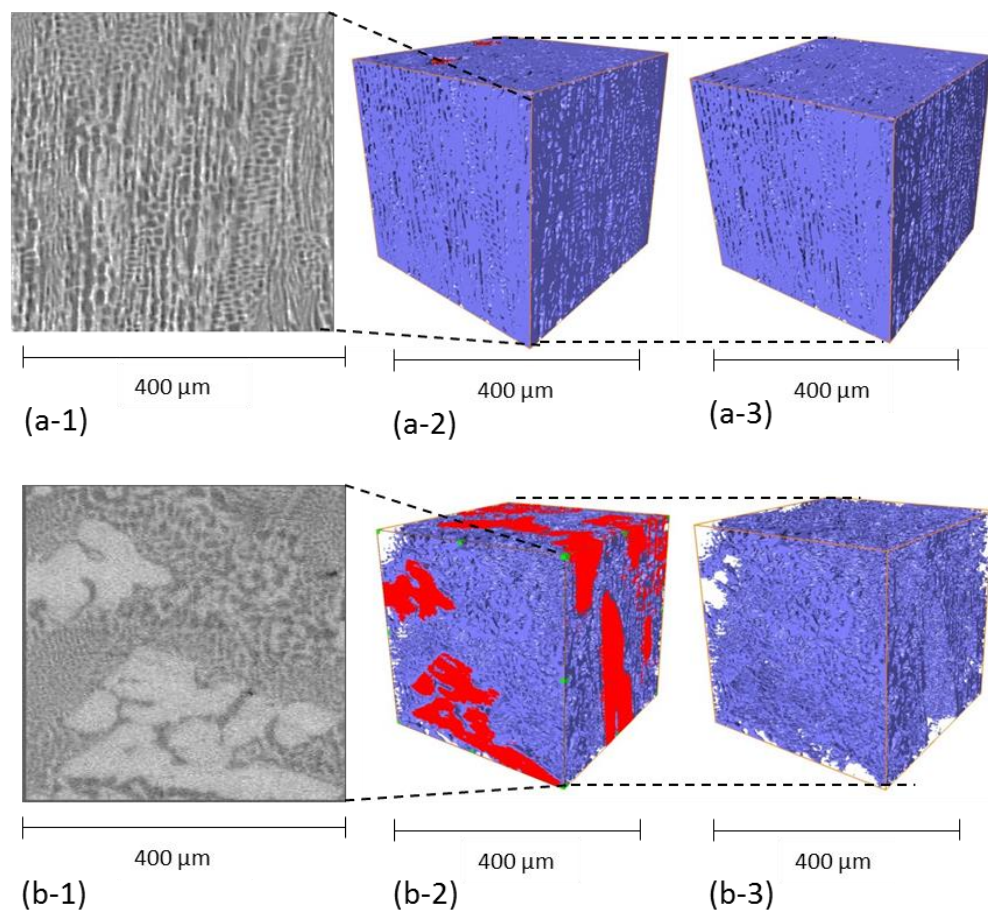


Fig. 5.24. A series of images of the eutectic structures of Al-35Cu (a) without, (b) with 120V 1Hz of EMP treatment. The tomography data were obtained from I13, DLS.

5.5 Summary

The solidification experiments of Sn-18%Pb, Al-15%Cu and Al-35%Cu alloys under pulse electromagnetic fields of the different magnetic fluxes and well-controlled thermal conditions were carried out.

The results of solidification microstructure of solidification of those alloys were revealed and analysed 2-D microstructures using optical microscopy, scanning electron microscopy and 3-D microstructure using X-ray tomography. The results show that the microstructures of alloys with EMP treatment are significantly difference from the ones without treatment.

From the 2-D microstructures of those alloys, the measured microstructure, i.e. primary dendrite trunk, primary dendrite spacing and secondary dendrite arms were identified showing the comparison of the microstructure change by the difference of discharge voltage of EMP. The microstructures of alloys with treatment were disturbed and change the size to smaller and finer related to the increase of discharge voltage.

3-D microstructure revealed the missing direction which unseen in 2-D microstructure. The true morphology of primary dendrite and θ phase of Al-15%Cu and Al-35%Cu, the truly information of microstructure size and direction were presented. Further, especially, the eutectic morphology of Al-Cu alloy were explored, i.e. the direction and connection of those colonies.

Chapter 6 : Modelling of the multiphysics in pulse electromagnetic fields

As described in Chapter 4, the helical copper coil (EMP coil) produces pulse magnetic flux, inductive current and Lorentz force inside the liquid metal held within the glass tubes. Finite element method and commercial software, Comsol Multiphysics [184] were used to simulate the pulse magnetic flux, the Lorentz force and the fluid flow enhanced by the Lorentz force in order to understand more quantitatively the effects of those coupled physics on the microstructural evolution of the metal alloys solidified in the pulse electromagnetic field.

6.1 The governing equations

Firstly, the pulse magnetic flux generated by the helical copper coil was simulated and the governing equations are [143]:

$$0 = \nabla \cdot \mathbf{B} = \nabla \cdot (\nabla \times \mathbf{A}) \quad (6.1)$$

$$\mathbf{B} = C \mu_0 \mu_r \mathbf{J}_e \quad (6.2)$$

$$\mathbf{J}_e = \frac{V_d}{Ac Z} \quad (6.3)$$

where \mathbf{B} is the magnitude of the magnetic field or the magnetic flux density measured by Tesla [T], \mathbf{A} is the magnetic vector potential, μ_0 (1.26×10^{-6} T m/A) is the permeability of free space, μ_r is the relative permeability of copper, \mathbf{J}_e [A/m^2] is the density of the input electric current passing through the coil, V_d (V) is the discharge voltage, Z (Ω) is the impedance of the LC circuit, Ac is the cross-section area of the wire (3.14 mm^2) of the coil, and C is a compensation coefficient ($C = 1$, if no energy loss is considered).

Secondly, the induced current generated inside the metal alloys by the magnetic field produced by the copper coil can be [185] calculated by

$$\mathbf{J} = \mu_0^{-1} \mu_r^{-1} \mathbf{B} \quad (6.4)$$

Where \mathbf{J} is the induced current density inside the molten alloy, and \mathbf{B} is induced magnetic flux density [85]

Thirdly, the pulse Lorentz force (\mathbf{F}) generated inside the metal alloy held within the quartz tube can be calculated [83, 162] by

$$\mathbf{F} = \mathbf{J} \times \mathbf{B} \quad (6.5)$$

Finally, the velocity field of the liquid metal (\mathbf{u}) was simulated using the Navier-Stoke equation [144] and the liquid metal was treated as an incompressive fluid flow with the Lorentz force as the body force. The heat flow and solidification were not considered in the simulation for simplicity. The governing equation is [185, 186]:

$$\rho \left(\frac{\partial \mathbf{u}}{\partial t} + \mathbf{u} \cdot \nabla \mathbf{u} \right) = \nabla [-p I_t + (\mu + \mu_T)(\nabla \mathbf{u} + (\nabla \mathbf{u})^T) - \frac{2}{3} \rho k_T I_t] + \mathbf{F} \quad (6.7)$$

Where ρ is the density of the liquid metal, p is pressure and \mathbf{u} is velocity, \mathbf{F} is the Lorentz force, I_t is the identity tensor, ∇ is Laplace operator.

From Reynold number,

$$Re = \frac{\rho u L}{\nu_s} \quad (6.8)$$

Where L is the characteristic length and ν_s is the viscosity of the melt at 625 °C. The calculated Re is 5928, therefore the fluid flow is turbulent flow.

The well-known k- ε model was used to take the turbulence into account in the fluid flow simulation [155], and the turbulence viscosity term, μ_T , in this model is given by

$$\mu_T = C_\mu \frac{\rho k_T^2}{\varepsilon} \quad (6.9)$$

where k_T is the turbulent kinetic energy, and ε is turbulent energy dissipation, and C_μ is a constant. The differential equations for k_T and ε are given by [187].

$$\rho(\mathbf{u} \cdot \nabla)k_T = \nabla \cdot \left(\frac{\mu_T}{\sigma_k} + \mu \right) \nabla k_T + G_T + \rho\varepsilon \quad (6.10)$$

$$\rho(\mathbf{u} \cdot \nabla)\varepsilon = \nabla \cdot \left(\frac{\mu_T}{\sigma_\varepsilon} + \mu \right) \nabla \varepsilon + C_1 \frac{\varepsilon}{k_T} G_T - C_2 \rho \frac{\varepsilon^2}{k_T} \quad (6.11)$$

where C_1 , C_2 , σ_k and σ_ε are constants and G_T is the turbulence shear generation term.

The MFD was firstly simulated by the equation 6.2 from the input current density of 40, 80, 120, 160, 200 and 240 V. Then the ICD was simulated from the each simulated magnetic flux (equation 6.4). At each computational point in the domain, the simulated MFD and ICD were used to simulate Lorentz force. Finally, the Lorentz force was used in the fluid flow model, equation 6.7 as the volume force.

6.2 The computational domains

Fig. 6.1a is a 3-D cut-off CAD drawing, showing a quartz tube mould containing a liquid melt set inside the EMP coil. This whole arrangement is actually an axis symmetrical geometry, therefore a 2-D axis symmetrical section (a dimension of 130 \times 30 mm as showed in Fig. 6.1b) through the

axis can be used as the computational domain in the simulation to represent the whole 3-D arrangement. Furthermore, the 2-D domain itself is a symmetrical geometry against line P4-P4, and therefore, only half domain and the related data are needed to be described here. Fig. 6.2a shows the enlarged upper half domain, with the highlight on the subdomains of (1) liquid melt (SB1), (2) the quartz tube mould (SB2), (3) the helical coils (SB3) and the free space filled with air (SB4). Fig. 6.2b shows the corresponding triangle mesh structures for each sub-domain. The size of each sub-domain and its properties used in the simulation are summarised in Table 6.1. Each turn of the helical copper coil was defined as the Single-Turn Coil domain [185], and the whole helical coil was simulated using 45 such evenly and symmetrically distributed single-turn coils. The distance (pitch) between the adjacent coils is 1.25 mm.

6.3 The mesh structure

Unstructured triangular mesh [155] was generated using topology mesh function for the computational domain with the mesh size ranging from 0.042 to 9.39 mm as shown in Fig.6.2b. The domain for the liquid metal alloy was meshed using extra fine mesh, especially at the corner, and the area near the quartz tube. The total number of mesh elements is 267052.

6.4 The boundary and initial conditions

For the magnetic flux simulation, all boundaries of the sub-domains were set as insulation boundary, i.e. the boundary does not receive any external magnetic flux from outside. Zero magnetic flux density was initialized when the simulation started. For the melt flow simulation, fixed wall boundary conditions were set at the bottom boundary (contacting the Duratec rod) and the side boundary (contacting the quartz tube). However, at the top boundary (contacting air), a slip wall boundary condition was defined. The initial volume force and velocity of the liquid metal were set as zero when simulation started. The pulse current was input in the copper coil with the full width at half maximum (FWHM) ~ 25 ms, the amplitude varied by voltage input (40-240V). The time step for calculating was set 1 ms.

6.5 The materials properties

The simulation focused on studying the pulse magnetic fluxes and Lorentz forces acting on the liquid metal. The phenomena occurred in the time scale of milliseconds. It is very short comparing to the metal solidification event. Therefore, the constant temperature was assumed for the melt, and temperature-independent material properties were used during the pulse simulation. However, temperature dependent materials properties, such as viscosity and density were defined and used in the simulation. Constant properties were used for air, the quartz tube, the coil as detailed in Table 6.1.

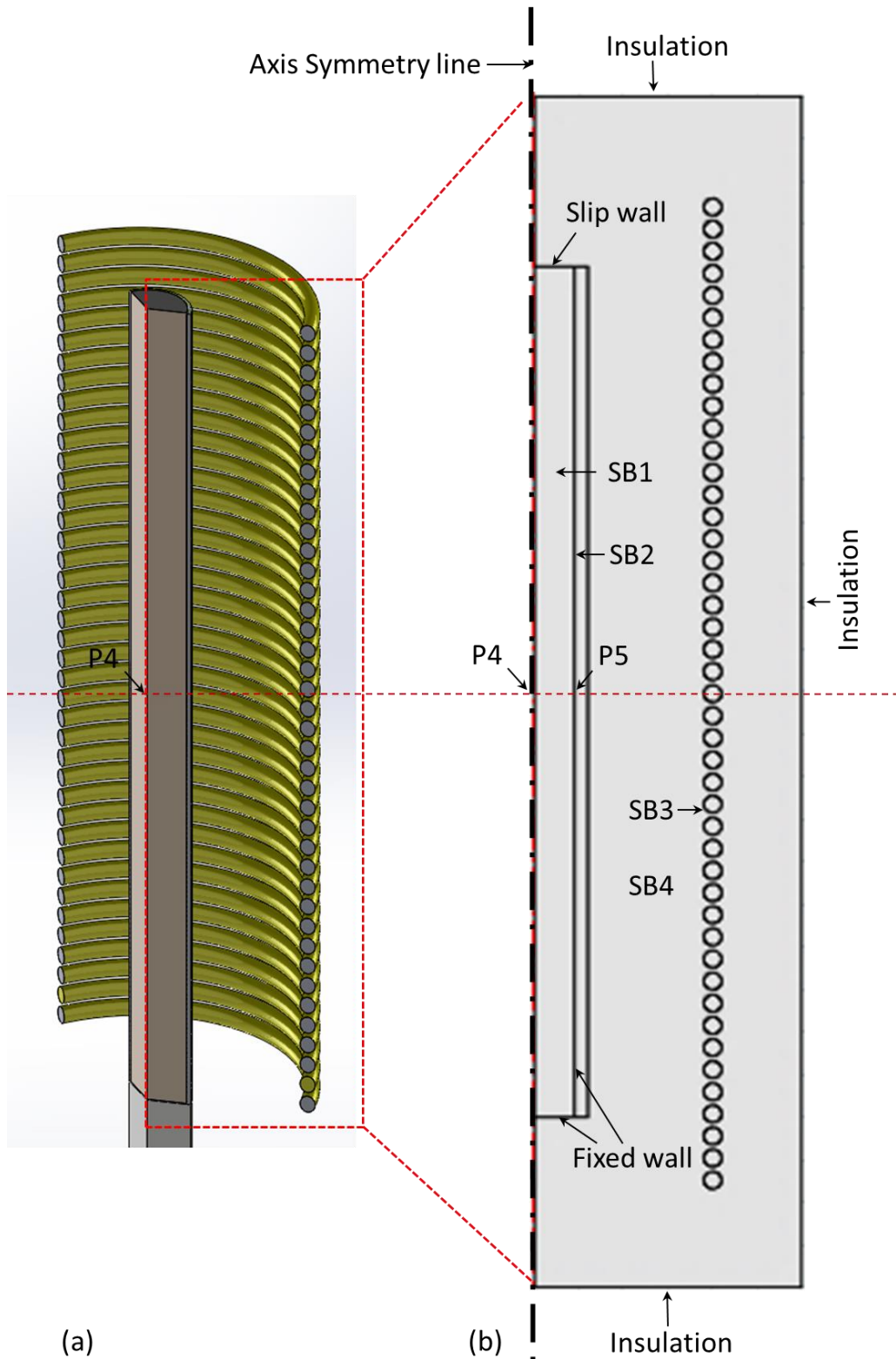


Fig. 6.1. (a) A 3-D cut-off, showing a glass tube mould containing liquid melt inside the EMP coil, (b) The 2-D axis-symmetry computational domain used in the simulation.

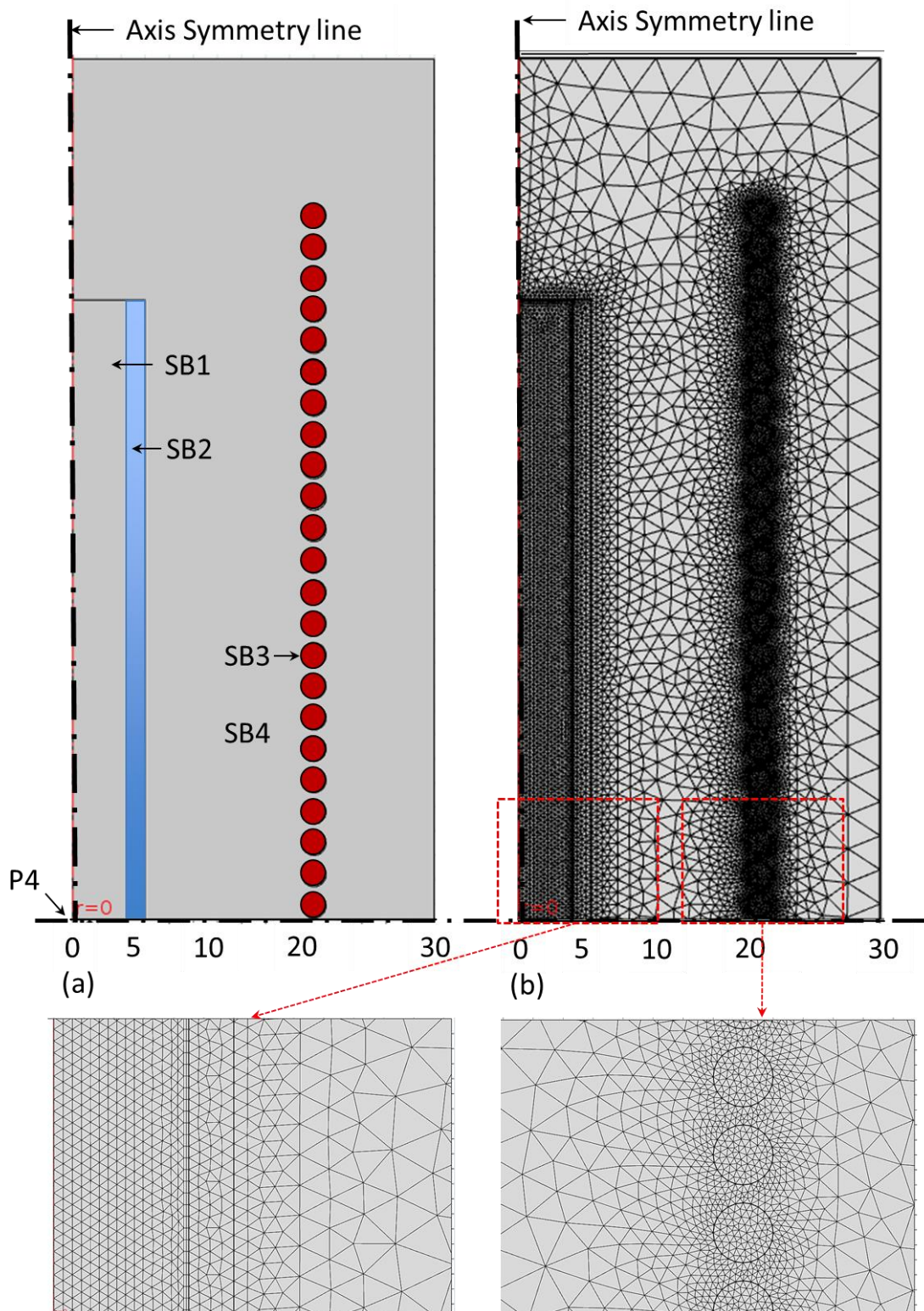


Fig. 6.2. (a) The upper half of the computational domain, and (b) the corresponding mesh structures for each sub-domains and the close-up of the mesh structure for SB1, SB2 and SB3.

Table 6.1. The computational sub-domains, size and materials properties used in the simulation [178, 188-192]

Sub-domain	Alloy melt (SB1)	Tube mould (SB2)	EMP coil (SB3)	Empty space (SB4)
Size (High × Wide, mm)	100 × 4.5	100 × 1.5	Ø2 × 45 turns	130 × 30
Materials and properties	Al-15Cu	Quartz (SiO ₂)	Cu	Air
Density (g/cm³)	3.63	2.20	8.7	1.2×10 ⁻³
Temperature (°C)	625	25	25	25
Coefficient of thermal expansion (× 10⁻⁶ °C⁻¹)	27.95[193]	55	17	-
Resistivity (×10⁻⁸ Ω m)	11.85[189]	1×10 ¹⁴	1.6	2.3×10 ²⁴
Viscosity at 625 °C (mPa S)	2.48[190]	-	-	-
Relative Permeability	1.11	1	1[194]	1

6.6 The results of the simulation

6.6.1 Magnetic flux density

The simulations of the magnetic flux density (MFD) were firstly carried out without the quartz tube mould and the alloy melt (the Quartz tube and the alloy melt sub-domains were disabled), in order to obtain data to compare with the measured MFD using the Guass meter described in Chapter 4. The simulated MFD distributions for each different discharge voltage are showed in Fig. 6.3. Clearly, apart from the areas near the top end (bottom end as well) of the helical coil, the MFD was uniformly distributed in the computational domain with its intensity increasing with the increase of the discharge voltages. The stream line and arrows indicate the magnetic flux direction.

To validate the simulation, the simulated data at P4 was extracted to compare with the measured data already presented in Fig. 4.15 of Chapter 4. Only five voltages (40, 80, 120, 160 and 200 V) were used in the measurement so as to avoid the possible damage of the EMP coil because of very strong pulsing action was found when discharge voltage > 200 V was used in the experiment.

Table 6.2. A summary of the input discharge voltage, measured and simulated magnetic flux density (MFD), induced current density (ICD) and Lorentz force

Input variable	Capacitor discharge voltage (V)		40	80	120	160	200	240
Measured variable	MFD peak at the centre of the EMP coil, i.e. point, P4 in Fig. 6.1 (mT)		270	600	890	1150	1470	-
Simulated variable	Compensation coefficient, C	Sub-domains used in the simulation						
MFD peak at P4 (mT)	1	SB3 + SB4	351	707	1065	1422	1780	2122
	0.85	SB3 + SB4	300	604	901	1215	1520	1825
	0.85	SB1+SB2+SB3+SB4	331	665	996	1330	1663	1996
ICD peak at P5 ($\times 10^6$ A/m²)	0.85	SB1+SB2+SB3+SB4	1.56	3.13	4.58	6.27	7.85	9.45
Lorentz force peak at P5 (N)	0.85	SB1+SB2+SB3+SB4	2.48	9.8	21.5	39.4	61.6	89.1

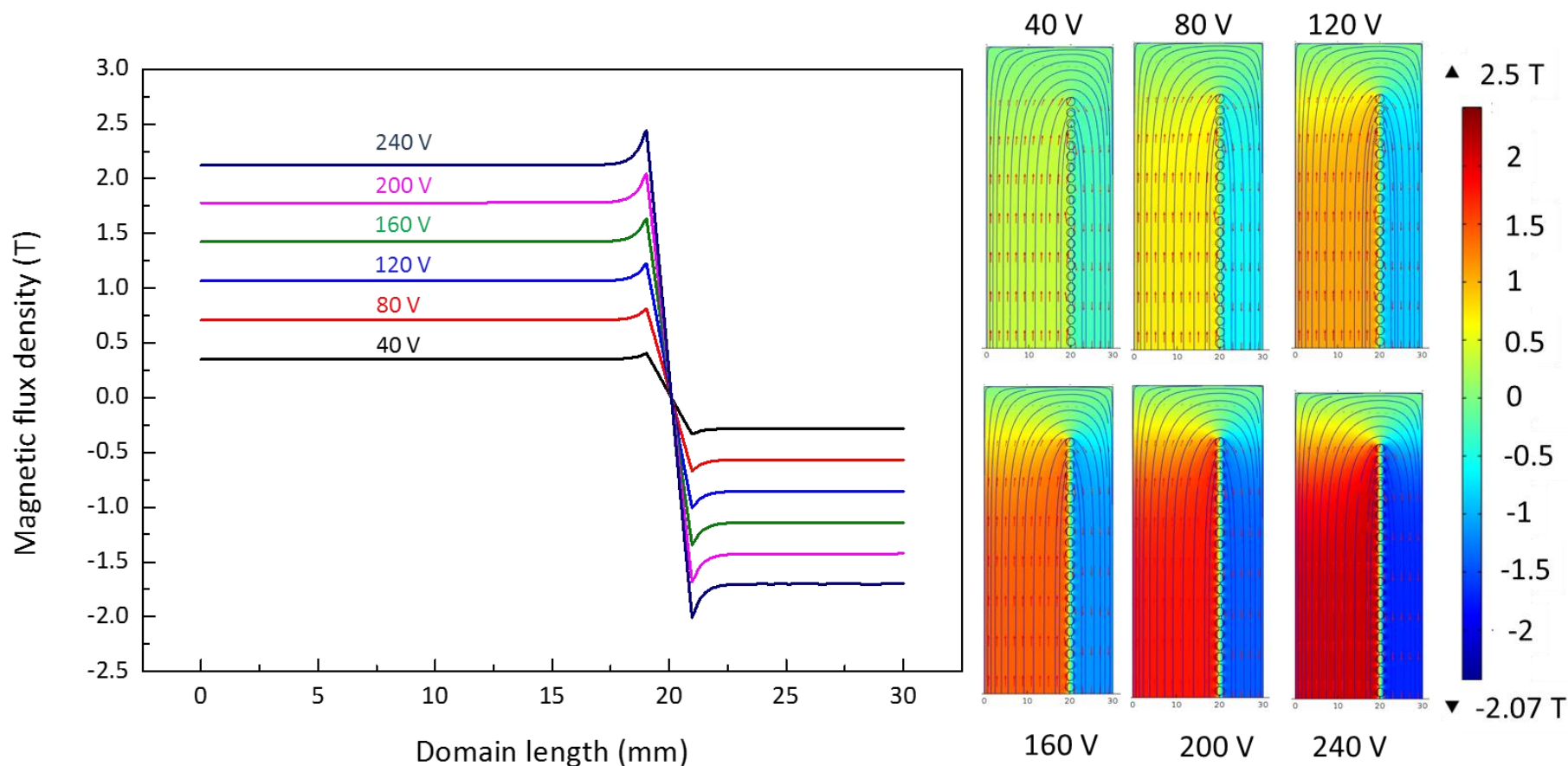


Fig. 6.3. The simulated magnetic flux densities using the discharging voltages of 40, 80, 120, 160, 200 and 240 V. The simulation was carried out by disabling quartz tube and the melt sub-domains (with $C=1$). The line profiles showed on the left are actually the simulated data along the line P4-P4 for each case, they are superimposed together for easy comparison.

Fig. 6.4 shows the simulated MFD profiles without melt superimposed with the measured profiles. The simulated and measured pulse profiles are very similar, but the peak values of the simulated pulses (with $C = 1$) are 10~15% higher than those of the measured ones (Fig.6.4a). This is because that, if $C = 1$ is used in the modelling, any possible energy loss, such as the generation of joule heat [195], in the discharging circuit and the coil was not considered. To take the energy loss into account, the compensation coefficient, $C=0.85$, was assumed in Eq. 6.2, and the results (Fig.6.4b) show that, the simulated pulses at all different voltages almost matched the measured ones with the peak values summarised in Table 6.2. The corresponding FWHM for each case was measured at 0.25, 0.45, 0.55, 0.65 and 0.70 ms, respectively. The differences of the peak values between the measured and the simulated MFD for all the discharging voltages are within 2%. This indicates that the designed EMP device has an energy conversion efficiency of 85%, i.e. 85% of the stored energy is transferred as the pulse energy into the melt.

Moreover, Fig. 6.5 and 6.6 show the simulated MFD distributions (with $C=0.85$) of both cases, 1) without tube and melt and 2) with the tube and melt sub-domain included, respectively. To compare the difference of the simulated results with and without the tube and melt sub-domains, Fig. 6.7 plots and superimposes the MFD pulse profiles extracted at point P4 for each case with different discharge voltages. The pulse profiles created by the same discharge voltage are very similar, however the peak values of the MFD for the cases without tube and melt are slightly lower than those of the cases with pulse. The comparison is summarized Table 6.2.

Obviously, the presence of the quartz tube and melt increase the peak magnetic flux density to 6 %. Moreover, the peak value of the simulated magnetic flux density increase linearly with the increase of the discharge voltage as clearly demonstrated in Fig. 6.8 with the slope of 8.3 mT/V for the case of without melt and 8.8 mT/V for that case of with melt in the simulation

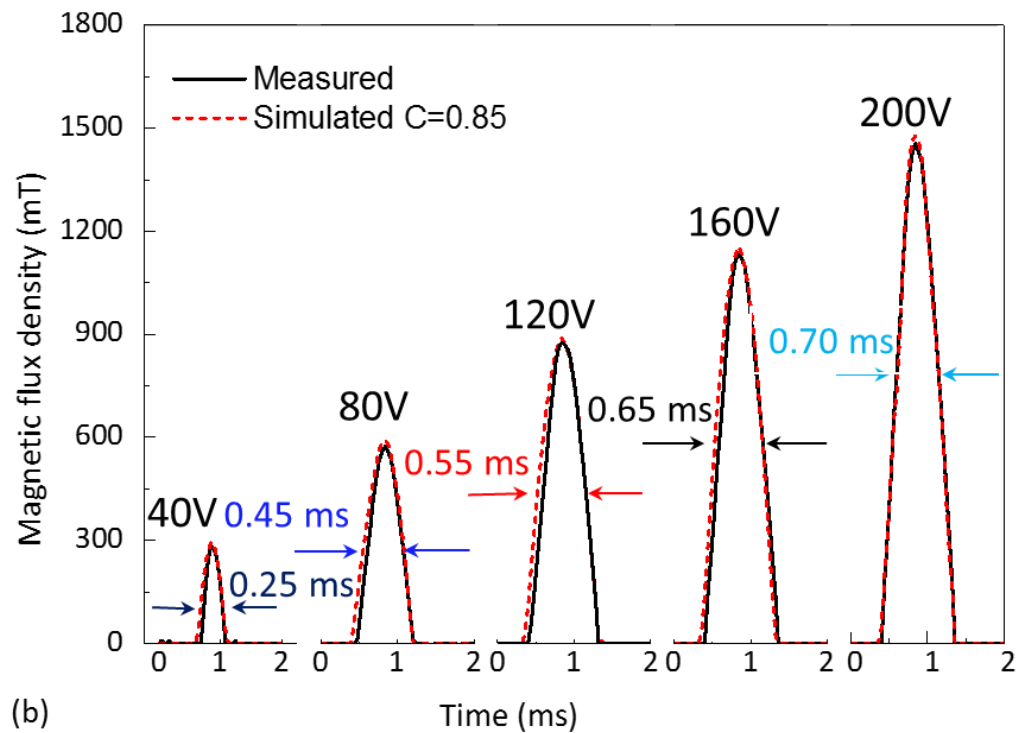
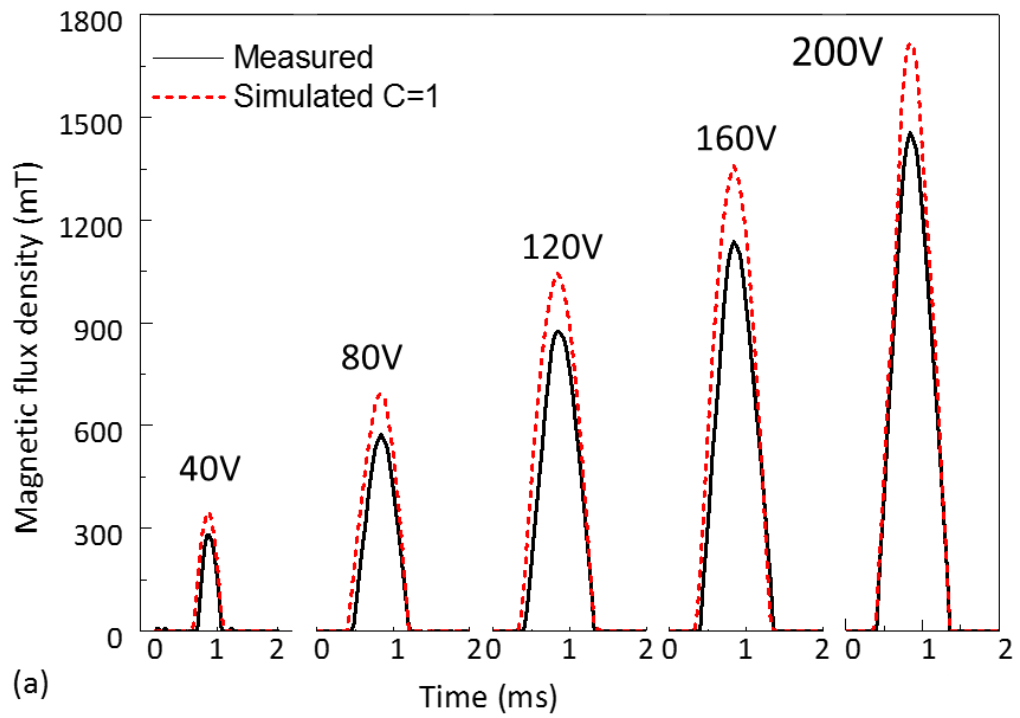


Fig. 6.4. Comparison of the measured and simulated magnetic flux density profiles with (a) $C = 1$, and (b) $C = 0.85$.

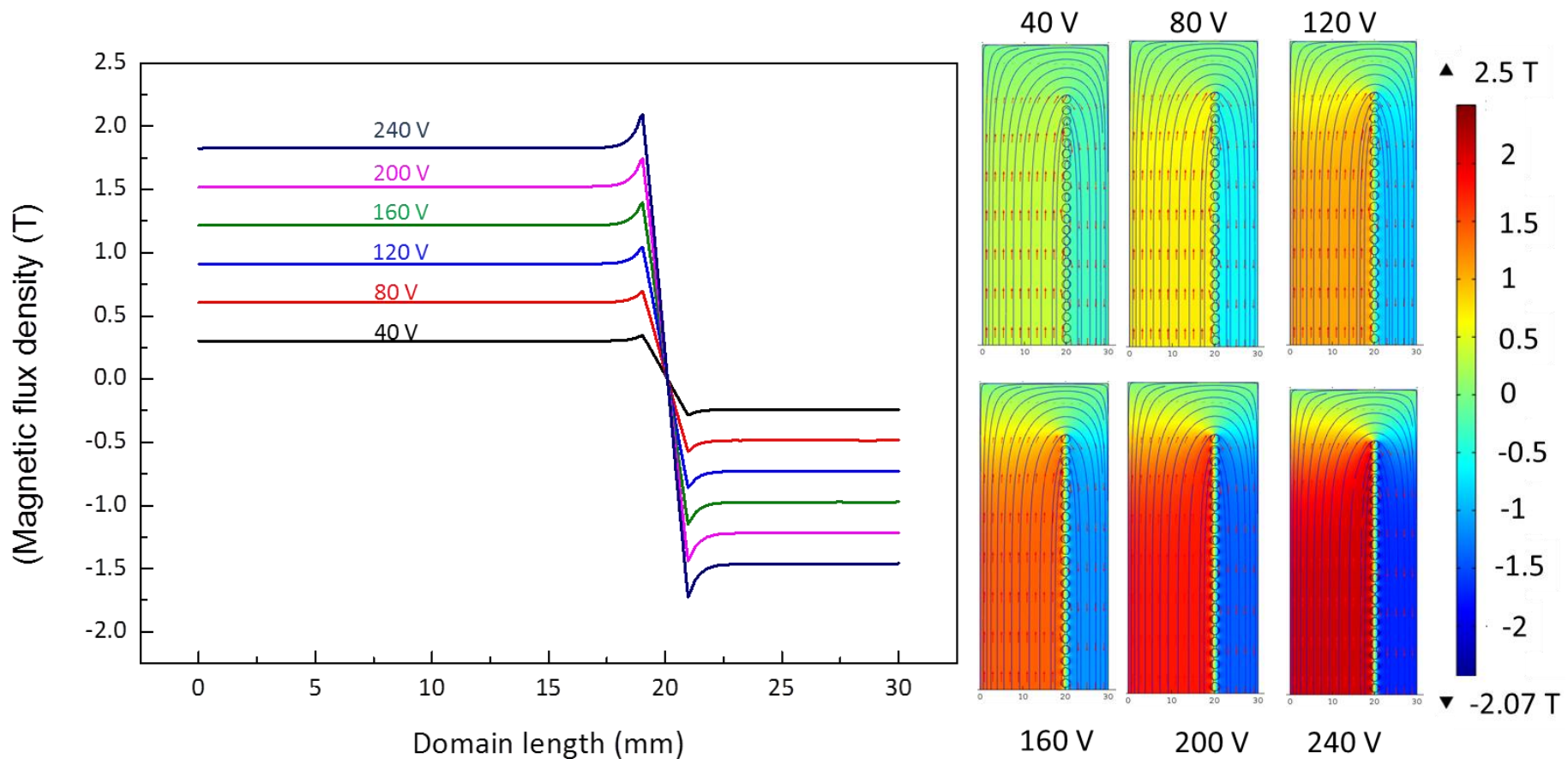


Fig. 6.5. The simulated magnetic flux densities using the discharging voltages of 40, 80, 120, 160, 200 and 240 V. The simulation was carried out by disabling quartz tube and the melt subdomains (with $C=0.85$). The line profiles showed on the left are actually the simulated data along the line P4-P4 for each case, they are superimposed together for easy comparison.

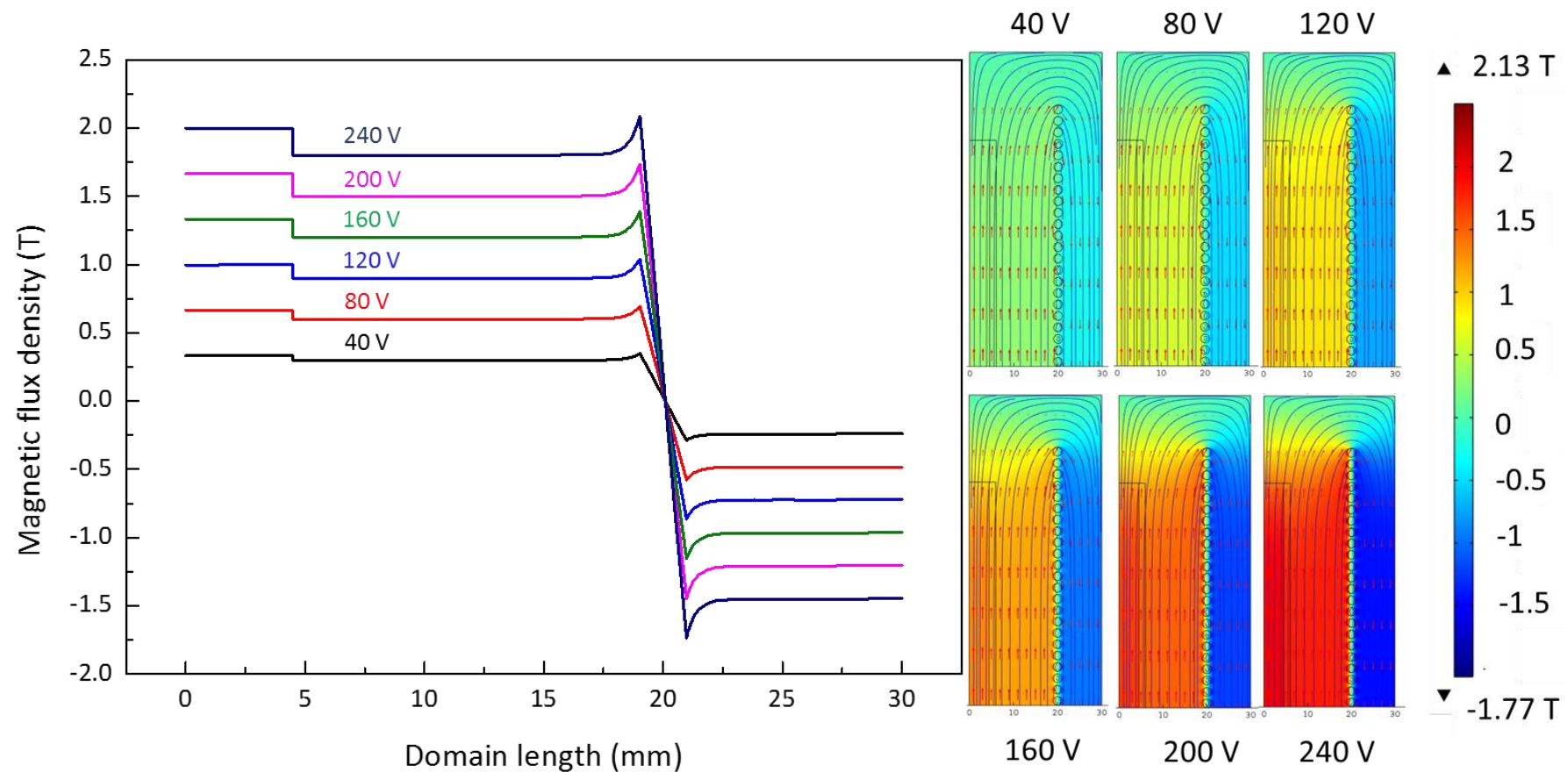


Fig. 6.6. The simulated magnetic flux densities using the discharging voltages of 40, 80, 120, 160, 200 and 240 V. The simulation was carried out by enabling the quartz tube and the melt subdomains. The line profiles showed on the left are actually the simulated data along the line P4-P4 for each case, they are superimposed together for easy comparison.

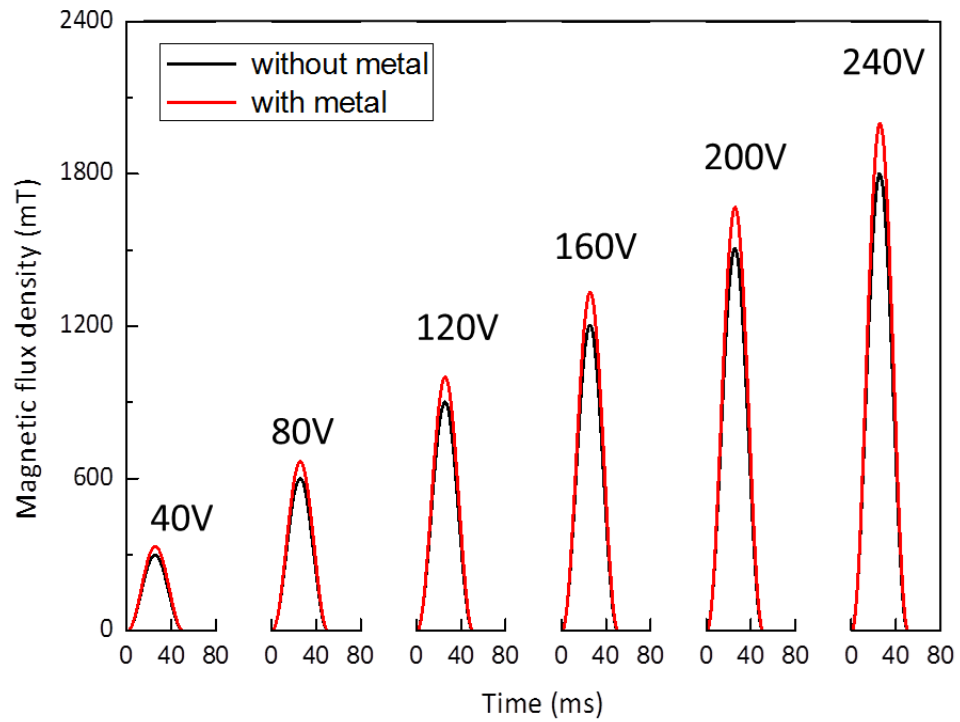


Fig. 6.7. The simulated magnetic flux density profiles versus the discharge voltages with and without the quartz tube and the alloy melt.

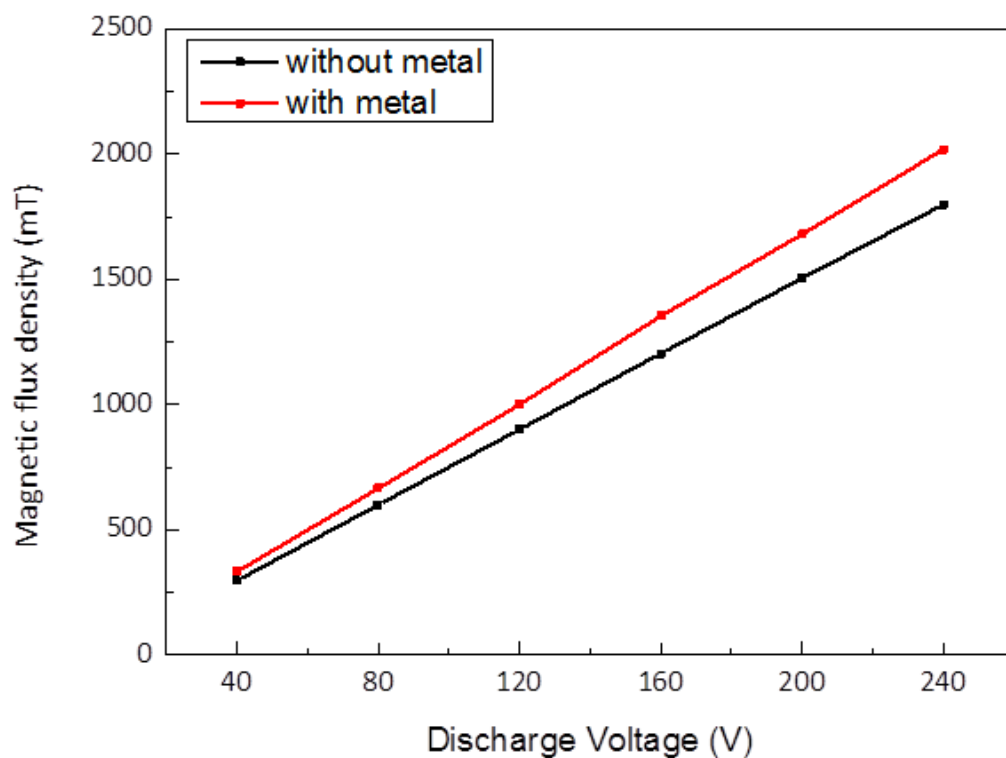


Fig. 6.8. The simulated magnetic flux density peak value as a function of the discharge voltage with and without the quartz tube and the alloy melt.

6.6.2 The induced currents

Fig. 6.9 shows the simulated distribution of the induced current density (ICD) inside the alloy melt. The simulation was carried out with the quartz tube and alloy melt domain enabled, and the magnetic flux density with $C=0.85$ were used as the input for Eq. 6.4. Apparently the ICD concentrated along the boundary of the melt near the wall of the quartz tube (sub-graph in Fig. 6.9), and the ICD increases with the increase of the discharge voltage. The data at point, P5 were chosen to plot the peak profiles of the ICD at different discharge voltages (Fig. 6.10). Obviously, the peak value increases proportionally with the discharge voltage because the MFD increases with the similar rate.

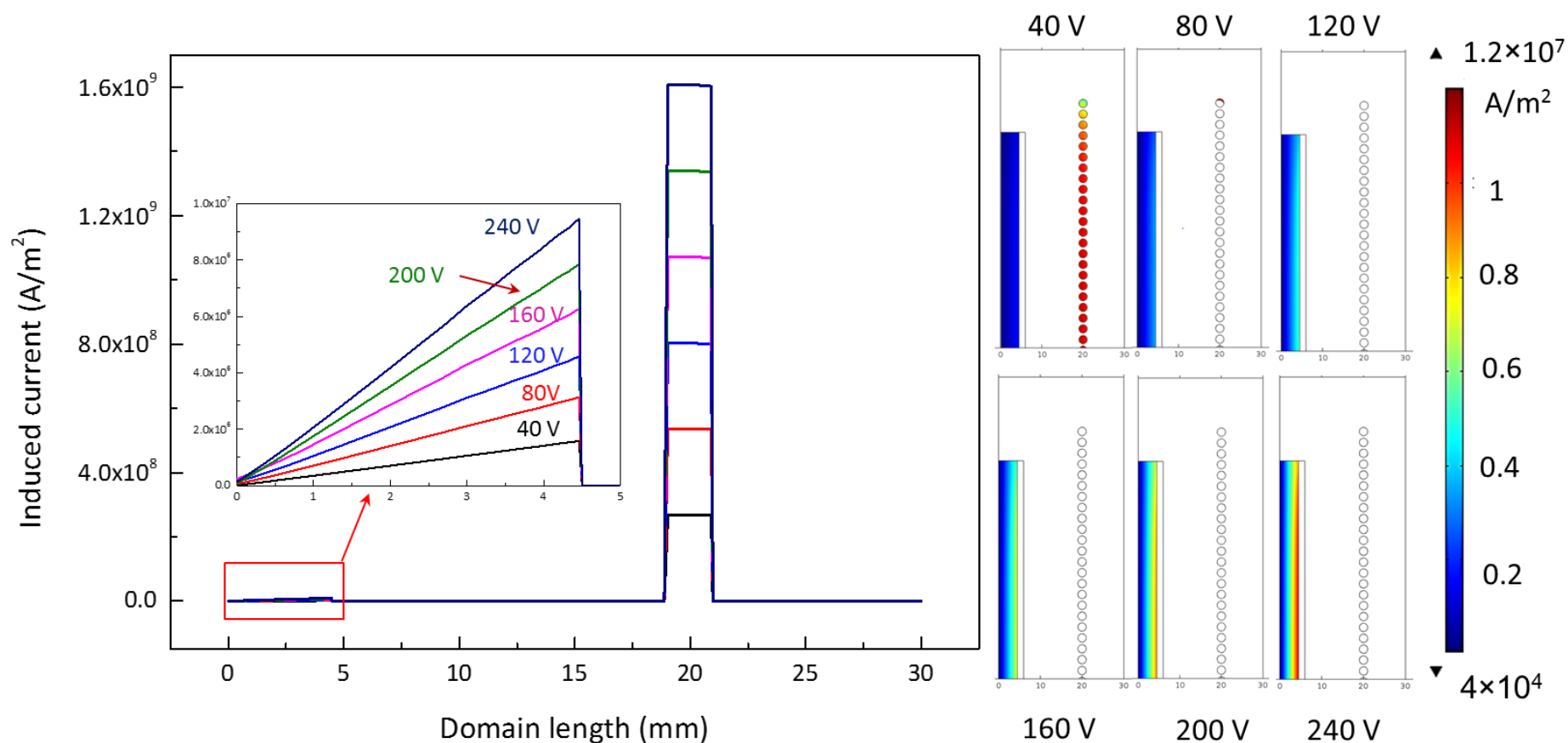


Fig. 6.9. The simulated induced current density distributions inside the alloy melt for the discharge voltage of 40, 80, 120, 160, 200 and 240 V respectively. The line profiles showed on the left are actually the simulated data along the line P4-P4 for each case, they are superimposed together for easy comparison.

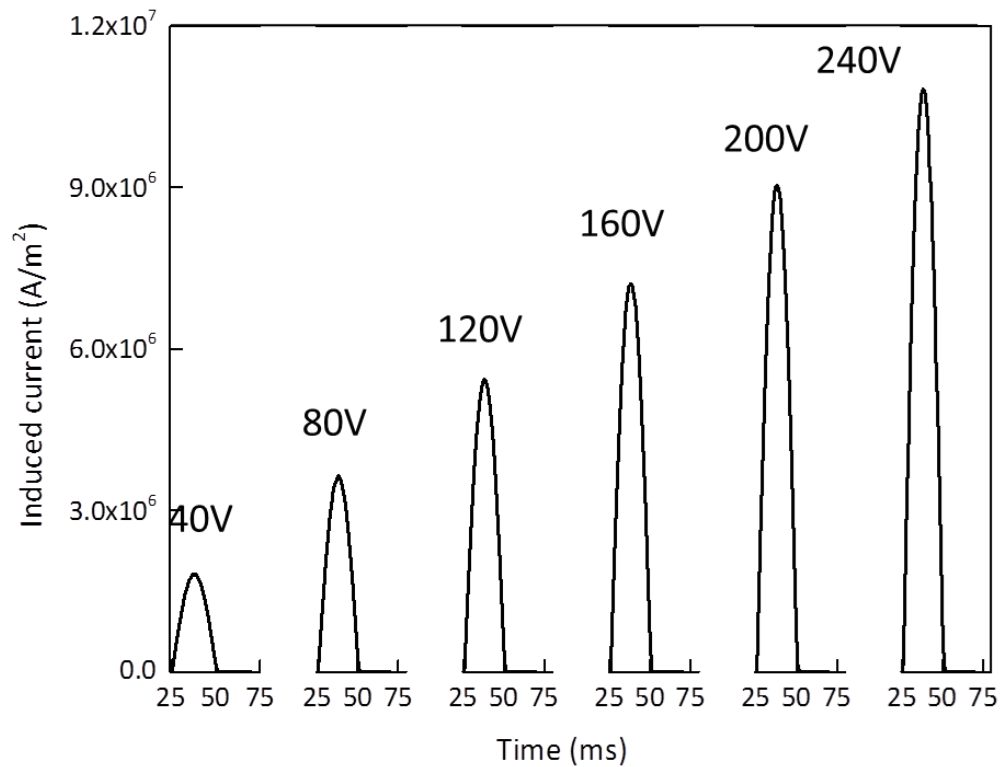


Fig. 6.10. The simulated induced current density profiles and peak values for the discharge voltage of 40, 80, 120, 160, 200 and 240 V, respectively.

6.6.3 The Lorentz force

Using the MFD and the ICD obtained above as the inputs for Eq. 6.5, the Lorentz forces inside the alloy melt (F) were calculated and showed in Fig. 6.11 for different discharging voltages using the same computational domain and mesh structure. The simulated data at point, P5 were extracted to show the Lorentz force profiles and its peak value (Fig. 6.12). The results show that, as the discharging voltage increased from 40 to 240 V, the Lorentz force increased from 2.4 to 89 N. Furthermore, the force is much stronger at the outer boundary layer of the alloy melt, and point inwards and then outwards in the one pulse cycle, i.e. ~ 35 ms as seen in Fig. 6.13, the force superimposed with one pulse cycle profile showing the direction of force according to change of the input pulse and time.

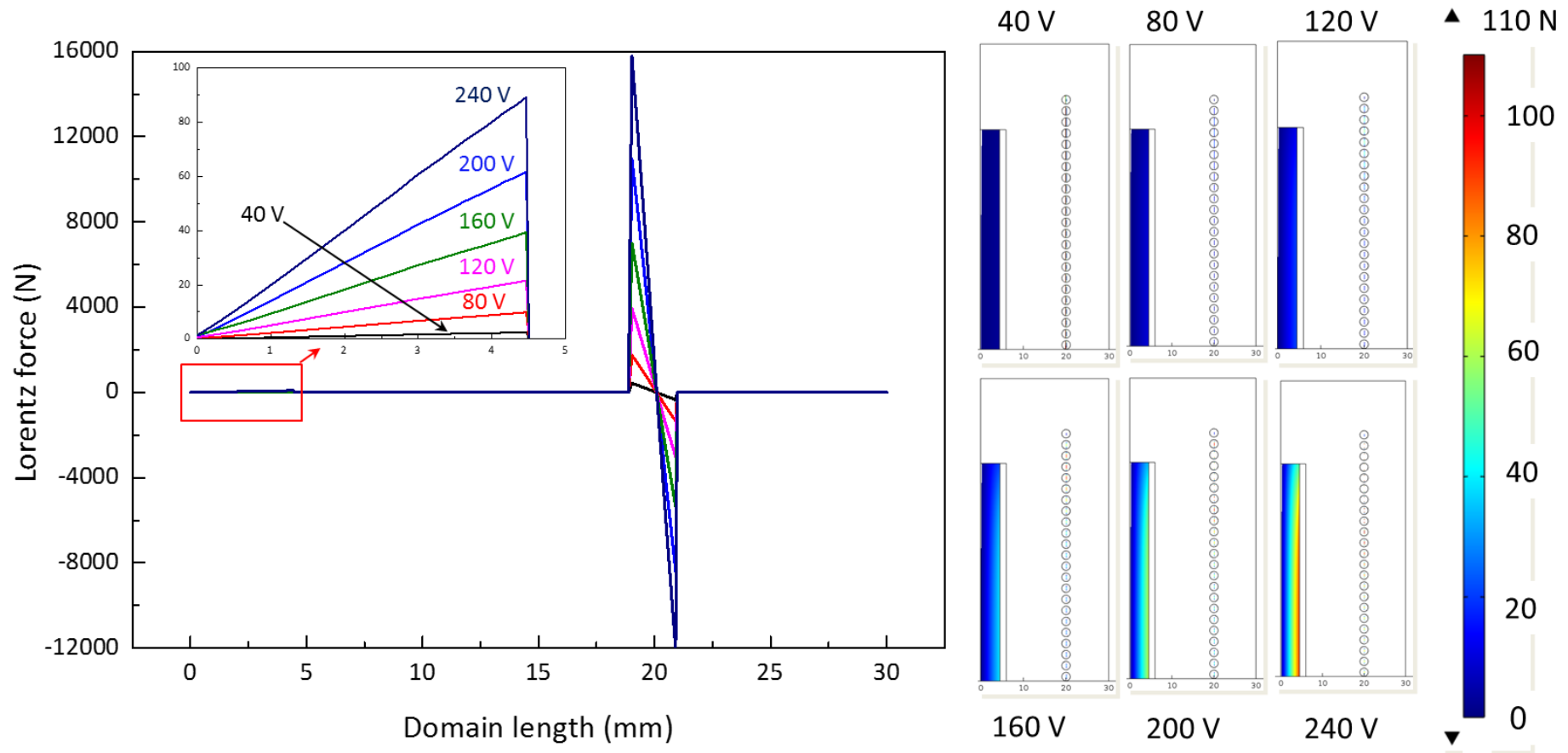


Fig. 6.11. The simulated Lorentz force distribution acting on the alloy melt for the case of 40, 80, 120, 160, 200 and 240 V discharge voltage. The line profiles showed on the left are actually the simulated data along the line P4-P4 for each case, they are superimposed together for easy comparison.

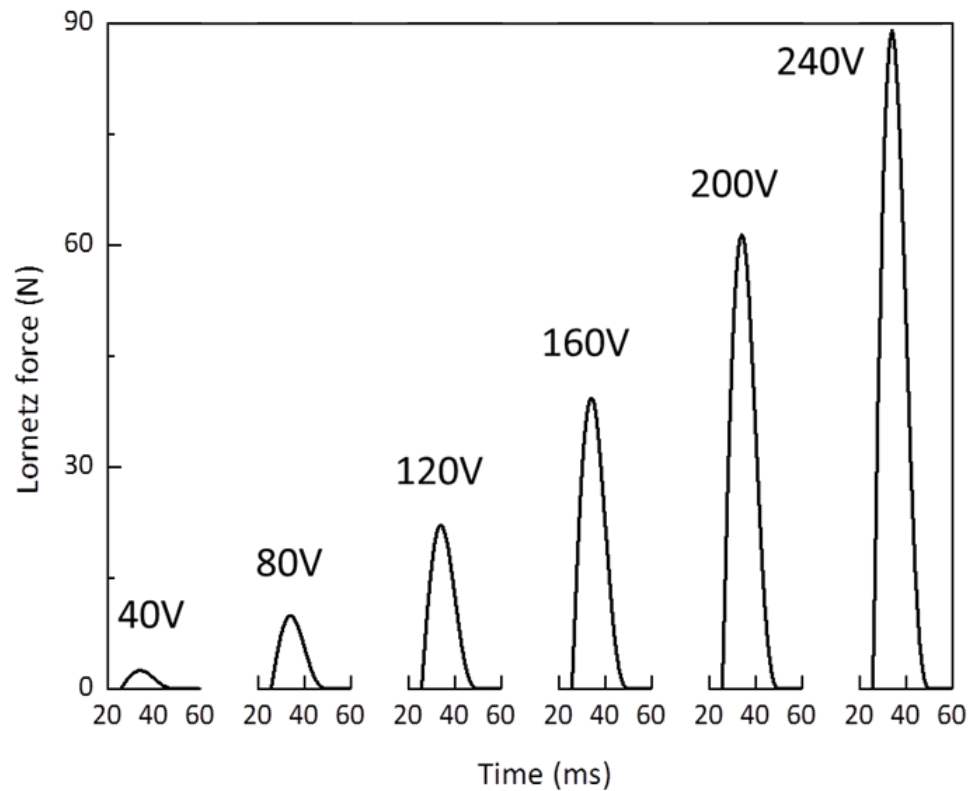


Fig. 6.12. The simulated Lorentz force profiles and its peak values acting on the alloy melt at point P5 for the case of 40, 80, 120, 160, 200 and 240 V discharge voltage

Fig.6.13 shows that the Lorentz force increased related to the increase of amplitude of the input pulse current, the direction point towards centre of the melt. Until the amplitude reached the maximum, the increase of Lorentz force was zero, the force direction had two directions (towards centre and another towards the side) according to the balance of increase and decrease of amplitude. Finally, the force decreased related to the decrease of amplitude of the input pulse current, then the direction of force changed direction toward the side.

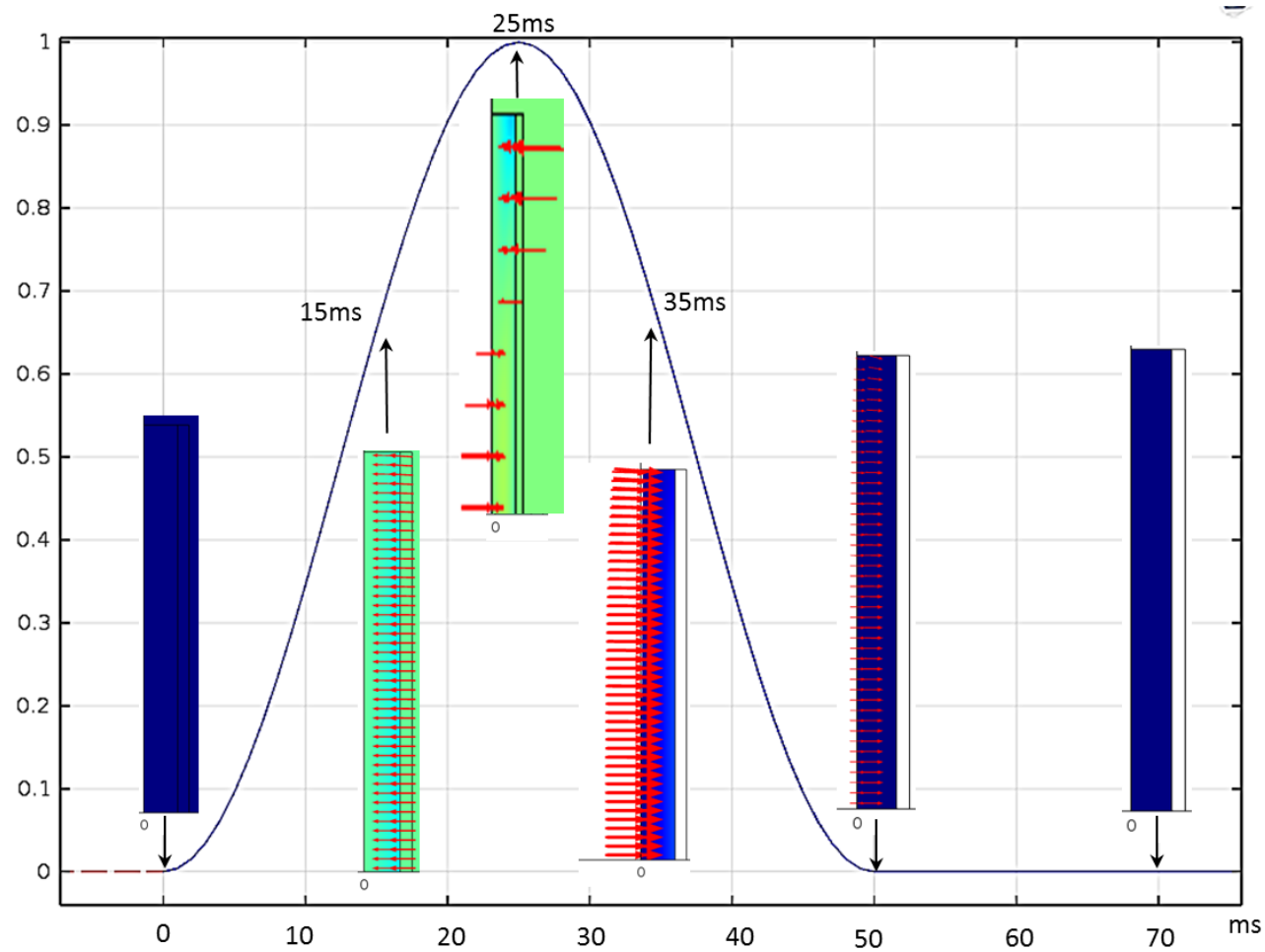


Fig. 6.13. The change of the direction of Lorentz force in one pulse cycle for the case of 120 V.

6.6.4 The velocity field inside liquid metal

The Lorentz forces obtained above were used as the volume force in Eq. 6.7 to simulate the velocity field of the alloy melt using the fluid flow module of available from Comsol for the case of 40, 80, 120, 160, 200 and 240 V discharge voltage.

Fig. 6.14 illustrates the melt flow velocity field at different time step within one pulse cycle. The velocity field shows that, in general, the lower and upper half of the melt inside the quartz tube have a similar flow pattern with a circulating flow starting from the central region (at 0 mm region) of the tube and move upwards and downward at the same time. Apparently, the velocity field also behave cyclically following the frequency of the field applied, i.e. 1 Hz in this case. Fig. 6.15 shows the changes of the melt velocity field with one pulse profile at the time step.

Fig. 6.16 shows the changes of the melt velocity field with the increase of the discharge voltage at the simulated time step of 0.035 s (when the maximum Lorentz force occurred). Increasing discharge voltage from 40 V to 240 V results in the increase of the maximum velocity from 0.02 to 0.42 m/s accordingly. However, the simulation shows that, in all cases, and for this particular quartz tube geometry, higher velocity always occur at the top and bottom central regions of the tube. In the majority of the middle section of the tube, the flow velocity is $\sim 50\%$ of the maximum velocity found at the top and bottom section.

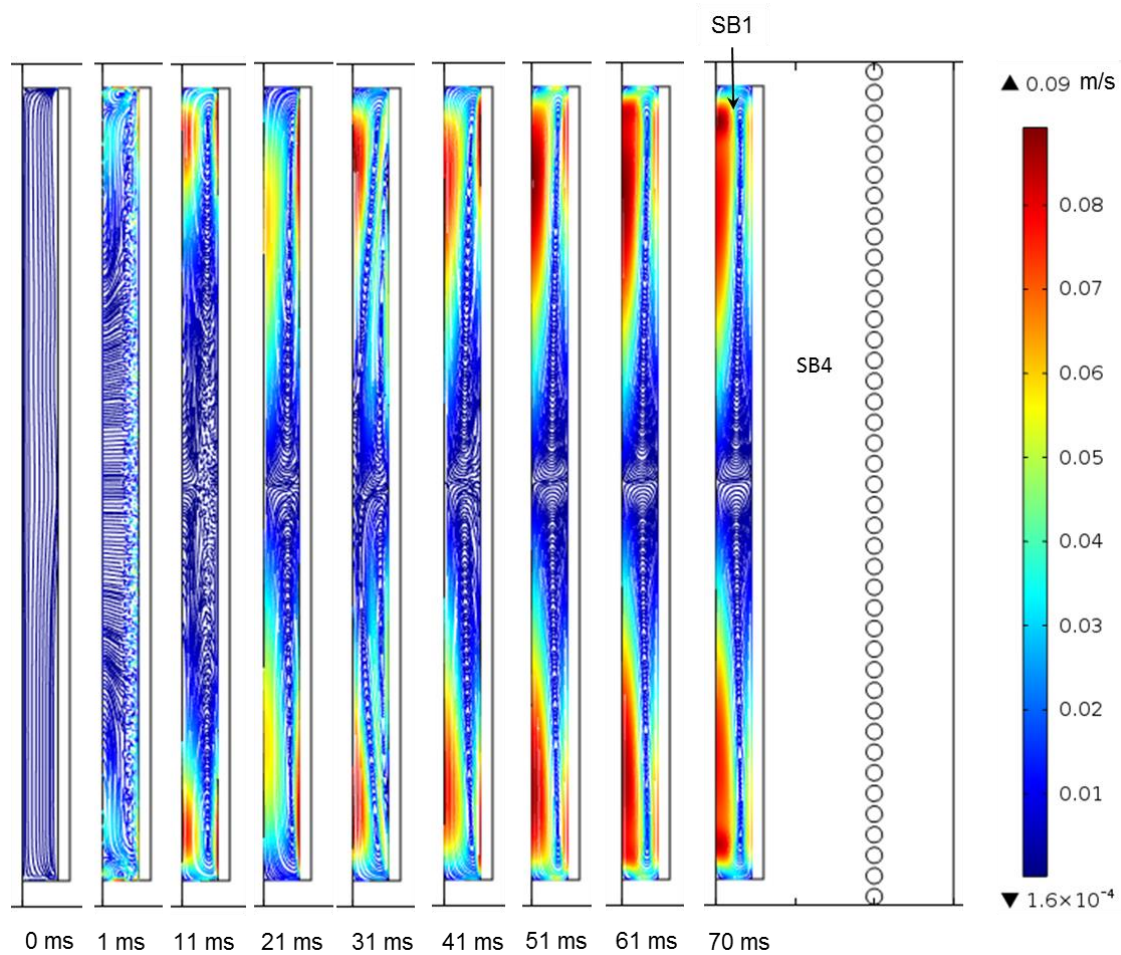


Fig. 6.14. The simulated velocity fields inside the alloy melt for the case of 120 V discharge voltage.

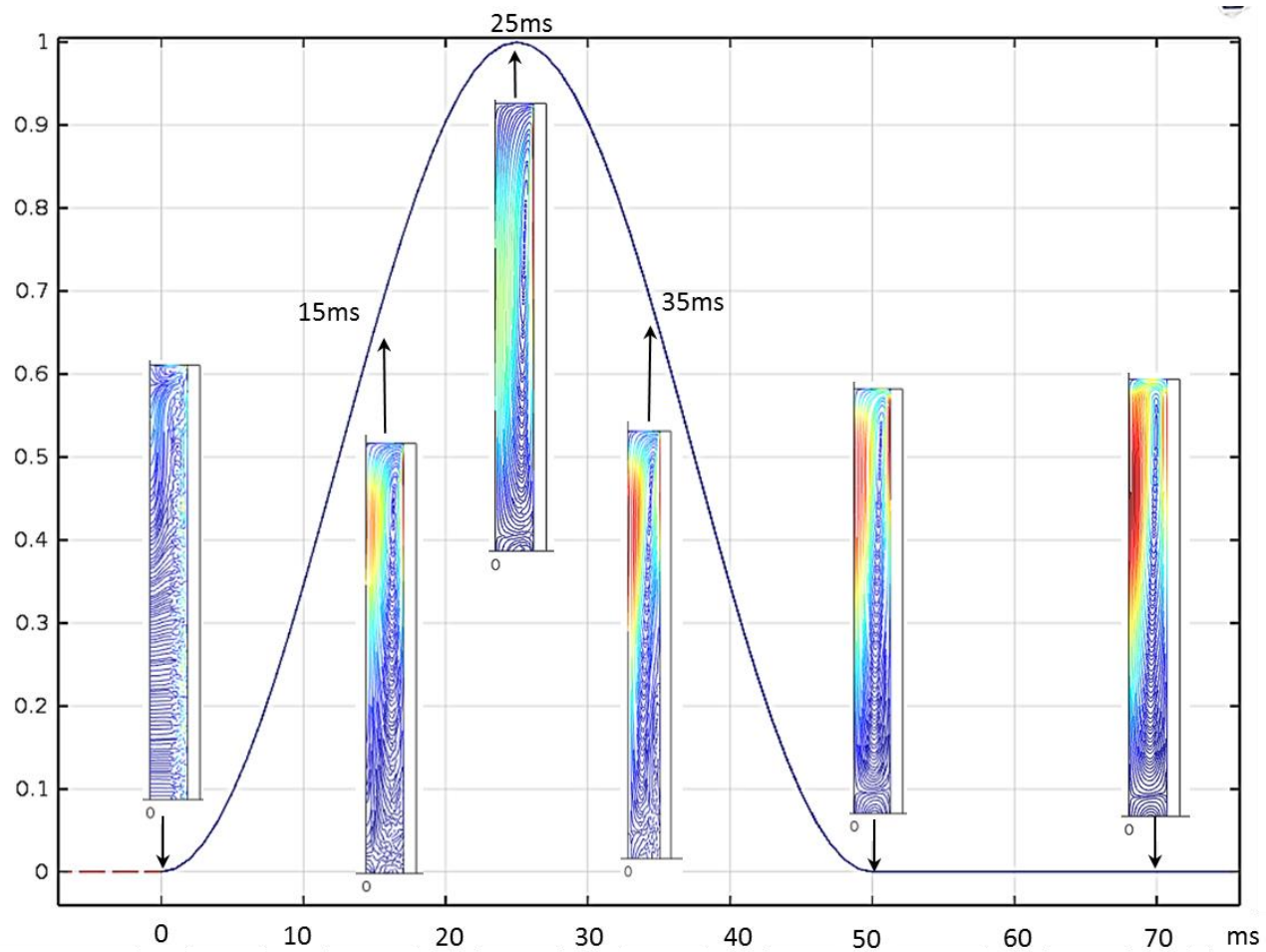


Fig. 6.15. The simulated velocity fields inside the alloy melt in one pulse cycle for the case of 120 V

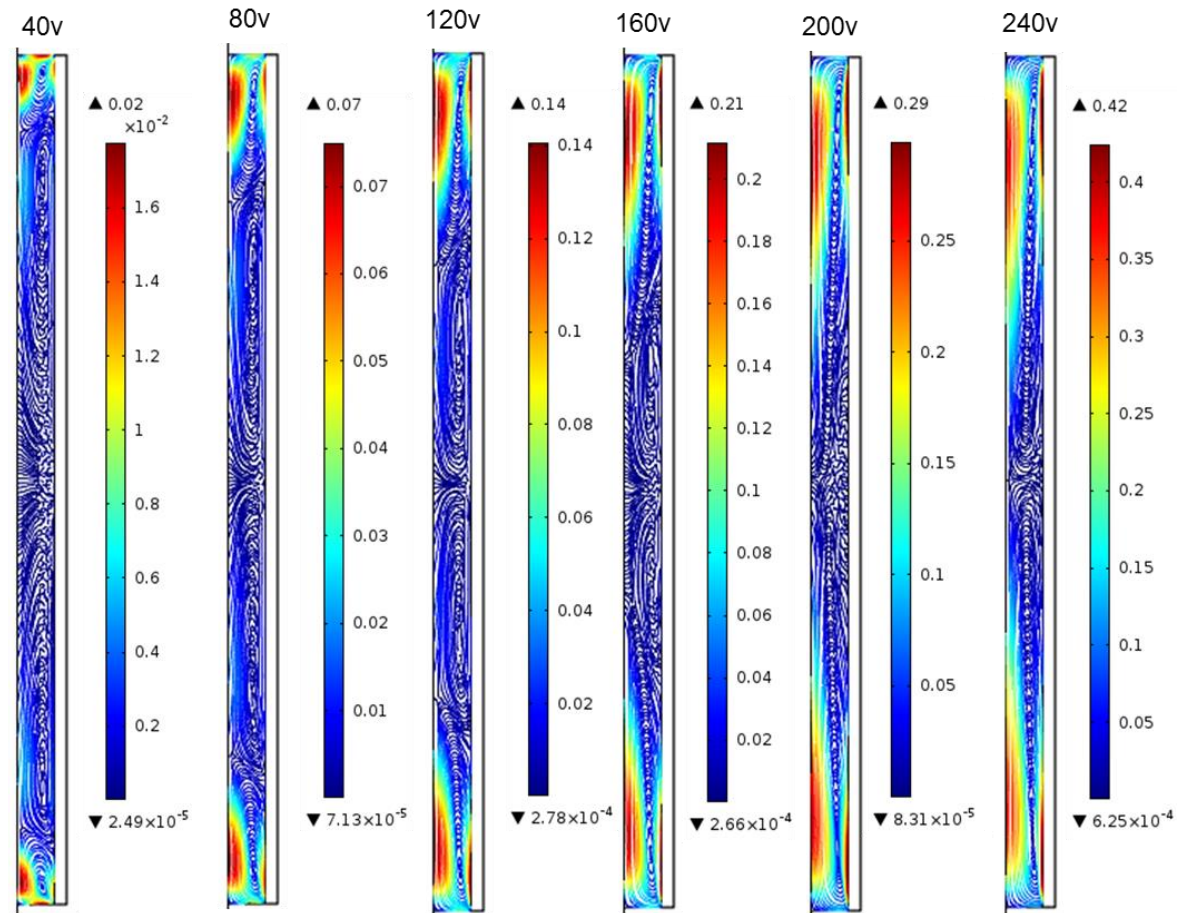


Fig. 6.16. The simulated velocity field at the simulated time step of 0.035 s (when the maximum Lorentz force occurred) for the discharge voltage of 40, 80, 120, 160, 200 and 240 V, respectively.

6.7 Summary

The finite element based model was developed to simulate the magnetic flux density, induced current and Lorentz force of the pulse magnetic field. The simulated magnetic flux densities were compared with the measured data, and the model was therefore validated. The results show that the simulated magnetic flux densities were about 10-15% higher than measured ones. A compensation coefficient was introduced to take into account the effect of energy loss during the generation of the pulse electromagnetic field. As a result, the simulation with the energy loss considered matched the measured data with an error of 2%.

After validating the model, the induced currents, Lorentz forces and the corresponding velocity fields inside the alloy melt produced by different discharge velocity were simulated and presented.

Chapter 7 : Discussion

By analyzing the large amount of experimental and computational data generated from this research, and comparing the results from this research with those from other researchers in this field published in the open literatures, this chapter gives very detailed discussions on the significance of the research findings, and the new scientific contributions to this very important research field.

The discussions are focusing on the novelties of the EMP device developed, the links between the results obtained from the pulse electric current and the pulse electromagnetic field, and how the simulation and modeling help to understand the experimental results more quantitatively. The dominant control parameters for achieving sensible grain refinement using the pulse electromagnetic field method are also presented.

7.1 The novelty of the EMP device

The EMP device (as described in Chapter 4) is designed for conducting pulse electromagnetic field solidification experiments in university laboratory and Synchrotron X-ray beamlines. Comparing to the many other similar apparatus or devices in open literatures as reviewed in Chapter 2, the key novelties of this EMP device are:

7.1.1 Programmable pulse control

A trigger unit linked with a Thyristor switch is designed and embedded between the charging and discharging units (Fig. 4.3, 4.4, 4.7 in Chapter 4) to control the charging of the capacitor bank, and the amplitudes, durations and frequencies of the pulse current discharged into the working coil. The trigger unit is the key control unit to adjust the amplitude of pulse current and discharge frequency. As shown in Eq. 4.4, the maximum amplitude of a

pulse current is achieved when the charging time is $\geq 5 \times R_1 C$. If less than $5 \times R_1 C$ is used, lower pulse amplitude can be realized as shown in Fig. 4.6 and Fig. 7.1. The discharge frequency of the pulse can be set by the solid state relay (Fig. 4.6 in Chapter 4). The characteristic discharging time of the pulse for this EMP is $\sim 5 \times Z C$ or ~ 0.5 ms; and the discharge frequency is defined by the combination of the charging time (T1) and relaxing time (T2) as shown in Fig. 7.1. By decreasing or increasing (T1+T2), different frequencies of the pulse can be realized from 0 to 10 Hz for this EMP device.

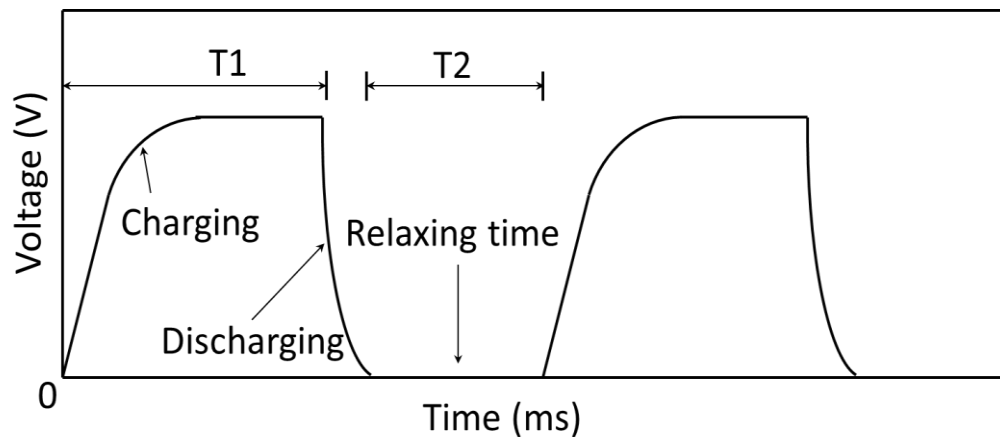


Fig. 7.1. The characteristic profiles for current charging and discharging.

7.1.2 Systematic and module-based design

The EMP device is systematically designed and manufactured with functional and upgradable modules with very flexible input and output parameters to suit a wide range of solidification experiments.

Firstly, variable input voltages are available, because of the use of a variac transformer to provide the charging power. This provides the possibility of using the EMP device with different power supplies of different voltages. In this case, the variac transformer (electricity supplied from the 240V mains in the laboratory) can deliver the variable input voltages in the range of 0-

270 V to charge the capacitor. Of course, large capacity variac transformer can be used if high voltage input power, e.g. 380V is used

Secondly, the module design of the capacitor bank allows the capacitance of the charging unit to be easily increased or decreased to suit the EMP device to different experiments, such as samples of different size and alloys, etc.

Thirdly, the working coil used in the pulse generating unit is made from 2 mm diameter enamelled copper wire. Mouldable mastic (see details in chapter 4) is used to cast and wrap around the copper coil to protect the coil from being overheated by the hot metal alloys during operation. From the temperature measurement showed in Chapter 5, it indicated that there is no obvious joule heating generated from this smaller copper coil to influence the sample during solidification. Therefore the EMP device can be operated safely without the use of water to cool the coil as in many other PMO research apparatus (Fig. 7.2).

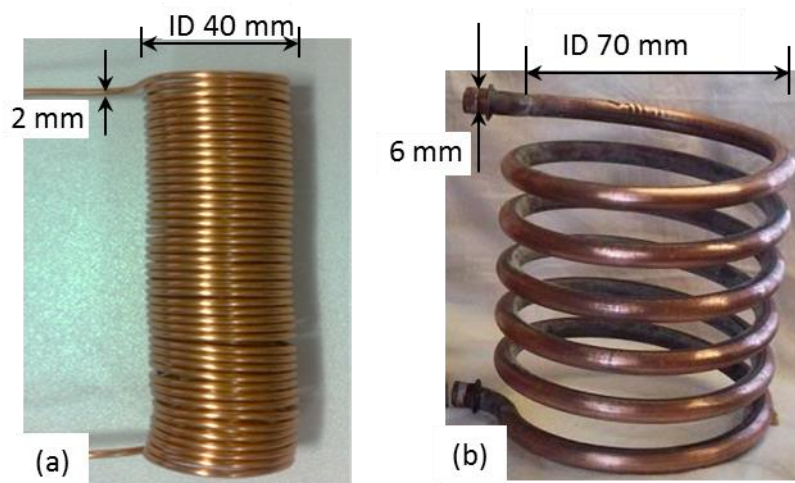


Fig. 7.2. The comparison of (a) the copper coil used in this research and (b) the hollow tube copper coil used for PMO experiments in other research

Fourthly, Glass tubes (quartz or borosilicate tubes) were used as the mould to contain to liquid alloys during casting while other researchers used ceramic or steel moulds. Quartz has very low electric conductivity compared to metals, therefore the induced currents generated inside the quartz tube

is very low and can be ignored as clearly showed in the simulation and modelling (Fig. 6.6 in Chapter 6). Consequently, the effects of the mould on the changes of solidification microstructures can be ignored. Compared to the ceramic or steel moulds coated with boron nitride coatings, quartz does not wet with the metal alloys, especially for Al based alloys, therefore coating is not needed, and basically there is no contamination to the alloy melt during melting and solidification. In addition, quartz has very low X-ray attenuation coefficient, ideal for being used as the mould to contain metal for doing in situ solidification research using X-ray.

Finally, EMP device uses very short pulse of ~ 0.5 ms duration each. Compared to the continuous electromagnetic stirrings or other methods reviewed in Chapter 2, it is a very energy efficient device, Chapter 5 demonstrated that, with the use of much less energy, it can achieve the similar results delivered by those very high energy consuming methods [47].

7.1.3 Advanced facility for in situ solidification research

The programmable capability allows very accurate pulse parameters to be used in the solidification experiments, and the synchronisation of the pulse parameters with other parameters and/or operation during the solidification experiments, such as the temperature of the melt, the withdrawal speed of the mould as detailed described in Chapter 5. Therefore, very accurate and detailed solidification experiments can be conducted using this device, especially it can be used in the Synchrotron X-ray beamlines to study in situ the evolution of solidification microstructures under different pulses in real time using radiography (similar to those explained in Chapter 3) and tomography techniques in the future.

The success of this device has led to the winning of 9 shifts (3 days) of synchrotron X-ray beam time from the beamline TOMCAT of PSI to study in situ the solidification microstructure evolution under pulse magnetic field

using X-ray tomography, and the experiment will be conducted in 10-13 June 2015.

Based on the advanced feature of this device, a beam time proposal was also submitted to DLS to apply further beam time for in situ solidification studies of different alloys under pulse electromagnetic field.

7.2 Validation of modeling versus experiment

For any simulation or modelling, it is very important to validate the simulated results against the experimental measurements to provide confidence on how accuracy the simulated results are. In this research the magnetic flux is the most important parameter for all experiments. Therefore comprehensive measurements (in Chapter 4) and simulation (in Chapter 6) were carried out. Here the comparison between the measured and simulated results is made for the purpose of validating the simulations.

The magnetic flux densities at different discharging voltages were measured using a Gauss meter as shown in Fig. 4.15 of Chapter 4. All measured magnetic flux densities have similar profiles with the Full Width at Half Maximum (FWHM) for all cases with duration of less than 1 ms (Fig. 4.15) The characteristics of the pulses are, of course, governed by Eq. 4.6. It clearly shows that as the discharging voltage increased from 40V to 200V, the measured magnetic flux density peaks increase linearly (Fig. 4.16).

Fig. 6.4a shows that all simulated magnetic flux densities are about 10-15% higher than the measured ones when the compensation coefficient $C=1$ is used. However, when $C= 0,85$ is used (Fig. 6.4b), the simulated profiles and peak values match the measured ones for all cases. This implies that there is 15% energy loss for the EMP device, most likely due to the joule heat generated when releasing the pulses. This also provide a systematic validation for the simulation, hence, all simulations relevant to the experiments are carried out using $C= 0,85$. In this way, all variables simulated in the pulse electromagnetic field, including the induced current,

Lorentz force and velocity field can be used with much confidence on helping to interpret the phenomena observed from the solidification experiments and the microstructural characterization.

7.3 Dendrite growth in a static magnetic field with PEC

The real-time image sequences presented in Chapter 3 (summarized in Table 3.3) allow the dendrite growth and fragmentation behaviour in a static magnetic field with the applications of different pulse electric currents to be understood more precisely as discussed in this section.

7.3.1 Dendrite fragmentation due to natural convection

Fig. 3.6 shows a dendrite tip is broke off, flowing up into the liquid zone under the bouncy force (without the application of a PEC). The difference in the solute ahead of the dendrite cause the dendrite to flow up as the dendrite is lighter than the solute around it. In this case, the dendrite tip detached from its branch is a self-fragmentation phenomenon, Similar phenomena were observed by Ruvalcaba [196] and they are common in solidification as observed and discussed by Liotti [67]. The dendrite was fragmented due to the solute liquid trapped around the root of the dendrite becomes enriched in copper as solidification proceeds, a solute-enrichment-driven remelting process at the root, and this is enhanced by the effect of natural convection. The dendrite root became small and finally detached. The dendrite flew up to the liquid zone by the buoyant force, due to the difference in density of the melt. This driven force was discussed by Mathiesen [99] during the in situ observation of Al-20%Cu alloy.

7.3.2 Enhanced melt flow due to PEC

The image sequence V2 shows that a dendrite tip fragmented from it's own branch and flew up into the liquid zone again driven by buoyant force. However, the dendrite was showed to oscillate cyclically while flowing up. The cyclic movement happened when the PEC was applied (a current of 300

mA and 1 Hz since waveform), Fig. 3.9 shows the tracked path of the dendrite, and it followed the frequency of the PEC.

This is direct evidence that the fragmented dendrite experienced the cyclic Lorentz force delivered by the interaction between the sine wave current and the permanent magnetic field due to the magnet. In addition, the liquid surround the dendrite also experienced the Lorentz force and flew according to the frequency of the Lorentz force, similar to the movement of the fragmented dendrite. This further confirms that although the Lorentz force created in this case is very small (0.3 mN), it still can produce convection flow in the melt to move the melt and any nuclei and growing crystals in the melt as argued by Mazuruk [78].

7.3.3 Effects of PEC on dendrite in semisolid region

The images (V3-1 to V3-8 in Fig 3.11) show the directional growth of a series of parallel dendrites under the controlled temperature gradient. Firstly, the dendrites grew rapidly and the dendrite length increased quickly, then they slowed down and finally reached a near constant value (Fig. 3.12).

After the dendrites growth was stabilized, a PEC was applied a small dendrite tip was fragmented and flew up (see V3-10). The moving path of dendrite is shown in Fig. 3.15, moving up while cyclically in the horizontal direction as the 1 Hz Lorentz force is acting on the dendrite tip.

It is interested to see that the fragmented dendrite tip is from the dendrite that has a wider gap with its neighbouring dendrite. This space allows the vibration of the dendrite to be easily seen (Fig. 3.11). The simulation of Guo [197] showed that on the top of the dendrite front, melt flow circulation was strong, more easily causing interdendritic flow between the dendrites below, leading to more frequent breaking ups of dendrites. This video in this case gives a strong evidence in this aspect.

7.3.4 Effects of PEC on solid dendrite arrays

Fig. 3.17a and 3.19a show two image sequences where solid dendrites arrays were subject to the vibration of PEC. The whole dendrites vibrated and the movement were tracked and plotted in Fig. 3.17b and 3.19b. The plots show that the dendrites vibrated related to the frequency of the PEC applied. The movement of the dendrites followed the given frequency of PEC. Difference in PEC frequencies lead to different vibration movement. At low frequency (1 Hz) the dendrite shook with high amplitude (long distance), at high frequency (10 Hz) the dendrite vibrated in a short distance. Both image sequences show that the Lorentz force can "vibrate" the dendrites, but cannot break them.

The evidence gathered from the in situ experiment demonstrate that the Lorentz force generated from the PEC applied can move the liquid melt, and the crystals floating in the melt, enhance dendrite fragmentation in the semisolid region, and vibrate solid dendrite arrays. However the Lorentz force in this case is still not enough to break the solid dendrite arrays. So for bulk alloy samples much strong force is needed to have sufficient effect on the microstructure. The next sections discuss the experiments by using the EMP device to generate stronger force to alter the solidification microstructures.

7.4 Solidification microstructures in pulse magnetic field

7.4.1 Effects of EMP on dendrite growth

Fig 5.7a and 5.8 show the samples made without EMP treatment. The alloys were melted and then withdrawn out from the furnace with constant speed into the EMP coil, but the EMP was not applied. Clearly, long columnar dendritic microstructures were formed. However, the dendrites are not perfectly parallel to each other because the furnace is not perfectly designed for achieving directional solidification.

Then, experiments with EMP using discharging voltages of 40V, 80V and 120 V were conducted. As showed by modelling, the magnetic flux density is uniform through the alloy melt in horizontal direction, but concentrates in the middle of the alloys in vertical direction. Li [198] argued that the magnetic flux is in parallel with the growth of dendrites, therefore does not affect much on the growth of dendrites.

However, the interaction between the pulsed magnetic field and the induced current generates Lorentz force pointing towards the centre of the melt [162]. As showed in the simulation, the induced current is concentrated along the edge of the melt, the Lorentz force is therefore also concentrate along the edge, decreasing exponentially towards the centre of the glass tube mould.

Fig. 5.9 shows that, using discharging voltage of 40 V, long columnar dendrites were formed, but the size of the main trunk is smaller compared to that without EMP. At 80V, a mixture of long columnar and some equiaxed (see Fig. 5.10) was presented. Finally at 120V (Fig. 5.11), equiaxed dendrites were presented in the whole volume.

It is obvious that the microstructure of the alloys changed from the columnar to equiaxed as the EMP discharge voltage increased from 40 to 120 V and the Lorentz force peak increased from 2.48 N to 21.5 N (Table 6.2) or 0.01 to 0.1 MPa. Clearly, more and more stronger force present in the central region of the liquid melt as the voltage increased, leading to the changes in the microstructure in the inner region as showed in the SEM images for the corresponding voltage cases (especially Fig. 5.9-11), Apparently, in the outer region of the sample, more smaller dendrites were found than in the inner region. As demonstrated in the cases of the in situ studies, the stronger force can break the dendrites or push the nuclei inwards from the mould surface during solidification, causing a complete homogenously refined grains in the case of 120 V.

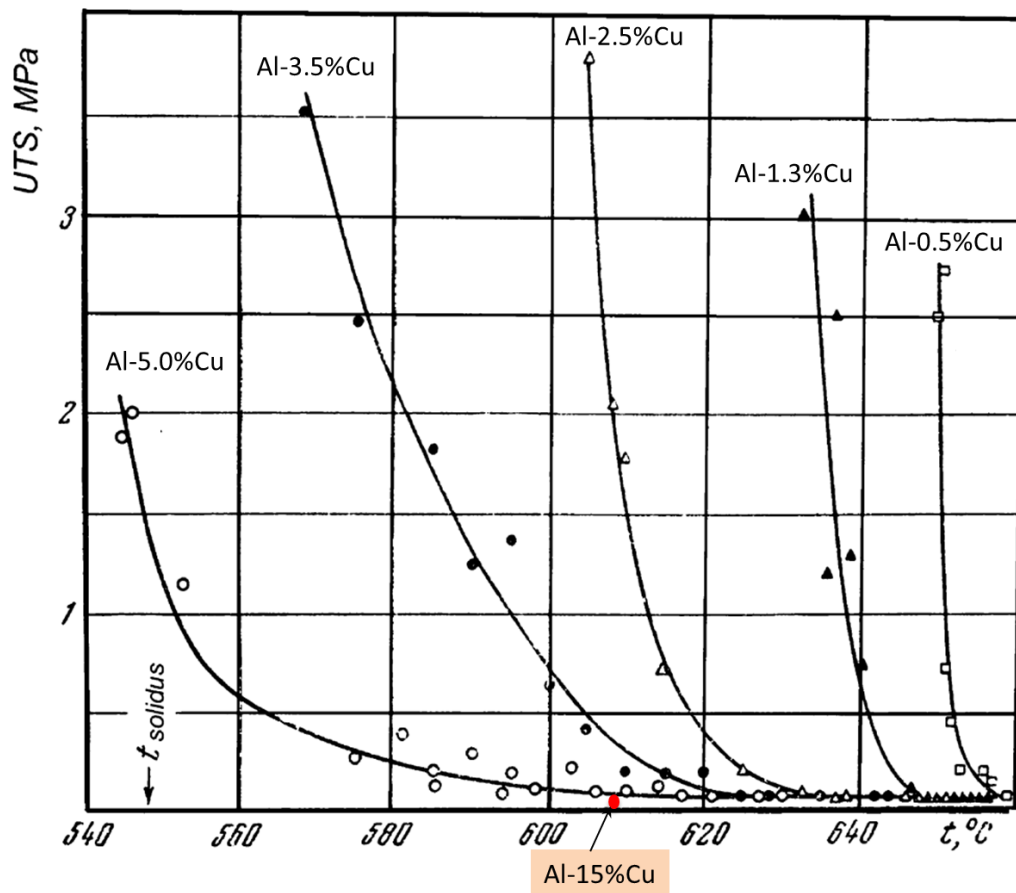


Fig. 7.3. The strength of the Al-Cu alloy as function of temperature [199].

Fig. 7.3 shows the strength of the Al-Cu alloy as function of temperature [199]. The strength of the Al-15Cu is well below 0.1 MPa at the casting temperatures used in this research, indicating that the Lorentz forces due to EMP is enough to disturb and/or break any growing dendrites during solidification for all cases studied here. At higher discharging voltage, the higher Lorentz force can effectively push the growing grains to move from outer surface into the centre of melt, and Fig. 5.11 clearly shows this evidence where more refined grain were found in the central region.

The force also stirs the melt, flowing (as seen in Fig. 6.14) and conveying the nuclei or floating crystals into other region of the melt [72]. The crystals grow during floating with the liquid metal until it solidified so that the random orientated grains formed. The convection flow surround the dendrites also promote dendrite remelting, and if the flow is strongly

circulating in the bulk liquid, a uniform temperature distribution in liquid can be generated. This phenomenon will lead to the generation of nuclei uniformly distributed in the bulk liquid. All above help the formation of the equiaxed grain structures [200].

The effect of the pulse is confirmed by a dedicated experiment where the pulses were applied only onto the lower half of sample, but not apply to the upper half of the sample (Fig. 5.20). The results notably identified that the lower part of the sample has small dendrites while columnar dendrites are presented in the upper part of the sample because after the EMP stopped, the growing dendrites from the lower half continued to grow into columnar dendrites without interruption and any blocking.

7.4.2 Effects of EMP on the growth of intermetallic phases

Fig. 5.14 shows that, without EMP, the primary intermetallic phases (θ phases) formed long and unidirectional morphology. The θ phases were quite parallel to each other and grew against gravity. Moreover, the θ phases contain more Cu, and so the majority of them sink to the lower part of the sample as clearly seen in Fig. 5.14.

Fig. 5.15 shows that the primary θ phases became shorter with EMP applied. Most of the long θ phases changed to a shorter phase and exhibited a periodic pattern which is the result of the disruption caused by frequent pulses.

Magnetic flux actually uniformly distributed in the primary and eutectic phases. Zhu [201] studied and stated that the θ phases are forced to grow in the same direction in the high magnetic field (10 T) in order to decrease the magnetization energy. However, in this work, the magnetic flux density is lower than 10 T and in a pulsed form (a short time of magnetic field comparing with Zhu's work), the θ phases were showed to be more affected by the pulsed force. Fig. 5.15 provides strong evidence that the θ phases

were disrupted during the growth and formed shorter periodical patterns as shown in Fig. 7.4.

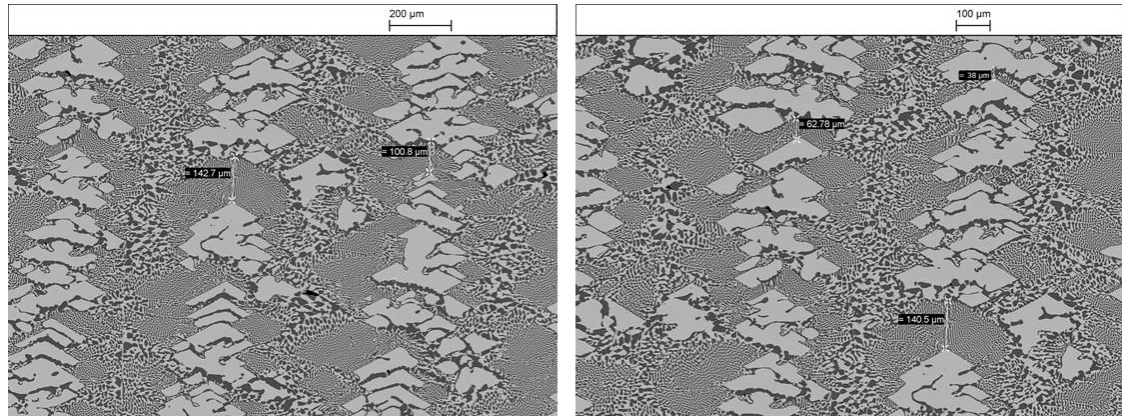


Fig. 7.4. The primary phases (Al_2Cu) with the measured periodic distance between them

It is very interesting to see that the majority of the primary phases showed in Fig. 7.4 exhibits the intermittent but periodic pattern because of the applied EMP, distance between each broken primary phases is around $38 \mu m$ and the big distance between the is ~ 60 or $140 \mu m$. While the withdrawal speed of the quartz tube for the Al-35%Cu was $30 \mu m/s$, and these evidences indicated that the growth of the θ phases were more likely disrupted and even broken when the pulsed Lorentz forces come around in every 1, 2 or 4 seconds, despite not all θ phases exhibited such as periodical patterns that resonate the frequency of the EMP applied. These may be due to either the applied force were still not strong enough to cause a complete disruption to the growth of all θ phases, or there were not enough free space for the growing θ phases to move away from their original direction of growth, and then finally be “seen” after solidified.

In summary, all results shown above clearly demonstrated that that the structure of alloys, including primary dendrites and primary phases are showed to be refined by the EMP applied. From the microstructures of alloys with and without EMP, the average size of primary dendrite trunk and

primary phase of intermetallic phases were measured and summarized in Fig. 7.5 as functions of the applied pulse voltages.

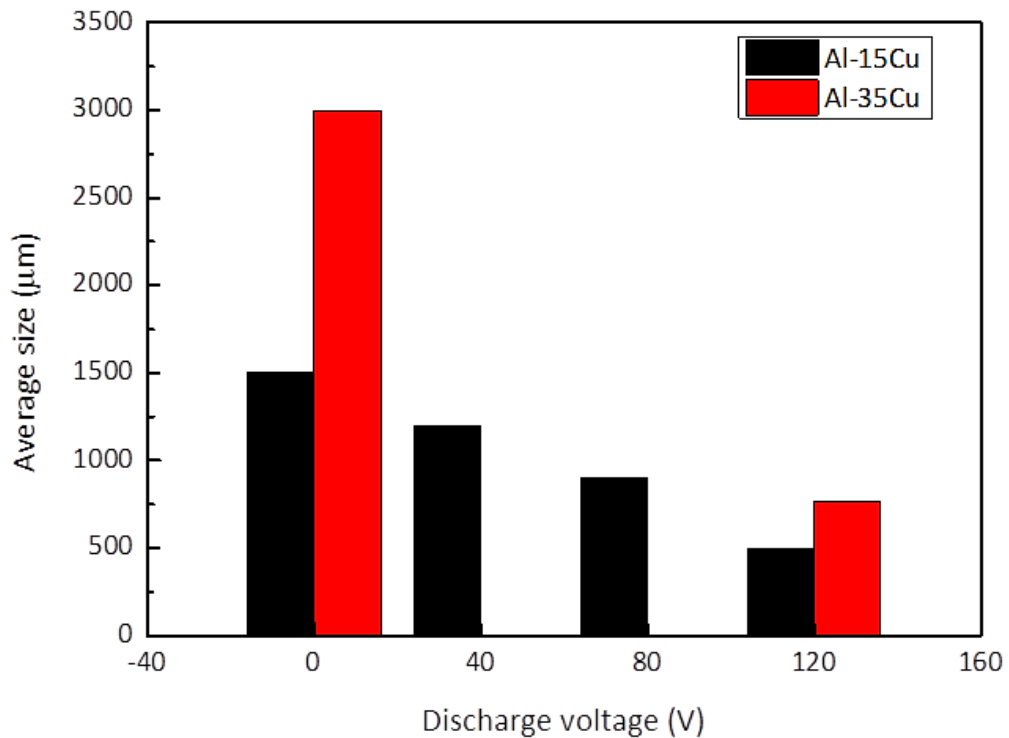


Fig. 7.5. The histogram showing the relationship between the average sizes of the primary dendrite trunk (Al-15%Cu) and θ phases (Al-35%Cu) as functions of EMP discharging voltage.

7.4.3 Effects of EMP on the growth of eutectic phase and solute distribution

Fig. 5.12-13 and 5.16 show that the EMP can influence the eutectic colony. Clear solute diffusion zones appeared in almost all eutectic colonies of the samples treated by EMP. The magnetic field was found to make layer-pattern compounds formed at the interface as reported in [202]. This mainly caused by enhanced solute diffusion at atomic scale due to intensive magnetization by the magnetic field applied.

The solute diffusion coefficient (D) can be enhanced by the transition frequency of atoms (Γ) and resulting in the development of an enhanced solute diffusion zone [203] when the magnetic field is high enough. The relationship of the diffusion coefficient and transition frequency is:

$$D = a^2 Pr \Gamma \quad (7.1)$$

where D is diffusion coefficient, a is the transition distance of atoms, Γ is mean transition frequency, and Pr is the probability of transition in the direction.

As seen from Fig. 5.13 and 5.16, the diffusion zone is formed near the edge of eutectic colonies. Cu is diamagnetic, while Al is paramagnetic materials. Hence when a magnetic field applied, in the diffusion layer, Cu atoms decreases but Al atoms increases [204], leading to the formation of such diffusion zones.

7.5 The advantage of 3-D microstructure analysis

Although the 2-D optical and SEM images can show the difference of the microstructures treated using different EMP parameters. However, the third dimension information is missing which is necessary for having a full 3-D microstructures in order to understand fully the true morphology of the structures.

Fig. 5.18 shows the reconstructed 3-D microstructures for Al-15Cu obtained using X-ray tomography. The 3-D information clearly illustrates the true morphology and the grain orientations. For the case without EMP (Fig. 5.18a), large and long dendrites (primary and secondary dendrites) grew vertically and formed a big dendrite network.

In the case of EMP applied (Fig. 5.18b), many shorter and equiaxed dendrites were found, using 3-D segmentation, those equiaxed dendrites can be easily separated to show their true 3-D morphology.

For the intermetallic phases in Al-35Cu alloy, Fig. 5.21a shows that, without EMP, the primary phases are very long columnar grown in the direction against gravity. While with EMP, Fig. 5.21b shows that there are two forms of primary phases: i) vertically straight column and ii) honeycomb-shaped horizontal column (perpendicular to gravity). The straight column is in the centre of the sample while the horizontal column is near the edge of sample, clearly the vertical column is formed in the central region where the force has much less effect, but horizontal column is from the edge where strong Lorentz force change its growing direction from vertically to horizontally.

Here, the 3-D information clearly shows the characteristics of the true microstructures formed under the conditions of without and with EMP, which cannot be fully revealed by the 2-D microstructures shown by the optical microscope or SEM especially in the case of the eutectic morphology, and the 3-D information shows the complex connection among each constituent in the eutectic colonies, impossible to understand using a 2-D image slice.

In addition, quantitative analysis of 3-D microstructure provides much more rich information and accuracy, for example, the volume fraction, grain or dendrite size and the orientation, etc.

Chapter 8 : Conclusions and future works

8.1 Conclusions

Based on the comprehensive analyses made on the results obtained from the in situ solidification experiments using pulse electric current and pulse electromagnetic field, and the corresponding simulations of the variables and multiphysics in the pulse electromagnetic field, the primary conclusions of this thesis are:

- A novel electromagnetic pulse device and a solidification apparatus were designed, built and commissioned in this research. It can generate programmable electromagnetic pulses with tuneable amplitudes, durations and frequencies to suit different alloys and sample dimensions for solidification research at university laboratory and at synchrotron X-ray beamlines. The success of this development has led to the winning of 9 shifts beam time at TOMCAT of PSI for in situ tomography studies of the evolution of solidification microstructure under pulse electromagnetic field. The planned experiment will be carried out in 10-13 June 2015.
- The results from the in situ with pulse electric current plus a static magnetic field experiments have revealed that Lorentz force as small as 0.3 mN can still influence the alloy melt and the floating dendrites, and even can create an enhanced melt flow in the semisolid temperature region to promote the fragmentation of dendrites. However the force is not sufficient enough to have sensible effect on the solid dendrite arrays when the liquid melt is in much small percentage.
- Systematic studies made using the novel pulse electromagnetic device have demonstrated that at a discharging voltage above 120 V, a complete equiaxed dendritic structure can be achieved for Al-15Cu alloy samples, the strong Lorentz force not only disrupt the growing directions

of primary dendrites, it is also sufficient enough to disrupt the growing directions of primary intermetallic Al_2Cu phases in the Al-35Cu alloys, resulting a refined microstructures. The applied electromagnetic fields also have significant effects on refining the eutectic structures and promoting the solute diffusion across the eutectic laminar structure. The research has demonstrated that the pulse electromagnetic field is a promising green technology for metal manufacture industry.

- The multiphysics simulation of the pulse electromagnetic field and the corresponding measurements have revealed that the designed device has an energy conversion efficiency of 85%, i.e 85% of the input energy can be converted into electromagnetic energy to act on the samples. Measurements and simulations also show that the Lorentz force and magnetic flux are the dominant parameters for achieving the grain refinement and enhancing the solute diffusion.
- The 3-D microstructures obtained by X-ray tomography technique shows much rich information than using 2-D techniques, and the true 3-D microstructure and morphologies of the samples treated with and without EMP have been clearly revealed by the 3-D dataset, further demonstrating more quantitatively how the applied pulse electromagnetic field change the solidification microstructures.

8.2 Future works

- It will be valuable to study other alloy systems using the developed pulse electromagnetic field device, especially for those having different electric conductivity compared to Al and Cu, such as Ni or Ti. The differences due to the alloy systems will be then quantified.
- In situ tomography experiment will give direct observation and evidence on how the pulse forces act on the growing phases to clarify the basic physics of how the growing phases are disrupted, and allow more practical approaches to be implemented in the future. Such experiment is scheduled at beamline TOMCAT of PSI in 10 -13 June 2015.

References

- 1 Kashyap, K. & Chandrashekar, T. Effects and mechanisms of grain refinement in aluminium alloys. *Bulletin of Materials Science* 24, 345-353 (2001).
- 2 Qian, M., John, D. H. S. & Frost, M. T. Zirconium alloying and grain refinement of Magnesium alloys *The Minerals, Metals & Materials Society* (2003).
- 3 Shi, H. & Zhang, W. Effects of electromagnetic stirring on microstructure of solidified aluminum alloys. *Transaction of Nonferrous Metals Society of China* 13, 1171-1174 (2003).
- 4 Ma, J. et al. Improving the Carbon Macrosegregation in High-Carbon Steel by an Electric Current Pulse. *Metals and Materials International* 15, 603-608 (2009).
- 5 Nakada, M., Shiohara, Y. & Flemings, M. C. Modification of Solidification Structures by Pulse Electric Discharging. *ISIJ International* 30, 27-33 (1990).
- 6 Liao, X., Zhai, Q., Luo, J., Chen, W. & Gong, Y. Y. Refining mechanism of the electric current pulse on the solidification structure of pure aluminum. *Acta Materialia* 55 3103-3109 (2007).
- 7 Li, L. et al. Columnar to Equiaxed Transition During Solidification of Small Ingot by Using Electric Current Pulse. *Journal of Iron and Steel Research, International* 16, 7-12 (2009).
- 8 Hall, E. O. The Deformation and Ageing of Mild Steel: III Discussion of Results. *Proceedings of the Physical Society Section B* 64 (1951).
- 9 Phillips, R. *Crystals, Defects and Microstructures Modeling Across Scales*. (The Press Syndicate of the University of Cambridge, 2001).

- 10 Weertman, J. R. Mechanical Behavior of Nanocrystalline Metals, https://uqu.edu.sa/files2/tiny_mce/plugins/filemanager/files/4300270/10.%20Mechanical%20Behavior%20of%20Nanocrystalline%20Metals.pdf. (Accessed 5 August 2014)
- 11 G.Dunlop et al. The Effect of Grain Size on the Mechanical Properties of AM-SC1 (2003) in Magnesium: Proceedings of the 6th International Conference Magnesium Alloys and Their Applications (ed K. U. Kainer), Wiley-VCH Verlag GmbH & Co. KGaA, Weinheim, FRG. doi: 10.1002/3527603565.ch14
- 12 J.W. Morris, J. The influence of grain size on the mechanical properties of steel. (2001).
- 13 Petch, N. J. The Cleavage Strength of Polycrystals. Journal of the Iron and Steel Institute 174, 25-28 (1953).
- 14 Vlasceanu, M. Effect of grain refinement on the microstructure, dendrite coherency and porosity of AZ91E magnesium alloy Master of Applied Science (MASc) thesis, Ryerson University, (2011).
- 15 J.A.Dantzig & M.Rappaz. Solidification. 1st edn, (Taylor and Francis Group.LLC, 2009).
- 16 Flemings, M. C. solidification processing. (McGraw-Hill 1974).
- 17 Kurz, W., Bezencon, C. & Gaumann, M. Columnar to equiaxed transition in solidification processing. Science and Technology of Advanced Materials 2, 185-191 (2001).
- 18 Zimmermann, G., Sturz, L., Schmitz, B., and Meyer, I. Investigation of the columnar-to-equiaxed transition during solidification of a transparent alloy using a Texus module. In 19th ESA Symposium on European Rocket and Balloon Programmes and Related Research (Bad Reichenhall, Germany) (2011).

- 19 Martorano, M. A., Beckermann, C. & Gandin, C. A. A Solutal Interaction Mechanism for the Columnar-to-Equiaxed Transition in Alloy Solidification. *Metallurgical and Materials Transaction A* 34A, 1657-1674 (2003).
- 20 Gabalcova, Z. & Lapin, J. Experimental study of columnar to equiaxed transition during directional solidification of intermetallic Ti-46Al-8Nb alloy *Metal* 19-21 (2009).
- 21 Campbell, J. & Harding, R. A. *Solidification Defects in Castings, the Basic Level lecture of IRC in Materials* (The University of Birmingham, 1994).
- 22 Ghosh, A. Segregation in cast products. *Sadhana* 26, 5-24 (2001).
- 23 Thomas, B. G. Modeling of Hot Tearing and Other Defects in Casting Processes 22A, 362-374 (2009).
- 24 Peti, F. & Grama, L. Aanalyze of the possible causes of porosity type defects in Aluminium high presure die cast parts. *Scientific Bulletin of the Petru Maior University of Targu Mures* 8 (2011).
- 25 Rappaz, M., Drezet, J.-M. & Gremaud, M. A New Hot-Tearing Criterion. *Metallurgical and Materials Transactions A* 30A, 449-455 (1999).
- 26 Li, S. *Hot Tearing in Cast Aluminum Alloys: Measures and Effects of Process Variables* Doctor of Philosophy thesis, The Worcester Polytechnic Institute, (2010).
- 27 Walkington, W. *Gas porosity-A guide to cerrecting the problems* (USA: Wheeling, Ill. : NADCA, c2006.).
- 28 Zhang, L., and Thomas, B.G. Inclusions in continuous casting of steel. In *XXIV National Steelmaking Symposium* (Morelia, Mich, Mexico), pp. 138-183 (2003).

- 29 Kim, J. Y., Lee, J. H. & Nahm, S. H. Effect of casting defect on mechanical properties of 17-4 ph stainless steel. *International Journal of Modern Physics B* 20, 4463-4468 (2006).
- 30 Xiao, W. et al. Casting Defects and Mechanical Properties of High Pressure Die Cast Mg-Zn-Al-RE Alloys. *Advanced Engineering Materials* 14, 68-76 (2012).
- 31 Das, A., Liu, G. & Fan, Z. Investigation on the microstructural refinement of an Mg-6 wt.% Zn alloy. *Materials Science and Engineering A* 419, 349-356 (2006).
- 32 Gutierrez-Urrutia, I. & S. Zaefferer, D. R. The effect of grain size and grain orientation on deformation twinning in a Fe-22 wt.% Mn-0.6 wt.% C TWIP steel. *Materials Science and Engineering A* 527, 3552-3560 (2010).
- 33 Fu, H.Z., and Liu, L. Progress of directional solidification in processing of advanced materials. In *Materials Science Forum*, 607-612 (2005).
- 34 Gueijman, S. F., Schvezov, C. E. & Ares, A. E. Vertical and horizontal directional solidification of Zn-Al and Zn-Ag diluted alloys. *Materials Transactions* 51, 1861-1870 (2010).
- 35 Song, C. J., Han, Q. & Zhai, Q. Review of grain refinement methods for as-cast microstructure of magnesium alloy. *China foundry* 6 (2009).
- 36 Petrič, M., Medved, J. & Mrvar, P. Effect of the grain refinement, modification and the cooling rate on microstructure of the AlSi10Mg alloy. *Materials and Geoenvironment* 53, 385-401 (2006).
- 37 Moffatt, H. K. Electromagnetic stirring. *Physics Fluids A* 3, 1336-1343 (1991).
- 38 Eskin, G. I. & Eskin, D. G. in *Ultrasonic Treatment of Light Alloy Melts, Second Edition Advances in Metallic Alloys*, 129-170 (CRC Press, 2014).

- 39 Kashyap, K. T. & Chandrashekar, T. Effects and mechanisms of grain refinement in aluminium alloys *Bulletin of Materials Science* 24, 345-353 (2001).
- 40 Johnsson, M., Backerud, L. & Sigworth, G. K. Study of the mechanism of grain refinement of aluminum after additions of Ti- and B-containing master alloys. *Metallurgical Transactions A* 24, 481-491 (1993).
- 41 Bermingham, M. J., McDonald, S. D., StJohn, D. H. & Dargusch, M. S. Beryllium as a grain refiner in titanium alloys. *Journal of Alloys and Compounds* 481, L20-L23 (2009).
- 42 Tamirisakandala, S., Bhat, R. B., Tiley, J. S. & Miracle, D. B. Grain refinement of cast titanium alloys via trace boron addition. *Scripta Materialia* 53, 1421-1426 (2005)
- 43 Guo, M. & Suito, H. Influence of Dissolved Oerium and Primary Inclusion Particles Ce₂O₃ and Ce₂SO₄ on Solidification Behavior of Fe-0.20massoloC-0.02 masso/oPAlloy. *ISIJ International*. 39, 722-729 (1999).
- 44 Dahle, E. S. *Grain Refinement of High Alloyed Steel With Cerium Addition*, Master thesis, in Department of Materials Science and Engineering (Norwegian University of Science and Technology, 2011).
- 45 Li, J., Ma, J., Gao, Y. & Zhai, Q. Research on solidification structure refinement of pure aluminum by electric current pulse with parallel electrodes. *Materials Science and Engineering A* 490, 452-456 (2008).
- 46 Eskin, G. I. *Ultrasonic Treatment of Light Alloy Melts*. 2nd Edition, CRC Press, London, UK, 2014
- 47 Kolesnichenko, A. F., Podoltsev, A. D. & Kucheryava, I. N. Action of Pulse Magnetic Field on Molten Metal. *ISIJ International* 34, 715-721 (1994).

- 48 P.Chernysh, V., N.Briskman, A. & S.Gladyshko, V. Welding of corrosion-resistant Austenitic steels using electromagnetic stirring of the pool. *Weld Prod* 20, 20-24 (1973).
- 49 Li, X. B., Lu, F. G., Cui, H. c. & Tang, X. H. Migration behavior of solidification nuclei in pure Al melt under effect of electric current pulse. *Transaction of Nonferrous Metals Society of China* 24, 192–198 (2014).
- 50 Asai, S. Birth and Recent Activities of Electromagnetic Processing of materials. *ISIJ International* 29, 981-992 (1989).
- 51 Garnier, M. Electromagnetic Processing of Liquid Materials in Europe. *ISIJ International* 30, 1-7 (1990).
- 52 Takahashi, K. & Taniguchi, S. Electromagnetic Separation of Nonmetallic Inclusion from Liquid Metal by Imposition of High Frequency Magnetic Field. *ISIJ International* 43, 820-827 (2003).
- 53 Thide, B. *Electromagnetic Field Theory*, Upsilon books, Uppsala, Sweden (2004).
- 54 Radjai, A., Miwa, K. & Nishio, T. An Investigation of the Effects Caused by Electromagnetic Vibrations in a Hypereutectic Al-Si Alloy Melt. *Metallurgical and Materials Transaction A* 29A, 1477-1484 (1998).
- 55 Thess, A., Votyakov, E., Knaepen, B. & Zikanov, O. Theory of the Lorentz force flowmeter. *New Journal of Physics* 9, 1-27 (2007).
- 56 Garner, R., Gregory, J., Taylor-Ashley, J. & Worthy, D. A Linear Electromagnetic Mass Driver Powered Elevator. *Journal of Physics Special Topics* (2013).
- 57 Kustusch, M. B. Student Understanding of Cross Product Direction and Use of Right-hand Rules: An Exploration of Representation and Context-dependence Doctor of Philosophy Physics thesis, North Carolina State University, (2011).

- 58 Israiloff, P. & Wagendristel, A. Mechanisms of grain refinement by mechanical effects on metals during solidification. *Z Metallk* 61, 743-750 (1970).
- 59 Nishimura, A. & Kawano, Y. Effect of direct vibration in an electromagnetic field on grain refinement of Aluminum alloys. *Journal of Japan Institute of Light Metals* 25, 193-199 (1975).
- 60 Takeuchi, H., Ikehara, Y., Yanai, T. & Matsumura, S. Quality improvement of continuously cast stainless steel blooms by electromagnetic stirring. *Tetsu To Hagane* 63, 1287-1296 (1977).
- 61 M.D.Sahu & V.A.Gadgil. Effects of electromagnetic fields on solidification of some Aluminium alloys. *Br Foundryman* 70, 89-92 (1977).
- 62 Mizutani, Y., Miwa, K., Tamura, T., Nakai, Y. & Otsuka, Y. Grain Refinement of Tough Pitch Copper by Electromagnetic Vibrations during Solidification. *Materials Transactions* 47, 1793-1797 (2006).
- 63 Li, M. J., Tamura, T., Omura, N. & Miwa, K. Microstructure formation and grain refinement of Mg-based alloys by electromagnetic vibration technique *Transactions of Nonferrous Metals Society of China* 20, 1192–1198 (2010).
- 64 Vives, C. Effects of Forced Electromagnetic Vibrations during the Solidification of Aluminum Alloys: Part I. Solidification in the Presence of Crossed Alternating Electric Fields and Stationary Magnetic Fields *Metallurgical and Materials Transaction B* 27B, 445-455 (1996).
- 65 Zhao, Z., Wang, J. & Liu, L. Grain refinement by pulse electric discharging and undercooling mechanism. *Materials and Manufacturing Processes* 26, 249-254 (2011).
- 66 Ma, J., Li, J., Gao, Y. & Zhai, Q. Grain refinement of pure Al with different electric current pulse modes. *Materials Letters* 63, 142-144 (2009).

- 67 Liotti, E. et al. A synchrotron X-ray radiography study of dendrite fragmentation induced by a pulsed electromagnetic field in an Al-15Cu alloy. *Acta Materialia* 70, 228-239 (2014).
- 68 Misra, A. K. Misra Technique 1 Applied to Solidification of Cast Iron *Metallurgical transaction A* 17A, 358-360 (1986).
- 69 Willers, B., Eckert, S., Michel, U., Haase, I. & Zouhar, G. The columnar-to-equiaxed transition in Pb-Sn alloys affected by electromagnetically driven convection. *Materials Science and Engineering A* 402, 55-65 (2005).
- 70 Ogasawara, T., Yoshikawa, N., Taniguchi, S. & Asai, T. Electromagnetic Flow around Two Non-conducting Particles and the Interaction Forces Different Diameter Cases. *ISIJ International* 43, 862-868 (2003).
- 71 Yoshikawa, T. & Morita, K. Refining of Si by the Solidification of Si-Al Melt with Electromagnetic Force. *ISIJ International* 45, 967-971 (2005).
- 72 Campanella, T., Charbon, C. & Rappaz, M. Grain Refinement Induced by Electromagnetic Stirring: A Dendrite Fragmentation Criterion. *Metallurgical and Materials Transaction A* 35A 3201-3210 (2004).
- 73 Hernandez, F. C. R. & Sokolowski, J. H. Effects and on-line prediction of electromagnetic stirring on microstructure refinement of the 319 Al-Si hypoeutectic alloy. *Journal of Alloys and Compounds* 480 416-421 (2009).
- 74 Du, Y., Lu, Y., Wang, T., Li, T. & Zhang, G. Effect of electromagnetic stirring on microstructure and properties of Al 0.5 CoCrCuFeNi alloy *Procedia Engineering* 27, 1129 - 1134 (2012).
- 75 Yao, L., Hao, H., Gu, S. W., Dong, H. W. & Zhang, X. G. Effects of electromagnetic stirring on microstructure and mechanical properties of super light Mg-Li-Al-Zn alloy *Transaction of Nonferrous Metals Society of China* 20, s388-s392 (2010).

- 76 Liu, Z., Mao, W.-m. & Liu, X.-m. Characterization on morphology evolution of primary phase in semisolid A356 under slightly electromagnetic stirring Transaction of Nonferrous Metals Society of China 20, s805-s810 (2010).
- 77 Yesilyurt, S., Motakef, S., Grugel, R. & Mazuruk, K. The effect of the traveling magnetic field (TMF) on the buoyancy-induced convection in the vertical Bridgman growth of semiconductors. Journal of crystal growth 263, 80-89 (2004).
- 78 Mazuruk, K. Control of melt convection using traveling magnetic fields. Advances in Space Research 29, 541-548 (2002).
- 79 Metan, V., Eigenfeld, K., Rübiger, D., Leonhardt, M. & Eckert, S. Grain size control in Al-Si alloys by grain refinement and electromagnetic stirring. Journal of Alloys and Compounds 487, 163-172 (2009).
- 80 Zaïdat, K., Mangelinck-Noël, N. & Moreau, R. Control of melt convection by a travelling magnetic field during the directional solidification of Al-Ni alloys. Comptes Rendus Mécanique 335, 330-335 (2007).
- 81 Gong, Y. Y., Luo, J., Jing, J., Zan, Q. & Zhai, Q. Structure refinement of pure aluminum by pulse magneto-oscillation. Materials Science and Engineering A 497, 147-152 (2008).
- 82 Pei, N., Gong, Y. Y., Li, R., Xia, Z. & Zhai, Q. Mechanism of pulse magneto-oscillation grain refinement on pure Al. China foundry 8, 47-50 (2011).
- 83 Yin, Z. X. et al. Refining of pure aluminum cast structure by surface pulsed magneto-oscillation. Journal of Materials Processing Technology 212, 2629-2634 (2012).
- 84 Li, B. et al. Effect of temperature field on solidification structure of pure al under pulse magneto-oscillation. China foundry 8, 172-176 (2011).

- 85 Samanta, D. & Zabarar, N. Control of macrosegregation during the solidification of alloys using magnetic fields. *International Journal of Heat and Mass Transfer* 49, 4850-4486 (2006).
- 86 Shu, D., Sun, B., Li, K., Wang, J. & Zhou, Y. Effects of Secondary Flow on the Electromagnetic Separation of Inclusions from Aluminum Melt in a Square Channel by a Solenoid. *ISIJ International* 42, 1241-1250 (2002).
- 87 Diamond.Light.Source. About us,
<http://www.diamond.ac.uk/Home/About/How-Diamond-Works.html>
(Accessed 13 June 2014).
- 88 Philliona, A. B. et al. In situ X-ray observation of semi-solid deformation and failure in Al-Cu alloys. *Acta Materialia* 59, 1436-1444 (2011).
- 89 Advanced.Photon.Source. Argonne Home
http://www.aps.anl.gov/About/APS_Overview (Accessed 13 June 2014).
- 90 Hussein, N. S. et al. Mapping single-crystal dendritic microstructure and defects in nickel-base superalloys with synchrotron radiation. *Acta Materialia* 56, 4715-4723 (2008).
- 91 Lightsources.org. Light Sources of the world,
<http://www.lightsources.org/regions/europe> (Accessed 13 June 2014).
- 92 Limodina, N. et al. In situ and real-time 3-D microtomography investigation of dendritic solidification in an Al-10 wt.% Cu alloy. *Acta Materialia* 57, 2300-2310 (2009).
- 93 Li, B., Brody, H. D., Black, D. R., Burdette, H. E. & Rau, C. Real time observation of dendritic solidification in alloys by synchrotron microradiography. *Journal of Physics D: Applied Physics* 39, 4450-4456 (2006).

- 94 Delaleau, P., Mathiesen, R. H., Schaffer, P. L., Arnberg, L. & Beckermann, C. in Modeling of Casting, Welding, and Advanced Solidification Process-XII. (eds Steve L. Cockcroft & Daan M. Maijer).
- 95 Carlsson, C. A. & Carlsson, G. A. Basic physics of X-ray imaging (Department of Radiation Physics, Faculty of Health Sciences, Linköping university, 1996).
- 96 Seltzer, S. X-Ray Mass Attenuation Coefficients, <http://physics.nist.gov/PhysRefData/XrayMassCoef/tab3.html> (Accessed 25 July 2014).
- 97 Hahn, J.E.P. X-ray Absorption Spectroscopy. (The University of Michigan, Ann Arbor, MI, USA). http://www.umich.edu/~jphgroup/XAS_Course/Harbin/CCC2_XAS.pdf. (Accessed 19 September 2014).
- 98 Mathiesen, R. H. et al. Time-Resolved X-Ray Imaging of Aluminum Alloy Solidification Process. Metallurgical and Materials Transactions B 33B, 613-623 (2002).
- 99 Mathiesen, R. H. & Arnberg, L. Stray crystal formation in Al-20 wt.%Cu studied by synchrotron X-ray video microscopy. Materials Science and Engineering A 413-414, 283-287 (2005).
- 100 Mathiesen, R. H. & Arnberg, L. Time-Resolved X-Ray Imaging in Studies of Advanced Alloy Solidification Processes. JCPDS-International Centre for Diffraction data (2006).
- 101 Arnberg, L. & H.Mathiesen, R. The Real-Time, High-Resolution X-Ray Video Microscopy of Solidification in Aluminum alloys. The Journal of The Minerals, Metals & Materials Society 59, 20-24 (2007).
- 102 L.Schaffer, P., Mathiesen, R.H., and Arnberg, L. High resolution X-ray imaging of alloy solidification. In The 5th Decennial International Conference on Solidification Processing, Sheffield (2007).

- 103 Dong, Q. et al. In Situ Observatin of columnar-to-equixed transition in directional solidification using synchrotron X-radiation imaging technique. *Materials Science and Engineering A* 530, 271-276 (2011).
- 104 Yasuda, H. et al. Development of X-ray Imaging for Observing Solidification of Carbon Steels. *ISIJ International* 51, 402-408 (2011).
- 105 Offi, F. et al. The attenuation length of low energy electrons in Yb. *Journal of Physics: Condensed Matter* 22, 1-5 (2010).
- 106 Arnberg, L. & Mathiesen, R. H. Imaging of Aluminium Alloy Solidification by Synchrotron X Radiation *Materials Forum* 28, 47-52 (2004).
- 107 Davis, T., Gao, D., Gureyev, T., Stevenson, A. & Wilkins, S. Phase-contrast imaging of weakly absorbing materials using hard X-rays. *Nature* 373, 595-598 (1995).
- 108 Mathiesen, R. H., Arnberg, L., Mo, F., Weitkamp, T. & Snigirev, A. Time-Resolved X-Ray imaging of Dendritic Growth in Binary Alloys. *Physical Review Letters* 83, 5062-5065 (1999).
- 109 Bogno, A. et al. In situ analysis of dendritic equiaxed microstructure formation in Al-Cu alloys by synchrotron X-ray radiography. *Transactions of The Indian Institute of Metals* 62, 427-431 (2009).
- 110 Billia, B. et al. In Situ Synchrotron X-ray Characterization of Microstructure Formation in Solidification Processing of Al-based Metallic Alloys. *ISIJ International* 50, 1929-1935 (2010).
- 111 H.Yasuda, Nagira, T., Yoshiya, M., Uesugi, M., Nakatsuka, N., Kiire, M., Sugiyam, A., Uesugi, K., and Umetani, K. In-situ observation of peritectic solidification in Sn-Cd and Fe-C alloys. In *The 3rd International Conference on Advances in Solidification Process* (2011).

- 112 Mirihanage, W. U., Arnberg, L. & Mathiesen, R. H. In-situ observation of transient columnar dendrite growth in the presence of thermo-solutal convection. *Materials Science and Engineering* 33 (2012).
- 113 Bogno, A., Nguyen-Thi, H., Reinhart, G., Billia, B. & Baruchel, J. Growth and interaction of dendritic equiaxed grains: In situ characterization by synchrotron X-ray radiography. *Acta Materialia* 61, 1303-1315 (2013).
- 114 Li, B., Brody, H. D. & A.kazimairov. Real-time obseravation of dendrite coarsening in Sn-13%Bi alloy by synchrotron microdiagraphy. *Physical Review E* 70, 1-4 (2004).
- 115 Mathiesen, R. H., Arnberg, L., P.Bleuet & Somogyi, A. Crystal Fragmentation and Columnar-to-equiaxed Transitions in Al-Cu Studied by Synchrotron X-Ray Video Microscopy. *metallurgical and Materials Transactions A* 37A, 2515-2524 (2006).
- 116 Shuleshova, O. et al. In situ observation of solidification processes in g-TiAl alloys by synchrotron radiation. *Acta Materialia* 58, 2408-2418 (2010).
- 117 S.Boden, Eckert, S., Willers, B. & G.Gerbeth. X-Ray Radioscopic Visualization of the Solutal Convection during Solidification of a Ga-30 Wt Pct In Alloy. *Metallurgical and Materials Transactions A* 39A, 613-623 (2008).
- 118 Thi, H. N. et al. Preliminary in situ and real-time study of directional solidification of metallic alloys by x-ray imaging techniques. *Journal of Physics D: Applied Physics* 36, A83 (2003).
- 119 Buffiere, J. Y., Maire, E., J. A., Masse, J. P. & Boller, E. In Situ Experiments with X ray Tomography: An Attractive Tool for Experimental Mechanics. *Experimental Mechanics* 50, 289-305 (2009).

- 120 Ramachandran, G. N. & Lakshminarayanan, A. V. Three-dimensional Reconstruction from Radiographs and Electron Micrographs: Application of Convolutions instead of Fourier Transforms. *Proceedings of the National Academy of Sciences of the United States of America* 68, 2236-2240 (1971).
- 121 Solomon, C. & Breckon, T. *Fundamentals of Digital Image Processing*. 1st Edition, (A John Wiley & Son, Ltd., 2011).
- 122 Yu, Y. & Wang, J. in *Image Processing (ICIP)*, 19th IEEE International Conference, 2085-2088 (Orlando, Florida, 2012).
- 123 Xie, Y., Chen, L. & Hofmann, U. G. Reduction of periodic noise in Fourier domain optical coherence tomography images by frequency domain filtering. *Biomed Tech* 57, 830-831 (2012).
- 124 Cherepanov, K. A. Electrical simulation of the solidification of steel ingots. *Stal*, 792-794 (1969).
- 125 Peel, D. A. & Pengelly, A. E. Heat transfer, solidification, and metallurgical structure in the continuous casting of aluminium. 186-196 (1970).
- 126 Mirković, D. & Schmid-Fetzer, R. Solidification curves for commercial Mg alloys obtained from heat-transfer modeled DTA experiments. *International Journal of Materials Research* 97, 119-129 (2006).
- 127 Samoilovich, Y. A., Yasnitskii, L. N. & Kabakov, Z. K. Hydrodynamic phenomena accompanying solidification of a continuous ingot under conditions of inductive MHD action *Magnetohydrodynamics* New York, N.Y. 19, 450-457 (1983).
- 128 Bermudez, A., and Durany, J. Mathematical model for the solidification of metal casting in a mold, *Proceedings of the IMACS International Symposium*, 305-310 (1983).
- 129 Clyne, T. W. Numerical modelling of directional solidification of metallic alloys. *Metal Science* V 16, 441-450 (1982).

- 130 Ding, Y., Yuan, X., Guo, T. & Hu, Y. Phase field simulation of dendrite growth under convection. *Acta Metallurgica Sinica (English Letters)* 23, 121-128 (2010).
- 131 Chen, S., Chen, J. & Yu, J. Simulation of grain growth during solidification of twin-roll continuously cast pure aluminum with a modified CA model. *Xiyou Jinshu Cailiao Yu Gongcheng/Rare Metal Materials and Engineering* 42, 2462-2466 (2013).
- 132 Delaleau, P., Beckermann, C., Mathiesen, R. H. & Arnberg, L. Mesoscopic simulation of dendritic growth observed in X-ray video microscopy during directional solidification of Al-Cu alloys. *ISIJ International* 50, 1886-1894 (2010).
- 133 Ren, Z., Dong, H., Deng, K. & Jiang, G. Influence of high frequency electromagnetic field on the initial solidification during electromagnetic continuous casting. *ISIJ International* 41, 981-985 (2001).
- 134 Li, T. J., Li, X. T., Zhang, Z. F. & Jin, J. Z. Effect of multielectromagnetic field on meniscus shape and quality of continuously cast metals. *Ironmaking and Steelmaking* 33, 57-60 (2006).
- 135 Toh, T., Takeuchi, E., Hojo, M., Kawai, H. & Matsumura, S. Electromagnetic control of initial solidification in continuous casting of steel by low frequency alternating magnetic field. *ISIJ International* 37, 1112-1119 (1997).
- 136 Song, X. P., Cheng, S. S. & Cheng, Z. J. Mathematical modelling of billet casting with secondary cooling zone electromagnetic stirrer. *Ironmaking and Steelmaking* 40, 189-198 (2013).
- 137 Szekely, J. & Chang, C. W. Electromagnetically driven flows in metals processing. *JOM* 28, 6-11 (1976).

- 138 Le, Q.-c., Guo, S.-j., Zhao, Z.-h., Cui, J.-z. & Zhang, X.-j. Numerical simulation of electromagnetic DC casting of magnesium alloys. *Journal of Materials Processing Technology* 183, 194-201 (2007).
- 139 Qian, Z.-D., Li, B.-W., Jia, G.-L. & He, J.-C. Numerical Computation of Electromagnetic Fields in Metals Using A Modified Finite-difference Time Domain Method. *ISIJ International* 41, 683-688 (2001).
- 140 Zhang, P., Zheng, L., Iseler, G. & Bliss, D. in American Society of Mechanical Engineers, Heat Transfer Division, (Publication) HTD.5th Edition, 115-122.
- 141 Deng, J., Li, C., Zhao, Z., Tu, F. & Yu, H. Numerical simulation of magnetic flux and force in electromagnetic forming with attractive force. *Journal of Materials Processing Technology* 184, 190-194 (2007).
- 142 Wang, B., Yang, Y., Ma, X. & Tong, W. Simulation of electromagnetic-flow fields in Mg melt under pulsed magnetic field *Transactions of Nonferrous Metals Society of China* 20, 283-288 (2010).
- 143 Basham, E., Yang, Z. & Liu, W. Circuit and Coil Design for In Vitro Magnetic Neural Stimulation Systems. *IEEE Transaction on Biomedical Circuits and Systems* 54, 1-12 (2008).
- 144 Currie, I. G. *Fundamental Mechanics of Fluids*, 4th Edition. (Taylor & Francis, 2012).
- 145 Natarajan, T. T. & El-Kaddah, N. Finite element analysis of electromagnetic and fluid flow phenomena in rotary electromagnetic stirring of steel. *Applied Mathematical Modelling* 28, 47-61 (2004).
- 146 Vizman, D., Fischer, B., Friedrich, J. & Müller, G. 3D numerical simulation of melt flow in the presence of a rotating magnetic field. *International Journal of Numerical Methods for Heat and Fluid Flow* 10, 366-384 (2000).

- 147 Mihelčić, M. & Wingerath, K. Three-dimensional simulations of the Czochralski bulk flow in a stationary transverse field and in a vertical magnetic field: Effects on the asymmetry of the flow and temperature distribution in the Si melt. *Journal of Crystal Growth* 82, 318-326 (1987).
- 148 Hall, M. C. & Walker, J. S. Heat and mass transfer through a liquid metal in an infinitely long, rotating cylinder with a uniform, transverse magnetic field. *International Journal of Heat and Mass Transfer* 36, 3509-3514 (1993).
- 149 Weiqiang, Z., Yuansheng, Y., Qingmin, L., Yuefeng, Z. & Zhuangqi, H. Numerical simulation of fluid flow in electromagnetic centrifugal casting. *Modelling and Simulation in Materials Science and Engineering* 4, 421 (1996).
- 150 Spitzer, K.-H., Dubke, M. & Schwerdtfeger, K. Rotational electromagnetic stirring in continuous casting of round strands. *Metallurgical Transactions B* 17, 119-131 (1986).
- 151 Chung, S. & Yoon, J. Numerical analysis of effect of electromagnetic stirring on solidification phenomena in continuous casting. *Ironmaking & steelmaking* 23, 425-432 (1996).
- 152 Ma, X., Yang, Y. & Wang, B. Effect of pulsed magnetic field on superalloy melt. *International Journal of Heat and Mass Transfer* 52, 5285-5292 (2009).
- 153 Smirnov, S. A. et al. Mathematical simulation of electromagnetic stirring of liquid steel in a DC arc furnace. *High temperature* 48, 68-76 (2010).
- 154 Baokuan, L. I., Okane, T. & Umeda, T. Modeling of molten metal flow in a continuous casting process considering the effects of argon gas injection and static magnetic-field application. *Metallurgical and Materials Transactions B: Process Metallurgy and Materials Processing Science* 31, 1491-1503 (2000).

- 155 Tu, J., Yeoh, G.-H. & Liu, C. Computational Fluid Dynamics. 2nd Edition, (Elsevier, 2013).
- 156 Liang, D. et al. Grain refinement of commercial pure Al treated by Pulsed Magneto-Oscillation on the top surface of melt. China foundry 12, 48-53 (2015).
- 157 Cambridge Quality Technology. Electromagnetic instigation of dendritic break-up. www.cambridgequalitytechnology.co.uk (Accessed 13 June 2013)
- 158 Compton, A. J. Basic Electromagnetism and its Applications. 1st Edition, 77-80 (Chapman and Hall, 1986).
- 159 C.Rakete et al. Compact x-ray microradiograph for in situ imaging of solidification processes: Bringin in situ x-ray micro-imaging from the synchrotron to the laboratory. Review of Scientific Instruments 82, 1-10 (2011).
- 160 Livshiz, Y., and Gafri, O. Technology and equipment for industrial use of pulse magnetic fields. In Digest of Technical Papers-IEEE International Pulsed Power Conference, 475-478 (1999).
- 161 Gao, Y., Li, Q., Gong, Y. Y. & Zhai, Q. Comparative study on structural transformation of low-melting pure Al and high-melting stainless steel under external pulsed magnetic field. Materials Letters 61, 4011- 4014 (2007).
- 162 Li, Q., Song, C., Li, H. & Zhai, Q. Effect of pulsed magnetic field on microstructure of 1Cr18Ni9Ti austenitic stainless steel. Materials Science and Engineering A 466, 101-105 (2007).
- 163 Sahay, K. & Dwivedi, B. Design and Analysis of Supercapacitors Energy Storage System for Energy Stabilization of Distribution Network. Electrical Power Quality and Utilisztion 15 (2009).

- 164 Dan, S. & Ning, L. The Research on the Quick Discharge Circuit of Shunt Capacitor. *Journal of Power and Energy Engineering* 2, 579-585 (2014).
- 165 Bakhoum, E. G. Constant voltage ultracapacitor. *Journal of Renewable and Sustainable Energy* 4 (2012).
- 166 L.Boylestard, R. *Introductory Circuit Analysis*. 10th Edition, (Pearson Education, Inc., 2003).
- 167 Hartmad, W. & Romheld, M. Design of a high cuffwznt pulse generator for magneto forming. *IEEE* 310-313 (2004).
- 168 Zaber. Motorized Linear Slide, 75 mm travel, RS-232 plus manual control,
http://www.zaber.com/products/product_detail.php?detail=T-LSR075A&tab=Accessories (Accessed 10 July 2014)
- 169 zaber_wiki. Software/Zaber Console,
http://www.zaber.com/wiki/Software/Zaber_Console (Accessed 10 July 2014)
- 170 Feng, H. et al. Continuous melting and directional solidification of silicon ingot with an electromagnetic cold crucible. *China foundry* 9, 24-27 (2012).
- 171 Nave, R. Solenoid, <http://hyperphysics.phy-astr.gsu.edu/hbase/magnetic/solenoid.html#c3> (Accessed 10 July 2014)
- 172 Stephan, J. M., Gieschke, P., Paul, O. & Ruther, P. Spatially Resolved Measurement of Magnetic Flux Density Using a 32×32 CMOS-Integrated Hall Sensor Array *Procedia Engineering* 5, 981-984 (2010).
- 173 Honeywell Inc. Hall effect sensing and application.
http://sensing.honeywell.com/index.php?ci_id=47847 (Accessed 20 June 2014)

- 174 Popovic, R. S., Randjelovic, Z. & Manic, D. Integrated Hall-effect magnetic sensors. *Sensors and Actuators A: Physical* 91, 46-50 (2001).
- 175 GAUSSMETERS / GM08. Hirst Magnetic Instruments Ltd. <http://www.gaussmeter.co.uk/product/gauss-meter-gm08/> (Accessed 3 November 2014)
- 176 AbdulMatin, M. Microstructure evolution and thermomechanical fatigue of solder materials, Phd Thesis, Eindhoven University of Technology, (2005).
- 177 Kovács, J., Rogozsán, B., Rónaföldi, A., and Roósz, A. Unidirectional solidification of Sn- Pb alloys under forced melt flow. In *The 3rd International Conference on Advances in Solidification Processes* (IOP Publishing Ltd) (2011).
- 178 Plevachuk, Y. et al. Density, Viscosity, and Electrical Conductivity of Hypoeutectic Al-Cu Liquid Alloys. *Metallurgical and Materials Transaction A* 39A (2008).
- 179 Massalski, T. B., Okamoto, H., Subramanian, P. & Kacprzak, L. Binary alloy phase diagrams. vol. 3. ASM International, 1990, 1485 (1990).
- 180 Pandey, A.B. High temperature heat treatable aluminum alloys including copper, magnesium and lithium; used at temperatures from -420-650 degrees F. (-251-343 degrees C.); strengthened by dispersion of particles based on the L12 intermetallic compound Al₃X; castings; high strength, ductility, noncracking, toughness. (Google Patents) (2011).
- 181 John, C. *Casting practice the 10 rules of castings*. (Elsevier Butterworth-Heinemann, 2004).
- 182 Ashton, A. et al. Dawn Science v1.5 (DLS Edition). ZENODO. zenodo.14084 (2014).

- 183 Basham, M. et al. Data Analysis Workbench (DAWN) Journal of synchrotron radiation, 22, 3 (2015)
- 184 COMSOL Multiphysics. Introduction to COMSOL Multiphysics. <https://uk.comsol.com/documentation/IntroductionToCOMSOLMultiphysics.pdf> (Accessed 10 May 2014).
- 185 Quintana, I., Azpilgain, Z., Pardo, D., and Hurtado, I. (2011). Numerical Modeling of Cold Crucible Induction Melting In The COMSOL Conference (Stuttgart).
- 186 Dinesh, J. Modelling and Simulation of a Single Particle in Laminar Flow Regime of a Newtonian Liquid, proceeding of the COMSOL Conference 2009, <http://www.comsol.com/paper/modelling-and-simulation-of-a-single-particle-in-laminar-flow-regime-of-a-newton-7389> (accessed 4 March 2015)
- 187 Kuzmin, D., Mierka, O. & Turek, S. On the implementation of the κ - ϵ turbulence model in incompressible flow solvers based on a finite element discretisation. International Journal of Computing Science and Mathematics 1, 193-206 (2007).
- 188 Bernard, D., Nielsen, Ø., Salvoc, L. & Cloetens, P. Permeability assessment by 3D interdendritic flow simulations on microtomography mappings of Al-Cu alloys. Materials Science and Engineering: A 392, 112-120 (2005).
- 189 Ho, C. Y. et al. Electrical Resistivity of Ten Selected Binary Alloy Systems. J.Phys.Chem.Ref.Data 12 (1983).
- 190 Konstantinova, N. Y., Popel, P. S. & Yagodin, D. A. The Kinematic Viscosity of Liquid Copper-Aluminum Alloys. High temperature 47 (2009).
- 191 Technical Data, <http://www.robsonscientific.co.uk/technical-data> (Accessed 12 August 2014)

- 192 Pawar, S. D., Murugavel, P. & Lal, D. M. Effect of relative humidity and sea level pressure on electrical conductivity of air over Indian Ocean. *Journal of Geophysical Research: Atmospheres* 114, D02205 (2009).
- 193 Hidnert, P., and Krider, H.S. Thermal expansion of Aluminum and various important Aluminum alloys. *Scientific Papers of the Bureau of Standards* 48 (1952).
- 194 Guerrier, P., Hattel, J.H., Guerrier, P., and Hattel, J.H. Numerical modeling of magnetic induction and heating in injection molding tools. In *Proceedings of International Conference on Advanced Manufacturing Engineering and Technologies (NEWTECH 2013)* (Kungl. Tekniska högskolan I Stockholm) (2013).
- 195 S. Bartkevičius & Novickij, J. The influence of pulsed magnet heating on maximal value of generated magnetic field *Measurement Science Review* 7 (2007).
- 196 Ruvalcaba, D., Mathiesen, R. H., Eskin, D. G., Arnberg, L. & Katgerman, L. In situ observations of dendritic fragmentation due to local solute-enrichment during directional solidification of an aluminum alloy. *Acta Materialia* 55, 4287-4292 (2007).
- 197 Guo, Z., Mi, J., Xiong, S. & Grant, P. S. Phase Field Simulation of Binary Alloy Dendrite Growth Under Thermal- and Forced-Flow Fields: An Implementation of the Parallel-Multigrid Approach. *Metallurgical and Materials Transaction B* 44 (2013).
- 198 Li, X. et al. Columnar-to-equiaxed transitions in al-based alloys during directional solidification under a high magnetic field. *Journal of Crystal Growth* 312, 267-272 (2010).
- 199 Eskin, D. G., Suyitno & Katgerman, L. Mechanical properties in the semi-solid state and hot tearing of aluminium alloys. *Progress in Materials Science* 49, 629-711 (2004).

- 200 Zhang, Z., Xun, J. & Shi, L. Study on Multiple Electromagnetic Continuous Casting of Aluminum Alloy. *Journal of Materials Science & Technology* 22 (2006).
- Zhu, W., Ren, Z., Ren, W., Zhong, Y. & Deng, K. Effects of high magnetic field on the unidirectionally solidified Al–Al₂Cu eutectic crystal orientations and the induced microstructures. *Materials Science and Engineering A* 441, 181-186 (2006).
- 202 Li, D.-g. et al. Diffusion layer growth at Zn/Cu interface under uniform and gradient high magnetic fields. *Materials Science and Engineering: A* 495, 244-248 (2008).
- 203 Zhao, J., Yang, P., Zhu, F. & Cheng, C.-q. The effect of high magnetic field on the growth behavior of Sn–3Ag–0.5Cu/Cu IMC layer. *Scripta Materialia* 54, 1077-1080 (2006).
- 204 Li, X., Ren, Z. & Fautrelle, Y. Effect of a high axial magnetic field on the microstructure in a directionally solidified Al–Al₂Cu eutectic alloy. *Acta Materialia* 54, 5349-5360 (2006).

List of Figures

Fig. 2.1.	The relationship of grain size and yield stress of steel and iron	5
Fig. 2.2.	The formation of dendrite microstructures during the solidification of columnar dendrite and equiaxed dendrite.	7
Fig. 2.3.	Schematic of the right hand rule, the Lorentz force generated in an electromagnetic vibration technique, the direct-contact pulse electric current technique and the contact pulse electric current technique.....	15
Fig. 2.4.	Schematic of the Lorentz force generated from the interaction between an induced current and the induced magnetic field, the setup of the electromagnetic stirring and pulse magneto oscillation, the travelling magnetic field, and the Lorentz force directions..	16
Fig. 2.5.	The X-ray linear attenuation coefficients of typical metal elements in the X-rays energy range of 1-200 keV	27
Fig. 2.6.	The sample thickness and attenuation length of Al-15%Cu and Al-35%Cu and Al ₂ Cu phase and Al, Cu phase	31
Fig. 2.7.	The attenuation length of Al-15wt%Cu, Al, Cu and Al ₂ Cu phase for the energy range 3-30 keV.....	32
Fig. 2.8.	The principle and setup of X-ray imaging and tomography experiments	35
Fig. 2.9.	The procedure of 3-D reconstruction	37
Fig. 2.10.	Overview of image processing procedure	38
Fig. 2.11.	The comparison of images between original, Fourier domain image, Fourier transform with bandrejected filter on the periodical noise and processed images	41

Fig. 3.1. The solidification apparatus mounted on the sample stage of beamline B16 of DLS, the pulse signal generator, the temperature control and data login system, the solidification apparatus and experimental setup, the mounting of the quartz holder held by the mechanical clamp and pressed against the copper heating plates, and the Al-15%Cu thin foil sample encapsulated inside the quartz sample holder with two chromel wires 51

Fig. 3.2. The fluorescent image of the square-shaped X-ray beam illuminating the Duratec ceramic plates and the sample under heating, the image were taken with control room light turning on and the light turning off 53

Fig. 3.3. A typical raw X-ray image that contains an array of faint dendrites, and many lines of periodical noises and defects and the same image processed using Fourier transform and inverse Fourier transform techniques, and the array of dendrites are clearly revealed. 56

Fig. 3.4. The temperature profiles measured by the two thermocouples, T1 and T2 in the experiment V1 58

Fig. 3.5. The distance of dendrite detach from its arm and detached dendrite velocity 58

Fig. 3.6. The fragmentation of a dendrite without PEC (from experiment V1) 60

Fig. 3.7. The temperature profiles measured by the two thermocouples attached to the upper (T1) and lower (T2) heaters in experiment V2 62

Fig. 3.8. The cyclic movement path of the dendrite after detached from its primary dendrite under the PEC 62

Fig. 3.9. The cyclic movement of the detached dendrite tip under the applied PEC. Images are extracted from the video of experiment V2 63

Fig. 3.10. The temperature profiles measured by the two thermocouples attached to the upper (T1) and lower (T2) heaters in experiment V3 65

Fig. 3.11. Eight images selected from the video of experiment V3, showing the growth of 10 dendrites against gravity before applying PEC. The growths of four dendrites, D1, D2, D3 and D4 are tracked 68

Fig. 3.12. The grown lengths of dendrites D1-D4 as a function of time 71

Fig. 3.13. The growth of dendrite D1 and the moment of the dendrite tip breaks off. 71

Fig. 3.14. The growth of dendrite D2 and the moment of the dendrite tip breaks off 72

Fig. 3.15. The cyclic movement path of the broken off dendrite tip from D1 with a frequency of 1Hz 72

Fig. 3.16. The temperature profiles measured by the two thermocouples attached to the upper (T1) and lower (T2) heaters in experiment V4 73

Fig. 3.17. Four images from the video of experiment V4, showing an array of solid dendrites oscillate harmonically under the 1 Hz PEC applied and the oscillated path of the wobbled dendrite 74

Fig. 3.18. The temperature profiles measured by the two thermocouples attached to the upper (T1) and lower (T2) heaters in experiment V5 75

Fig. 3.19. Four images from the video of experiment V5, showing an array of solid dendrites oscillate harmonically under the 10 Hz PEC applied and the oscillated path of the wobbled dendrites..... 76

Fig. 4.1. A photo, showing each functional unit of the programmable EMP device, the small-scale solidification apparatus and the temperature control system..... 78

Fig. 4.2. The schematic setup of EMP and induced force 80

Fig. 4.3. The conceptual design of the electric circuit for the EMP device..... 80

Fig. 4.4. The electric circuit used in the simulation..... 83

Fig. 4.5. The voltage charging profiles for the charging unit when using different combination of R1 and C 87

Fig. 4.6. The charging and discharging profiles in three cycles for the optimized circuit design..... 88

Fig. 4.7. The actual circuit design of the EMP device..... 93

Fig. 4.8. Two photos showing the Aluminium container box for EMP charging unit and the electric and electronic components inside the charging unit..... 95

Fig. 4.9. The pulse generating unit with a connection box connected to the cooper coil wrapped by Fiberfrax mastic and the helical copper coil inside the Fiberfrax mastic..... 95

Fig. 4.10. The box containing the trigger unit..... 96

Fig. 4.11. A photo showing the assembled EMP device with all units 97

Fig. 4.12. A CAD drawing, showing the dimension and the materials used for making the electric resistance furnace. 99

Fig. 4.13. A photo and a 3-D CAD drawing, showing the assembly of the furnace, the glass tube mould and linear stage 99

Fig. 4.14. Photos, showing a Hall probe positioned in the middle of the coil, a Gauss meter connected to an oscilloscope for data display and the interlink between the oscilloscope and Digital Storage Oscilloscope (DSO) software. 101

Fig. 4.15. The measured magnetic flux density with different charging voltages. 101

Fig. 4.16.The measured magnetic flux density peak value as a function of the discharging voltage. 102

Fig. 5.1. The Sn-Pb phase diagram, and the Sn-18Pb alloy selected for the experiment..... 105

Fig. 5.2. The Al-Cu binary phase diagram [180], and the Al-15Cu and the Al-35Cu alloys used in the experiments. 105

Fig. 5.3. A schematic, and a photo, showing the counter-gravity casting apparatus used in the research. 107

Fig. 5.4. Two CAD drawings, showing the furnace heating coil, the glass tube containing alloy melt mounted on a Duratec ceramic rod and stage, and the EMP coil..... 109

Fig. 5.5. The temperatures of the samples for calculating the cooling rates for Sn-18Pb, Al-15Cu and Al-35Cu..... 112

Fig. 5.6. The measured temperature profiles at P1, P2, and P3 for Sn-18Pb, Al-15Cu and Al-35Cu during the solidification experiments. 117

Fig. 5.7. The solidification microstructures of the Sn18Pb alloy samples cast without and with 1 Hz EMP of 40 V, 80 V, and 120 V; and 10 Hz EMP of 40 V, 80 V, 120 V and the example of microstructure measurement..... 120

Fig. 5.8. The macro and microstructure of sample Al-15Cu0V..... 124

Fig. 5.9. The macro and microstructure of sample Al-15Cu40V..... 125

Fig. 5.10. The macro and microstructure of sample Al-15Cu80V..... 126

Fig. 5.11. The macro and microstructure of sample Al-15Cu120V 127

Fig. 5.12. A series of SEM backscattered electron images, showing the eutectic colonies and the θ phases within the colonies of the Al15Cu samples cast without EMP and with 1 Hz EMP of 40 V, 80 V, and 120 V..... 129

Fig. 5.13. A series of backscattered electron images with EDX lines scans, illustrating the solute diffusion zones along the boundaries of the θ phases inside the eutectic colonies for the Al15Cu samples cast by without and with 1 Hz EMP of 40 V, 80 V and 120 V..... 130

Fig. 5.14. The macro and microstructure of sample, Al-35Cu0V..... 132

Fig. 5.15. The macro and microstructure of sample, Al-35Cu120V 133

Fig. 5.16. Backscattered electron images with EDX lines scans, illustrating the solute diffusion zones along the boundaries of the θ phases inside the eutectic colonies for the Al35Cu samples 135

Fig. 5.17. Series images showing a SEM microstructural feature of interest marked by the dotted lines, a needle-shaped sample for tomography scans, the reconstructed 3-D microstructure and the selected segmentation a primary Al dendrite. 138

Fig. 5.18. The 3-D primary Al dendrites of Al15Cu samples cast without EMP and with EMP of discharge voltage 120 V 1 Hz. The X-ray images taken from lab based X-ray CT scan..... 140

Fig. 5.19. Comparison of the 2-D and 3-D dataset for the primary Al dendrites from the samples Al15Cu0V and Al15Cu120V. The tomography obtained from I13, DLS..... 142

Fig. 5.20. The 2-D and 3-D microstructure of Al15Cu120VH with EMP treatment on half-sample. The tomography obtained from TOMCAT, PSI. 143

Fig. 5.21. The 3-D primary θ phases of Al35Cu samples cast without EMP and with EMP of 1Hz, 120 V. The X-ray images taken from lab based X-ray CT scan. 144

Fig. 5.22. Comparison of the 2-D and 3-D dataset for the θ phases of Al35Cu without and with 120V 1Hz of EMP treatment. The tomography obtained from I13, DLS..... 145

Fig. 5.23. A series of images of the eutectic structures of Al15Cu without and with 120V 1Hz of EMP treatment. The tomography data were obtained from I13, DLS. 147

Fig. 5.24. A series of images of the eutectic structures of Al35Cu without and with 120V 1Hz of EMP treatment. The tomography data were obtained from I13, DLS. 148

Fig. 6.1. A 3-D cut-off showing a glass tube mould containing liquid melt inside the EMP coil and the 2-D axis-symmetry computational domain used in the simulation 155

Fig. 6.2. The upper half of the computational domain, and the corresponding mesh structures for each sub-domains and the close-up of the mesh structure for SB1, SB2 and SB3..... 156

Fig. 6.3. The simulated magnetic flux densities using the discharging voltages of 40, 80, 120, 160, 200 and 240 V. The simulation was carried out by disabling quartz tube and the melt sub-domains (with $C=1$). 160

Fig. 6.4. Comparison of the measured and simulated magnetic flux density profiles with $C = 1$, and $C = 0.85$ 162

Fig. 6.5. The simulated magnetic flux densities using the discharging voltages of 40, 80, 120, 160, 200 and 240 V. The simulation was carried out by disabling quartz tube and the melt subdomains (with $C=0.85$). 163

Fig. 6.6. The simulated magnetic flux densities using the discharging voltages of 40, 80, 120, 160, 200 and 240 V. The simulation was carried out by enabling the quartz tube and the melt subdomains 164

Fig. 6.7. The simulated magnetic flux density profiles versus the discharge voltages with and without the quartz tube and the alloy melt..... 165

Fig. 6.8. The simulated magnetic flux density peak value as a function of the discharge voltage with and without the quartz tube and the alloy melt.. 165

Fig. 6.9. The simulated induced current density distributions inside the alloy melt for the discharge voltage of 40, 80, 120, 160, 200 and 240 V respectively..... 167

Fig. 6.10. The simulated induced current density profiles and peak values for the discharge voltage of 40, 80, 120, 160, 200 and 240 V.. 168

Fig. 6.11. The simulated Lorentz force distribution acting on the alloy melt for the case of 40, 80, 120, 160, 200 and 240 V discharge voltage 169

Fig. 6.12. The simulated Lorentz force profiles and its peak values acting on the alloy melt at point P5 for the case of 40, 80, 120, 160, 200 and 240 V discharge voltage 170

Fig. 6.13. The change of the direction of Lorentz force in one pulse cycle for the case of 120 V. 171

Fig. 6.14. The simulated velocity fields inside the alloy melt for the case of 120 V discharge voltage. 173

Fig. 6.15. The simulated velocity fields inside the alloy melt in one pulse cycle for the case of 120 V 174

Fig. 6.16. The simulated velocity field at the simulated time step of 0.035 s for the discharge voltage of 40, 80, 120, 160, 200 and 240 V. 175

Fig. 7.1. The characteristic profiles for current charging and discharging..... 178

Fig. 7.2. The comparison of the copper coil used in this research and the hollow tube copper coil used for PMO experiments in other research 179

Fig. 7.3. The strength of the Al-Cu alloy as function of temperature. 186

Fig. 7.4. The primary phases (Al_2Cu) with the measured periodic distance between them 188

Fig. 7.5. The histogram showing the relationship between the average sizes of the primary dendrite trunk (Al-15%Cu) and θ phases (Al-35%Cu) as functions of EMP discharging voltage..... 189



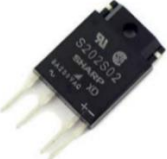
List of Tables

Table 3.1. The synchrotron X-ray experiments that produced the results presented in this Chapter	47
Table 3.2. The in situ experiments conducted and the parameters used.	55
Table 3.3. The parameters used for the five anti-parallel (with gravity) directional solidification experiments	57
Table 4.1. The time needed to fully charge the EMP device when using R1 and C of different values	85
Table 4.2. The main components used in each unit of the EMP device	90
Table 5.1. A summary of the alloys, samples and the parameters used for the solidification experiments without and with electromagnetic fields	113
Table 5.2. A summary of the microstructure measurement from Sn-Pb samples without and with electromagnetic fields.....	121
Table 5.3. A summary of the microstructure measurement from Al-Cu samples without and with electromagnetic fields from 2-D microstructure images.....	136
Table 5.4. A summary of the microstructure measurement from Al-Cu samples without and with electromagnetic fields from 3-D microstructure images.....	146
Table 6.1. The computational sub-domains, size and materials properties used in the simulation	157
Table 6.2. A summary of the input discharge voltage, measured and simulated magnetic flux density (MFD), induced current density (ICD) and Lorentz force.....	159

Appendices

Appendix 1.

Table A. 1. *The components used in EMP.*

Unit	Component	Component photo and model
The charging unit	Microswitch	
		Microswitch with Lever
	Single Pole Double Throw (SPDT) Relay ...	
		30A SPDT Power Relay 240Vac
	Solid state relay	
		Sharp solid state relay

	<p>Single Pole Double Throw (SPDT) Relay ...</p>	
		<p>15A/12Vdc SPDT Miniature Relay</p>
	<p>Cooling Fan</p>	
		<p>120mm Black PC Case Fan</p>
	<p>Emergency switch</p>	
		<p>APEM A01ES+A0154B Switch, Emergency DPST</p>
<p>The pulse generating unit</p>	<p>Connector</p>	
		<p>Neutrik Speakon : Series 2 Pole Speakon Connector</p>

Appendix 2. Manufacturing and calculating for Furnace

To manufacture the furnace, there are 4 steps as follows:

Step 1: to find out the total power of the furnace

$$Area_{in} = \pi h_h d_h \quad (A-1)$$

Where $Area_{in}$ the surface area of inner furnace, h_h is height of heating zone, d_h is diameter of heating zone. Thus, total power for the heating needs is

$$P_{total} = P' \times Area_{in} \quad (A-2)$$

Step 2: calculate the diameter of heating element: D_{em}

$$D_{em} = 34.4 \times \sqrt[3]{\frac{P^2 \times \rho_t}{V_h^2 \times v_{per}}} \quad (A-3)$$

Where P is power of heating element (kw), V_h is voltage of heating element, v_{per} is permitted power load on surface (Watt/cm²) and ρ_t is resistivity of heating element at designed temperature.

Length of heating element: L_{em}

$$L_{em} = \frac{V_h^2 \times area_{cross}}{10^3 \times P \times \rho_t} \quad (A-4)$$

Where $area_{cross}$ is the area cross section of heating element

Step 3: length of the helical coil

L_{he} is total length of helical coil, D_{he} is diameter of helical coil

Step 4: verify the dimension of heating element

$$v_{effective} = \frac{10^3 \times P}{\pi \times D_{em} \times L_{em}} \leq v_{per} \quad (A-5)$$